UNIVERSITAT POLITÈCNICA DE VALÈNCIA

Instituto Universitario Mixto de Tecnología Química

(UPV-CSIC)

"Propiedades optoelectrónicas en perovskitas halogenadas y su aplicación en energía y sensores"

TESIS DOCTORAL

Presentada por:

Rocío García Aboal

Dirigida por:

Dr. Pedro Enrique Atienzar Corvillo

Dr. Fernando Ramiro Manzano

Valencia, Septiembre 2021

D. PEDRO ENRIQUE ATIENZAR CORVILLO, científico titular en el Instituto de Tecnología Química (UPV-CSIC) y D. FERNANDO RAMIRO MANZANO, investigador postdoctoral en el Instituto de Ciencia Molecular (ICMol-UV).

CERTIFICAN, que la presente tesis doctoral, titulada: **"*Propiedades optoelectrónicas en perovskitas halogenadas y su aplicación en energía y sensores*"**, ha sido desarrollada por ROCÍO GARCÍA ABOAL, en el marco del programa de doctorado de Química Sostenible, bajo su dirección, en el Instituto Universitario Mixto de Tecnología Química (UPV-CSIC) de la Universitat Politècnica de València.

D. Pedro Atienzar Corvillo D. Fernando Ramiro Manzano

Agradecimientos

Nunca imaginé que cuando escribiera estas líneas ya no estarías entre nosotros. Te echo tanto de menos!! Nuestras charlas interminables, tus bromas, tu risa,…tu valentía, tus ganas de vivir, tus consejos,…pero sobre todo cada beso, caricia y mirada con las que conseguías solucionarlo todo. Gracias por todo el amor que nos has dado y por todas las cosas que nos has enseñado. Espero que desde donde estés veas lo mucho que te necesitamos, y que nos cuides y protejas como lo has hecho siempre. Te quiero y te querré sin límites Mami.

A mi Padre, Mateo. Gracias por ser como eres! Gracias por enseñarme a ser fuerte y valiente. Por enseñarme que todo en esta vida se consigue con esfuerzo pero sobre todo con conocimiento. Gracias a vosotros soy la mujer que soy, y sin vuestra confianza y apoyo esto no hubiera sido posible. Te quiero Papi.

A cada una de mis 5 hermanas: Vito, Iria, Yayo, Marina y Alicia. Podría ponerme a describir lo maravillosas que sois cada una de vosotras, pero no me llegarían todas las páginas del mundo. Gracias por aguantarme y apoyarme… por nuestros buenos y malos momentos… por las risas y recuerdos!! En definitiva gracias por ser mis hermanas. Y gracias papis por regalarme estos 5 tesoros.

Al hombre que me enamora cada día varias veces, Juan. Sabes que sin ti no estaría escribiendo estas líneas. Gracias por ser tú…fuerte y luchador! Por acompañarme y apoyarme a pesar de todos los malos momentos. Por hacerme fuerte y hacer que crea más en mí!! Recuerda que juntos aprenderemos y mejoraremos, porque juntos somos invencibles.

Al resto de mi gran familia. En especial a mis cuñis: Lucía, Víctor, Toñe y Tamara. Gracias por ser como sois, por todo lo que nos aportáis, por estar siempre. Sin vosotros no seriamos la gran familia que somos. A mis sobris, Mateo e Iria, por aportarnos luz y alegría cada día. A mis tíos, primos y abuela. Y a la familia que se elige, en especial a Carmen y Luis. Gracias por hacer de cada momento uno inolvidable, y por estar siempre en el momento adecuado.

A todas las personas que he conocido durante esta etapa y que a partir de ahora son esenciales en mi vida. A Ana (mi Ana), sin nuestras tardes de terapia estos últimos meses hubieran sido muy duros. Gracias por tu ayuda, apoyo y amistad. Eres una persona excepcional. Elena, mi compi en todas las facetas, gracias por todos nuestros momentazos, dramáticos

o no, pero siempre necesarios. A Sonia, gracias por estos años de amistad (y los que nos quedan!). Gracias por estar ahí siempre, tan servicial y única. Y gracias a Dani por ser tu media mitad. Gracias a los dos por dejarme compartir con vosotros momentos únicos, y por ser mi familia cuando más lo necesitaba. Andrea, mi Andrea!! A pesar de la lejanía de estos meses (y de la del ITQ-Depar) siempre has estado ahí. Gracias por tu dulzura y alegría, gracias por ser mi amiga.

Al resto de compañeros, que en menor a mayor medida, han contribuido a que esta tesis fuera más real. Mis compañeros de la CPI (Roberto, Paco, Isabelle, Marta y Daniela), gracias por todo lo que me habéis enseñado, por todos los buenos momentos y por toda la paciencia que habéis tenido conmigo. A mis compañeros del ITQ, del G3 y del A4 (Amparo, Esther, Aicha, Abde, Josep, Iván, Javi…) y a todos mis compañeros del Depar (Cristina, María, Arianna, Herme…), gracias por acogerme como una más de vuestro grupo, por toda vuestra ayuda y por todos las buenas historias y momentos del laboratorio. A mis chicas de pilas (María, Sara..) sois unos soles, gracias por adoptarme más de una vez en vuestro laboratorio. En definitiva, gracias a todas las personas que me han acompañado en todo este proceso (se que más de una se me olvida).

A mis niñas murcianas (Elena, Anabel, Noelia, Mónica…). Gracias por acompañarme desde hace años en mis locuras. Sois una parte de mí y sin vosotras muchas veces no me levantaría.

Por último y no menos importante a mis directores de tesis, Pedro y Fernando. Gracias por darme esta oportunidad y dejarme vivir esta gran experiencia. Gracias por enseñarme tantas cosas, pero sobre todo por dejarme crecer tanto a nivel personal como profesional.

Asimismo, agradecer al Proyecto “PGC2018-099744-B-I00” del Ministerio de Ciencia, Innovación y Universidades la financiación para la impresión de esta tesis doctoral.

Gracias a cada uno de vosotros por compartir conmigo tanto mis alegrías como mis frustraciones, mis risas y mis llantos, mi bromas y mi mal genio. Creedme si os digo que he aprendido mucho de cada uno de vosotros. Y que esta etapa ha servido para hacerme aún más fuerte. Gracias de todo corazón.

Conocimiento

Papi

Tesoro

Mami

Lista de símbolos y abreviaturas

A	Catión orgánico
B	Catión divalente
X	Anión
ABX_3	Fórmula general de perovskitas halogenadas
ABO_3	Fórmula general de óxidos de perovskita
Cl	Cloro
Br	Bromo
I	Iodo
Pb	Plomo
Sn	Estaño
Cs	Cesio
2D	Dos dimensiones
LEDs	Ligth-emitting Diodes (Dispositivos emisores de luz)
TiO_2	Dióxido de Titanio
%	Porcentaje
3D	Tres dimensiones
H_2O	Agua
O_2	Oxígeno
H_2	Hidrógeno
BX_6	Octaedros
t	Factor de tolerancia de Goldschmidt
r_a	Radio iónico del catión A
r_b	Radio iónico del catión B
r_x	Radio iónico del anión X
MA	Metilamonio
FA	Formamidina
DMA	Dimetilamonio
EA	Etilamonio
GA	Guanidina
A_2BX_4	Fórmula general perovskita con estructura 2D

A'	Catión orgánico de mayor tamaño
n	Espesor de la capa de octaedros
1D	Monodimensional
0D	Cero dimensionalidad
nm	Nanómetro
eV	Electronvoltios
µm	Micrómetro
µs	Microsegundo
cm	Centímetro
V	Voltios
S	Siemens
Ref	Referencia
DMF	Dimetilformamida
DMSO	Dimetilsulfóxido
AX, BX_2	Fórmula general precursores
mbar	Milibares
CVD	Chemical Vapor Deposition (Deposición de vapor químico)
LARP	Ligand-assited Reprecipitation (Método de reprecipitación)
MOF	Metal-Organic framework (Compuestos organometálicos porosos)
OA	Ácido Oleico
OABr	Bromuro de octilamonio
ODE	Octadeceno
PLQY	Photoluminescence Quantum Yield (Rendimiento cuántico en fotoluminiscencia)
OLA	Oleilamina
°C	Grados Celsius
J_{sc}	Densidad de corriente en cortocircuito
mA	Miliamperios
V_{oc}	Voltaje en circuito abierto
FF	Factor de forma
PCE	Photocurrent Quantum Efficiency (Eficiencia de conversión de energía)
QD	QuantumDot (Punto cuántico)

A	Amperio
mW	Milivatio
UV	Ultravioleta
CO_2	Dioxido de carbono
n	Índice de refracción
SEM	Scanning Electron Microscope (microscopía electrónica de barrido)
rpm	Revoluciones por minuto
NA	Sin aditivo
CHP	*Ciclohexilpirrolidona*
TBP	*Terct-butilpiridina*
PL	Fotoluminiscencia
OT	Transmitancia óptica
n_r	Índice de refracción real
n_i	Índice de refracción imaginario
PDMS	Polidimetilsiloxano
CD	Disco compacto
DVD	Disco de video digital
h^+	Hueco
e^-	Electrón
B/B^+	Especie oxidada
A/A^-	Especie reducida
BC	Banda de conducción
Ti	Titanio
Ta	Talio
Cu	Cobre
µmol	Micromoles
gCat	Gramo de catalizador
AQY	Apparent Quantum Efficiency (Eficiencia cuántica aparente)
TON	Turnover number (Número de recambio)
OMS	Organización mundial de la salud
CH_4	Metano

O_3	Ozono
NO_2	Dióxido de nitrógeno
NH_3	Amoniaco
FTIR	Fourier transform Infrared Spectroscopy (Espectroscopía infrarroja por transformada de Fourier)
SAW	Surface acoustic wave sensor (Sensores de Ondas acústicas de superficie)
QCM	Quartz Crystal Microbalance (Microbalanza de cristal de cuarzo)
R_0	Resistencia inicial
R	Cambios en los valores de resistencia
ppm	Partes por millón
COV	Compuestos orgánicos volátiles
mL	Mililitro
min	Minutos
EMT	Electron Transport Material (Material transportador de electrones)
HTM	Hole Transport Material (Material transportador de huecos)
Spiro-OMETAD	N2,N2,N2′,N2′,N7,N7,N7′,N7′-octakis(4-methoxyphenyl)-9,9′-spirobi[9H-fluorene]-2,2′,7,7′-tetramine
PCMB	[6,6]fenil-C61-ácido butírico metil ester
FTO	Fluorine-doped Tin Oxide (Oxido de estaño dopado con Fluor)
SubPc	Subftalocianinas de boro
PEABr	Bromuro de feniletilo
OPh,ISubPc	Subftalocianinas de boro con un grupo fenoxi

Resumen

La creciente urbanización e industrialización de las sociedades en las últimas décadas han provocado una alta demanda de energía. No obstante, mientras no se desarrollen fuentes de energía renovables que se constituyan como un reemplazo plausible de las actuales, la liberación de gases de efecto invernadero y sus consecuencias sobre el cambio climático difícilmente serán atajadas. Por ello, se está llevando a cabo una intensa búsqueda de energías renovables para un futuro inmediato. En los últimos años, la perovskita ha alcanzado una gran popularidad, centrando numerosos esfuerzos de investigación debido a sus propiedades ópticas y eléctricas únicas. Como por ejemplo su alto coeficiente de absorción y su alta movilidad de carga.

Esta tesis comprende seis artículos científicos en torno a las perovskitas de haluro metálico. Por un lado, 3 trabajos estudian los fenómenos ópticos que ocurren en el seno del material, con la finalidad de lograr una mejor comprensión de éstos. Puesto que el conocimiento de estos fenómenos ópticos a nivel individual (cristales aislados) permite modular y adaptar su síntesis y morfología para aplicaciones determinadas.

Por otro lado, las perovskitas han sido implementadas en distintos dispositivos para su aplicación en tres campos: fotocatálisis, sensores y fotovoltaica. Por primera vez, se ha logrado utilizar este material para la obtención de hidrógeno llevando a cabo la reacción en fase vapor. Asimismo, diversas composiciones de perovskita se han usado para decorar grafeno y detectar niveles traza de Compuestos Orgánicos Volátiles (COV) como benceno y tolueno. Y finalmente se ha desarrollado una estrategia para insertar en la estructura de la perovskita moléculas orgánicas, de forma que se permite una ampliación de la fotorrespuesta en el espectro visible.

Por lo tanto, las perovskitas se han implementado exitosamente en aplicaciones de diversa índole, constituyéndose como un material prometedor y fácilmente adaptable a los distintos requisitos de cada campo de estudio.

Resum

La creixent urbanització i industrialització de les societats durant les últimes dècades han provocat una alta demanda d'energia. No obstant això, fins que no es desenvolupen fonts d'energia renovables que puguen ser un reemplaçament plausible de les actuals, l'alliberament de gasos d'efecte hivernacle i les seues conseqüències sobre el canvi climàtic seran difícilment aturades. Per tant, s'està duent a terme una intensa cerca d'energies renovables per a un futur immediat. En els últims anys, la perovskita ha aconseguit una gran popularitat, centrant nombrosos esforços de recerca a causa de les seues propietats òptiques i elèctriques úniques. Per exemple, el seu al coeficient d'absorció i la seua alta mobilitat de càrrega.

Aquesta tesi reuneix sis articles científics al voltant de les perovskites d'halur metàl·lic. Per una banda, 3 treballs estudien els fenòmens òptics que ocorren en el material, amb la finalitat d'assolir una major comprensió d'aquests. Donat que el coneixement d'aquests fenòmens òptics a nivell individual (cristalls aïllats) permeten modular i adaptar la seua síntesi i morfologia per a determinades aplicacions.

Per altra banda, les perovskites han sigut implementats en diferents dispositius per a la seua aplicació en tres camps: fotocatàlisi, sensors i fotovoltaica. Per primera vegada, s'hi ha aconseguit utilitzar aquest material per a l'obtenció d'hidrogen duent a terme la reacció en fase vapor. Així mateix, diverses composicions de perovskita s'han utilitzat per a decorar grafè i detectar nivells traça de Compostos Orgànics Volàtils (COV) com benzè i toluè. I finalment s'ha desenvolupat una estratègia per a inserir en l'estructura de la perovskita molècules orgàniques, de forma que es permet una ampliació de la fotoresposta en l'espectre del visible.

Per tant, les perovskites s'han implementat exitosament en aplicacions de diversa índole, constituint-se com un material prometedor i fàcilment adaptable als diferents requisits de cada camp d'estudi.

Abstract

During the last decades, the growing urbanization and industrialization result in a significant need for energy. However, since feasible renewable energy sources should be further developed to replace the current energy source, the release of greenhouse gases and their climate change consequences are difficult to overcome. For that reason, the development of renewable energy sources has been attracting growing research efforts. Recently, perovskites gathered great interest owing to their outstanding optical and electrical properties. For instance, their high absorption coefficient and superior charge mobility.

This thesis comprises six scientific articles about metal halide perovskites. On one hand, 3 works study the optical phenomena that occur within the material in order to achieve a better understanding. The deep knowledge of these optical phenomena's at the individual level (isolated crystals) enable the modulation and tuning of their synthesis and morphology to match specific applications.

On another hand, perovskites have been implemented in several devices for their application in three research fields: photocatalysis, sensors, and photovoltaic. For the first time, this nanomaterial was successfully employed for obtaining hydrogen carrying out the reaction in the vapor phase. Likewise, several perovskite compositions have been used for decorating graphene and detect trace levels of Volatile Organic Compounds (VOC) as benzene and toluene. And finally, it has been developed a strategy to insert organic molecules in the perovskite structure, resulting in an enhanced photoresponse in the visible range.

Therefore, perovskites have been successfully implemented in several applications, becoming a promising material and easily adaptable to the different requirements needed in each field of study.

TABLA DE CONTENIDOS

CAPÍTULO 1

INTRODUCCIÓN

1. INTRODUCCIÓN

1.1. Antecedentes históricos

En 1839, Gustav Rose descubrió en los montes Urales un nuevo mineral compuesto por titanio y calcio ($CaTiO_3$) denominándolo perovskita en honor al mineralogista L.A. Perovski (1792-1856)[1]. Presenta una estructura cristalina iónica peculiar formada por dos cationes de distinta composición y tamaño, denominados de forma general A y B, junto con un anión, denominado X. La presencia de esta topología iónica (ABX_3) en diversas composiciones ha tenido como consecuencia la generalización del nombre perovskita a cualquier material o familia de materiales que comparten esta estructura cristalina.

Las perovskitas más estudiadas son los conocidos como óxidos de perovskita (ABO_3), donde las posiciones "A" y "B" pueden estar ocupadas por la gran mayoría de cationes de la tabla periódica. Esto conlleva una gran flexibilidad en su composición (por ejemplo $CaTiO_3$, $BaTiO_3$, $LaMnO_3$, etc.)[2,3] así como una gran versatilidad en sus propiedades, las cuales han sido estudiadas en profundidad durante las últimas décadas. Posiblemente, una de sus propiedades más reseñables es su actividad catalítica, y en concreto sus aplicaciones como fotocatalizadores[4,5].

Estos óxidos de perovskita presentan a su vez una gran estabilidad tanto ambiental como térmica[6,7]. Sin embargo, esta excelencia da lugar a un gran inconveniente, pues se requieren altas temperaturas para su preparación[8] y por tanto su coste de fabricación es elevado. Por ello, durante los últimos años muchos grupos de investigación han centrado sus esfuerzos en sintetizar otro tipo de perovskitas que aporten una versatilidad similar pero cuyo proceso de preparación sea más sencillo y económico.

Entre estos tipos de perovskita se encuentran las perovskitas de haluro metálico, donde en la posición "X" se sitúa un halógeno (Cl^-, Br^- o I^-), en la posición B un catión divalente (Pb^{2+}, Sn^{2+}, etc.) y en la posición A un catión con carácter inorgánico (Cs, etc.) u orgánico (metilamonio, formamidinio, etc.). En este último caso se les conoce

como perovskitas híbridas de haluro metálico. El componente orgánico le confiere un carácter híbrido (orgánico-inorgánico), proporcionando una flexibilidad estructural que no puede ser alcanzada en perovskitas puramente inorgánicas. Asimismo, la diversidad química permite ajustar y modular sus propiedades físicas con métodos de síntesis sencillos y asequibles[9].

Con todo ello, la primera perovskita hibrida fue sintetizada por Weber y colaboradores en 1978 (Figura 1), concretamente la perovskita 3D de fórmula molecular $CH_3NH_3PbX_3$ ($X=Br^-$, Cl^-, I^-)[10]. A raíz de este descubrimiento las perovskitas se han convertido en un material prometedor para diferentes aplicaciones de diversa índole, destacando su empleo en el ámbito de la energía.

En los años 90, cuando alcanzó su época de mayor desarrollo, Mitzi y colaboradores[11–13] sintetizaron y caracterizaron por primera vez dispositivos electrónicos basados en este tipo de perovskita. Incluso llegaron a desarrollar dispositivos optoelectrónicos basados en perovskita 2D[14,15], estructura de la cual hablaremos más adelante. Además, en estos años de esplendor, se estudió la posibilidad de implementar el material en dispositivos emisores de Luz (LEDs, del inglés "ligth-emitting diode"), desarrollándose el primer dispositivo de estas características en 1994[16] (Figura 1).

Durante muchos años, se estudió la inversión del sistema optoelectrónico para conseguir recolectar luz en lugar de emitirla, consiguiendo así una célula solar. No obstante, a pesar de los esfuerzos de diversos grupos, no fue hasta 2009 cuando se publicó el primer artículo sobre una celda solar. En concreto, basada en nanopartículas de $CH_3NH_3PbI_3$ sobre una capa mesoporosa de óxido de titanio (TiO_2), logrando una eficiencia del 3.8%[17]. Además, hasta el año 2014 no se demostró la emisión láser de estos materiales[18] o su aplicación en fotocatálisis[19]. Sin embargo, en muy pocos años se ha conseguido emisiones láser de bajo umbral[20] y aún más notable si cabe, igualar prácticamente al silicio en el desarrollo de dispositivos fotovoltaicos[21–23], llegando a eficiencias del 25%[24]. Cabe indicar que tales rendimientos son tan altos que hoy en día los esfuerzos se centran en conferirles una mayor estabilidad para una posible aplicación real[25].

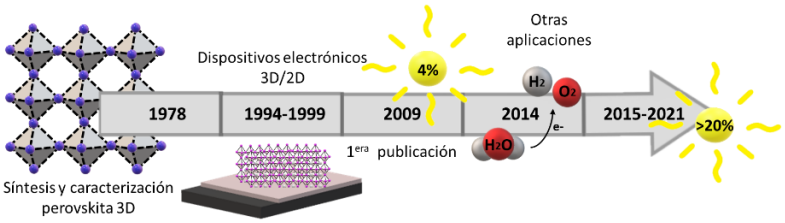

Figura 1. Cronología de los principales hitos en la investigación de las perovskitas híbridas.

1.2. Estructura

Tal y como se ha mencionado anteriormente, la formula química general que presentan estos materiales viene definida por ABX_3, donde A es generalmente un catión voluminoso y electropositivo, B es un catión más pequeño perteneciente a los metales de transición mientras que X es un anión[26,27]. La Figura 2 ilustra su estructura cristalina, que consiste en una red tridimensional (3D), que puede definirse como octaedros BX_6 unidos por los vértices, con el catión A ocupando el hueco formado entre los octaedros, dando lugar a una pseudo estructura cúbica centrada en el cuerpo.

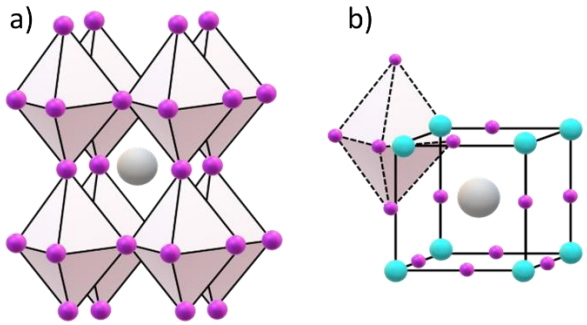

Figura 2. a) Estructura cristalina y b) celda unidad de la estructura 3D de perovskita híbrida. Queda representado cada elemento por un color: A de color gris, B azul y X violeta.

Todos los materiales que reciben el nombre de perovskita cristalizan con esta estructura y solamente difieren en la conectividad de los octaedros. Asimismo, para obtener una perovskita estable existe un requisito imprescindible basado en los tamaños de los iones que la forman. Una ligera distorsión puede producir notables modificaciones en la red cristalina, dando lugar a configuraciones inestables e incluso disminuir el número de coordinación de cada anión[28]. De hecho, en el año 1926, V. M. Goldschmidt creó una modelo para evaluar la estabilidad de las perovskitas dependiendo del radio iónico de los iones que la forman. Esta fórmula recibe el nombre de **factor de tolerancia de Goldschmidt (t)**, y predice tanto la estabilidad como la distorsión que se produce en la estructura cristalina[29].

$$t=\frac{r_a+r_x}{\sqrt{2}(r_b+r_x)} \qquad (1)$$

Donde r_a y r_b son los radios iónicos de los cationes A y B, respectivamente, mientras que r_x es el radio correspondiente al anión X. En la Figura 3 podemos observar el valor de t y la estructura que se obtiene, en el caso de la perovskita $APbBr_3$, dependiendo de los radios iónicos de los cationes que la formen.

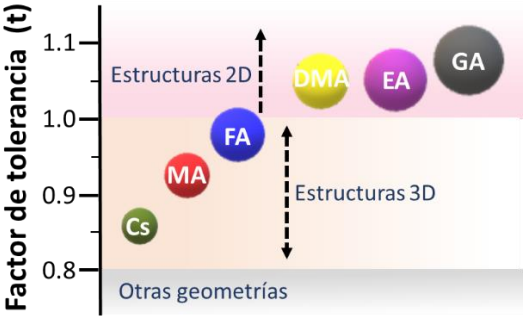

Figura 3. Valores del factor de Goldschmidt (t) para la perovskita híbrida $APbBr_3$. Siendo A cationes orgánicos e inorgánicos de diferente radio: Cesio (Cs), Metilamonio (MA), Formamidina (FA), Dimetilamonio (DMA), Etilamonio (EA) y Guanidina (GA).

Para una simetría cúbica ideal cabe esperar un valor de t igual a 1, aunque en la mayoría de los casos los valores están comprendidos entre 0.8 y 0.9. A medida que el valor de t disminuye, los enlaces BX se comprimen, lo que implica la elongación de la distancia entre A y X. Este fenómeno provoca el giro de los octaedros en la estructura para aliviar las tensiones provocadas por el desajuste en los tamaños de los cationes. Por lo que se produce la distorsión de la estructura llegando a dar lugar a otras simetrías posibles como tetragronal, ortorrómbica y monoclínica. Por el contrario, cuando t es mayor que 1 se alargan/comprimen los enlaces BX/AX, siendo más estable en este caso la simetría hexagonal[30].

Cuando los valores de t son mucho más elevados que 1, la estructura 3D se disgrega dando lugar a las perovskitas de baja dimensionalidad. En particular, la adición de cationes orgánicos de elevado/a tamaño/longitud A' que parcialmente substituyen a A tiene como consecuencia la formación de planos de octaedros que

subdividen el cristal iónico dando lugar a una estructura laminar, llamada quasi-2D. Este es el caso de la ocupación parcial de A por grupos aromáticos o cadenas alquilo[30]. En esta configuración, la estructura se mantiene cohesionada a través de interacciones π-π o fuerzas Van der Waals respectivamente. En el caso donde todo el catión A sea sustituido, se alcanza el límite 2D, y su fórmula pasa a ser A'_2BX_4, que consiste en una monocapa de octaedros separada por una bicapa de cationes A'. En este caso, las capas inorgánicas se unen con las orgánicas mediante enlaces de hidrógeno derivados de la interacción del catión orgánico con los halógenos de la red inorgánica. Debido a restricciones geométricas del catión, la interacción generalmente se produce entre dos halógenos puente y un halógeno terminal (configuración puente) o entre dos halógenos terminales y uno puente (configuración terminal)[14]. Esta unión entre los octaedros y las láminas es un parámetro destacable de la estructura, ya que influye sobre el espaciamiento de las láminas, la alineación y la rotación de los octaedros, afectando de manera directa a las transiciones estructurales[13].

Al contrario que en la estructura 3D, donde el catión A se sitúa en una cavidad rígida y definida, en las estructuras 2D la distancia entre las láminas puede variar dependiendo del tamaño o longitud del mismo catión. En consecuencia, se pueden incorporar cationes orgánicos funcionales más grandes y complejos, por lo que esta mayor longitud tiene una influencia significativa en el espaciado de la red inorgánica, y en consecuencia, en sus propiedades físicas[13].

Un ejemplo de las estructuras quasi 2D, que representa una fase intermedia entre las 2D y 3D, son las denominadas fases Ruddlesden-Popper[31]. Fue descrita por primera vez en 1957 por S.N. Ruddlesden y P. Popper y presentan la fórmula general $A'_2A_{n-1}B_nX_{3n+1}$, donde A y A' son dos cationes orgánicos de diferente tamaño y n un número entero, el cual indica el número de octaedros en cada lámina (Figura 4).

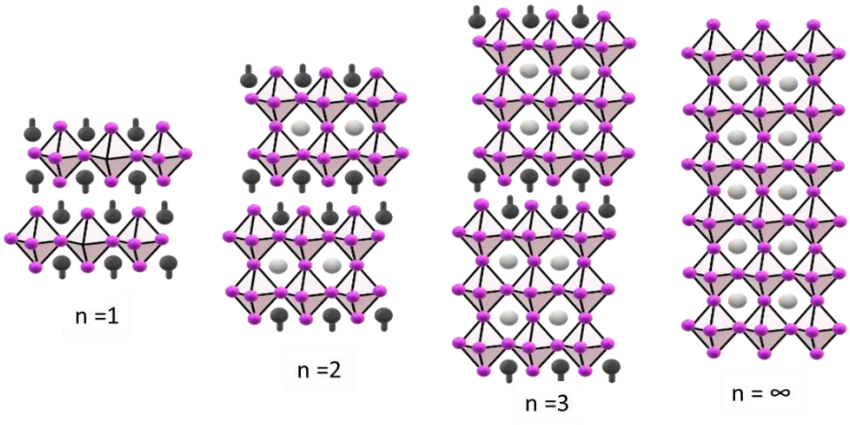

Figura 4. Estructura tipo Ruddlesden-Popper para diferentes valores de n. Queda representado cada elemento por un color: A gris, A´negro y X violeta.

Al igual que en las estructuras 2D, el catión orgánico actúa como espaciador entre los octaedros, dando lugar a la formación de capas orgánicas e inorgánicas apiladas en una dirección. La distancia entre láminas y el espesor de la capa de octaedros (n) se puede controlar experimentalmente ajustando la relación entre ambos cationes[32]. En consecuencia, las propiedades ópticas y eléctricas pueden ser moduladas.

Por último, para valores elevados de t (t>>1), es posible otro tipo de estructuras de baja dimensionalidad (Figura 5). Concretamente, la estructura monodimensional (1D) o con dimensionalidad cero (0D). Los sistemas 1D consisten en cadenas de octaedros que comparten un solo vértice con un octaedro adyacente, mientras que los sistemas 0D presentan los octaedros totalmente aislados entre ellos. En ambos casos, tanto la red orgánica como la inorgánica se encuentran aisladas, lo que implica una mayor restricción en la movilidad de los electrones y un mayor confinamiento, comprometiendo su aplicabilidad en determinados sistemas[33].

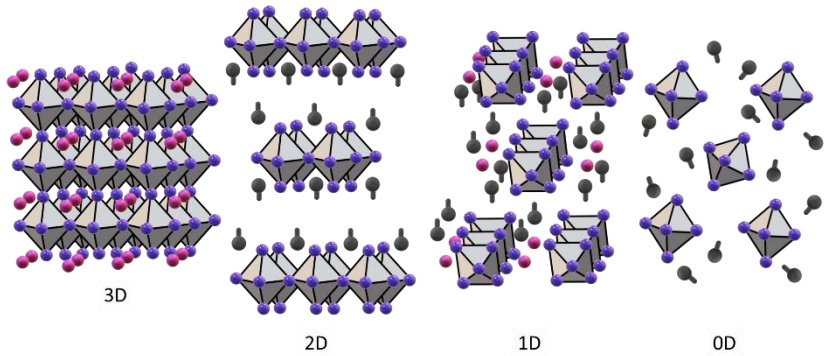

Figura 5. Diferentes estructuras de diferente dimensionalidad que pueden adoptar las perovskitas. Queda representado cada elemento por un color: A rosa, A' negro y X azul.

1.3. Propiedades y limitaciones

1.3.1. Propiedades

Las perovskitas híbridas presentan propiedades ligadas a su estructura y composición que las hacen únicas. Una de sus propiedades más característica es la fácil modificación de su composición, así como la amplia variedad de alteraciones estructurales que permite, lo que conlleva cambios en sus propiedades ópticas y eléctricas[30].

Es bien conocido que la banda de conducción de las perovskita está formada principalmente por los orbitales p de los átomos metálicos, mientras que la banda de valencia viene dada por los orbitales p del halógeno. Por tanto, cualquier **modificación en la composición** puede modular los niveles de energía (Figura 6a). A modo de ejemplo, tomando como base la estructura estándar 3D, un solo cambio en el halógeno permite desplazar la emisión del material desde la región del azul al infrarrojo cercano (Figura 6b), y la modificación del elemento metálico ampliar su región espectral, llegando incluso a sobrepasar los 900 nm[30].

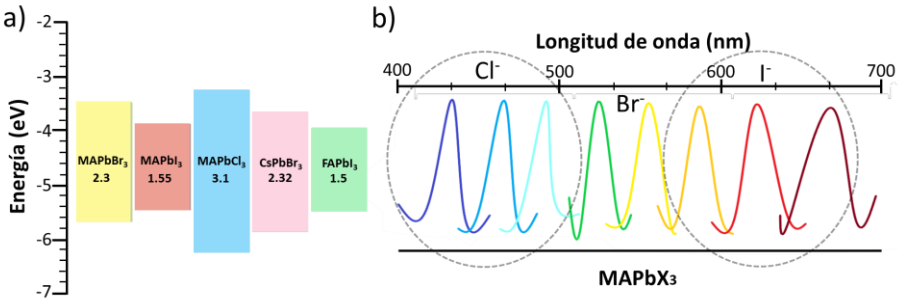

Figura 6. a) Estructura de bandas dependiendo de la composición de la perovskita 3D (ABX_3). b) Desplazamiento en la emisión de la perovskita por el cambio del halógeno en la estructura.

En el caso de la perovskitas con estructura 2D, el cambio en el grosor de las láminas de octaedros y su composición también permite ajustar la posición espectral de emisión. Adicionalmente, es posible

explotar la separación entre las láminas de octaedros, ya que al incluir cationes orgánicos más grandes se modifica su ancho de banda[30].

A diferencia de un semiconductor convencional, las perovskitas presentan **estructura iónica**, por lo que son altamente solubles en agua y en disolventes polares. Esta propiedad les confiere una baja barrera energética en la formación de cristales[34], permitiendo su síntesis a temperatura ambiente en tiempos muy cortos (minutos) y obteniendo un material de gran calidad (altamente cristalino). Además, los reactivos necesarios como los métodos de síntesis son considerados sencillos y de bajo coste.

Asimismo, la estructura iónica les confiere propiedades superficiales que tiene implicaciones importantes en sus propiedades físicas. Por un lado, el aumento del área de superficie conllevaría a priori una alta recombinación, pero la atracción electroestática entre los huecos y electrones generados favorece una **separación efectiva** y una **movilidad de las cargas más eficiente**. Es decir, se obtienen materiales con velocidades de recombinación varios ordenes de magnitud menores con respecto a otros semiconductores[35] y así como con portadores de mayor vida útil y largas longitudes de difusión (Tabla 1)[36].

Material	Distancia de difusión (μm)	Tiempo de vida (μs)	Movilidad ($cm^2V^{-1}S^{-1}$)	Ref.
$MAPbI_3$ policristalino	0.1-1	0.001-1	1-10	[37]
$MAPbI_3$ cristal	2-8	0.5-1	24-105	[38]
$MAPbBr_3$ policristalino	0.3-1	0.05-0.16	30	[39]
$MAPbBr_3$ cristal	3-17	0.1-1	24-115	[40]

Tabla 1. Valores de distancia de difusión, tiempo de vida y movilidad de portadores para diferentes composiciones y configuraciones de perovskita híbrida.

Otra de las ventajas que presentan las perovskitas híbridas frente a otros materiales son sus **altos coeficientes de absorción** y su **baja energía de excitación**[41]. Ambas propiedades le confieren una alta y

eficiente generación de portadores[42]. Ciertos estudios llevados a cabo mediante técnicas ópticas como las medidas de fotoluminiscencia en tiempo resuelto, revelan información tanto de los procesos de difusión de los portadores[36] como de la distancia de difusión[43]. Estos estudios concluyen que las distancias de difusión y la movilidad de los portadores en un cristal aislado son mucho más altas que los registrados en capas policristalinas delgadas[38]. Esto se debe a la ausencia de límites de grano, que aumenta sustancialmente la longitud de difusión del portador[40].

Otra característica reseñable de estos materiales es su **tolerancia a la presencia de defectos**[44]. Los defectos presentes en el material son críticos para la movilidad y vida de los portadores, y afectan de manera negativa tanto a la recombinación como al rendimiento obtenido en determinadas aplicaciones. Que el material tenga tolerancia a la presencia de los mismos significa que forma relativamente pocos, y en su gran mayoría intrínsecos o estructurales (vacantes, etc.). Estos actúan como trampas superficiales y son de baja energía tanto de formación como de eliminación, por lo que pueden ser eliminados fácilmente, y no tienen un efecto significativo sobre los portadores.

Asimismo, a grandes rasgos los pocos defectos presentes en el material (extrínsecos) suelen concentrarse cerca a los límites de grano, sirviendo como centro de recombinación no radiativa[45]. Estos defectos se pueden minimizar aplicando algún tratamiento posterior a su síntesis, o durante el mismo proceso de cristalización (por ejemplo modificando el disolvente) u obteniendo cristales más grandes donde se reducen drásticamente los límites de grano[46]. Por todo ello, el empleo de cristales aislados facilita el estudio de transporte en estos materiales. En particular, un cristal individual con unas caras controladas provee de información más fehaciente que una capa policristalina, donde la presencia de borde de grano limita y perturba las propiedades intrínsecas del material. Sirva de ejemplo el estudio de fotoluminiscencia en un cristal individual, donde la ausencia de defectos en forma de borde de grano aumenta la transparencia del material, limitando por lo tanto la autoabsorción[35].

Además la **naturaleza iónica** de la perovskita puede servir como modelo sencillo para el estudio de mecanismos y cinéticas de intercambio de iones en estado sólido[47]. En particular, se ha observado mediante técnicas ópticas que la interdifusión de aniones, la cual genera gradientes de concentración de haluros, se produce más fácilmente que la de los cationes[48]. De hecho, este es un campo de estudio relevante, ya que se cree que muchos de los fenómenos que ocurren en este material se deben a la migración de los iones, desde la presencia de histéresis en un dispositivo solar hasta la estabilidad del material bajo iluminación[49].

1.3.2. Limitaciones

Una de las limitaciones más importante que presentan las perovskitas híbridas, es su **baja estabilidad** en condiciones de humedad, temperatura y oxígeno ambiental[50]. Esta susceptibilidad a la degradación química y estructural es una consecuencia de la baja energía de formación de estos materiales y de la posibilidad de configurar la red cristalina con diferente composición.

En particular, numerosos estudios han demostrado que las perovskitas con estructura 3D son altamente susceptibles a la degradación por la humedad. Por ejemplo es conocido que la perovskita con fórmula $MAPbI_3$ forma fases hidratadas tras la exposición a altos niveles de humedad[51]. Un camino a seguir para paliar esta limitación sería adecuar la composición. Por ejemplo, cambiar el catión orgánico A (metilamonio) por uno de mayor tamaño (formamidinio)[52], consiguiendo un mayor carácter hidrofóbico del material. También es posible su cambio por uno de carácter inorgánico (cesio)[53], aportando una mayor estabilidad térmica. O incluso por una mezcla de ambos cationes[54], resultando finalmente en una menor degradación del material tanto térmica como en presencia de agua.

Otra posibilidad es la utilización de perovskitas con estructura 2D. La presencia de cationes orgánicos grandes con cadenas alquílicas o aromáticas le confiere cierto carácter hidrofóbico, y supone una protección a las condiciones ambientales[55,56]. Adicionalmente, presenta menos defectos estructurales y vacantes susceptibles de ser núcleos de degradación. Esta última propiedad estructural es común

en materiales 2D, y tiene como consecuencia unas propiedades mecánicas excelentes[57]. Sin embargo, presentan un mayor apantallamiento y confinamiento lo que reduce su eficiencia tanto en emisión como en colección de luz[58].

Con todo ello, numerosos estudios plantean escenarios de compromiso, donde se mezclen perovskitas 2D y 3D para aprovechar y optimizar las mejores propiedades de cada estructura minimizando las penalizaciones de sus inconvenientes[25].

Aparte de los factores ambientales existe otra gran limitación, su **toxicidad**. Las perovskitas que contienen plomo en su composición, perovskitas con las que se han obtenido mayores eficiencias en dispositivos fotovoltaicos, presentan una alta toxicidad que conlleva un alto riesgo para la salud humana y el medio ambiente[59]. Aunque mediante una gestión adecuada de residuos no debería de ser un problema, se sigue investigando en cationes alternativos al plomo. Algunos estudios han reportado dispositivos de perovskitas empleando estaño que llegan a alcanzar unas eficiencias no desdeñables del 6%[60]. No obstante, siguen siendo muy bajas en comparación con las que contienen plomo debido a su mayor ancho de banda y a problemas con su estado de oxidación.

1.4. Métodos de síntesis

1.4.1. Síntesis de cristales aislados y capas delgadas

Como se ha comentado anteriormente, una de las principales ventajas de las perovskitas híbridas es la facilidad de su síntesis. Al fin y al cabo, es un compuesto iónico que puede obtenerse mediante la precipitación de sus precursores. Esto no implica que el proceso de fabricación carezca de importancia, ya que las características finales del material tales como morfología, tamaño de cristal/grano y defectos estructurales, determinan sus propiedades objeto de estudio[41,61]. Por ello, elegir un método adecuado de síntesis presenta algunos desafíos, como seleccionar un disolvente apto tanto para el componente orgánico como inorgánico, elegir el sustrato ideal para que la deposición sea homogénea o que la temperatura óptima de cristalización evite la degradación de los precursores. A continuación se presentan una serie de métodos, con los que se pueden obtener tanto **películas delgadas** como **cristales aislados** de alta calidad. Estos métodos pueden clasificarse en dos grupos: métodos en disolución y métodos en fase vapor.

Los métodos más sencillos y quizá los más utilizados son los **métodos en disolución** (Figura 9a)[62]. En estos métodos, los precursores de perovskita, la sal halógena del metal de transición y el haluro del catión orgánico, se disuelven en un disolvente polar común, como por ejemplo dimetilformamida (DMF) o dimetilsulfoxido (DMSO)[63]. Una vez los precursores se encuentran en disolución, se puede realizar la cristalización del material por diferentes vías.

Una de ellas es la **técnica de recubrimiento por giro** (del inglés "spin coating")[64], método simple y ampliamente utilizado, especialmente para la deposición de capas delgadas. Por norma general, se aplica una pequeña cantidad de la disolución de precursores en el centro del sustrato, el cual gira a una velocidad determinada, de forma que el material se reparte por todo el sustrato por el efecto de la fuerza centrífuga. Además, el proceso de giro favorece la evaporación del disolvente. Por lo tanto, la velocidad de rotación es un parámetro significativo puesto que nos permite

controlar la deposición del material, determinando el espesor final y la homogeneidad de la capa obtenida.

Otra técnica es la conocida como **deposición por gota** (del inglés "drop casting"). Este método solamente implica la transferencia de la disolución de los precursores de perovskita al sustrato elegido, en el cual el disolvente puede evaporarse a temperatura ambiente o controlada. En este caso, el espesor de la capa de perovskita depende fuertemente de la concentración de precursores, ya que una disolución muy concentrada puede hacer que el proceso de cristalización se acelere. Por otro lado, la tensión superficial entre la disolución y el sustrato, la viscosidad de la disolución y la temperatura aplicada afectará en gran medida a la calidad y la uniformidad del material obtenido. Generalmente, se obtienen muestras menos homogéneas que con el método de recubrimiento por giro. La ventaja principal de esta técnica es que no requiere de ningún equipo especial para su aplicación[45].

Ambos métodos pueden llevarse a cabo en una o dos etapas[65]. En este último caso, se deposita una capa del haluro del metal de transición en el sustrato, por cualquiera de las técnicas anteriores. Posteriormente, el sustrato se sumerge en una disolución de catión orgánico[36,61], o bien se deposita una capa del mismo. De esta forma los cationes se intercalan y reaccionan rápidamente con el haluro metálico en el sustrato, formando una capa cristalina de material híbrido[27]. El principal inconveniente es que pueden quedar restos del precursor metálico, como impurezas, en la capa final, pudiendo perjudicar en la eficiencia de los dispositivos electrónicos. También cabe destacar que el disolvente final elegido para el catión orgánico no debe disolver ni al haluro metálico ni a la perovskita final.

Otro método más orientado a la síntesis de cristales aislados es el método conocido como **"anti-disolvente"**[40] (del inglés "antisolvent"). Este procedimiento se basa en la inversión de la solubilidad, es decir, la disolución de precursores se introduce en una atmósfera saturada de un disolvente donde ni los precursores ni la perovskita final sean solubles. En esa atmósfera saturada se produce un intercambio de los disolventes, provocando como resultado la cristalización de la

perovskita. Con este método se obtienen cristales a temperatura ambiente con muy pocos defectos y gran tamaño[66].

Posteriormente, después de cada deposición por cada uno de estos métodos, se suele aplicar un tratamiento térmico para eliminar completamente los retos de disolvente, y así mejorar la cristalinidad y pureza de la perovskita. También suele ser importante realizar un tratamiento previo de la superficie del sustrato elegido, con ácido o plasma de oxígeno, con la finalidad de favorecer la adhesión de la perovskita y obtener una morfología uniforme[67].

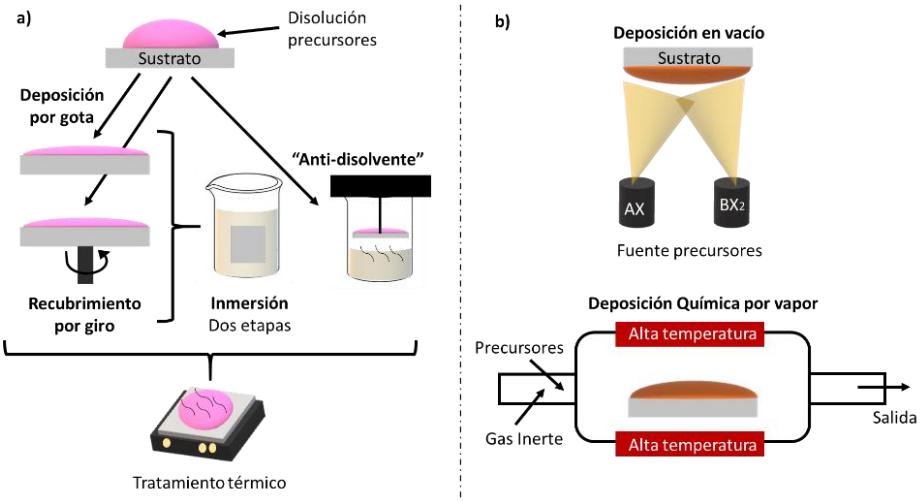

Figura 7. Métodos de preparación de perovskita en disolución (a) y de deposición en vapor (b).

Otro tipo de preparación de muestras son los **métodos de deposición en vapor** (Figura 7b), aunque se usan con menor frecuencia ya que suelen ser más complejos y de mayor coste. No obstante, su principal ventaja es que permite obtener capas más homogéneas y con un grosor más controlado que con los métodos en disolución, por lo que es ideal para obtener capas delgadas[68]. Asimismo, no se usa ningún tipo de disolvente, por lo que son métodos menos tóxicos.

La técnica en vapor más empleada consiste en la **deposición en vacío** (del inglés "vacuum deposition"), con doble fuente de precursores (AX, BX_2). Las películas de perovskita se preparan

generalmente en una cámara de alto vacío (10^{-5}-10^{-6} mbar), donde los precursores se cargan en crisoles separados y se calientan hasta la temperatura de sublimación correspondiente. Además, esta técnica permite ajustar la composición y estequiometria durante todo el proceso[69]. Asimismo, el sustrato donde se deposita la perovskita se mantiene a temperatura ambiente durante todo el proceso, y si se cumple la relación estequiométrica entre los precursores, la perovskita puede formarse sin necesidad de llevar a cabo ningún tratamiento térmico posterior[70]. Esto es interesante cuando se tienen que emplear sustratos sensibles a la temperatura, permitiendo la deposición de la perovskita sobre cualquier material[71]. No obstante, existe una variante de la técnica donde solamente se utiliza una fuente de precursor. En este caso, la perovskita previamente sintetizada (en forma de capa o polvo) se conecta a dos electrodos en una cámara de alto vacío. A continuación, se aplica una alta corriente al metal, causando la evaporación instantánea del material, el cual es transferido a otro sustrato, manteniéndose la estequiometria y composición inicial[72].

Otra técnica relevante que puede usarse en la preparación de compuestos de perovskita es la **deposición de vapor químico** (CVD, del inglés “chemical vapor deposition”). En este método, los precursores se llevan térmicamente a la fase gaseosa y son transportados al sustrato mediante una corriente de gas inerte[73]. Esta técnica puede emplearse para la síntesis de otros semiconductores y materiales. Además, con la optimización de diferentes parámetros, como el tiempo de deposición o la temperatura, se pueden conseguir películas de mayor calidad.

En el desarrollo de esta tesis hemos empleado los métodos en disolución. Por un lado, por su sencillez y rápida aplicación. Y por otro lado, son más adecuados para la obtención de cristales aislados de manera que se facilita el estudio de los fenómenos fundamentales que ocurren en el material.

1.4.2. Síntesis de nanocristales

Cuando el objetivo es sintetizar nanocristales de perovskita híbrida, se deben hacer uso de otros métodos de síntesis totalmente diferentes a los explicados anteriormente. Estos métodos son

generalmente sencillos y permiten obtener nanopartículas coloidales estables (Figura 8). Entre ellos se encuentran el método de precipitación inducida por un disolvente, la reprecipitación con la ayuda de un ligando (LARP), el método de emulsión, el método asistido por el uso de una plantilla y el método de inyección en caliente.

El **método de precipitación inducida** por un disolvente consiste en añadir los precursores de perovskita junto con ácido oleico (OA) y bromuro de octilamonio (OABr), en un disolvente no coordinativo como el octadeceno (ODE). Finalmente, los nanocristales se cristalizan mediante precipitación inducida debido a la adición de un disolvente a una determinada temperatura[74]. En general el tamaño de los nanocristales se puede controlar con un ligando de cadena larga, y con la ayuda del OA, que evita la agregación de los nanocristales asegurando su estabilidad. Modificando la relación molar de los precursores se puede mejorar el rendimiento cuántico de fotoluminiscencia (PLQY)[75] , además de poder modular su tamaño[76].

En el caso del **método de reprecipitación** (LARP, del inglés "ligand-assited precipitation") con la ayuda de un ligando, los precursores de perovskita, junto a Oleilamina (OLA) y OA, se disuelven en un disolvente polar como DMF en lugar de octadeceno. Seguidamente se añade gota a gota una disolución de los precursores de perovskita en tolueno, bajo agitación vigorosa[77], obteniéndose así los nanocristales.

El **método de emulsión,** en comparación con otros métodos de síntesis, proporciona un mejor control del tamaño durante la cristalización. Este proceso de síntesis implica la mezcla de dos disolventes inmiscibles entre sí, como DMF y n-hexano, para formar una emulsión. Seguidamente se añade un demulsificante, como por ejemplo, acetona o tert-butanol, para producir la mezcla de los disolventes e inducir la cristalización de los nanocristales[78]. Con este método es posible obtener los nanocristales en polvo sólido, pudiéndose redisolver para su uso en películas finas o en la fabricación de dispositivos. Además, se pueden sintetizar estructuras de nanocristales con capas múltiples si se ajusta la relación de ligandos de cadena larga y corta.

No obstante, a diferencia de los métodos explicados anteriormente, en el **método de cristalización asistido por una plantilla**, la formación de los nanocristales es inducida por la cinética de cristalización en un sustrato específico (molde) en lugar de con la ayuda de un ligando orgánico. Se pueden preparar fácilmente induciendo los precursores de la perovskita dentro de los poros del material que se usa como plantilla. Por ejemplo, es posible la síntesis de nanocristales de $MAPbBr_3$ dentro de sílice mesoporosa[79], en una capa de óxido de aluminio[80], o sobre compuestos organometálicos porosos (MOFs)[81].

El **método de inyección en caliente** es uno de los métodos más utilizados, especialmente para la síntesis de nanocristales de $CsPbBr_3$ y para nanocristales de perovskita de composición totalmente inorgánica[80]. Esta síntesis implica la mezcla de precursores (PbX_2) en ODE, junto a OA y OLA. Tras la total solubilidad del precursor, se inyecta rápidamente oleato de cesio previamente preparado en condiciones secas. El proceso de inyección puede llevarse a cabo a temperaturas comprendidas entre 140-200°C, y estas determinarán el tamaño de los nanocristales finales. La reacción puede pararse en 5-10 segundos enfriando la reacción en un baño de hielo o con la adición de tert-butanol para completar la precipitación de los nanocristales. Existen otros métodos recientemente publicados, como la preparación de nanocristales utilizando un **proceso de ultrasonidos**[82]. Esto permite una síntesis fácil, escalable, en un solo paso y libre de disolvente polares, obteniendo nanocristales de alta calidad.

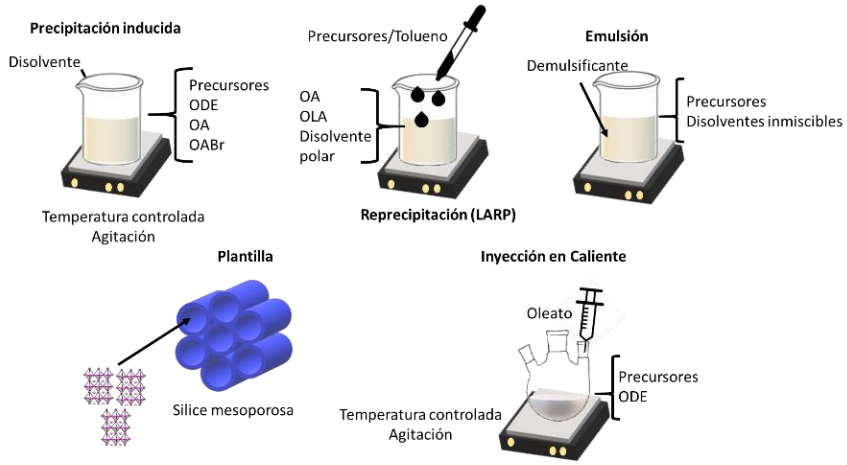

Figura 8. Métodos de síntesis para nanocristales de perovskita.

Las propiedades ópticas de los nanocristales están fuertemente relacionadas con su forma, tamaño y química superficial, debida al cambio de la estructura de la banda. De hecho, dependiendo de la temperatura de reacción, el tiempo, los ligandos tensoactivos, el uso de ligandos de cadena larga y la composición de los precursores, pueden formarse diferentes geometrías como nanoplaquetas (2D)[83], nanocables (1D)[84], esferas[85] y nanobarras[86]. Además, una pequeña variación de la temperatura de reacción puede modular el tamaño, ya que una ligera reducción de la temperatura puede provocar una disminución en el tamaño de los mismos[80].

1.5. Aplicaciones

La creciente demanda del uso de energías renovables a nivel mundial debido al cambio climático está centrando muchos esfuerzos de investigación en el estudio de nuevos materiales con potencial aplicación en el campo de la energía. Particularmente, la perovskita híbrida presenta propiedades ópticas y eléctricas excepcionales, situándose en el centro de muchas investigaciones. Y en este caso, su principal y más atractiva aplicación, consiste en su uso como **célula fotovoltaica**.

Actualmente existen numerosos materiales para la conversión fotovoltaica, siendo el silicio el referente en el mercado y en cierto modo un patrón de medida de eficiencia. En el año 2001 surgió la conocida como célula de Gräztel[87], célula solar híbrida con un rendimiento considerable (aproximadamente 12%) y cercano a la células de silicio policristalino del mercado. Este tipo de células pronosticaban un exitoso futuro debido a su bajo coste de fabricación, flexibilidad y modificaciones en el componente orgánico. Sin embargo, su eficiencia suponía la mitad de las células monocristalinas de silicio o de otros materiales (Semiconductores III-V). Además, la degradación del componente orgánico y del electrolito líquido que contenía, limitaba su aplicación en condiciones reales. Surgieron modificaciones para aumentar su estabilidad (transportadores de huecos sólidos), sin embargo esto suponía una penalización en cuanto a la eficiencia.

Material	Jsc (mA cm^{-2})	Voc(V)	FF(%)	PCE (%)	Ref
$FAPbI_3$ (QD)	16.7	1.12	0.71	13.2	[88]
$(FAPbI_3)_{1-x}(MAPbBr_3)_x$	24.7	1.06	77.5	20.2	[89]
$MAPbI_3$	23.8	1.08	76.2	19.7	[90]
$MAPbI_{3-x}Cl_x$	22.4	0.92	82.0	18.0	[46]
$CsPbI_3$ (QD)	14.0	1.22	0.77	13.1	[91]
$CsPbI_2Br$	13.1	1.32	0.70	12.0	[92]

Tabla 2. Resumen de los parámetros característicos de varios ejemplos de celdas solares basadas en perovskita híbrida.

Las perovskitas híbrida se han convertido en un material prometedor en este campo gracias a su elevada eficiencia y a su síntesis de bajo coste. Además, las posibilidades de modificación en su composición, así como la alta generación de cargas y transporte de las mismas, favorecen sus altos rendimientos (Tabla 2).

La primera célula basada en perovskita híbrida se llevó a cabo en 2009 con eficiencias de 3.8%[17], pero no fue hasta 2016 cuando se alcanzó un avance significativo y se han llegado a conseguir eficiencias de más de un 25%[24]. A pesar de estas eficiencias, el principal inconveniente que presentan es su alta degradación en presencia de oxígeno o en condiciones de humedad[50]. Para intentar solventar el problema de la inestabilidad, en estos últimos años se ha estado estudiando la implantación de perovskitas con configuración 2D en celdas solares[93]. Ya que pese a presentar una menor eficiencia que las perovskitas con estructura 3D, son más estables a las condiciones ambientales.

Las células de perovskita híbrida han marcado un hito en la generación de energía fotovoltaica, puesto que en pocos años han igualado prácticamente las eficiencias del silicio monocristalino. La gran importancia de este hecho radica en que los materiales comúnmente empleados en investigación y el mercado de células solares evolucionan extremadamente lento, por lo que ligeros incrementos (décimas de unidades de eficiencia) pueden suponer grades logros tanto desde el punto de vista científico como en la repercusión a nivel energético mundial.

Debido a las propiedades de emisión de luz que presentan las perovskitas híbridas en el rango del visible e infrarrojo cercano (altas eficiencias de fotoluminiscencia), así como a la capacidad en el ajuste y pureza del color debido a su composición, también es un material prometedor para su aplicación en **diodos emisores de luz** (LEDs)[94]. El rendimiento eléctrico y óptico en los dispositivos LEDs es muy sensible a la calidad de la película de material, por lo que es importante reducir al máximo los defectos e impurezas, así como conseguir regiones activas ultra finas de manera que se obtenga un mayor confinamiento

de los portadores, y en consecuencia una mejora de la recombinación radiativa[95].

Su aplicación en LEDs se remonta a 1994, cuando un grupo de científicos japoneses fue capaz de desarrollar LEDs basados en perovskita que trabajaban a temperatura de nitrógeno líquido[16]. Pero, no fue hasta el año 1999 cuando Mitzi y colaboradores consiguieron el primer dispositivo que trabajara a temperatura ambiente[96], aunque con eficiencias muy bajas. A partir del año 2014 se empiezan a solucionar los problemas de rendimiento y estabilidad, llegando en pocos años a obtener eficiencias altas (Tabla 3)[97].

Material	Relación on/off	Sensibilidad (AV^{-1})	Intensidad luz ($mW\ cm^{-2}$)	Longitud de Onda (nm)	Ref
$CsPbBr_3$ (nanoparticulas)	3094	1.9	10	504	[98]
$CsPbBr_3$ (nanofibras)	2000	3	20	365	[99]
$CsPbCl_3$(nanofibras)	2000	0.014	15	405	[100]
$MAPbBr_3$ (capa)	33	0.036	0.2	780	[101]4
$CsPbI_3$ (nanoparticulas)	340	0.1	0.1	650	[102]

Tabla 3. Resumen de los resultados más destacados de varios ejemplos de dispositivos LEDs basados en perovskita híbrida.

Asimismo, la mayoría de los materiales que son válidos para células fotovoltaicas o LEDs, también lo son para fotodetectores. Al igual que en las aplicaciones anteriores se han de minimizar la mayoría de defectos que disminuyen la capacidad de respuesta y eficiencia. Este problema ya se ha abordado usando monocristales de baja dimensión, llegando a conseguir un dispositivo con nanofibras de $MAPbBr_3$ de luz visible y de alto rendimiento[103], o bien haciendo una hibridación de la perovskita con otras heteroestructuras[104].

Al mismo tiempo, algunos trabajos han reportado que la perovskita híbrida puede actuar como **guía de onda**. Se ha demostrado

que nanofibras con diferente composición permiten el guiado de la luz a la largo de su estructura. La alta eficiencia cuántica y las largas distancias de difusión de portadores son los que permiten el guiado de la luz a lo largo de su estructura, con pequeñas pérdidas en su propagación[105].

También se ha reportado en la literatura que la perovskita híbrida puede actuar como emisor **láser**[106] debido a su alto rendimiento de luminiscencia. La primera vez que se demostró una alta eficiencia a escala de nanocavidad Fabry-Pérot fue en nanofibras de $MAPBI_3$[18], gracias a su morfología, dimensiones de cristal y la presencia de pocos defectos. Este alto rendimiento láser se atribuye a la baja recombinación no radiativa, aunque sí que se ha llegado a observar que dependiendo del método de síntesis, del que depende la morfología y cristalinidad del material, se obtienen rendimientos menores[107].

Es muy importante para esta aplicación la sintonización de la longitud de onda (420-820 nm), alcanzándolo fácilmente con la composición y la estequiometria. Por ejemplo, $CsPbI_3$ o $CsPbBr_3$, demuestran tener altas eficiencias láser a temperatura ambiente en la región del azul o ultravioleta (UV)[103]. Asimismo, nanofibras de perovskita híbrida, con composición $MAPBI_3$, presentan emisión láser en el rojo[104].

En los últimos años, se está haciendo muy popular el uso de la perovskita para convertir la energía solar en energía química a través de la **fotosíntesis artificial**, produciendo los llamados combustibles solares. Estos combustibles generalmente se obtienen por la reducción de protones en hidrógeno, por la ruptura catalítica del agua, o por la reducción de CO_2 en productos orgánicos de valor añadido.

Las perovskitas presentan la capacidad de llevar a cabo este tipo de reacciones[108]. De hecho ya existen trabajos donde se produce la conversión de energía solar a hidrógeno, sobre todo empleando las perovskitas con oxígeno en la estructura[19]. La reducción de CO_2 también se ha logrado con estos materiales, aunque con una eficiencia mucho menor. Es tal el auge de la perovskita como material alternativo a semiconductores convencionales que en los últimos años se están

comenzando a estudiar otras muchas aplicaciones, como por ejemplo, los **moduladores electroópticos** gracias a sus propiedades como guía de onda[109,110]. También, debido a la movilidad iónica que presentan, se está estudiando su capacidad para el almacenamiento de energía, y por lo tanto, su uso como **baterías**[111] o **supercondensadores**[112]. E incluso, recientemente, como **sensor** para la detección de gases contaminantes[113]

1.6. Propiedades ópticas en cristales micrométricos

Debido a las excelentes propiedades ópticas que presentan las perovskitas híbridas en cuanto a emisión y absorción de luz, en los últimos años, están siendo objeto de numerosos estudios tanto de carácter fundamental como en vistas a posibles aplicaciones.

Un material viene definido por sus propiedades básicas tales como densidad o punto de ebullición, e incluso más específicas como su estructura cristalina. Todas ellas, corresponden a propiedades fundamentales para campos específicos de estudio. En el caso de querer estudiar sus propiedades ópticas, es decir, la interacción de la luz con la materia, el índice de refracción y el coeficiente de absorción del material son dos parámetros fundamentales.

El **índice de refracción (n)** se puede definir como la relación de reducción de la velocidad de la luz cuando se propaga por un medio. Es decir, nos indica cuánto ha cambiado su velocidad la luz al atravesar un material. De hecho, la velocidad de la luz en el vacío es quizás la constante más fundamental que disponemos, a partir de la cual se han definido magnitudes tan básicas como el metro y el segundo. Bajo este contexto, el índice de refracción supone un parámetro fundamental, directamente relacionado con el patrón de patrones, la luz.

La reducción de la velocidad de la luz (n) tiene como consecuencia dos fenómenos muy conocidos observables a simple vista, como es el aparente cambio de dimensiones e inclinación de un objeto al introducirlo en un medio acuoso o simplemente las reflexiones de la luz sobre la superficie de un material. En particular, el ángulo de incidencia y el contraste de índices de refracción en una interfase entre dos medios (o materiales) determinan tanto la intensidad, dirección (y polarización) de luz reflejada, así como la transmitida. Una vez en el interior del material, esta última puede verse absorbida. La magnitud de esta atenuación de la luz depende del espesor a atravesar. En particular, decae exponencialmente tal y como lo haría el tiempo de vida de una especie pero en este caso, en función del espesor recorrido por la luz y como factor en la exponencial, el coeficiente de extinción. Esta magnitud representa la parte imaginaria del índice de refracción. Así pues, conocidos el índice de refracción, regularmente asociado a

su parte real y su coeficiente de absorción, se puede determinar a priori la reflexión, transmisión y absorción que muestra un material.

De sobra es conocido que el cambio de la absorción, y por tanto, el cambio del coeficiente de absorción de un material es función de la longitud de onda, es de remarcar, que a su vez también cambia el índice de refracción. De hecho, ambas magnitudes están inter-relacionadas, puesto que un pico de absorción supone un cambio acusado del índice de refracción. En conclusión, es básico conocer la dispersión de ambas magnitudes en un material, en el rango espectral de interés.

Para determinar ambos parámetros, regularmente se emplea la elipsometría, fundamentada en los cambios de polarización en reflexión de una capa determinada de un material. Es una técnica generalmente macroscópica, que requiere una deposición o recubrimiento controlado y homogéneo de un substrato de características determinadas. En el caso de muestras policristalinas, y sobretodo granuladas, esta técnica puede arrojar un alto error puesto que son necesarias consideraciones adicionales, no solo el factor de llenado del empaquetamiento, sino también las múltiples reflexiones, interferencias, así como una gran superficie de absorción adicional en el borde de grano.

Una posible estrategia para minimizar las incertidumbres y realizar estudios más veraces es emplear un único cristal. En este caso se suprimen efectos negativos o enmascaramientos colectivos, y se pueden observar fenómenos de interés como las oscilaciones Fabry-Pérot[114].

Una **cavidad tipo Fabry-Pérot** consiste básicamente en dos espejos paralelos, separados por una distancia determinada (Figura 9) formando una cavidad. Donde al menos, uno de los reflectores (o ambos) muestra(n) cierto grado de transparencia permitiendo insertar o recoger luz al sistema. De esa forma, los fotones que entran en la cavidad, para simplificar consideramos que de manera perpendicular, son transmitidos a través de un espejo, y consecuentemente reflejados en el otro, haciendo un viaje de ida y vuelta volviendo a su posición inicial continuamente. En el caso de volver en fase, se genera

una interferencia constructiva de la luz y por lo tanto una amplificación de la luz. Esta condición se cumple para ciertas longitudes de la cavidad y de onda dando lugar a una serie de modos, los cuales se revelan en un espectro puesto que dan lugar a una serie de picos característicos.

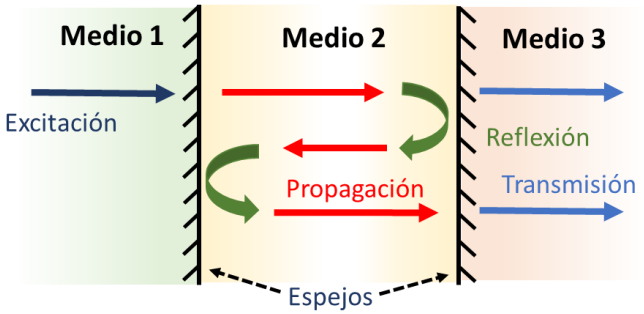

Figura 9. Esquema básico de una cavidad Fabry-Pérot.

El hecho de que en un material se comporte como cavidad Fabry-Pérot implica que es susceptible de que la luz que lo atraviese permanezca confinada gracias a las reflexiones que se producen en sus caras, que actúan como espejos (Figura 9). Este fenómeno es indispensable en dispositivos láser, de manera que la luz recorre varias veces el material y es amplificada de manera coherente. En la literatura se ha demostrado que cristales aislados de perovskita híbrida presentan este comportamiento[115].

Por otro lado, se ha demostrado que en estructuras 1D de perovskitas híbridas se pueden dar las condiciones específicas de **guía de onda**[116]. Estas estructuras 1D o nanofibras son dispositivos con alto índice de refracción, con la propiedad de confinar y guiar a la luz eficientemente a lo largo de su estructura. Cuando la luz insertada en el interior del material llega a la superficie de la fibra, que limita con un medio con índice de refacción menor, se refleja. Este proceso, al igual que en la cavidad descrita anteriormente se produce repetitivamente a lo largo de la fibra, dando lugar a modos, siendo en este caso propagantes. De esa manera la luz confinada se desplaza a la largo de la fibra (Figura 10). De hecho, el contraste de índice junto con el tamaño de la sección del material de alto índice (núcleo de la fibra) determinan la cantidad de luz confinada en su interior para cada

uno de los modos propagados, los cuales describen diversos ángulos de incidencia con los límites de la fibra.

No obstante, a pesar de que la mayor parte de la luz se propaga en el interior del material, cierta proporción se propaga en el exterior (llamado "cladding"). En esta región la luz decae exponencialmente, es decir evanescentemente. Al igual que en el caso de la cavidad Fabry-Pérot, a mayor contraste de índices, mayor es la luz reflejada y por tanto está más tiempo confinada, mostrando una mayor interacción con la perovskita. El factor geométrico juega un papel clave, ya que en secciones de gran (reducido) tamaño, la luz no estaría prácticamente confinada, pero dispersa en todo el material (se guiaría fundamentalmente por el cladding). Por ello existe un tamaño óptimo, frecuentemente cercano a la longitud de onda en el medio donde la luz está muy confinada en el núcleo de la fibra, mostrando una gran interacción con la materia mientras se propaga.

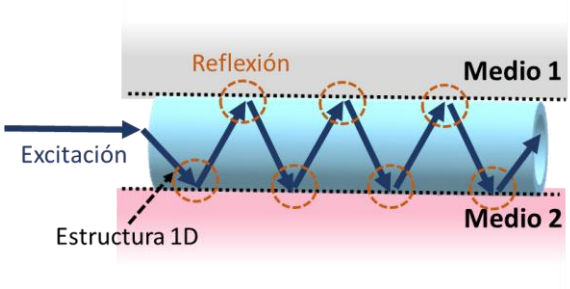

Figura 10. Esquema de la propagación de la luz dentro de una guía de onda.

Como se ha indicado, para poder estudiar de manera exhaustiva los fenómenos que ocurren en el material, y comprobar si se cumplen determinados fenómenos ópticos, es necesario conseguir cristales aislados de perovskita híbrida. La síntesis es relativamente sencilla, pudiéndose obtener buenos resultados por métodos por deposición en vapor[68] o en disolución[62]. No obstante y en ese caso, la perovskita suele seguir direcciones de cristalización preferentes, por lo que es difícil obtener geometrías determinadas y con pocas irregularidades. Es por esto que es importante investigar otros métodos de síntesis alternativos que permitan obtener cristales más regulares y con determinadas dimensiones.

En un primer trabajo se realiza un **estudio sobre el crecimiento de cristales aislados** usando el método de deposición de recubrimiento por giro[64]. Método rápido, versátil, reproducible y económico. Aunque hay muchos parámetros que influyen en la formación de los cristales[117], el estudio se centra de forma más exhaustiva en la influencia de la velocidad de rotación relacionándola además con el empleo de aditivos. Se ha seleccionado ambos parámetros, puesto que el primero es el parámetro fundamental de la técnica y en cuanto al segundo, se ha demostrado recientemente sus posibilidades de control de la cristalización[117], gracias a que favorecen una evaporación más lenta. En conclusión, se establece una relación entre la velocidad de giro y el uso de aditivos con el efecto que producen en la geometría, tamaño y defectos del cristal.

Aunque los cristales que se obtienen son de tamaño micrométrico, son lo suficientemente grandes como para estudiar sus propiedades físicas y químicas (Figura 11). De hecho, una de las mejores pruebas sencillas y no destructivas para conocer la calidad de un cristal es midiendo sus propiedades ópticas. En general, cuanto menos defectos y más cristalinidad presenten las muestras, mejor podrá comportarse como una cavidad y presentar resonancias ópticas, al albergar reflectores plano paralelos más ideales. Sin embargo, esto también depende de otros factores como el acoplamiento de la luz, la absorción del material, y de la geometría y tamaño del cristal.

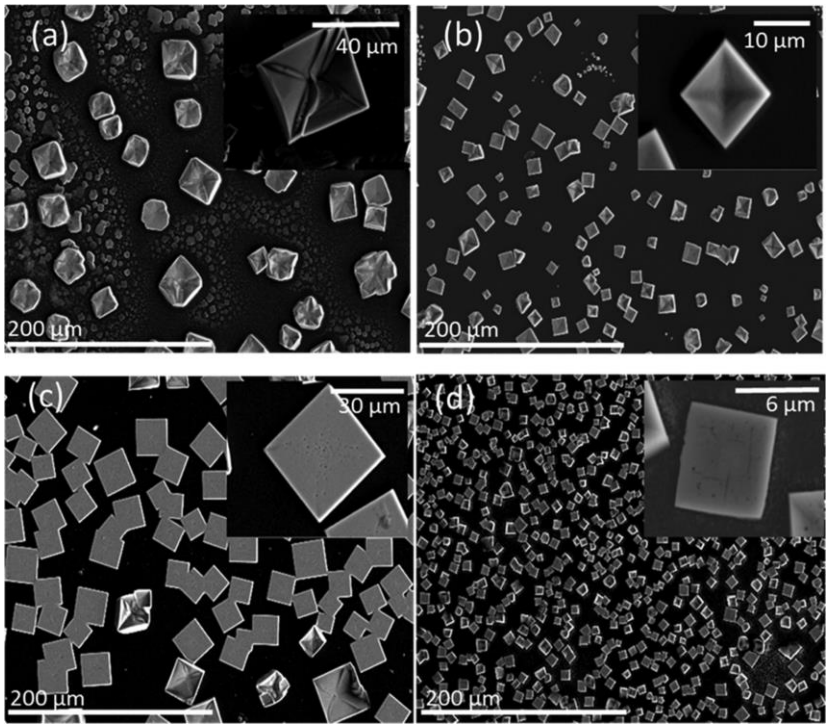

Figura 11. Imágenes de microscopía electrónica de barrido (SEM) de cristales de $MAPbBr_3$ sobre sustratos de cuarzo obtenidos a una velocidad fija de 1000 rpm, para los diferentes aditivos. [a)Sin aditivo (NA); b) Ciclohexilpirrolidona (CHP); c) Dimetilsulfoxido (DMSO); d) Tertbutilpiridina (TBP)].

Recordando que la condición de resonancia se produce por los múltiples reflejos de la luz en las caras del cristal, que finalmente conduce un fenómeno de interferencia constructiva. De esta manera, en un cristal con forma de pirámide no se espera este fenómeno o bien que sus efectos estén muy limitados debido a su complicada geometría. Sin embargo, las caras paralelas de un cristal plano son óptimas para producir las resonancias tipo Farby-Pérot[118]. De hecho, este fenómeno no sólo se observa en el espectro de transmitancia, sino que también en el de fotoluminiscencia. En ambos casos aparecen una serie de picos producidos por los modos resonantes de la luz.

Aunque el resonador óptico es un elemento fundamental de la fotónica, en la actualidad existen escasos estudios teóricos sobre el fenómeno de cavidad óptica sobre cristales micrométricos[119] y

aparentemente ninguno que ajuste el espectro de fotoluminiscencia (PL) con picos Fabry-Pérot. Es por ello, que en un segundo trabajo se desarrolla un **método para determinar los parámetros ópticos** fundamentales a través de estos modelos. Para demostrar que el método desarrollado es válido, hemos utilizado como referencia una cavidad plana asimétrica. Se trata de un cristal aislado, igualmente obtenido por el método de recubrimiento por giro sobre un sustrato de cuarzo. La luz pasa a través de dos interfases, aire/perovskita y perovskita/cuarzo donde los medios separados por las mismas presentan una diferencia en el índice de refracción. Esta diferencia favorece que se produzcan múltiples reflexiones y por tanto el fenómeno de cavidad óptica.

El método propuesto consiste en ajustar simultáneamente la transmitancia óptica (OT) y la fotoluminiscencia (PL). De esta manera, el modelo permite una fiel determinación de los componentes real (n_r) e imaginario (n_i) del índice de refracción del material, alrededor del borde de absorción. Adicionalmente, se tienen en cuenta cómo afectan otros parámetros del sistema en el fenómeno de cavidad. Por ejemplo, se estudia el efecto de la apertura numérica del objetivo o el espesor del cristal. Los resultados que se obtienen (Figura 12) se comparan con otros valores de la literatura obtenidos por otros métodos.

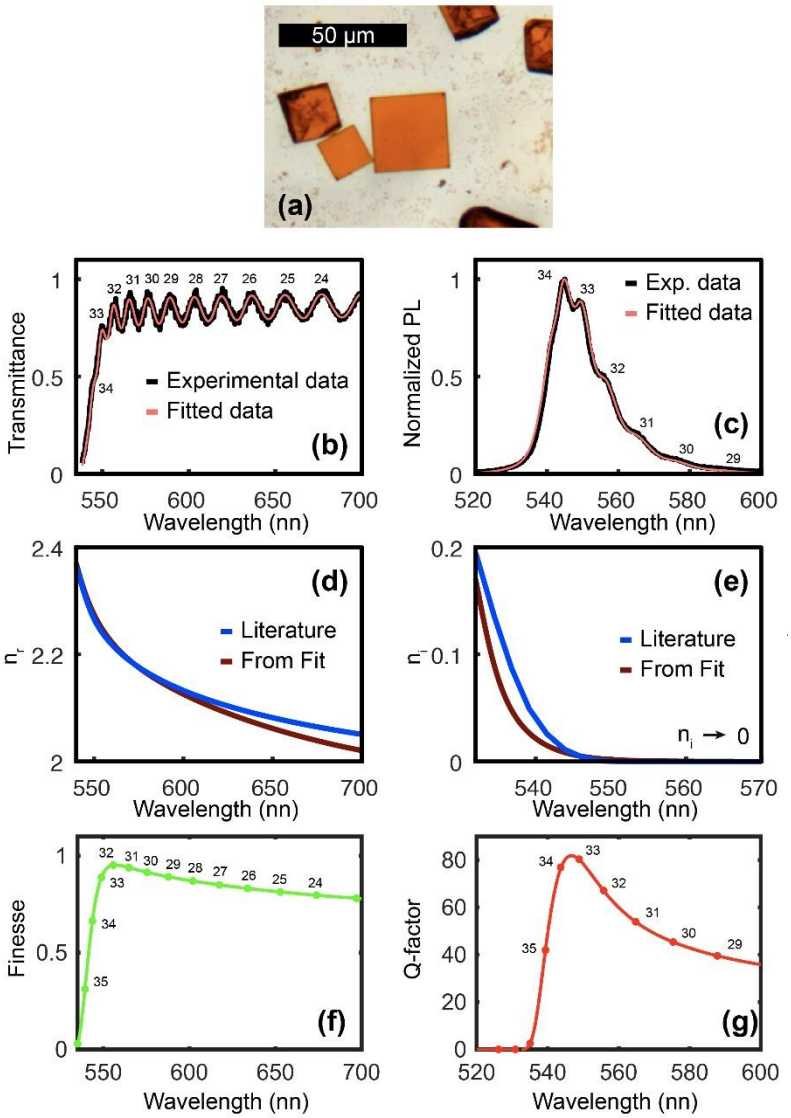

Figura 12. a) Imagen de microscopio óptico del cristal con geometría plana de $MAPbBr_3$ medido (estructura cuadrada en el centro de la imagen). b) y c) Datos experimentales y ajuste teórico de las curvas para los espectros de Transmitancia (OT) y Fotoluminiscencia (PL). d) parte real y e) parte imaginaria del índice de refracción y la comparación con datos de la bibliografía[120]. f) finura y g) factor de calidad para todos los modos identificados.

Con la finalidad de estudiar el fenómeno de guía de onda en las perovskitas híbridas, en un último trabajo se propone un método simple y de bajo costo para obtener **estructuras 1D o nanofibras** (Figura 13). El método de síntesis se basa en el inclusión de una disolución de precursores en la ranuras de tamaño submicrométrico de un molde en polidimetilsiloxano (PDMS). El molde de PDMS se consigue mediante una réplica de un CD o DVD comercial (policarbonato), ofreciendo diferentes tamaños de ranuras y distribución. Con este método se pueden obtener nanofibras de diferente composición ($MAPbBr_3$ y $CsPbBr_3$) con un tamaño y ancho homogéneo. Además con unas dimensiones determinadas dependiendo de la plantilla empleada.

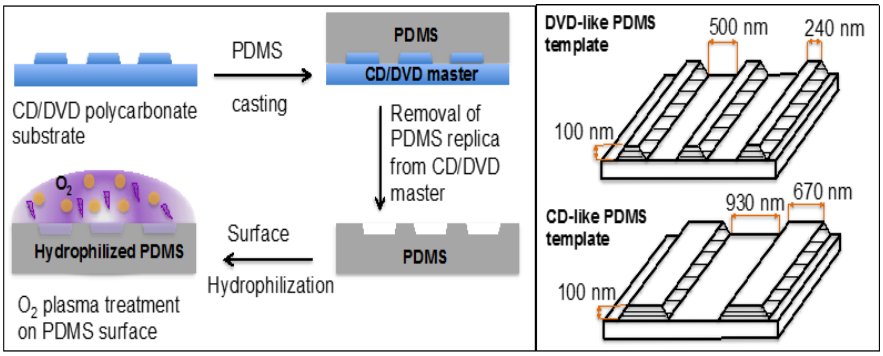

Figura 13. Ilustración esquemática de la preparación de los moldes de PDMS.

Para confirmar la viabilidad del material sintetizado y sus propiedades de guía de onda a lo largo de la estructura, se realizan medidas ópticas de fotoluminiscencia. La metodología consiste en variar la distancia entre el punto de excitación y el punto de recolección. En particular, se fija el punto de recolección de la señal en el extremo de la fibra, mientras que el de excitación es desplazado a lo largo de la misma.

El modelo presentado anteriormente para obtener los parámetros ópticos también es aplicable en nanofibras de perovskitas. En este caso, el espesor representa la longitud de la fibra y tanto el índice de refracción y extinción del material son substituidos por valores eficaces, puesto que la luz se guía tanto en la fibra como en la proximidad de la misma. Con este modelo, corroboramos los datos

experimentales obtenidos para el espectro de luminiscencia de una nanofibra con un espesor determinado. El ajuste realizado por el modelo, es totalmente coherente con los datos experimentales, por lo que podemos decir que nuestro material se comporta como una guía de onda.

Al igual que el método teórico puede ser aplicado para demostrar y corroborar diferentes fenómenos ópticos, así como, para la obtención de parámetros fundamentales de la perovskita híbrida, no está limitado únicamente a este material, pudiendo ser utilizado para estudiar otro tipo de materiales.

1.7. Perovskita híbrida como fotocatalizador

La sostenibilidad ambiental y el uso de energías renovables representan dos de los mayores desafíos a los que se enfrenta la sociedad actual[121]. La rápida urbanización e industrialización conlleva un uso intenso de los recursos disponibles, así como, una contaminación masiva produciendo una escasez de agua. Además el aumento mundial de la actividad humana está incrementando la emisión de gases de efecto invernadero que afectan de manera directa al calentamiento global. Todo esto provoca, que nuestro planeta sufra serios problemas medioambientales, con un crecimiento continuo de la demanda energética, lo que hace más necesario el uso de energías alternativas renovables. Es por ello que esta temática se ha convertido en uno de los principales desafíos en investigación y muchos grupos centran sus trabajos en perseguir un uso sostenible de energía en nuestro planeta.

Para mitigar estos problemas es importante desarrollar energías alternativas sostenibles y que puedan satisfacer la demanda energética actual[122]. Una de las opciones más atractivas es el uso de la luz solar debido a su accesibilidad[123]. Además, es una fuente de energía sostenible e inagotable[124], y cuya explotación tiene un efecto mínimo adverso sobre el medioambiente. Con su uso masivo, concretamente para la producción de combustibles solares (hidrógeno, metano), se podría reducir la dependencia a los combustibles fósiles, y por lo tanto, se podría conseguir una disminución de la contaminación.

La técnica que se presenta como alternativa y como ruta principal para convertir la energía solar en combustibles químicos es la conocida como fotocatálisis[124]. Esta técnica surge en los años 70, cuando Fujishima y colaboradores demostraron por primera vez que el dióxido de titanio (TiO_2) era capaz de generar fotocorriente y a su vez disociar el hidrógeno a partir del agua. Siguió en auge en los años siguientes, alcanzando grandes avances gracias a su carácter multidisciplinar. Principalmente los trabajos se centraron en su uso para la descontaminación de medios acuosos, de la atmósfera y de suelos.

El **proceso fotoquímico** se inspira en la fotosíntesis natural y está relacionado con la capacidad de un material para absorber fotones y

acelerar una reacción extremadamente lenta (Figura 14). La fotocatálisis se inicia mediante la absorción de luz, es decir la excitación de un fotón con una energía mayor que la energía de la banda prohibida del material fotoactivo. Esto induce la promoción de electrones y formación de huecos en las bandas de conducción y valencia, respectivamente. Estos pares electrón-hueco (también conocido como excitón) tienden a recombinarse fácilmente con la consiguiente pérdida de energía regularmente en forma de luz o calor[125]. Lo pocos portadores de carga que no se recombinan migran a la superficie del material, donde posteriormente ocurrirán las reacciones redox[126].

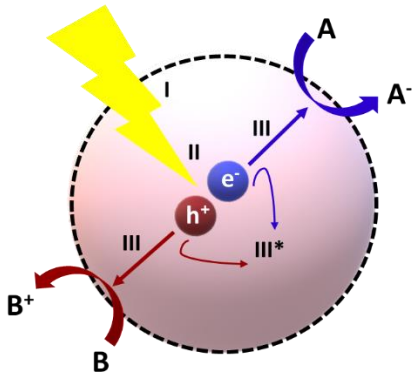

Figura 14. Etapas de un proceso fotocatalítico. i) Absorción de luz, ii) separación de cargas fotogeneradas, iii) transferencia de electrones y huecos, iii*) recombinación individual de las cargas, iv) reacciones redox donde A y B se refieren a las reacciones de oxidación y reducción.

A lo largo de los años los materiales más estudiados en fotocatálisis han sido los óxidos metálicos. Sobretodo el óxido de titanio (IV), debido a su alta fotoestabilidad, ausencia de toxicidad y abundancia[127]. El problema es que la mayoría de estos materiales presentan un alto índice de recombinación de cargas[128] y una banda prohibida que limita su uso a la radiación UV. Cuando son iluminados con radiación solar baja su eficiencia, ya que solo se aprovecha un 5% de la misma[129]. Esto se debe a que la luz solar que alcanza la superficie de la tierra contiene una fracción muy pequeña de radiación UV (Figura 15).

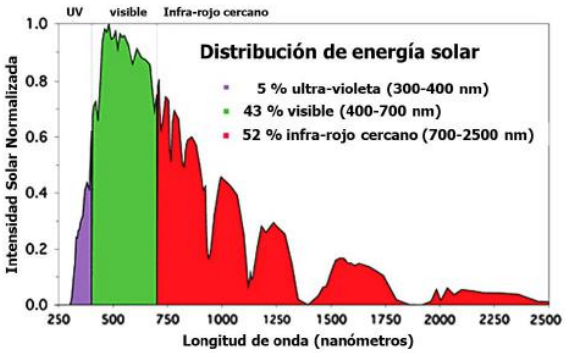

Figura 15. Espectro solar que alcanza la superficie de la tierra[130].

Con la finalidad de mejorar la eficiencia de este proceso, se están explorando nuevas rutas en el diseño de fotocatalizadores. Para ello hay ciertos parámetros importantes a considerar, entre ellos la generación, difusión y transporte de las cargas[131]. Una vez fotogenerados los portadores deben ser separados eficientemente, de manera que disminuya la tasa de recombinación, y que puedan ser transportados a lo largo del material hacia la superficie del catalizador. Es por eso que una longitud de difusión alta y un buen transporte de carga son cruciales[132].

La configuración de las bandas de energía es otro punto importante a tener en cuenta[133]. Es requisito indispensable que la energía del electrón fotoexcitado sea mayor que el correspondiente nivel redox de la reacción, y el potencial de la banda de conducción (BC) del fotocatalizador debe ser situado a un valor energético superior. Por otro lado, si se consigue una modulación de la banda prohibida del material[134], se puede conseguir que el material absorba en un rango mayor del espectro y en consecuencia obtener una mayor eficiencia. Por ejemplo, ampliando el espectro de absorción hasta las 600 nm se conseguiría un rendimiento del 16% y si se ampliara hasta los 800 nm un 32%. Para conseguir este objetivo se usan diferentes estrategias entre ellas el uso de estructuras nanométricas[135], modificación de la superficie o interfases[136] y el uso de dopantes metálicos o no metálicos[137]. La presencia de defectos afecta a la estructura electrónica del material y por lo tanto, también puede utilizarse como estrategia para conseguir un mejor rendimiento[138].

Debido a las características excepcionales que presentan las perovskitas, han demostrado ser un candidato prometedor para fotocatálisis. Entre las propiedades que destacan para su aplicación en este campo esta su **alta absorción en el rango del UV-Visible**[139], su baja energía de excitación con una posición de banda prohibida óptima, su larga difusión de cargas con respecto a otros materiales[140] y su buen balance de transferencia de carga. También, su síntesis sencilla y de bajo coste hace que sea un material muy accesible.

Además, las perovskitas presentan la posibilidad de **modificar su banda prohibida**[80]. El mero cambio del halógeno puede producir una reducción en la banda prohibida, abarcando una mayor región del espectro visible y en consecuencia un mejor actividad catalítica[141]. Incluso la presencia de defectos puede hacer que cambien sus propiedades optoelectrónicas, los cuales pueden ser modificados y controlados durante el proceso de síntesis[142]. Este es el motivo por el cual hay una gran cantidad de perovskitas híbridas que pueden ser utilizadas como fotocatalizadores.

Uno de los procesos más comunes para la producción de energía y a la que se le está dedicando una gran atención es la **fotoelectrólisis de agua**. La producción de H_2 y O_2 usando un fotocatalizador tiene gran potencial debido al gran interés medioambiental y su coste económico. Para que la reducción del agua se lleve a cabo es condición indispensable que la posición de niveles de energía de la banda de conducción del catalizador sea más negativa que el potencial de reducción del agua (hidrógeno). Y la banda de valencia más positiva que el potencial de oxidación para producir oxígeno. Además el catalizador debe ser estable en disolución acuosa y bajo iluminación.

Las perovskitas más comúnmente utilizadas para la producción de hidrógeno a partir de agua y luz solar son las perovskitas inorgánicas que contienen Ti y Ta[108] en la estructura. Por el contrario, no existe ningún trabajo sobre el uso de perovskitas híbridas, ya que es bien conocida su inestabilidad en presencia de agua, luz e incluso humedad[143]. En cualquier caso, la presencia de agua tiene una influencia negativa en el rendimiento de los dispositivos fotovoltaicos basados en compuestos iónicos, debido a que se hidrata la superficie

de los mismos y en consecuencia disminuye la conductividad eléctrica y la migración de cargas[144].

En el caso de la fotocatálisis, puede ocurrir que la humedad no tenga un efecto tan negativo en el proceso. En la bibliografía existen ejemplos donde no se observa fotocorriente, pero si actividad fotocatalítica[145]. Esto puede ser debido a que las condiciones experimentales eviten la degradación de la perovskita, es decir, que el proceso sea lo suficientemente rápido para que la perovskita no se degrade en presencia de agua y sea está ultima la que se disocie. Además, en este proceso los pares electrón-hueco no necesitan migrar de partícula en partícula hacía el exterior necesario en dispositivos fotovoltaicos, sino que la reacción se produce en la superficie de cada partícula conductora, donde la humedad debería de ser reactiva[146].

Teniendo en cuenta la hipótesis anterior y con el fin de proporcionar información sobre la actividad fotocatalítica de las perovskitas híbridas, se presenta un estudio donde se reporta la actividad catalítica para la producción de hidrógeno de una perovskita híbrida de cobre $MA_2CuCl_xBr_{4-x}$, cuya síntesis y actividad fotovoltaica ya es conocida[147]. Se selecciona esta perovskita con la finalidad de evitar el uso de materiales tóxicos, como el plomo, y porque ha sido demostrado que la presencia de cobre hace que las propiedades fotoquímicas de la perovskita no se vean tan influenciadas por la humedad[148].

En particular, se muestra la actividad catalítica de dos perovskitas de cobre con diferente composición, $MA_2CuCl_2Br_2$ y $MA_2CuCl_{0.5}Br_{3.5}$. El experimento se lleva a cabo en fase gaseosa bajo radiación solar, y sin necesidad de un agente sacrificante. Además, para demostrar que la actividad catalítica se ve afectada por la composición, se compara con otras perovskitas que contienen plomo. Los experimentos concluyen que la perovskita de cobre presenta una mayor actividad que su análoga de plomo (Tabla 4).

Photocatalyst	µmol H2/gcat	AQY[a] (%)	TON[c]
$MA_2CuCl_2Br_2$	141.21	0.7153 (0.73)[b]	5.06 (12.05)[d]
$MA_2CuCl_{0.5}Br_{3.5}$	94.23	0.4773	4.00
$Cs_2CuCl_2Br_2$	9.03	0.0457	0.51
$MAPbBrI_2$	5.16	0.0261	0.30
$MAPbClI_2$	2.89	0.0146	0.15
$MAPbI_3$	2.69	0.0136	0.17
$MAPbCl_3$	2.54	0.0129	0.09
$MAPbBr_3$	2.11	0.0107	0.10

Tabla 4. Datos de producción de H_2 obtenidos a las 24 horas de reacción para diferentes tipos de perovskita.[a] Rendimiento cuántico aparente calculado mediante la ecuación: AQY = 2·número de moléculas de hidrógeno producidas/ número de fotones incidentes. [b]Rendimiento cuántico aparente para la producción de oxígeno. [c]TON calculado a las 24 horas. [d]TON calculado a las 54 h

Frente a las condiciones experimentales este material es estable, tal y como se demuestra en las diferentes técnicas de caracterización. Por tanto, este estudio demuestra que a pesar de que la humedad es perjudicial para las perovskitas, especialmente en su aplicación fotovoltaica, es posible utilizarlas para procesos que requieren de una mínima humedad para favorecer la migración de la carga entre partículas. Todo esto se consigue gracias a las condiciones experimentales en las que se desarrolla la reaccion fotocatalítica. Concretamente, se lleva a cabo la reacción en fase vapor lo que permite que la perovskita híbrida sea estable durante la reacción.

1.8. Perovskita híbrida como sensor de gas

El uso de combustibles fósiles para la producción de energía es la principal fuente de contaminación del aire. Según la Organización de la Salud (OMS), nueve de cada diez personas están expuestas a aire contaminado, provocando 7 millones de muertes en todo el mundo cada año[149]. Por esta razón, esta organización define la contaminación atmosférica como el riesgo ambiental más significativo para la salud humana y como el principal desafío para el cambio climático.

Los gases emitidos, como el dióxido de carbono (CO_2), metano (CH_4) u ozono (O_3), son los responsables del efecto invernadero, y además peligrosos para la salud humana por encima de niveles muy bajos de exposición. El dióxido de nitrógeno (NO_2), se genera principalmente en la combustión a alta temperatura en los vehículos[150], en exposiciones largas puede causar graves problemas de salud, como enfermedades respiratorias, cardíacas o cáncer de pulmón. Por otro lado, el amoniaco (NH_3) emitido mayoritariamente en procesos agrícolas y por el ganado, es irritante y corrosivo[151]. Su exposición a niveles elevados provoca toxicidad aguda que puede producir ataques respiratorios, quemaduras, e incluso la muerte[152]. También es importante la detección de otros compuestos aromáticos, como benceno y tolueno, debido a su peligrosidad hacia la salud humana por sus efectos cancerígenos. De hecho, actualmente los principales países europeos están limitando la entrada de vehículos en las grandes ciudades, con la finalidad de controlar y limitar la contaminación en las mismas[153].

Para controlar esta situación se necesitan sensores de gases sencillos, estables y sensibles, para monitorizar y detectar contaminantes a nivel de concentración traza. De hecho, el establecimiento de una amplia red de sensores para la monotorización de los contaminantes es un desafío para nuestra sociedad actual. Esto requiere dispositivos económicos, de bajo consumo y suficientemente selectivos. Sin embargo, la gran mayoría de los procedimientos de detección de gases disponibles se asocian con instrumentación compleja y de alto costo, como por ejemplo técnicas cromatográficas[154] o espectroscopía infrarroja por transformada de

Fourier (FTIR)[155]. Estas técnicas proporcionan lecturas de gases precisas y selectivas, pero implican el uso de personal capacitado, alto consumo de energía y su miniaturización sigue siendo un problema[156].

En los últimos años se han estudiado ampliamente otras opciones, sensores ópticos, gravimétricos y electroquímicos. Los dispositivos ópticos presentan alta sensibilidad, lo que permite la detección de contaminantes a niveles traza[157], pero actualmente son caros y presentan baja portabilidad. Los dispositivos gravimétricos, como los sensores de ondas acústicas de superficie (SAW) o las microbalanzas de cristal de cuarzo (QCM), son muy sensibles a los gases con tiempos de respuesta cortos[158,159]. Sin embargo, son muy complejos, de alto costo y muy sensibles a la humedad y temperatura[160]. En el caso de la detección electroquímica, es la técnica más popular debido a su bajo coste, buena selectividad, bajo consumo y repetibilidad[161]. El principal problema que presentan es su variabilidad con la temperatura y su dificultad de minituarización[162].

Frente a estas alternativas, los **sensores químicos resistivos** han surgido como una opción fácil y económica[163]. Estos dispositivos pertenecen a la familia de sensores de gas en estado sólido, en la que la interacción del gas objetivo con la superficie del sensor es reversible y produce cambios en su resistencia. Es decir, cuando los gases interaccionan con el material del sensor se produce una transferencia de carga entre las moléculas absorbidas, y el mecanismo de adsorción/desorción del gas induce una transferencia de carga que se transforma en un cambio en la señal eléctrica. La respuesta de los sensores se define generalmente como la diferencia entre el valor de resistencia inicial (R_0) y el cambio de la propiedad física medida (R), normalizado a R_0. Estos cambios son monitorizados y cuantificados, por lo que pueden correlacionarse con la naturaleza de las especies gaseosas y con su concentración.

En las últimas décadas, este tipo de sensores se han centrado en los óxidos metálicos[164], ya que presentan alta sensibilidad, buena reproducibilidad y tiempos de respuesta bajos[165]. Sin embargo, requieren altas temperaturas de operación y por lo tanto un alto consumo de energía[166]. Además, estas temperaturas disminuyen a

largo plazo la estabilidad de los sensores, debido a los cambios irreversibles que se produce en su estructura cristalina[167]. Asimismo, mejorar su selectividad es aún un desafío importante, ya que puede mejorarse pero aumentando la complejidad y el coste económico del dispositivo.

En los últimos años, las investigaciones se han centrado en nanomateriales de carbono, en particular, nanotubos de carbono y grafeno. Las nanoestructuras de carbono de baja dimensionalidad aportan unas mejores propiedades debido a la relación superficie/volumen. La mayoría de los átomos están en la superficie, de manera que están más expuestos al ambiente químico, lo que implica también una alta sensibilidad. Además, estas nanoestructuras suelen tener alta cristalinidad, alta movilidad de portadores, facilidad de miniaturización y bajos niveles de ruido[168]. Estos dispositivos también permiten trabajar a temperatura ambiente, lo que disminuye drásticamente el consumo de energía. Sin embargo, los átomos de carbono unidos covalentemente a través de enlaces sp^2 implican una baja reactividad química con el medio ambiente. Por ello se diseñan rutas para lograr materiales de carbono con una mayor sensibilidad, como, por ejemplo, la creación controlada de defectos, la substitución de grupos funcionales, y la decoración con metales o nanopartículas de óxidos metálicos, entre otros.

Gracias a las propiedades semiconductoras que presentan, las perovskitas son un candidato válido para el desarrollo de sensores de gases. Además, estas pueden ser implementadas fácilmente en sensores de gases debido a su fácil síntesis, favoreciendo la obtención de dispositivos de bajo coste y que además pueden trabajar a temperatura ambiente. La principal desventaja que presentan las perovskitas es su inestabilidad en condiciones ambientales y de humedad. Recientemente se ha desarrollado un sensor de gas formado por un híbrido de grafeno y nanocristales de perovskita, donde se consigue una protección muy efectiva de los nanocristales gracias al carácter hidrofóbico del grafeno[113]. Con este sensor se ha conseguido la detección de NO_2 y NH_3 en concentraciones de partes por billón (ppb) y partes por millón (ppm) respectivamente.

Aunque actualmente existen diversos trabajos en los que se estudian las propiedades de sensado de las perovskitas híbridas, en ninguno se analizan los efectos que produce la diferente composición sobre el mismo. Es decir, hace falta un estudio exhaustivo que muestre si los cambios en el catión (A) o en el anión (X) en la estructura de perovskita (ABX_3) tienen una influencia significativa en las propiedades de detección de gases. Por lo tanto, en un artículo que forma parte de esta tesis se presenta un estudio completo sobre el papel que desempeñan varios cationes (A) y haluros (X) en la detección de compuestos orgánicos volátiles (COV). El material activo que se usa es un material híbrido grafeno-perovskita, que se ha demostrado que confiere una alta estabilidad a las perovskitas y que presenta unas buenas propiedades de detección frente a otros gases[113]. Para este estudio se han sintetizado diferentes nanocristales de perovskita. En particular, se han sintetizado nanocristales de perovskita con tres cationes diferentes: metilamonio (MA), formamidinio (FA) y cesio (Cs). Y tres perovskitas con tres aniones distintos: cloro (Cl^-), yodo (I^-) y bromo (Br^-). Sin embargo, debido a la alta inestabilidad de la perovskita con anión triyoduro ($MAPbI_3$) se ha sintetizado una perovskita híbrida con mezcla de yodo y bromo ($MAPbBr_{2.5}I_{0.5}$)[144].

Los nanomateriales híbridos obtenidos se depositaron sobre sustratos de alúmina con electrodos interdigitados de platino. Los experimentos de detección de gases se realizaron utilizando una cámara de teflón hermética de 35 cm^3. Esta cámara se conectó a un sistema de mezcla y suministro de gas, que utiliza botellas calibradas de gases y aire seco puro. Los dispositivos se utilizaron para la detección de compuestos aromáticos como benceno y tolueno en el rango de ppm. Además, estos dispositivos han sido utilizados en condiciones de bajo consumo energético, trabajando a temperatura ambiente y con un bajo caudal (100 mL/min), lo que no implica el uso de bombas.

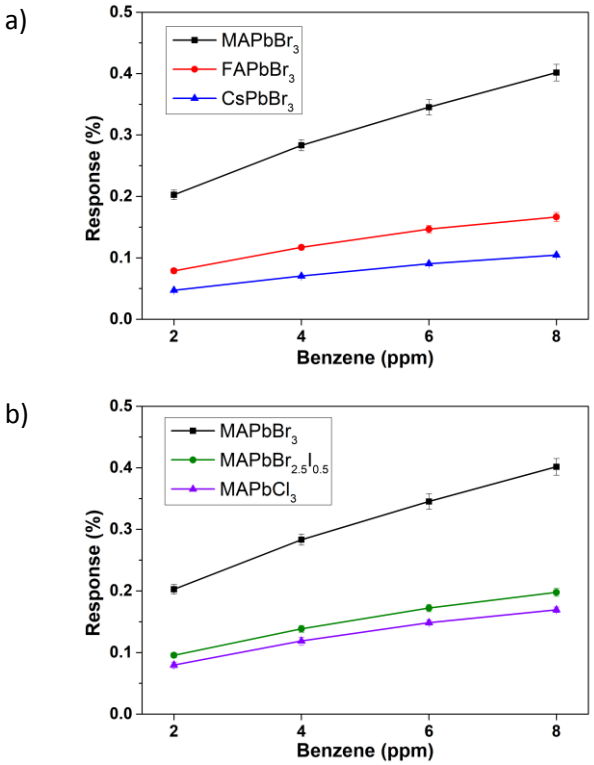

Figura 16. Curvas de calibración para benceno. a) en función del tipo de catión, b) o de aniones en la estructura de la perovskita.

En la Figura 16, se muestran las curvas de calibración para el caso del benceno, tanto para los diferentes cationes (Figura 16a) y aniones (Figura 16b) en la estructura de la perovskita. En cuanto al efecto de catión, MA muestra una clara mejora. Respecto al caso del anión, el Br ofrece una mayor respuesta y sensibilidad. En el caso de la detección de tolueno, se observa un comportamiento equivalente.

1.9. Dispositivos fotovoltaicos

Como se ha comentado en el apartado anterior, muchos expertos afirman que estamos al inicio de una crisis energética mundial debido al continuo incremento de la demanda energética y los problemas medioambientales por lo que, el desarrollo de alternativas renovables para suplir la demanda de energía es uno de los mayores retos de nuestra sociedad. Una de las alternativas con mayor proyección son los dispositivos fotovoltaicos. La fabricación y desarrollo de dispositivos eficientes y de bajo costo podrían sustituir las fuentes convencionales de energía eléctrica.

En la actualidad existen diferentes tipos de células fotovoltaicas disponibles. Las células más comunes son las formadas por silicio. Este material es abundante en la naturaleza, estable en condiciones de iluminación y presenta un espectro de absorción que alcanza desde el ultravioleta al infrarrojo cercano[169]. Estas células han funcionado bien a lo largo de los años en términos de eficiencia y estabilidad. Sin embargo, el procesamiento del material requiere el uso de altas temperaturas, lo que se traduce en un mayor costo económico, y por ende, una aplicación comercial más limitada.

En los últimos años, las perovskitas híbridas han atraído un gran interés para esta aplicación. Esto se debe a sus buenas propiedades de absorción, a su valor óptimo de banda prohibida y a la buena difusión de portadores. Además, su síntesis e implementación en los dispositivos es fácil y económica[170]. Asimismo, tienen una cierta flexibilidad que les permite amoldarse a diferentes superficies y formar parte de dispositivos plegables[171]. Como se ha dicho anteriormente, en los últimos años las perovskitas híbridas de haluro de plomo ($APbX_3$) han logrado significativas eficiencias, situándose en valores alrededor del 25%. Estos valores de eficiencia son totalmente competitivos con las células convencionales de silicio, por lo que se posiciona como alternativa de bajo costo a la tecnología actual.

Por el momento, las células solares de perovskita con yodo en su estructura son las que ofrecen la máxima eficiencia de conversión[172]. Esto es debido a que esta composición de perovskita exhibe una cobertura total del espectro del visible. Sin embargo, en comparación

con las perovskitas que presentan bromo en su estructura, ofrecen una menor estabilidad a la luz y a la humedad[173].

Las células formadas por perovskita híbrida funcionan como una célula de unión p-n en estado sólido. La perovskita absorbe la luz con la que el dispositivo es iluminado, generando electrones y huecos. La capa de perovskita se encuentra entre dos contactos selectivos. Por un lado, tenemos una capa que funciona como material transportador de electrones (EMT), generalmente dióxido de titanio (TiO_2). Mientras que un segundo contacto funciona como material transportador de huecos (HTM), típicamente spiro-OMETAD o [6,6]fenil-C61-ácido butírico metil ester (PCBM). Por lo tanto, los electrones y huecos generados en la perovskita son recogidos selectivamente por cada una de las capas, de manera que fluyen a través del circuito externo. En la Figura 17 se muestra el diagrama de bandas de un dispositivo con una configuración típica.

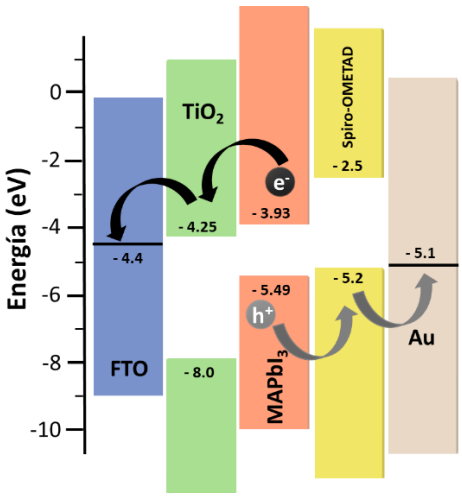

Figura 17. Diagrama de energía de una configuración típica para una celda solar de perovskita. FTO/TiO_2/Perovskita ($MAPbI_3$)/Spiro-OMETAD/Au.

A pesar de los grandes avances en el aumento de las eficiencias de las células fotovoltaicas formadas por este material, todavía hay muchos obstáculos a superar antes de su comercialización. Para que el dispositivo pueda considerarse, se debe de garantizar la producción estable de energía en condiciones ambientales reales de radiación

solar, temperatura y presencia de humedad y oxígeno. Sin embargo, es bastante conocida la inestabilidad de la perovskita en estas condiciones[55]. Además, otro problema es la presencia de plomo, que presenta una alta toxicidad[59].

Para solventar el problema del plomo se ha intentado fabricar células con otros metales diferentes, como por ejemplo estaño. Pero presentan también problemas de estabilidad al exponerse al aire, lo que limita el rendimiento de los dispositivos[174]. Por otro lado, para evitar la degradación de la perovskita en condiciones ambientales, se han estudiado dispositivos con estructura 2D[175]. Como ya se ha comentado con anterioridad, en esta estructura, la presencia de cationes orgánicos largos con cadenas alquílicas o aromáticas aportan un mayor carácter hidrofóbico. Aunque la misma presencia de estos cationes orgánicos le confieren peores propiedades de transporte de cargas, que se traduce en la obtención de eficiencias muy bajas.

Recientemente, han surgido unos candidatos prometedores conocidas como **perovskitas híbridas multidimensionales**. Las perovskitas multidimensionales 2D/3D, conocidas también como fases Ruddlesden-Popper ($R_2A_{n-1}B_nX_{3n+1}$), han sido descritas anteriormente a lo largo de la tesis, y donde el número de capas de octaedros viene determinado por n. Puede variar de 1 a ∞, de manera que cuando n es igual a 1 la estructura se corresponde con una estructura 2D y cuando n tiene un valor de ∞ corresponde a un material 3D.

Estas estructuras multidimensionales combinan propiedades de ambas configuraciones. Por un lado, el alto rendimiento obtenido para las perovskitas 3D, manteniendo el excelente transporte de carga y su absorción característica. Y por otro lado, mantienen la estabilidad en condiciones ambientales de las perovskitas con estructuras 2D[176]. Además, son capaces de incorporar una amplia gama de cationes orgánicos que confieren a la estructura una cierta flexibilidad. Es decir, el espaciado entre las capas de la perovskita multidimensional puede permitir la intercalación de moléculas huésped. Esta estrategia ya ha sido utilizada en otros materiales 2D[177], con el propósito de conferir a los materiales nuevas propiedades.

Hoy en día, los trabajos de incorporación o dopaje en la estructura de la perovskita son escasos[178]. Uno de los dopajes más comúnmente utilizados es el intercambio de un átomo de la red cristalina, introduciendo defectos en la bandas, modificando el nivel de Fermi y en consecuencia favoreciendo una unión p/n[179]. También se han reportado estudios donde se introducen nanopartículas metálicas dentro de la estructura, consiguiendo una mejora en la fotorrespuesta del material[180]. En esta tesis se presenta por primera vez la incorporación de un compuesto organometálico en la capa intermedia de los cationes orgánicos, encontrándose así dentro de la estructura de la perovskita multidimensional (Figura 18).

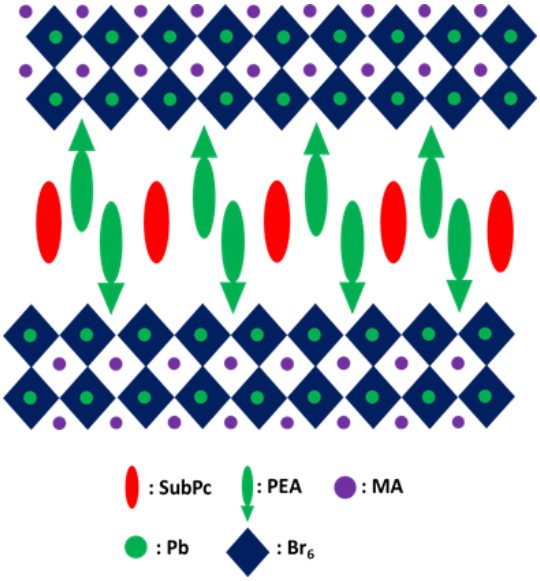

Figura 18. Representación esquemática de la molécula huésped (Subftalocianina-SubPc) entre las capas de ligandos orgánicos.

Como molécula orgánica huésped hemos elegido un derivado de subftalocianinas de boro (SubPc). Estas moléculas son macrociclos aromáticos, formada por tres átomos de diiminoisoindol y un átomo de boro central[181]. Presentan una estructura piramidal, donde el átomo de boro se encuentra conectado al átomo de nitrógeno de las tres isoindolinas, a través de dos enlaces covalentes y un enlace de coordinación. De este modo, todo el plano molecular constituye un sistema conjugado de 14 electrones-π. El único electrón en el último

orbital sp^3 dejado por el átomo de boro deficiente en electrones, está conectado a otro átomo o grupo aromático en la posición axial[182] (Figura 19).

Esta familia de compuestos presenta una alta estabilidad química y térmica, así como una buena procesabilidad en disolución. Además de unas propiedades ópticas similares a las ftalocianinas[181], que son cromofóricas y exhiben una absorción intensa en la región del espectro visible. Las diferentes configuraciones de grupos en la posición axial y periférica hacen que tenga una mejor modificación estructural[182] y una mejor actividad catalítica que las ftalocianinas.

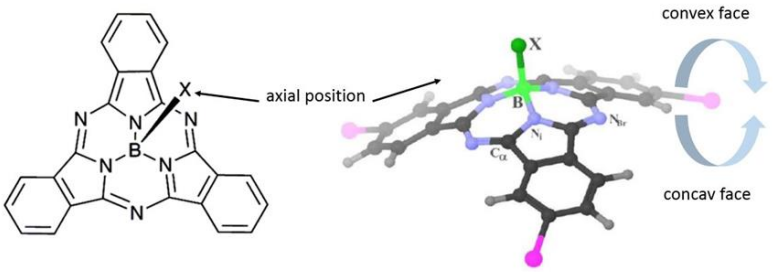

Figura 19. Molécula de SubPC de la composición seleccionada e incorporada en la estructura de perovskita multidimensional.

Adicionalmente, también presentan una movilidad de carga apropiada, por lo que en los últimos años se han utilizado en el campo de la fotovoltaica[183]. Recientemente se ha utilizado como material transportador de huecos (HTM)[184], presentándose como alternativa al spiro-OMETAD gracias a su estabilidad y larga longitud de difusión. Además, existen otros trabajos donde se estudia su efecto protector frente a la degradación de la perovskita, o como agente pasivante de los defectos dentro de la película del material[185].

En el trabajo presentado se desarrolla una nueva metodología para incorporar moléculas de SubPc en la estructura cristalina de la perovskita híbrida de plomo. El proceso consiste en la preparación de una perovskita multidimensional 2D/3D, utilizando como catión orgánico grande, el bromuro de feniletilo (PEABr) y como catión orgánico monovalente el metilamonio (MA). Para introducir la

molécula orgánica como huésped, incorporamos una disolución de la misma a la disolución de precursores de perovskita. En concreto, hemos escogido una SubPC con boro, y con un grupo fenoxi en la posición axial (OPh,ISubPc). Esta molécula presenta una máxima absorbancia que complementa casi a la perfección con la absorción de la perovskita multidimensional 2D/3D.

La incorporación de SubPc entre las capas de perovskita 2D/3D se ve plasmada por diferentes técnicas. Por lo tanto, se demuestra que esta nueva metodología permite obtener una perovskita híbrida incorporando colorantes organometálicos, y una mejora de la fotorrespuesta del material hacia la región del visible.

1.10. Referencias

1. Rose, G. De novis quibusdam fossilibus quae in montibus Uraliis inveniuntur - Gustav Rose - Google Libros. *AG Schade* 3–5 (1839).

2. Ramadass, N. ABO3-type oxides-Their structure and properties-A bird's eye view. *Mater. Sci. Eng.* **36**, 231–239 (1978).

3. Peña, M. A. & Fierro, J. L. G. Chemical structures and performance of perovskite oxides. *Chemical Reviews* **101**, 1981–2018 (2001).

4. Tanaka, H. & Misono, M. Advances in designing perovskite catalysts. *Curr. Opin. Solid State Mater. Sci.* **5**, 381–387 (2001).

5. Bhalla, A. S., Guo, R. & Roy, R. The perovskite structure - A review of its role in ceramic science and technology. *Materials Research Innovations* **4**, 3–26 (2000).

6. Aguadero, A., de la Calle, C., Pérez-Coll, D. & Alonso, J. A. Study of the Crystal Structure, Thermal Stability and Conductivity of Sr(V0.5Mo0.5)O3+δ as SOFC Material. *Fuel Cells* **11**, 44–50 (2011).

7. Aguadero, A. *et al.* Structure, thermal stability and electrical properties of Ca(V0.5Mo0.5)O3 as solid oxide fuel cell anode. *J. Power Sources* **192**, 78–83 (2009).

8. Asamoto, M., Iwasaki, Y., Yamaguchi, S. & Yahiro, H. Synthesis of perovsite-type oxide catalysts, Ln(Fe, Co)O 3 (Ln = La, Pr, Sm, Gd, Dy, Ho, Er, and Yb), from the thermal decomposition of the corresponding cyano complexes. in *Catalysis Today* **185**, 230–235 (2012).

9. Saidaminov, M. I. *et al.* High-quality bulk hybrid perovskite single crystals within minutes by inverse temperature crystallization. *Nat. Commun.* **6**, 7586 (2015).

10. Weber, D. CH3NH3PbX3, ein Pb(II)-System mit kubischer Perowskitstruktur. *Zeitschrift fur Naturforsch. - Sect. B J. Chem. Sci.* **33**, 1443–1445 (1978).

11. Mitzi, D. B., Feild, C. A., Harrison, W. T. A. & Guloy, A. M. Conducting tin halides with a layered organic-based perovskite structure. *Nature* **369**, 467–469 (1994).

12. Mitzi, D. B., Wang, S., Feild, C. A., Chess, C. A. & Guloy, A. M. Conducting layered organic-inorganic halides containing 〈110〉-oriented perovskite sheets. *Science (80-.).* **267**, 1473–1476 (1995).

13. Mitzi, D. B., Feild, C. A., Schlesinger, Z. & Laibowitz, R. B. Transport, optical, and magnetic properties of the conducting halide perovskite ch3nh3sni3. *J. Solid State Chem.* **114**, 159–163 (1995).

14. Mitzi, D. B. Synthesis, structure, and properties of organic-inorganic perovskites and related materials. in *Progress in Inorganic Chemistry* **48**, 1–

121 (wiley, 1999).

15. Kagan, C. R., Mitzi, D. B. & Dimitrakopoulos, C. D. Organic-inorganic hybrid materials as semiconducting channels in thin- film field-effect transistors. *Science (80-.).* **286**, 945–947 (1999).

16. Era, M., Morimoto, S., Tsutsui, T. & Saito, S. Organic-inorganic heterostructure electroluminescent device using a layered perovskite semiconductor (C6H5C2H 4NH3)2PbI4. *Appl. Phys. Lett.* **65**, 676–678 (1994).

17. Kojima, A., Teshima, K., Shirai, Y. & Miyasaka, T. Organometal halide perovskites as visible-light sensitizers for photovoltaic cells. *J. Am. Chem. Soc.* **131**, 6050–6051 (2009).

18. Zhang, Q., Ha, S. T., Liu, X., Sum, T. C. & Xiong, Q. Room-temperature near-infrared high-Q perovskite whispering-gallery planar nanolasers. *Nano Lett.* **14**, 5995–6001 (2014).

19. Luo, J. *et al.* Water photolysis at 12.3% efficiency via perovskite photovoltaics and Earth-abundant catalysts. *Science (80-.).* **345**, 1593–1596 (2014).

20. Zhu, H. *et al.* Lead halide perovskite nanowire lasers with low lasing thresholds and high quality factors. *Nat. Mater.* **14**, 636–642 (2015).

21. Brittman, S., Adhyaksa, G. W. P. & Garnett, E. C. The expanding world of hybrid perovskites: Materials properties and emerging applications. *MRS Communications* **5**, 7–26 (2015).

22. Green, M. A., Ho-Baillie, A. & Snaith, H. J. The emergence of perovskite solar cells. *Nature Photonics* **8**, 506–514 (2014).

23. Stranks, S. D. & Snaith, H. J. Metal-halide perovskites for photovoltaic and light-emitting devices. *Nature Nanotechnology* **10**, 391–402 (2015).

24. Yoo, J. J. *et al.* Efficient perovskite solar cells via improved carrier management. *Nat. 2021 5907847* **590**, 587–593 (2021).

25. Wang, Z. *et al.* Efficient ambient-air-stable solar cells with 2D-3D heterostructured butylammonium-caesium-formamidinium lead halide perovskites. *Nat. Energy* **2**, 17135 (2017).

26. Papavassiliou, G. C., Mousdis, G. A. & Koutselas, I. B. Some new organic–inorganic hybrid semiconductors based on metal halide units: structural, optical and related properties†. *Adv. Mater. Opt. Electron.* **9**, 265–271 (1999).

27. Mitzi, D. B., Chondroudis, K. & Kagan, C. R. Organic-inorganic electronics. *IBM J. Res. Dev.* **45**, 29–45 (2001).

28. Papavassiliou, G. C. & Koutselas, I. B. Structural, optical and related properties of some natural three- and lower-dimensional semiconductor systems. *Synth. Met.* **71**, 1713–1714 (1995).

29. Goldschmidt, V. M. Die Gesetze der Krystallochemie. *Naturwissenschaften*

14, 477–485 (1926).

30. Saparov, B. & Mitzi, D. B. Organic-Inorganic Perovskites: Structural Versatility for Functional Materials Design. *Chemical Reviews* **116**, 4558–4596 (2016).

31. Tsai, H. *et al.* High-efficiency two-dimensional ruddlesden-popper perovskite solar cells. *Nature* **536**, 312–317 (2016).

32. Stoumpos, C. C. *et al.* Ruddlesden-Popper Hybrid Lead Iodide Perovskite 2D Homologous Semiconductors. *Chem. Mater.* **28**, 2852–2867 (2016).

33. Seth, S. & Samanta, A. Photoluminescence of Zero-Dimensional Perovskites and Perovskite-Related Materials. *Journal of Physical Chemistry Letters* **9**, 176–183 (2018).

34. Moore, D. T. *et al.* Crystallization kinetics of organic-inorganic trihalide perovskites and the role of the lead anion in crystal growth. *J. Am. Chem. Soc.* **137**, 2350–2358 (2015).

35. Fang, H. H. *et al.* Ultrahigh sensitivity of methylammonium lead tribromide perovskite single crystals to environmental gases. *Sci. Adv.* **2**, e1600534 (2016).

36. Tian, W., Zhao, C., Leng, J., Cui, R. & Jin, S. Visualizing Carrier Diffusion in Individual Single-Crystal Organolead Halide Perovskite Nanowires and Nanoplates. *J. Am. Chem. Soc.* **137**, 12458–12461 (2015).

37. Tanaka, K. *et al.* Comparative study on the excitons in lead-halide-based perovskite-type crystals CH3NH3PbBr3 CH3NH 3PbI3. *Solid State Commun.* **127**, 619–623 (2003).

38. Stranks, S. D. *et al.* Electron-hole diffusion lengths exceeding 1 micrometer in an organometal trihalide perovskite absorber. *Science (80-.).* **342**, 341–344 (2013).

39. Sheng, R. *et al.* Methylammonium lead bromide perovskite-based solar cells by vapor-assisted deposition. *J. Phys. Chem. C* **119**, 3545–3549 (2015).

40. Shi, D. *et al.* Low trap-state density and long carrier diffusion in organolead trihalide perovskite single crystals. *Science (80-.).* **347**, 519–522 (2015).

41. Song, T. Bin *et al.* Perovskite solar cells: Film formation and properties. *J. Mater. Chem. A* **3**, 9032–9050 (2015).

42. Fu, Y. *et al.* Nanowire Lasers of Formamidinium Lead Halide Perovskites and Their Stabilized Alloys with Improved Stability. *Nano Lett.* **16**, 1000–1008 (2016).

43. Xiao, R. *et al.* Photocurrent Mapping in Single-Crystal Methylammonium Lead Iodide Perovskite Nanostructures. *Nano Lett.* **16**, 7710–7717 (2016).

44. Brandt, R. E., Stevanović, V., Ginley, D. S. & Buonassisi, T. Identifying defect-tolerant semiconductors with high minority-carrier lifetimes: Beyond hybrid

lead halide perovskites. *MRS Commun.* **5**, 265–275 (2015).

45. DeQuilettes, D. W. *et al.* Impact of microstructure on local carrier lifetime in perovskite solar cells. *Science (80-.).* **348**, 683–686 (2015).

46. Nie, W. *et al.* High-efficiency solution-processed perovskite solar cells with millimeter-scale grains. *Science (80-.).* **347**, 522–525 (2015).

47. Peng, W. *et al.* Quantification of Ionic Diffusion in Lead Halide Perovskite Single Crystals. *ACS Energy Lett.* **3**, 1477–1481 (2018).

48. Lin, Q., Armin, A., Nagiri, R. C. R., Burn, P. L. & Meredith, P. Electro-optics of perovskite solar cells. *Nat. Photonics* **9**, 106–112 (2015).

49. Yuan, Y. & Huang, J. Ion Migration in Organometal Trihalide Perovskite and Its Impact on Photovoltaic Efficiency and Stability. *Acc. Chem. Res.* **49**, 286–293 (2016).

50. Divitini, G. *et al.* In situ observation of heat-induced degradation of perovskite solar cells. *Nature Energy* **1**, 1–6 (2016).

51. Leguy, A. M. A. *et al.* Reversible hydration of CH3NH3PbI3 in films, single crystals, and solar cells. *Chem. Mater.* **27**, 3397–3407 (2015).

52. Eperon, G. E. *et al.* Formamidinium lead trihalide: A broadly tunable perovskite for efficient planar heterojunction solar cells. *Energy Environ. Sci.* **7**, 982–988 (2014).

53. Eperon, G. E. *et al.* Inorganic caesium lead iodide perovskite solar cells. *J. Mater. Chem. A* **3**, 19688–19695 (2015).

54. McMeekin, D. P. *et al.* A mixed-cation lead mixed-halide perovskite absorber for tandem solar cells. *Science (80-.).* **351**, 151–155 (2016).

55. Smith, I. C., Hoke, E. T., Solis-Ibarra, D., McGehee, M. D. & Karunadasa, H. I. A Layered Hybrid Perovskite Solar-Cell Absorber with Enhanced Moisture Stability. *Angew. Chemie - Int. Ed.* **123**, 11414–11417 (2014).

56. Shang, Q. *et al.* Unveiling Structurally Engineered Carrier Dynamics in Hybrid Quasi-Two-Dimensional Perovskite Thin Films toward Controllable Emission. *J. Phys. Chem. Lett.* **8**, 4431–4438 (2017).

57. A. A. Griffith. *The Phenomena of Rupture and Flow in Solids on JSTOR*. **221**, (Royal Society, 1921).

58. Even, J., Pedesseau, L. & Katan, C. Understanding quantum confinement of charge carriers in layered 2D hybrid perovskites. *ChemPhysChem* **15**, 3733–3741 (2014).

59. Babayigit, A., Ethirajan, A., Muller, M. & Conings, B. Toxicity of organometal halide perovskite solar cells. *Nature Materials* **15**, 247–251 (2016).

60. Hao, F., Stoumpos, C. C., Cao, D. H., Chang, R. P. H. & Kanatzidis, M. G. Lead-

free solid-state organic-inorganic halide perovskite solar cells. *Nat. Photonics* **8**, 489–494 (2014).

61. Stranks, S. D., Nayak, P. K., Zhang, W., Stergiopoulos, T. & Snaith, H. J. Formation of thin films of organic-inorganic perovskites for high-efficiency solar cells. *Angew. Chemie - Int. Ed.* **54**, 3240–3248 (2015).

62. Burschka, J. *et al.* Sequential deposition as a route to high-performance perovskite-sensitized solar cells. *Nature* **499**, 316–319 (2013).

63. Li, W., Fan, J., Li, J., Mai, Y. & Wang, L. Controllable grain morphology of perovskite absorber film by molecular self-assembly toward efficient solar cell exceeding 17%. *J. Am. Chem. Soc.* **137**, 10399–10405 (2015).

64. Meyerhofer, D. Characteristics of resist films produced by spinning. *J. Appl. Phys.* **49**, 3993–3997 (1978).

65. Im, J. H., Kim, H. S. & Park, N. G. Morphology-photovoltaic property correlation in perovskite solar cells: One-step versus two-step deposition of CH3NH3PbI 3. *APL Mater.* **2**, 081510 (2014).

66. Kadro, J. M., Nonomura, K., Gachet, D., Grätzel, M. & Hagfeldt, A. Facile route to freestanding CH3NH3PbI3 crystals using inverse solubility. *Sci. Rep.* **5**, 11654 (2015).

67. Mozetič, M. Surface Modification to Improve Properties of Materials. *Materials (Basel).* **12**, 441 (2019).

68. Chen, Q. *et al.* Planar heterojunction perovskite solar cells via vapor-assisted solution process. *J. Am. Chem. Soc.* **136**, 622–625 (2014).

69. Liu, M., Johnston, M. B. & Snaith, H. J. Efficient planar heterojunction perovskite solar cells by vapour deposition. *Nature* **501**, 395–398 (2013).

70. Malinkiewicz, O. *et al.* Perovskite solar cells employing organic charge-transport layers. *Nat. Photonics* **8**, 128–132 (2013).

71. Fu, F. *et al.* Controlled growth of PbI 2 nanoplates for rapid prepara-tion of CH 3 NH 3 PbI 3 in planar perovskite solar cells. *Phys. Status Solidi* **212**, 2708–2717 (2015).

72. Mitzi, D. B. Thin-film deposition of organic-inorganic hybrid materials. *Chemistry of Materials* **13**, 3283–3298 (2001).

73. Tavakoli, M. M. *et al.* Fabrication of efficient planar perovskite solar cells using a one-step chemical vapor deposition method. *Sci. Rep.* **5**, 14083 (2015).

74. Schmidt, L. C. *et al.* Nontemplate Synthesis of CH 3 NH 3 PbBr 3 Perovskite Nanoparticles. (2014).

75. Gonzalez-Carrero, S., Galian, R. E. & Pérez-Prieto, J. Maximizing the emissive properties of CH3NH3PbBr3 perovskite nanoparticles. *J. Mater. Chem. A* **3**,

9187–9193 (2015).

76. Huang, H., Susha, A. S., Kershaw, S. V., Hung, T. F. & Rogach, A. L. Control of Emission Color of High Quantum Yield CH3NH3PbBr3 Perovskite Quantum Dots by Precipitation Temperature. *Adv. Sci.* **2**, (2015).

77. Levchuk, I. *et al.* Brightly Luminescent and Color-Tunable Formamidinium Lead Halide Perovskite FAPbX 3 (X = Cl, Br, I) Colloidal Nanocrystals. *Nano Lett* **17**, 8 (2017).

78. Huang, H. *et al.* Emulsion Synthesis of Size-Tunable $CH_3NH_3PbBr_3$ Quantum Dots: An Alternative Route toward Efficient Light-Emitting Diodes. *ACS Appl. Mater. Interfaces* **7**, 28128–28133 (2015).

79. Malgras, V., Henzie, J., Takei, T. & Yamauchi, Y. Hybrid methylammonium lead halide perovskite nanocrystals confined in gyroidal silica templates. *Chem. Commun.* **53**, 2359–2362 (2017).

80. Protesescu, L. *et al.* Nanocrystals of Cesium Lead Halide Perovskites (CsPbX3, X = Cl, Br, and I): Novel Optoelectronic Materials Showing Bright Emission with Wide Color Gamut. *Nano Lett.* **15**, 3692–3696 (2015).

81. Zhang, D., Xu, Y., Liu, Q. & Xia, Z. Encapsulation of CH3NH3PbBr3 Perovskite Quantum Dots in MOF-5 Microcrystals as a Stable Platform for Temperature and Aqueous Heavy Metal Ion Detection. *Inorg. Chem.* **57**, 4613–4619 (2018).

82. Tong, Y. *et al.* Highly Luminescent Cesium Lead Halide Perovskite Nanocrystals with Tunable Composition and Thickness by Ultrasonication. *Angew. Chemie - Int. Ed.* **55**, 13887–13892 (2016).

83. Bekenstein, Y., Koscher, B. A., Eaton, S. W., Yang, P. & Alivisatos, A. P. Highly Luminescent Colloidal Nanoplates of Perovskite Cesium Lead Halide and Their Oriented Assemblies. *J. Am. Chem. Soc.* **137**, 16008–16011 (2015).

84. Akkerman, Q. A. *et al.* Solution Synthesis Approach to Colloidal Cesium Lead Halide Perovskite Nanoplatelets with Monolayer-Level Thickness Control. *J. Am. Chem. Soc.* **138**, 1010–1016 (2016).

85. Sun, S., Yuan, D., Xu, Y., Wang, A. & Deng, Z. Ligand-Mediated Synthesis of Shape-Controlled Cesium Lead Halide Perovskite Nanocrystals via Reprecipitation Process at Room Temperature. *ACS Nano* **10**, 3648–3657 (2016).

86. Amgar, D., Stern, A., Rotem, D., Porath, D. & Etgar, L. Tunable Length and Optical Properties of CsPbX3 (X = Cl, Br, I) Nanowires with a Few Unit Cells. *Nano Lett.* **17**, 1007–1013 (2017).

87. Grätzel, M. Photoelectrochemical cells. *Nature* **414**, 338–344 (2001).

88. Ji, K. *et al.* High-efficiency perovskite quantum dot solar cells benefiting from a conjugated polymer-quantum dot bulk heterojunction connecting layer. *J. Mater. Chem. A* **8**, 8104–8112 (2020).

89. Yang, W. S. *et al.* High-performance photovoltaic perovskite layers fabricated through intramolecular exchange. *Science (80-.).* **348**, 1234–1237 (2015).

90. Ahn, N. *et al.* Highly Reproducible Perovskite Solar Cells with Average Efficiency of 18.3% and Best Efficiency of 19.7% Fabricated via Lewis Base Adduct of Lead(II) Iodide. *J. Am. Chem. Soc.* **137**, 8696–8699 (2015).

91. Swarnkar, A. *et al.* Quantum dot-induced phase stabilization of α-CsPbI3 perovskite for high-efficiency photovoltaics. *Science (80-.).* **354**, 92–95 (2016).

92. Zeng, Q. *et al.* Polymer-Passivated Inorganic Cesium Lead Mixed-Halide Perovskites for Stable and Efficient Solar Cells with High Open-Circuit Voltage over 1.3 V. *Adv. Mater.* **30**, (2018).

93. Koh, T. M. *et al.* Nanostructuring Mixed-Dimensional Perovskites: A Route Toward Tunable, Efficient Photovoltaics. *Adv. Mater.* **28**, 3653–3661 (2016).

94. Chen, Z. *et al.* High-Performance Color-Tunable Perovskite Light Emitting Devices through Structural Modulation from Bulk to Layered Film. *Adv. Mater.* **29**, 1603157 (2017).

95. Liang, D. *et al.* Color-Pure Violet-Light-Emitting Diodes Based on Layered Lead Halide Perovskite Nanoplates. *ACS Nano* **10**, 6897–6904 (2016).

96. Chondroudis, K. & Mitzi, D. B. Electroluminescence from an organic-inorganic perovskite incorporating a quaterthiophene dye within lead halide perovskite layers. *Chem. Mater.* **11**, 3028–3030 (1999).

97. Bao, C. *et al.* High Performance and Stable All-Inorganic Metal Halide Perovskite-Based Photodetectors for Optical Communication Applications. *Adv. Mater.* **30**, 1803422 (2018).

98. Pang, L. *et al.* Shape- and Trap-Controlled Nanocrystals for Giant-Performance Improvement of All-Inorganic Perovskite Photodetectors. *Part. Part. Syst. Charact.* **35**, 1700363 (2018).

99. Tang, X. *et al.* All-inorganic perovskite CsPb(Br/I)3 nanorods for optoelectronic application. *Nanoscale* **8**, 15158–15161 (2016).

100. Li, Y. *et al.* Controllable Vapor-Phase Growth of Inorganic Perovskite Microwire Networks for High-Efficiency and Temperature-Stable Photodetectors. **5**, (2018).

101. Hu, X. *et al.* High-performance flexible broadband photodetector based on organolead halide perovskite. *Adv. Funct. Mater.* **24**, 7373–7380 (2014).

102. Deng, H. *et al.* Flexible and semitransparent organolead triiodide perovskite network photodetector arrays with high stability. *Nano Lett.* **15**, 7963–7969 (2015).

103. Eaton, S. W. *et al.* Lasing in robust cesium lead halide perovskite nanowires.

Proc. Natl. Acad. Sci. U. S. A. **113**, 1993–1998 (2016).

104. Miyata, A. *et al.* Direct measurement of the exciton binding energy and effective masses for charge carriers in organic-inorganic tri-halide perovskites. *Nat. Phys.* **11**, 582–587 (2015).

105. Wang, Z. *et al.* Wavelength-tunable waveguides based on polycrystalline organic-inorganic perovskite microwires. *Nanoscale* **8**, 6258–6264 (2016).

106. Sutherland, B. R., Hoogland, S., Adachi, M. M., Wong, C. T. O. & Sargent, E. H. Conformal organohalide perovskites enable lasing on spherical resonators. *ACS Nano* **8**, 10947–10952 (2014).

107. Zhang, Q. *et al.* Advances in Small Perovskite-Based Lasers. *Small Methods* **1**, 1700163 (2017).

108. Soldat, J., Marschall, R. & Wark, M. Improved overall water splitting with barium tantalate mixed oxide composites. *Chem. Sci.* **5**, 3746–3752 (2014).

109. Deng, W. *et al.* Aligned Single-Crystalline Perovskite Microwire Arrays for High-Performance Flexible Image Sensors with Long-Term Stability. *Adv. Mater.* **28**, 2201–2208 (2016).

110. Deng, W. *et al.* Ultrahigh-Responsivity Photodetectors from Perovskite Nanowire Arrays for Sequentially Tunable Spectral Measurement. *Nano Lett.* **17**, 2482–2489 (2017).

111. Lu, Y., Wang, L., Cheng, J. & Goodenough, J. B. Prussian blue: A new framework of electrode materials for sodium batteries. *Chem. Commun.* **48**, 6544–6546 (2012).

112. Eames, C. *et al.* Ionic transport in hybrid lead iodide perovskite solar cells. *Nat. Commun.* **6**, 1–8 (2015).

113. Casanova-Cháfer, J., García-Aboal, R., Atienzar, P. & Llobet, E. Gas Sensing Properties of Perovskite Decorated Graphene at Room Temperature. *Sensors* **19**, 4563 (2019).

114. Yariv, A. *Photonics : optical electronics in modern communications /*. (Oxford University Press, 2007).

115. Jia, Y., Kerner, R. A., Grede, A. J., Rand, B. P. & Giebink, N. C. Continuous-wave lasing in an organic-inorganic lead halide perovskite semiconductor. *Nat. Photonics* **11**, 784–788 (2017).

116. Fu, Y. *et al.* Metal halide perovskite nanostructures for optoelectronic applications and the study of physical properties. *Nature Reviews Materials* **4**, 169–188 (2019).

117. Cohen, B. El & Etgar, L. Parameters that control and influence the organo-metal halide perovskite crystallization and morphology. *Frontiers of Optoelectronics* **9**, 44–52 (2016).

118. Grancini, G. *et al.* CH3NH3PbI3 perovskite single crystals: Surface photophysics and their interaction with the environment. *Chem. Sci.* **6**, 7305–7310 (2015).

119. Martin A. Green, R. P. R. T. M. B. J.-F. G. *Progress in Photovoltaics: Research and Applications | Wiley*. **26**, (2018).

120. Park, J. S. *et al.* Electronic Structure and Optical Properties of α-CH3NH3PbBr3 Perovskite Single Crystal. *J. Phys. Chem. Lett.* **6**, 4304–4308 (2015).

121. Nakata, K. & Fujishima, A. TiO 2 photocatalysis: Design and applications. *Journal of Photochemistry and Photobiology C: Photochemistry Reviews* **13**, 169–189 (2012).

122. Wang, D., Yin, F., Du, Z., Han, D. & Tang, J. Recent progress in quantum dot-sensitized solar cells employing metal chalcogenides. *Journal of Materials Chemistry A* **7**, 26205–26226 (2019).

123. Arutyunov, V. S. & Lisichkin, G. V. Energy resources of the 21st century: problems and forecasts. Can renewable energy sources replace fossil fuels? *Russ. Chem. Rev.* **86**, 777–804 (2017).

124. Wang, Q. & Domen, K. Particulate Photocatalysts for Light-Driven Water Splitting: Mechanisms, Challenges, and Design Strategies. *Chemical Reviews* **120**, 919–985 (2020).

125. Qian, R. *et al.* Charge carrier trapping, recombination and transfer during TiO2 photocatalysis: An overview. *Catal. Today* **335**, 78–90 (2019).

126. Li, X., Yu, J., Jaroniec, M. & Chen, X. Cocatalysts for selective photoreduction of CO 2 into solar fuels. *Chemical Reviews* **119**, 3962–4179 (2019).

127. Park, J. H., Park, J. H., Kim, S. & Bard, A. J. Novel carbon-doped TiO2 nanotube arrays with high aspect ratios for efficient solar water splitting. *NANO Lett.* 24--28 (2006).

128. Ola, O. & Maroto-Valer, M. M. Review of material design and reactor engineering on TiO2 photocatalysis for CO2 reduction. *Journal of Photochemistry and Photobiology C: Photochemistry Reviews* **24**, 16–42 (2015).

129. Lettmann, C., Hildenbrand, K., Kisch, H., Macyk, W. & Maier, W. F. Visible light photodegradation of 4-chlorophenol with a coke-containing titanium dioxide photocatalyst. *Appl. Catal. B Environ.* **32**, 215–227 (2001).

130. A. Primo and H. García. *New and Future Developments in Catalysis - 1st Edition*. (2013).

131. Mei, B., Han, K. & Mul, G. Driving Surface Redox Reactions in Heterogeneous Photocatalysis: The Active State of Illuminated Semiconductor-Supported Nanoparticles during Overall Water-Splitting. *ACS Catal.* **8**, 9154–9164 (2018).

132. Takanabe, K. Photocatalytic Water Splitting: Quantitative Approaches toward Photocatalyst by Design. *ACS Catal.* **7**, 8006–8022 (2017).

133. Zhenfu, Z., Zhihai, W., Jiong, C., Liang, J. & Yafei, H. Nanocomposites of Perovskite Quantum Dots Embedded in Magnesium Silicate Hollow Spheres for Multicolor Display. *J. Phys. Chem. C* **122**, 16887–16893 (2018).

134. Khan, M. M. *et al.* Band gap engineered TiO2 nanoparticles for visible light induced photoelectrochemical and photocatalytic studies. *J. Mater. Chem. A* **2**, 637–644 (2014).

135. Xu, C., Ravi Anusuyadevi, P., Aymonier, C., Luque, R. & Marre, S. Nanostructured materials for photocatalysis. *Chemical Society Reviews* **48**, 3868–3902 (2019).

136. Zheng, Z. *et al.* Hydrogenated titania: Synergy of surface modification and morphology improvement for enhanced photocatalytic activity. *Chem. Commun.* **48**, 5733–5735 (2012).

137. Liqiang, J. *et al.* Review of photoluminescence performance of nano-sized semiconductor materials and its relationships with photocatalytic activity. *Sol. Energy Mater. Sol. Cells* **90**, 1773–1787 (2006).

138. Zhang, H., Zhang, X., Yang, G. & Zhou, X. Point Defect Effects on Photoelectronic Properties of the Potential Metal-Free C2N Photocatalysts: Insight from First-Principles Computations. *J. Phys. Chem. C* **122**, 5291–5302 (2018).

139. Jiang, Q. *et al.* Surface passivation of perovskite film for efficient solar cells. *Nat. Photonics* **13**, 460–466 (2019).

140. Yettapu, G. R. *et al.* Terahertz Conductivity within Colloidal CsPbBr3 Perovskite Nanocrystals: Remarkably High Carrier Mobilities and Large Diffusion Lengths. *Nano Lett.* **16**, 4838–4848 (2016).

141. Guan, M. *et al.* Vacancy associates promoting solar-driven photocatalytic activity of ultrathin bismuth oxychloride nanosheets. *J. Am. Chem. Soc.* **135**, 10411–10417 (2013).

142. Ran, C., Xu, J., Gao, W., Huang, C. & Dou, S. Defects in metal triiodide perovskite materials towards high-performance solar cells: Origin, impact, characterization, and engineering. *Chemical Society Reviews* **47**, 4581–4610 (2018).

143. Wei, D. *et al.* Photo-induced degradation of lead halide perovskite solar cells caused by the hole transport layer/metal electrode interface. *J. Mater. Chem. A* **4**, 1991–1998 (2016).

144. Zhang, L., Ju, M. G. & Liang, W. The effect of moisture on the structures and properties of lead halide perovskites: A first-principles theoretical investigation. *Phys. Chem. Chem. Phys.* **18**, 23174–23183 (2016).

145. Baldovi, H. G. *et al.* Visible-light photoresponse of gold nanoparticles supported on TiO2: A combined photocatalytic, photoelectrochemical, and transient spectroscopy study. *ChemPhysChem* **16**, 335–341 (2015).

146. Zhao, Y. & Zhu, K. Organic-inorganic hybrid lead halide perovskites for optoelectronic and electronic applications. *Chemical Society Reviews* **45**, 655–689 (2016).

147. Cortecchia, D. *et al.* Lead-Free MA2CuClxBr4-x Hybrid Perovskites. *Inorg. Chem.* **55**, 1044–1052 (2016).

148. Panda, P. K. Review: Environmental friendly lead-free piezoelectric materials. *J. Mater. Sci.* **44**, 5049–5062 (2009).

149. Organización Mundial de la Salud. Available at: https://www.who.int/es. (Accessed: 9th January 2021)

150. Park, M., Shim, S. H., Jeong, S. H., Oh, K. J. & Lee, S. S. Nitrogen oxides emissions from the MILD combustion with the conditions of recirculation gas. *J. Air Waste Manag. Assoc.* **67**, 402–411 (2017).

151. McCubbin, D. R., Apelberg, B. J., Roe, S. & Divita, F. Livestock ammonia management and particulate-related health benefits. *Environ. Sci. Technol.* **36**, 1141–1146 (2002).

152. Stokstad, E. Ammonia pollution from farming may exact hefty health costs. *Science* **343**, 238 (2014).

153. Review of the EU Air policy - Environment - European Commission. Available at: https://ec.europa.eu/environment/air/quality/. (Accessed: 2nd June 2021)

154. Garg, A. *et al.* Zebra GC: A mini gas chromatography system for trace-level determination of hazardous air pollutants. *Sensors Actuators, B Chem.* **212**, 145–154 (2015).

155. Haus, R. *et al.* Mobile Fourier-transform infrared spectroscopy monitoring of air pollution. *Appl. Opt.* **33**, 5682 (1994).

156. Akbar, M., Restaino, M. & Agah, M. Chip-scale gas chromatography: From injection through detection. *Microsystems Nanoeng.* **1**, 1 (2015).

157. Hodgkinson, J. & Tatam, R. P. Optical gas sensing: A review. *Measurement Science and Technology* **24**, 012004 (2013).

158. Viespe, C. & Miu, D. Characteristics of Surface Acoustic Wave Sensors with Nanoparticles Embedded in Polymer Sensitive Layers for VOC Detection. *Sensors* **18**, 2401 (2018).

159. Alassi, A., Benammar, M. & Brett, D. Quartz crystal microbalance electronic interfacing systems: A review. *Sensors (Switzerland)* **17**, (2017).

160. Mujahid, A. & Dickert, F. L. Surface acousticwave (SAW) for chemical sensing

applications of recognition layers. *Sensors (Switzerland)* **17**, (2017).

161. Yunusa, Z., Hamidon, M. N., Kaiser, A. & Awang, Z. *Gas Sensors: A Review*. *Sensors & Transducers* **168**, (2014).

162. Khan, M., Rao, M. & Li, Q. Recent Advances in Electrochemical Sensors for Detecting Toxic Gases: NO2, SO2 and H2S. *Sensors* **19**, 905 (2019).

163. Schroeder, V., Savagatrup, S., He, M., Lin, S. & Swager, T. M. Carbon nanotube chemical sensors. *Chemical Reviews* **119**, 599–663 (2019).

164. Shendage, S. S. *et al.* Sensitive and selective NO2 gas sensor based on WO3 nanoplates. *Sensors Actuators, B Chem.* **240**, 426–433 (2017).

165. Dey, A. Semiconductor metal oxide gas sensors: A review. *Materials Science and Engineering B: Solid-State Materials for Advanced Technology* **229**, 206–217 (2018).

166. Lahlalia, A., Le Neel, O., Shankar, R., Selberherr, S. & Filipovic, L. Improved sensing capability of integrated semiconducting metal oxide gas sensor devices. *Sensors (Switzerland)* **19**, (2019).

167. Wang, C., Yin, L., Zhang, L., Xiang, D. & Gao, R. Metal Oxide Gas Sensors: Sensitivity and Influencing Factors. *Sensors* **10**, 2088–2106 (2010).

168. Llobet, E. Gas sensors using carbon nanomaterials: A review. *Sensors and Actuators, B: Chemical* **179**, 32–45 (2013).

169. Wang, A., Zhao, J. & Green, M. A. 24% efficient silicon solar cells. *Appl. Phys. Lett.* **57**, 602–604 (1990).

170. Anaya, M., Lozano, G., Calvo, M. E. & Míguez, H. ABX3 Perovskites for Tandem Solar Cells. *Joule* **1**, 769–793 (2017).

171. Liang, X. *et al.* Flexible Perovskite Solar Cells: Progress and Prospects. *Frontiers in Materials* **8**, 17 (2021).

172. Li, J. *et al.* Highly Efficient Thermally Co-evaporated Perovskite Solar Cells and Mini-modules. *Joule* **4**, 1035–1053 (2020).

173. Misra, R. K. *et al.* Effect of Halide Composition on the Photochemical Stability of Perovskite Photovoltaic Materials. *ChemSusChem* **9**, 2572–2577 (2016).

174. Shao, S. *et al.* Highly Reproducible Sn-Based Hybrid Perovskite Solar Cells with 9% Efficiency. *Adv. Energy Mater.* **8**, (2018).

175. Cao, D. H., Stoumpos, C. C., Farha, O. K., Hupp, J. T. & Kanatzidis, M. G. 2D Homologous Perovskites as Light-Absorbing Materials for Solar Cell Applications. *J. Am. Chem. Soc.* **137**, 7843–7850 (2015).

176. Li, P. *et al.* Phase Pure 2D Perovskite for High-Performance 2D–3D Heterostructured Perovskite Solar Cells. *Adv. Mater.* **30**, 1805323 (2018).

177. W. Jones, C. N. R. R. *Supramolecular Organization and Materials Design - Google Libros*. (2008).

178. Zhang, T. *et al.* Efficient CsSnI3-based inorganic perovskite solar cells based on a mesoscopic metal oxide framework via incorporating a donor element. *J. Mater. Chem. A* **8**, 4118–4124 (2020).

179. Lu, C. H., Biesold-Mcgee, G. V., Liu, Y., Kang, Z. & Lin, Z. Doping and ion substitution in colloidal metal halide perovskite nanocrystals. *Chemical Society Reviews* **49**, 4953–5007 (2020).

180. Carretero-Palacios, S., Jiménez-Solano, A. & Míguez, H. Plasmonic Nanoparticles as Light-Harvesting Enhancers in Perovskite Solar Cells: A User's Guide. *ACS Energy Letters* **1**, 323–331 (2016).

181. Bottari, G., De La Torre, G., Guldi, D. M. & Torres, T. Covalent and noncovalent phthalocyanine - Carbon nanostructure systems: Synthesis, photoinduced electron transfer, and application to molecular photovoltaics. *Chem. Rev.* **110**, 6768–6816 (2010).

182. Duan, C. *et al.* The Role of the Axial Substituent in Subphthalocyanine Acceptors for Bulk-Heterojunction Solar Cells. *Angew. Chemie - Int. Ed.* **56**, 148–152 (2017).

183. Mutolo, K. L., Mayo, E. I., Rand, B. P., Forrest, S. R. & Thompson, M. E. Enhanced open-circuit voltage in subphthalocyanine/C60 organic photovoltaic cells. *J. Am. Chem. Soc.* **128**, 8108–8109 (2006).

184. Wang, F. *et al.* Soluble hexamethyl-substituted subphthalocyanine as a dopant-free hole transport material for planar perovskite solar cells. *R. Soc. Open Sci.* **5**, 180617 (2018).

185. Li, C., Lv, X., Cao, J. & Tang, Y. Tetra-ammonium Zinc Phthalocyanine to Construct a Graded 2D–3D Perovskite Interface for Efficient and Stable Solar Cells. *Chinese J. Chem.* **37**, 30–34 (2019).

CAPÍTULO 2

OBJETIVOS

2. OBJETIVOS

Como ha quedado reflejado a lo largo de la introducción, el elemento central de esta tesis es profundizar el estudio de las perovskitas híbridas así como su aplicación en campos de gran interés. Este material ha alcanzado en los últimos años una gran popularidad, debido a sus propiedades excepcionales, tanto ópticas como eléctricas. Además, la alta demanda mundial de energía conlleva una intensa búsqueda de nuevos materiales para el desarrollo inmediato de energías renovables, favoreciendo la rápida expansión de la perovskita debido a su importante potencial.

La presente tesis doctoral comprende seis artículos científicos. Con la finalidad de mejorar su uso en futuras aplicaciones, tres de ellos se centran en el estudio fundamental de las propiedades optoelectrónicas de las perovskitas. Por otro lado, en los tres artículos siguientes, se estudia la implementación en diversas aplicaciones dentro del ámbito de la energía y de sensores. Siendo estos dos puntos los objetivos generales de la tesis.

Con respecto a los objetivos específicos, podemos dividirlos en dos bloques. En un primer bloque, referente al estudio fundamental, destacando cuatro objetivos principales:

1. Controlar la síntesis de cristales micrométricos de perovskita mediante el método de deposición por giro. Se pretende obtener cristales de un tamaño y geometría específicos mediante el control de dos parámetros (velocidad de rotación y el uso de aditivos). Además, se intenta lograr una mayor homogeneidad y menor número de defectos en los cristales.

2. Obtener cristales de perovskita híbrida en forma de nanofibras mediante el uso de plantillas. Las plantillas serán obtenidas por un método de bajo coste y además permitirán conseguir cristales de diferente tamaño dependiendo de la plantilla empleada.

3. Evaluar los fenómenos ópticos que ocurren en el material mediante medidas de fotoluminiscencia y transmitancia, con ayuda de un microscopio confocal desarrollado en nuestro grupo de investigación.

Asimismo, se pretende corroborar que ciertas geometrías de cristales de perovskita pueden comportarse como cavidad Fabry-Pérot y guía de onda.

4. Desarrollar un método teórico que nos permita estudiar de manera fundamental las propiedades ópticas del material. Mediante el uso del modelo teórico propuesto, obtener parámetros fundamentales como el índice de refracción (real e imaginario). Además, evaluar el efecto de otros parámetros externos del sistema que pueden afectar en la visibilidad de los fenómenos ópticos que ocurren en el material.

Por último y como objetivos específicos para la implementación de la perovskita en aplicaciones del ámbito de la energía y sensores:

5. Emplear las perovskitas híbridas como catalizadores para la producción de combustibles solares. Se persigue evaluar la influencia de la composición de la perovskita en la actividad catalítica de la misma, y dilucidar cuál es la composición que presenta una mayor actividad. Asimismo, se pretende asegurar, mediante diferentes técnicas de caracterización, la estabilidad del material en las condiciones de reacción propuestas.

6. Preparación de sensores resistivos integrando grafeno y nanocristales de perovskita de diferente composición. Se pretende evaluar las propiedades de detección de gases de los diferentes sensores y evaluar la influencia de la composición de la perovskita en el mecanimos de sensado. Además, obtener respuestas reproducibles para la detección de compuestos orgánicos volátiles.

7. Mediante el desarrollo de una metodología sencilla, introducir dentro de la estructura de la perovskita moléculas organometálicas (SubPc). El objetivo principal consiste en ampliar el espectro de fotorrespuesta del nuevo nanomaterial hacia la región del visible. Para ello se demostrará por diferentes técnicas de caracterización la presencia de SubPc en la estructura y finalmente, el nuevo material, se implementará en dispositivos fotovoltaicos.

La consecución de los objetivos indicados, permitirá el avance tanto en un conocimiento más fundamental del material como en la

adaptación del material para su implementación en aplicaciones de diversa índole. Conociendo de una manera más precisa parámetros y fenómenos ópticos nos ayudará a entender su comportamiento con la luz. Asimismo, si se consiguen implementar en las aplicaciones citadas, se reafirmará como material prometedor y fácilmente adaptable a diferentes campos de aplicación.

CAPÍTULO 3

PROPIEDADES ÓPTICAS

SECCIÓN 3.1

SINGLE CRYSTALS GROWTH OF HYBRID BROMIDE PEROVSKITES USING A SPIN COATING METHOD

Rocío García-Aboal, Roberto Fenollosa, Fernando Ramiro-Manzano, Isabelle Rodríguez, Pedro Atienzar and Francisco Meseguer

ACS. OMEGA 2018, 3, 5229−5236

DOI: 10.1021/acsomega.8b00447

SINGLE CRYSTALS GROWTH OF HYBRID BROMIDE PEROVSKITES USING A SPIN COATING METHOD

Rocío García-Aboal[a], Roberto Fenollosa[a], Fernando Ramiro-Manzano[a], Isabelle Rodríguez[a], Pedro Atienzar[a*] and Francisco Meseguer[a]

[a]Instituto Universitario de Tecnologia Química, CSIC-UPV, Universitat Politècnica de València, Av. de los Naranjos, Valencia 46022, Spain,

*Corresponding author: patienzar@itq.upv.es

KEYWORDS: Perovskite, single crystal, additives, optoelectronic, solar cell, spin coating, photoluminescence.

Abstract

Synthesis and studies of single crystals of hybrid perovskite are important for achieving a better understanding of the optoelectronic phenomena occurring in this material and for improving ongoing applications. Here we report on the growth of micrometer size single crystals of methylammonium lead bromide ($MAPbBr_3$) using the spin coating deposition method on a quartz substrate. We studied the influence of the rotation speed and the use of three different additives such as N-cyclohexyl-2-pyrrolidone, dimethyl Sulfoxide and 4-tert-butylpyridine in the crystal size and shape. The introduction of an additive in the precursor solution has revealed to be very useful for obtaining crystals with well defined geometries and for decreasing the amount of defects. This way, high quality single crystals that sustain optical resonating modes were obtained and characterized by transmittance and photoluminescence measurements.

1. INTRODUCTION

In the last years, hybrid perovskites[1-2] have attracted a great interest because of their potential application in the field of photovoltaics, where in a reduced period of time they reached efficiencies over 22%[3], a value that exceeds other emerging technologies such as quantum dot, dye sensitised solar cells or organic solar cells[4-5]. These materials have some advantages such as ease processing or low fabrication cost. Their synthesis can be attained

through various routes like those based on solution[1] and vapor-assisted[6] methods. However, they have also some limitations like a poor stability or the toxicity of the components. In this context, the delicate control over the crystal formation has been shown to play a key role in the physical properties and therefore in the reproducibility and efficiency[2] of perovskite based solar cells. Here, we study the formation and the properties of hybrid lead bromide perovskite single crystals. There are several methods for the synthesis of single crystals, such as inverse temperature crystallization (ITC)[7], antisolvent-assisted crystallization techniques (AVC)[8], top-seeded solution growth method (TSSG)[9-10] among others. In this work, we have used the spin coating method[11-13] because it is fast, versatile, reproducible, inexpensive and finally it requires moderate amounts of reactant. Although the size of the obtained crystals is in the micrometre range, they are large enough to study their physical and chemical properties and they could be used to develop photovoltaic devices with appropriate grain size. In contrast, most of the studies in this respect have been done in large single crystals with millimetre size which require a long time of preparation and several processing steps[8, 14].

Although there are many parameters of the spin coating method influencing the formation of perovskites such as rotation speed, annealing, concentration of precursors, solvents, atmosphere[15], among others, here we focus on the influence of the speed rotation and the admixture of three different additives to the basic precursor compounds. Recent studies have shown that the use of highly miscible low vapour pressure additives is very effective for improving perovskite crystallization[2,15-16], because they decrease the rate of evaporation of the precursor solution solvent. Based on former results concerning the preparation of the active layers of perovskite in photovoltaic devices, we selected Dimethylformaide (DMF) as the main solvent, and three different additives for the synthesis of single crystals. In general, all of the additives have in common both, the ability to be coordinated with the precursors and a high boiling point. The first one is N-cyclohexyl-2-pyrrolidone (CHP)[2], which at low concentration induces an homogenous crystal nucleation and growth, this favouring large reproducibility. It has a particularly high boiling

point (284 ºC) and low vapour pressure. Other investigated additive is 4-tert-butylpyridine (TBP). Shi et al. added this compound in the precursor solution resulting in a better crystallinity and a more homogeneous orientation of the crystals. This is probably due to the coordination of such compound with the Pb^{+2} atoms, and to its role as dispersing agent, that avoids the formation of aggregates[16]. Finally, we considered dimethyl sulfoxide (DMSO) as an interesting additive because it can coordinate easily to the $PbBr_2$ precursor[17].

Optical properties are closely related to the performance of photovoltaic devices. Therefore, we have undertaken as a characterization strategy of the crystals the study of their optical properties, particularly photoluminescence and transmittance, at the single crystal level, using for that purpose a home-made set-up[7], that allows us to test their behaviour as optical cavities.

2. RESULTS AND DISCUSSION

2.1. Influence of the rotation speed and additive

The synthesis procedure based on the spin coating process, under the specified conditions detailed in the experimental section, produces well isolated single crystals. Figure 1 shows the variation of the average size of the obtained crystals (black dots) with the speed of the spin coater under different conditions: (a) without additive (NA) and with the different additives: CHP (b), DMSO (c) and TPB (d). The error bars correspond to the standard deviation for each value, obtained by statistical means (see experimental section). The as-synthesized crystals are poly-disperse in size, in some cases with a dispersion value of about 50% no matter rotation speed and precursor solution. However, in general the average size of the crystals decreases as the rotation speed increases, following a law (gray curves) like ($\propto 1/\text{speed}^{\gamma}$) with different values of the exponent γ, which are indicated in the Figure caption. Such law is typical for the thickness of a deposited layer by spin coating, but with $\gamma=1/2$. We think that the distinct values of γ obtained for the crystal size stem from the fact that the growth of the crystals includes different stages where the removal of the excess of solvent as a consequence of the centrifugal force is

followed by an evaporation process that increases the viscosity and the precursors concentration. Nevertheless the experiments indicate that the quicker the solvent evaporation, the larger the number of crystal nucleation points, that ends up in a reduced average crystal size.

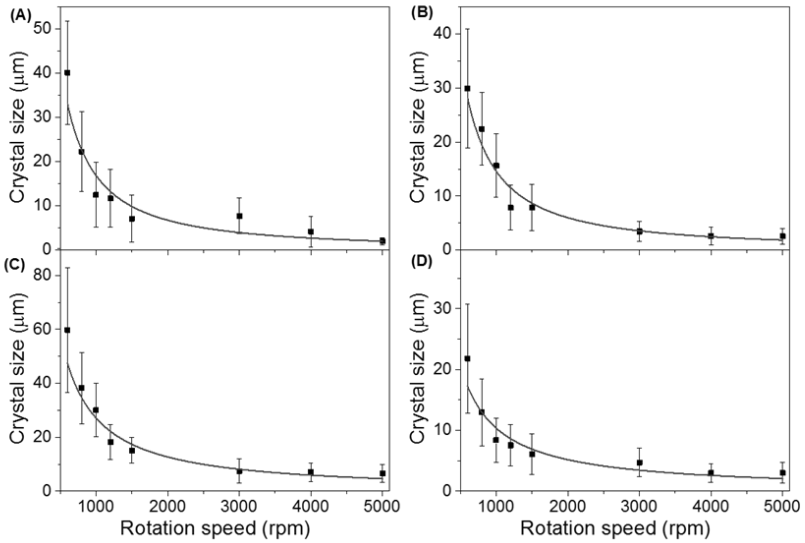

Figure 1. Average crystal size (dots) as a function of the spin coater rotation speed for a precursor solution without additive (A), and with (B) CHP, (C) DMSO and (D) TBP as additive. The error bars correspond to the standard deviation provided by statistical methods. The gray lines correspond to fits of experimental data to functions like ($\propto 1/\text{speed}^{\gamma}$), and the fitted values of γ are 1.3, 1.2, 1.2 and 0.9 for (A), (B), (C) and (D) respectively.

We didn't find any clear relation between the size of the crystals and the physical properties of the additives (Table 1, experimental section). Nevertheless, those solutions containing DMSO as additive produced the largest crystals, specially at low rotation speeds, while solutions with TBP as additive yielded the smallest ones. It can be explained by considering the different ability of coordination with Pb^{+2} and the solubility of the precursors. Shi et al.[16] indicated that the nitrogen atom on TBP favours the coordination with Pb^{+2} with respect oxygen atom on DMF, thus hindering the formation of large-sized bulks and aggregates and favouring therefore the formation of small

crystals. All the above is relevant for the preparation of high efficient photovoltaic solar cells, considering that there is an optimum crystal size depending of the device configuration, and in general large crystals are desired due to lower J-V hysteresis and less charge trapping and recombination at the grain boundaries[18-19].

Figure 2 (a), (b), (c) and (d) show scanning electron microscopy (SEM) images of $MAPbBr_3$ crystals grown on quartz substrates by spin coating at 1000 rpm, corresponding to samples NA, CHP, DMSO and TBP respectively. All of the samples contain well isolated single crystals that are pyramid shaped in general. However, crystals having other shapes, namely rods and plates, grow as well, at the same time. Plate-shaped structures are particularly interesting for testing the properties of the crystals as photonic microcavities, as we will see below. We found that in general, the use of an additive in the precursor solution produces crystals with better defined geometries and with less defects [Figure 2 (b), (c) and (d)] in comparison with those obtained without any additive [Figure 2 (a)]. This effect is even more pronounced for the CHP additive and it should be taken into account for the study of the optical properties, which can be strongly influenced by the geometry and the structural defects of the crystals.

X-ray diffraction (XRD) measurements (Figure 3) show that all the synthesized samples have in fact a crystalline nature with a characteristic cubic structure finger print (Pm-3m)[20]. In contrast to samples NA and TPB, samples DMSO and CHP show the appearance of (110) and (210) peaks suggesting that the crystals are highly oriented[8,21] with the planes parallel to the substrate. This feature occurs for all of the rotation speeds. It is very interesting, since it is well demonstrated that more oriented domains of perovskites in photovoltaic devices increases their photocurrent and therefore their final performance[22].

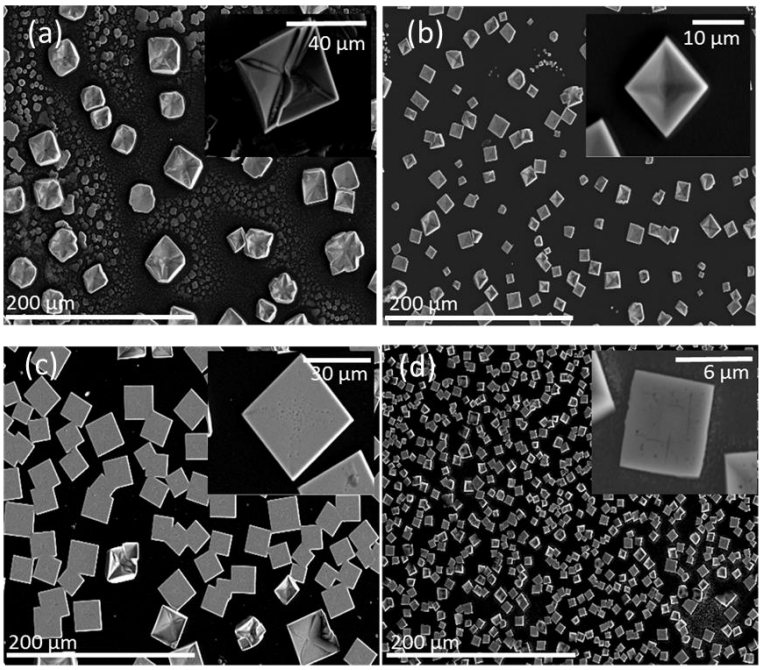

Figure 2. Scanning electron microscopy (SEM) images of $MAPbBr_3$ crystals grown on quartz substrates by spin coating at 1000 rpm, corresponding to samples NA (a), CHP (b), DMSO (c) and TBP (d).

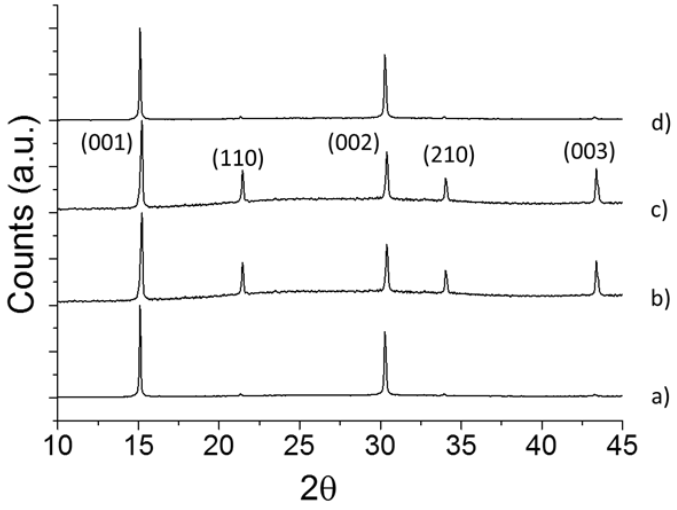

Figure 3. XRD of a layer of crystals of (a) NA, (b) CHP, (c) DMSO and (d) TBP samples.

Photoluminescence properties of the synthesized crystals were found to be influenced by the type of additive used in the precursor solution, rather than by the rotation speed. Figure 4 (a), (b), (c), and (d) shows optical microscopy images at x40 magnification of samples NA, CHP, DMSO and TBP respectively for a rotation speed of 1000 rpm, and Figure 4 (e), (f), (g) and (h) show their corresponding photoluminescence images. Optical microscopy images of all of the samples for all of the studied rotation speeds can be seen in the supporting information (Figures S1 to S4).

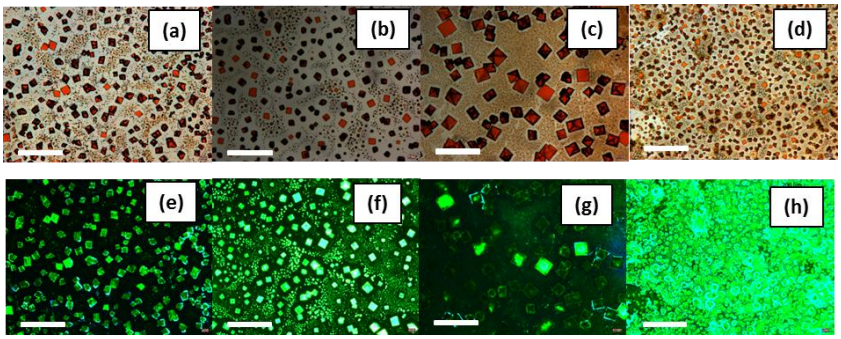

Figure 4. (a), (b), (c) and (d) Optical microscopy images at x40 magnification of samples NA, CHP, DMSO and TBP respectively, for a rotation of speed of 1000 rpm. (e), (f), (g) and (h) show the corresponding photoluminescence images. The scale bars correspond to 200 µm.

Samples CHP and TBP yield a bright green photoluminescence signal, while samples NA and DMSO give in general less intense signals. We attributed this effect to the amount of surface states produced during the crystallization process, which act as non-radiative recombination centers. This is an important result to be considered in future developments because such centers are strongly influenced by environmental conditions of moisture and light[23]. Figure 5A shows the optical absorbance and Figure 5B shows the normalized photoluminescence spectra of the sample areas of Figure 4. They are similar to those of previous reports of hybrid lead bromide perovskites[24-26], but slight differences in the position of the peak maximum and the asymmetry have arisen. While samples NA and TBP yielded a quite symmetric peak, with the maximum position at 535 nm, the peak maximum for samples CHP and DMSO was red-shifted to 540

nm, and they showed some asymmetric features, that consist of shoulders placed at about 552 nm and in the range from 555 nm to 600 nm approximately. Although a complete elucidation of these effects has not been achieved yet, we think they are related to the aging of the surface or structural inhomogeneities in the crystals[24,26-27] and to light re-absorption mechanisms[28-29].

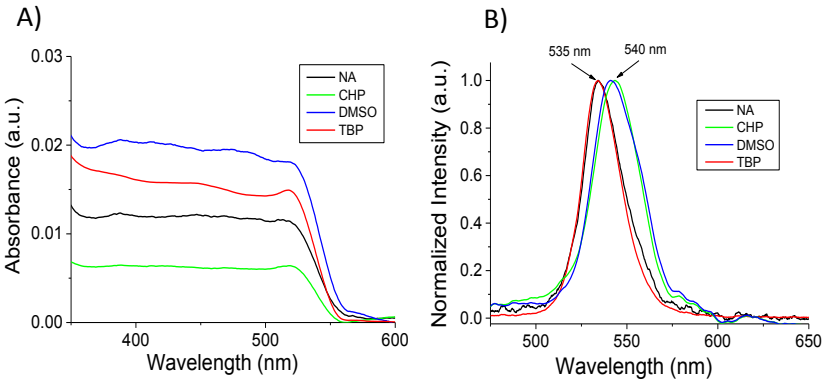

Figure 5. A) UV-Vis absorption spectra and B) Photoluminescence spectra of the sample areas of Figure 4, corresponding to samples NA, CHP, DMSO and TBP.

2.2. Synthesis of rod-shaped crystals

Rod-shaped single crystals were found in small amounts in sample CHP, specially at low rotation speeds. We studied the influence of the concentration of this particular additive in the precursor solution on the crystal formation. Figure 6 shows representative optical microscopy images of the obtained crystals for different CHP concentrations, from 5 to 60 % vol/vol in DMF. Moreover, Figure 7B shows the variation of the average size of the crystals and the ratio of rod/cuboid shaped crystals with respect to the CHP concentration. At low concentrations, squared like plates are dominant. However, for increasing values of the CHP content the formation of wire like structures is favoured, and the size of the plates is reduced. This was attributed to the fact that CHP contains a significant apolar region because of the cyclohexyl ring, thus inducing a preferential direction of growth probably due to screw dislocation defects.[30] A similar trend has been discussed for the preparation of other 1D structures.[31-32] On another hand, no significant variation in the crystals growth has been

observed in the case of DMSO and TBP additives when their concentration was increased.

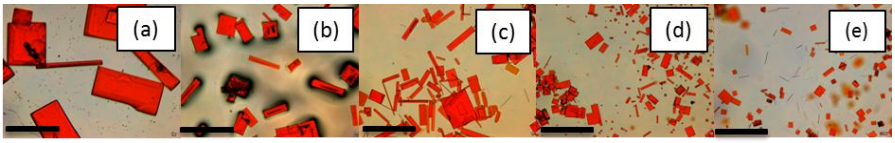

Figure 6. Optical Microscopy images of crystals synthesized by using increasing concentrations of CHP additive: (a) 5, (b) 15, (c) 25, (d) 50 and (e) 60 % vol/vol in DMF. The scale bars correspond to 200 µm.

The influence of the rotation speed in the formation of rod-shaped crystals was studied for the 5 % CHP vol/vol concentration in DMF precursor solution. As mentioned above, the growth of rod-shaped crystals is in general favoured by low rotation speeds. This indicates that slow evaporation rates of the solvent are required for them to be able to grow. Such a formation process has been observed by using slow evaporation rates in the drop casting method (see video in supplementary material). Moreover, we have found a threshold rotation speed value, at about 1000 rpm, which defines two main regions where crystals grow differently (Figure 7 A o B). Most of the crystals, say 80%, grow either in rod or cuboid like shapes depending on the rotation speed region, low or high respectively, where they were synthesized. An explanation of this threshold value constitutes currently an object of research.

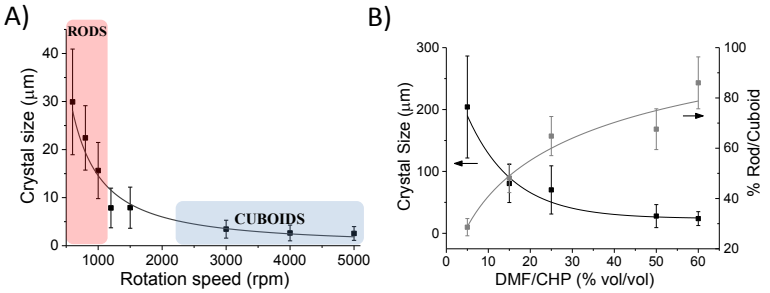

Figure 7. A) Curve of average crystal size vs. spin coater rotation speed obtained by using 5 % of CPH additive vol/vol concentration in DMF for the precursor solution. The two shaded areas indicate two regimes where crystals grow differently: in rod or in cuboid like shapes. B) Curves of average crystal size (black line) and rod/cuboids ratio (gray line) as a function of the CHP additive concentration. The error bars correspond to the standard deviation provided by statistical methods.

2.3. Optical properties of single crystals

A good proof for testing the quality of a crystal is its ability to sustain optical resonant modes because such modes can be strongly influenced by crystal defects. In general, the better the quality of a crystal, the more pronounced are its optical resonances. However, they depend as well on other factors like the coupling of light, the absorption of the material itself, and more importantly the geometry of the crystal, particularly the size of the crystal in comparison with the wavelength of light, and how its faces are orientated each other. Resonant conditions should allow a kind of feedback cycle of light inside the crystal, which is produced by multiple reflections at the crystal faces, and finally leads to an interference phenomenon. This way, a pyramid like shaped crystal is not expected to sustain any resonance because of its intricate geometry. However, the parallel faces of a plate shaped crystal are optimum for producing Fabry-Perot type resonances[27]. Figure 8(a) shows the photoluminescence (black curve) and the optical transmittance (red curve) spectra of a plate shaped crystal, that was synthesized at 800 rpm by using CHP as additive. Figure 8(b) shows an image of the measured crystal obtained by optical microscopy. It has well defined parallel faces with dimensions of 20.64 x 21.62 μm^2 in area and 1.5 µm in depth, as

deduced from a modeling process[33]. As expected, interference ripples appear in the transmittance spectrum in that range from where the absorption of the material somehow diminishes, say about 550 nm to longer wavelengths, thus confirming that the crystal itself can work as an optical microcavity, and it has a good structural quality. The photoluminescence spectrum shows ripples as well, coinciding with those of the transmittance spectrum, but they are less pronounced because of differences between the envelope curves[33]. Figure 8(c) shows for comparison the transmittance and the photoluminescence spectra of a pyramid shaped crystal (Figure 8(d)), where no resonances could be detected. In any case, it is interesting for future developments to take into account these resonant effects at the single crystal level, that in our opinion could help improving the efficiency of perovskite based solar cells.

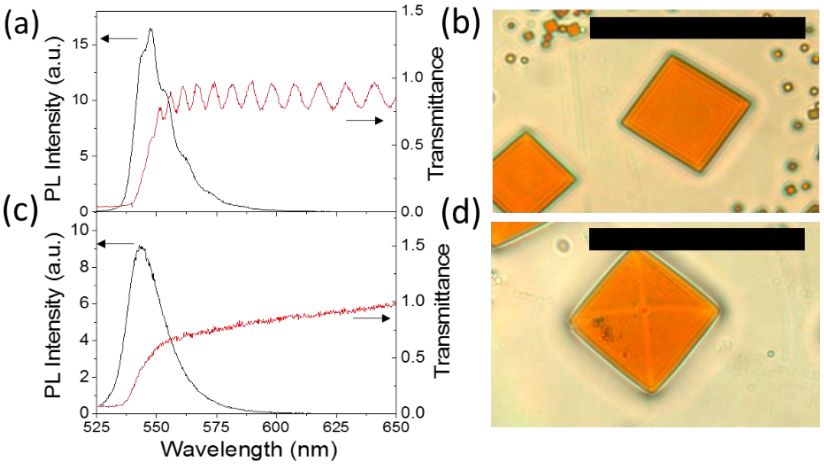

Figure 8. Photoluminescence (black curve) and transmittance (red curve) spectra of a plate shaped crystal (a) and a pyramid shaped crystal (c). Optical microscopy images of the crystals appear in (b) and (d) respectively. The scale bars correspond to 50 µm.

CONCLUSIONS

We have described the synthesis and characterization of single crystals of $MAPbBr_3$ prepared by a spin coating method at different rotation speeds. In addition, we studied the influence of three different additives previously used in high-performance inorganic–organic hybrid perovskite solar cells. We observed that the use of

additives, particularly CHP, produces crystals with a better defined geometry and with less defects, in comparison with crystals obtained without any additive, and at the same time, CHP and DMSO additives have a tendency to produce more oriented crystals. Also, we showed that increasing the concentration of CHP additive produces the formation of rods of $MAPbBr_3$. Finally, we demonstrated that single crystals of $MAPbBr_3$ prepared by this methodology can behave as resonating cavities.

3. EXPERIMENTAL SECTION

3.1 Materials

The precursors: lead bromide ($PbBr_2$), methylammonium bromide (MABr), the main solvent: dimethylformamide (DMF), and the three additives: N-cyclohexyl-2-pyrrolidone (CHP), 4-tert-butylpyridine (TBP), and dimethyl sulfoxide (DMSO) come from Sigma-Aldrich. They were used as received. Table 1 summarizes the physical properties of the solvent and additives.

Table 1. Properties of the solvent and additives used in the present study.

Compound	Structure	Boiling Point (°C)	Vapor pressure (mmHg, 25°C)	Viscosity (cPoise)
Dimethylformamide (DMF)	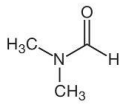	155	2.9	0.92
N-cyclohexyl-2-pyrrolidone (CHP)	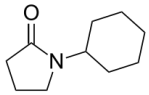	284-304	0.05	11.6
Dimethyl Sulfoxide (DMSO)	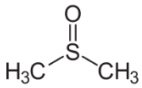	189	0.42	0.7
4-tert-Butylpyridine (TBP)	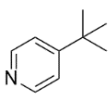	197	4.53	1.5

3.2. Synthesis of $MAPbBr_3$ perovskite single crystals

Precursor solutions were prepared by dissolving stoichiometric mixture of 1M MABr and 1M $PbBr_2$ in DMF[34], namely 120 mg MABr and 370 mg of $PbBr_2$ in 2 mL of DMF. In the case of solutions containing an additive (CHP, TBP or DMSO), 20 µL thereof was added into 380 µL of the precursor solution, resulting in a concentration of about 5% vol. In addition, for CHP the concentration was increased to obtain solutions with 15, 25, 50 and 60 % vol.

$MAPbBr_3$ crystals were grown by a spin coating process on quartz substrates of area ≈ 1 cm^2. In order to increase the hydrophilicity of the surface, the substrates had been previously treated with hydrochloridric acid, and cleaned with acetone and isopropanol, followed by exhaustive rinsing with distilled water. The spin coating process was performed at room temperature and in a controlled not-oxidizing atmosphere at different spin speed rates, in the range from 600 to 5000 rpm. In all the synthesis experiments, a volume of 20 µL of precursor solution was dropped in the middle of the substrate before the rotation process had started. Then the spinner was turned on, producing a homogeneous distribution of the precursor solution through the substrate, thus favouring the efficient removal of the solvent, and giving rise to the formation of crystals. We kept the rotation process on for 2 minutes, and after that the substrates containing the as-grown crystals were annealed for 2 minutes more at 90°C so as to remove completely any rest of solvent.

3.3. Optical microscopy and photoluminescence of polycrystalline samples

General views of the as-grown crystals were obtained at different magnifications by an optical microscope, Leica DM4000. It includes a module for fluorescence characterization, which consists of a mercury lamp and a bandpass filter LEICA (340-380 nm) as illumination source, and an optic spectrometer AVANTES AvaSpec-2048 fiber, which provides a resolution better than 0.5 nm. Photoluminescence of sample areas containing many crystals were obtained by using this setup.

3.4. X-ray diffraction experiments

X-ray polycrystalline film diffraction patterns of the samples were collected by a Bruker D8 Advance A25 X-ray diffractometer, operating at 45 kV and 80 mA Cu-K_α radiation (λ = 1.5406 Å equipped with a LYNXEYE XE 1-D detector. It records the diffraction signal of an area of 3 x 3 mm. No signals from the quartz substrate were detected.

3.5. Optical characterization of single crystals

Optical properties, specifically photoluminescence and transmittance, of single crystals were obtained by means of a home-made setup (see Figure 9). Basically it includes two branches, one for excitation and the other one for collection purposes, both focused by 20x Mitutoyo objectives at the same spot, with a typical size of about 1 micrometer. In the experiments reported here, both branches were oriented so that the collected light was in forward direction respect the incident or exciting light. The collection branch includes an iris where the spot is focused. It allows selecting the signal from a sample area of size in the micrometer and even sub-micrometer range. After the iris, a motorized mirror drives the signal either to a CCD camera, by means of which, the exact part of crystal being examined can be visualized, or to a spectrometer (iHR320-HORIBA), which is equipped with a liquid nitrogen refrigerated Si-CCD, and it is used for measuring the spectrum of the collected light.

White light of an halogen lamp was used for transmittance experiments, while excitation light of 405 nm of wavelength, provided by a solid state laser, was used for photoluminescence experiments. In all the cases, we worked with a moderate intensity of about 0.1 mW for avoiding fast crystal degradation.

Two types of crystal geometries were measured: pyramid and plate shaped samples. In both cases the crystal was oriented so that the largest face of the crystal was perpendicular to the incident or collected light.

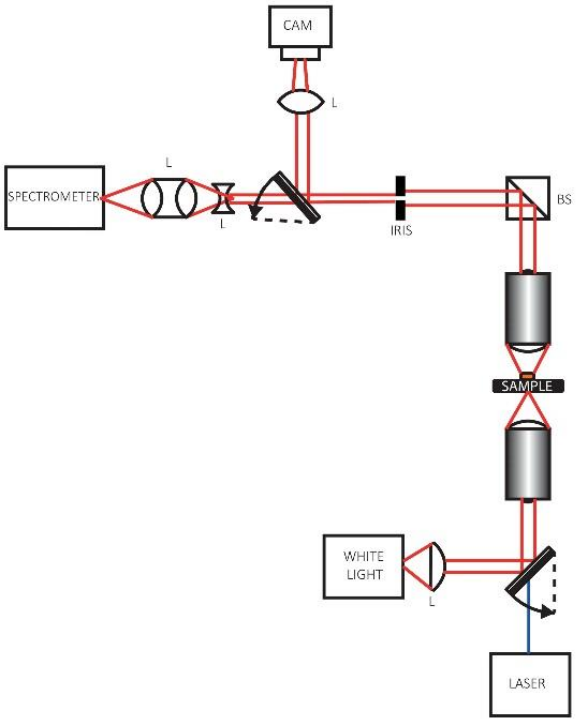

Figure 9. Schematic representation of the setup used for measuring the OT and PL spectrums, where the different acronyms are Lense (L), Beam splitter (BS), Spectrometer and Camera (CAM).

3.6. Crystal size measurement procedure

An optical microscope (Leica DM4000) was used to obtain a general overview of the crystals size and shape. Three samples were synthesized and studied for each speed/additive condition. Once the uniformity of each sample had been guaranteed by analyzing different sample areas, 60 - 80 crystals therein were measured by using the ImageJ software. We considered for each single crystal that area, which is parallel to the substrate, and measured the length of one of its sides. In those cases where the area had a rectangular shape, like for instance in rods, we measured the longer dimension. Histograms for each synthesis conditions were obtained by considering all the measurements of the three corresponding samples, that showed a good reproducibility, without significant differences in any case. The crystal size parameter was divided into five ranges in the histograms

and the obtained mode and standard deviation values are plotted in Figure 1. Also, they are detailed in table S1 of the supporting information.

Acknowledgments

Financial support from the Spanish Ministry of Economy and Competitiveness (Severo Ochoa, SEV-2016-0683), Intramural CSIC project 201680I006, and Fundación Ramón Areces (XVII Concurso Nacional para la adjudicación de Ayudas a la Investigación en Ciencias de la Vida y de la Materia) is gratefully acknowledged. This research was financially supported by the Spanish Ministry of Economy and Competitiveness (Mineco) of Spain (TQ2011-26455)2, MAT2015-69669-P, and regional government grant PrometeoII/2017/026.

Author information

Dr. Pedro Atienzar, E-mail: patienzar@itq.upv.es

Prof. Francisco Meseguer, E-mail: fmesegue@gmail.com

Rocío García-Aboal, E-mail: rogarab@itq.upv.es

Dr. Fernando Ramiro-Manzano, E-mail: ferraman@gmail.com

Dr. Roberto Fenollosa, E-mail: rfenollo@ter.upv.es

Dr. Isabelle Rodríguez, E-mail: mirodrig@upvnet.upv.es

References

1. Lee, M. M.; Teuscher, J.; Miyasaka, T.; Murakami, T. N.; Snaith, H. J., Efficient Hybrid Solar Cells Based on Meso-Superstructured Organometal Halide Perovskites. Science 2012, 338 (6107), 643-647.

2. Jeon, Y.-J.; Lee, S.; Kang, R.; Kim, J.-E.; Yeo, J.-S.; Lee, S.-H.; Kim, S.-S.; Yun, J.-M.; Kim, D.-Y., Planar heterojunction perovskite solar cells with superior reproducibility. Scientific Reports 2014, 4, 6953.

3. Yang, W. S.; Park, B.-W.; Jung, E. H.; Jeon, N. J.; Kim, Y. C.; Lee, D. U.; Shin, S. S.; Seo, J.; Kim, E. K.; Noh, J. H.; Seok, S. I., Iodide management in formamidinium-lead-halide–based perovskite layers for efficient solar cells. Science 2017, 356 (6345), 1376-1379.

4. Albero, J.; Atienzar, P.; Corma, A.; Garcia, H., Efficiency Records in Mesoscopic Dye-Sensitized Solar Cells. Chemical Record 2015, 15 (4), 803-828.

5. Lu, L.; Zheng, T.; Wu, Q.; Schneider, A. M.; Zhao, D.; Yu, L., Recent Advances in Bulk Heterojunction Polymer Solar Cells. Chemical Reviews 2015, 115 (23), 12666-12731.

6. Ávila, J.; Momblona, C.; Boix, P. P.; Sessolo, M.; Bolink, H. J., Vapor-Deposited Perovskites: The Route to High-Performance Solar Cell Production? Joule 2017.

7. Saidaminov, M. I.; Abdelhady, A. L.; Murali, B.; Alarousu, E.; Burlakov, V. M.; Peng, W.; Dursun, I.; Wang, L.; He, Y.; Maculan, G.; Goriely, A.; Wu, T.; Mohammed, O. F.; Bakr, O. M., High-quality bulk hybrid perovskite single crystals within minutes by inverse temperature crystallization. Nature Communications 2015, 6, 7586.

8. Shi, D.; Adinolfi, V.; Comin, R.; Yuan, M.; Alarousu, E.; Buin, A.; Chen, Y.; Hoogland, S.; Rothenberger, A.; Katsiev, K.; Losovyj, Y.; Zhang, X.; Dowben, P. A.; Mohammed, O. F.; Sargent, E. H.; Bakr, O. M., Low trap-state density and long carrier diffusion in organolead trihalide perovskite single crystals. Science 2015, 347 (6221), 519-522.

9. Dong, Q.; Fang, Y.; Shao, Y.; Mulligan, P.; Qiu, J.; Cao, L.; Huang, J., Electron-hole diffusion lengths >175 μm in solution-grown CH3NH3PbI3 single crystals. Science 2015, 347 (6225), 967-970.

10. Dang, Y.; Zhou, Y.; Liu, X.; Ju, D.; Xia, S.; Xia, H.; Tao, X., Formation of Hybrid Perovskite Tin Iodide Single Crystals by Top-Seeded Solution Growth. Angewandte Chemie International Edition 2016, 55 (10), 3447-3450.

11. Emslie, A. G.; Bonner, F. T.; Peck, L. G., Flow of a Viscous Liquid on a Rotating Disk. Journal of Applied Physics 1958, 29 (5), 858-862.

12. Meyerhofer, D., Characteristics of resist films produced by spinning. Journal of Applied Physics 1978, 49 (7), 3993-3997.

13. Lawrence, C. J., THE MECHANICS OF SPIN COATING OF POLYMER-FILMS. Phys. Fluids 1988, 31 (10), 2786-2795.

14. Dang, Y.; Liu, Y.; Sun, Y.; Yuan, D.; Liu, X.; Lu, W.; Liu, G.; Xia, H.; Tao, X., Bulk crystal growth of hybrid perovskite material CH3NH3PbI3. CrystEngComm 2015, 17 (3), 665-670.

15. Cohen, B.-E.; Etgar, L., Parameters that control and influence the organo-metal halide perovskite crystallization and morphology. Frontiers of Optoelectronics 2016, 9 (1), 44-52.

16. Shi, Y.; Wang, X.; Zhang, H.; Li, B.; Lu, H.; Ma, T.; Hao, C., Effects of 4-tert-butylpyridine on perovskite formation and performance of solution-processed perovskite solar cells. Journal of Materials Chemistry A 2015, 3 (44), 22191-22198.

17. Li, W.; Fan, J.; Li, J.; Mai, Y.; Wang, L., Controllable Grain Morphology of Perovskite Absorber Film by Molecular Self-Assembly toward Efficient Solar Cell Exceeding 17%. Journal of the American Chemical Society 2015, 137 (32), 10399-10405.

18. Kim, H.-S.; Park, N.-G., Parameters Affecting I–V Hysteresis of CH3NH3PbI3 Perovskite Solar Cells: Effects of Perovskite Crystal Size and Mesoporous TiO2 Layer. The Journal of Physical Chemistry Letters 2014, 5 (17), 2927-2934.

19. Salim, T.; Sun, S.; Abe, Y.; Krishna, A.; Grimsdale, A. C.; Lam, Y. M., Perovskite-based solar cells: impact of morphology and device architecture on device performance. Journal of Materials Chemistry A 2015, 3 (17), 8943-8969.

20. Zhu, Q.; Zheng, K.; Abdellah, M.; Generalov, A.; Haase, D.; Carlson, S.; Niu, Y.; Heimdal, J.; Engdahl, A.; Messing, M. E.; Pullerits, T.; Canton, S. E., Correlating structure and electronic band-edge properties in organolead halide perovskites nanoparticles. Physical Chemistry Chemical Physics 2016, 18 (22), 14933-14940.

21. Cho, N.; Li, F.; Turedi, B.; Sinatra, L.; Sarmah, S. P.; Parida, M. R.; Saidaminov, M. I.; Murali, B.; Burlakov, V. M.; Goriely, A.; Mohammed, O. F.; Wu, T.; Bakr, O. M., Pure crystal orientation and anisotropic charge transport in large-area hybrid perovskite films. Nature Communications 2016, 7, 13407.

22. Docampo, P.; Hanusch, F. C.; Giesbrecht, N.; Angloher, P.; Ivanova, A.; Bein, T., Influence of the orientation of methylammonium lead iodide perovskite crystals on solar cell performance. APL Materials 2014, 2 (8), 081508.

23. Brenes, R.; Guo, D.; Osherov, A.; Noel, N. K.; Eames, C.; Hutter, E. M.; Pathak, S. K.; Niroui, F.; Friend, R. H.; Islam, M. S.; Snaith, H. J.; Bulović, V.; Savenije, T. J.; Stranks, S. D., Metal Halide Perovskite Polycrystalline Films Exhibiting Properties of Single Crystals. Joule 2017, 1 (1), 155-167.

24. Chen, F.; Zhu, C.; Xu, C.; Fan, P.; Qin, F.; Gowri Manohari, A.; Lu, J.; Shi, Z.; Xu, Q.; Pan, A., Crystal structure and electron transition underlying photoluminescence of methylammonium lead bromide perovskites. Journal

of Materials Chemistry C 2017, 5 (31), 7739-7745.

25. Saidaminov, M. I.; Adinolfi, V.; Comin, R.; Abdelhady, A. L.; Peng, W.; Dursun, I.; Yuan, M.; Hoogland, S.; Sargent, E. H.; Bakr, O. M., Planar-integrated single-crystalline perovskite photodetectors. Nature Communications 2015, 6, 8724.

26. Wang, K.-H.; Li, L.-C.; Shellaiah, M.; Wen Sun, K., Structural and Photophysical Properties of Methylammonium Lead Tribromide (MAPbBr3) Single Crystals. Scientific Reports 2017, 7 (1), 13643.

27. Grancini, G.; D'Innocenzo, V.; Dohner, E. R.; Martino, N.; Srimath Kandada, A. R.; Mosconi, E.; De Angelis, F.; Karunadasa, H. I.; Hoke, E. T.; Petrozza, A., CH3NH3PbI3 perovskite single crystals: surface photophysics and their interaction with the environment. Chemical Science 2015, 6 (12), 7305-7310.

28. Diab, H.; Arnold, C.; Lédée, F.; Trippé-Allard, G.; Delport, G.; Vilar, C.; Bretenaker, F.; Barjon, J.; Lauret, J.-S.; Deleporte, E.; Garrot, D., Impact of Reabsorption on the Emission Spectra and Recombination Dynamics of Hybrid Perovskite Single Crystals. The Journal of Physical Chemistry Letters 2017, 8 (13), 2977-2983.

29. Fang, Y.; Wei, H.; Dong, Q.; Huang, J., Quantification of re-absorption and re-emission processes to determine photon recycling efficiency in perovskite single crystals. Nature Communications 2017, 8, 14417.

30. Meng, F.; Morin, S. A.; Forticaux, A.; Jin, S., Screw Dislocation Driven Growth of Nanomaterials. Accounts of Chemical Research 2013, 46 (7), 1616-1626.

31. Meng, F.; Jin, S., The Solution Growth of Copper Nanowires and Nanotubes is Driven by Screw Dislocations. Nano Letters 2012, 12 (1), 234-239.

32. Wu, H.; Meng, F.; Li, L.; Jin, S.; Zheng, G., Dislocation-Driven CdS and CdSe Nanowire Growth. ACS Nano 2012, 6 (5), 4461-4468.

33. Ramiro-Manzano, F.; García-Aboal, R.; Rodriguez, I.; Fenollosa, R.; Biasi, S.; Atienzar, P.; Meseguer, F., Optical properties organic/inorganic perovskite microcrystals through the characterization of Fabry-Pérot resonances. To be submitted 2018.

34. Heo, J. H.; Song, D. H.; Im, S. H., Planar CH3NH3PbBr3 Hybrid Solar Cells with 10.4% Power Conversion Efficiency, Fabricated by Controlled Crystallization in the Spin-Coating Process. Advanced Materials 2014, 26 (48), 8179-8183.

SUPPORTING INFORMATION: Single Crystals growth of Hybrid Bromide Perovskites using a Spin Coating Method

Rocío García-Aboal[a], Roberto Fenollosa[a], Fernando Ramiro-Manzano[a], Isabelle Rodríguez[a], Pedro Atienzar[a]* and Francisco Meseguer[a]

[a]Instituto Universitario de Tecnologia Química, CSIC-UPV, Universitat Politécnica de Valencia, Av. de los Naranjos, Valencia 46022, Spain,

*Corresponding author: patienzar@itq.upv.es

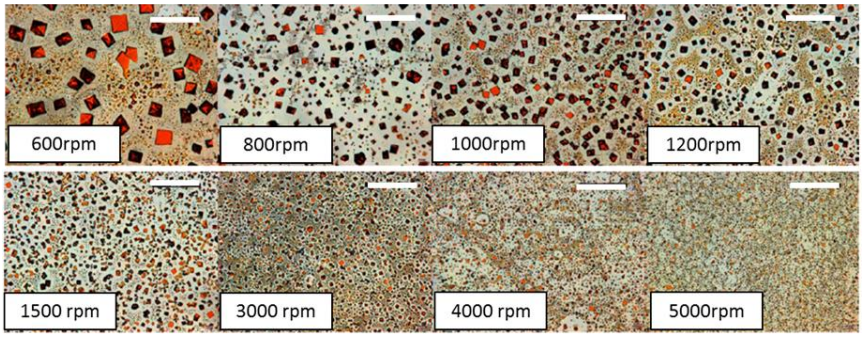

Figure S1. Optical microscopy images (x40 magnification) of $MAPbBr_3$ at different rotation speeds (rpm) for NA samples. The scale reference correspond to 200 µm.

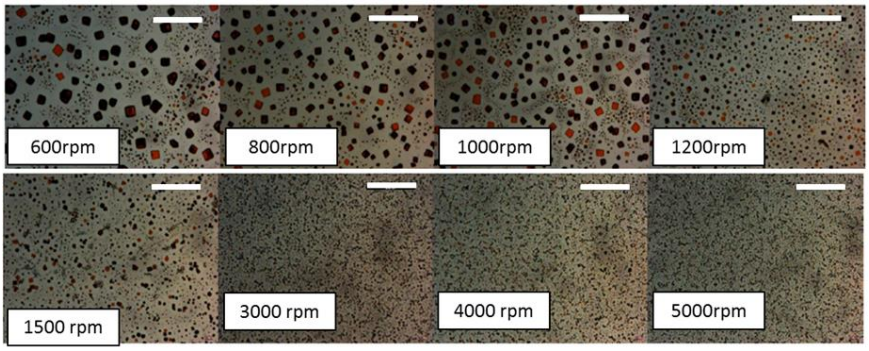

Figure S2. Optical microscopy images (x40 magnification) of $MAPbBr_3$ samples obtained through spin coating at different rpm with CHP additive. The scale reference correspond to 200 µm.

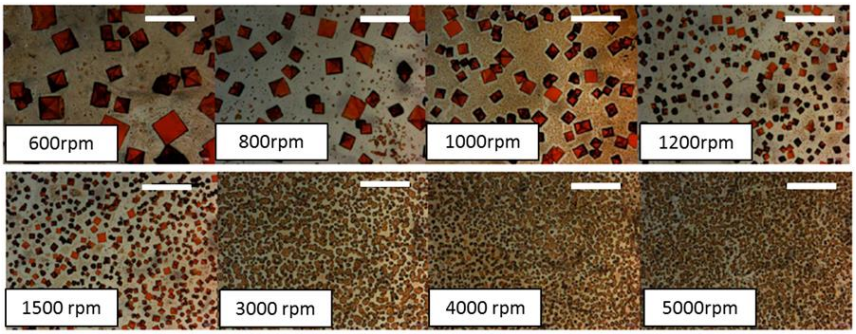

Figure S3. Optical microscopy images (x40 magnification) of $MAPbBr_3$ samples obtained through spin coating at different rpm with DMSO as additive. The scale reference correspond to 200 µm.

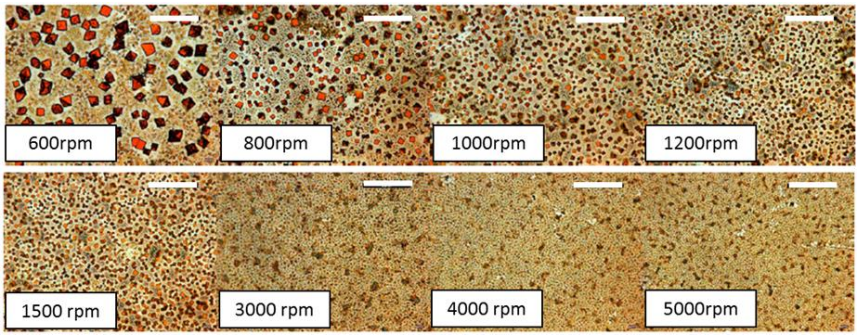

Figure S4. Optical microscopy images (x40 magnification) of $MAPbBr_3$ samples obtained through spin coating at different rpm with TBP as additive. The scale reference correspond to 200 µm.

Table S1. Size and standard deviation in µm for each sample prepared as a function of the rotation speed and additive.

	Rotation speed (rpm)							
	600	**800**	**1000**	**1200**	**1500**	**3000**	**4000**	**5000**
DMF	40.2 ± 11.7	22.7 ± 9.0	12.7 ± 7.4	11.7 ± 6.5	7.1 ± 5.3	7.7 ± 4.0	4.2 ± 3.5	2.0 ± 0.8
CHP	29.9 ± 11.0	22.42± 6.7	15.8 ± 5.8	7.9 ± 4.1	7.9 ± 4.3	3.4 ± 1.9	2.7 ± 1.6	2.5 ± 1.4
DMSO	59.8 ± 23.2	38.3 ± 13.2	30.0 ± 9.9	18.2 ± 6.6	15.1 ± 4.8	7.5 ± 4.6	7.1 ± 3.4	6.5 ± 3.3
TBP	21.8 ± 8.9	1.0 ± 5.5	8.4 ± 3.6	7.5 ± 3.4	6.1 ± 3.4	4.7 ± 2.3	2.9 ± 1.5	2.9 ± 1.7

SECCIÓN 3.2

OPTICAL PROPERTIES OF ORGANIC/INORGANIC PEROVSKITE MICROCRYSTALS THROUGH THE CHARACTERIZATION OF FABRY-PÉROT RESONANCES

Fernando Ramiro-Manzano, Rocío García-Aboal, Roberto Fenollosa, Stefano Biasi, Isabelle Rodriguez, Pedro Atienzar and Francisco Meseguer

Dalton Trans. 2020, 49, 12798

DOI: 10.1039/d0dt02254c

OPTICAL PROPERTIES OF ORGANIC/INORGANIC PEROVSKITE MICROCRYSTALS THROUGH THE CHARACTERIZATION OF FABRY-PÉROT RESONANCES†

Fernando Ramiro-Manzano,[a] Rocío García-Aboal,[a] Roberto Fenollosa,[a] Stefano Biasi,[b] Isabelle Rodriguez,[a] Pedro Atienzar,[a] and Francisco Meseguer.[a]

[a]Instituto de Tecnología Química (CSIC-UPV), Universitat Politécnica de Valéncia,Av. Tarongers s/n, 46022 Valencia, Spain. E-mail: ferraman@fis.upv.es

[b]Laboratorio di Nanoscienze, Dipartimento di Fisica, University of Trento,Via Sommarive 14, 38123 Povo, TN, Italy

Abstract

The precise knowledge of the optical properties, specifically the refractive index, of organic/inorganic perovskites is essential for pushing forward the performance of the current photovoltaic devices that are being developed from these materials. Here we show a robust method for determining the real and the imaginary part of the refractive index of $MAPbBr_3$ thin films and micrometer size single crystals with planar geometry. The simultaneous fit of both, the optical transmittance and the photoluminescence spectra to theoretical models defines unambiguously the refractive index and the crystal thickness. Because the method relies on the optical resonance phenomenon occurring in these microstructures, it can be used to further develop optical microcavities from perovskites or from other optical materials.

1. INTRODUCTION

Organic/Inorganic perovskites have emerged as a new material for cutting edge applications in photon harvesting[1–9] and light emission[10-21]. In a very short period of time we have witnessed extraordinary achievements in the perovskite-rush race for high efficiency solar cells[2,4,9], in spite of the fact that this material suffers of important drawbacks as a poor chemical, thermal and even optical stability, which hampers the development of market devices[22]. In this rich but

difficult scenario, one of the key factors for achieving notable improvements is to have an accurate knowledge of the refractive index of the materials, especially at wavelengths near the optical absorption/emission region. In order to determine the wavelength dispersion of the real and imaginary part of this parameter, many researchers make use of different optical techniques like ellipsometry, which is appropriate for macroscopic samples. However, different approaches are required for characterizing micrometer size structures or small crystal domains of an optical material. Such micro or nanostructures (thin films, planar prisms and microwires) show strong interference effects because they behave as optical Fabry-Pérot type resonators. The resonant response of this kind of cavities has been extensively studied and modelled through their transmittance/ reflectance spectra. In fact, it represents the most general case of an optical resonator[23,24]. Also, the interference phenomenon is expected to appear in the photoluminescence spectra[24], but few theoretical modelling studies have arisen in this regard[25,26]. Here we show a method for determining the optical parameters of a micrometer size structure by fitting simultaneously its optical transmittance (OT) and its photoluminescence (PL) spectra. It allows a faithful determination of the real (n_r) and the imaginary (n_i) components of the refractive index value at a wavelength bandwidth around the optical absorption edge. This results as an in-situ source of information employing common characterization techniques at the microscale, and thus enriching the derived results. In this way this could avoid the use of additional equipment such as commercial ellipsometers and prism couplers. Although we have applied it to the case of perovskite-based microstructures, it can be used for extracting the optical parameters of other materials. For obtaining high fit robustness, the ingredients are: the presence of PL emission and modal structure in the spectra. In order to explain the underlying idea of the method we have used an asymmetrical planar cavity that reproduces faithfully our experimental conditions. In the next section we explain the theoretical model to fit both OT and PL spectra, starting from a simple configuration where only light with k-vector perpendicular to the cavity surface is considered. Then we include the effect of the numerical aperture of the collecting microscope objectives, and analyse the influence of the

cavity thickness. Finally, in the results section, several fitted optical parameters, specially the refractive index values for a perovskite cavity, are shown and compared with other values appearing in the literature, that were obtained by different approaches.

2. MODELLING DETAILS

2.1. Optical transmittance and photoluminescence of a Fabry-Pérot cavity at normal incidence/collection

The type of Fabry-Pérot cavity studied here is composed by the active material (AM) constituted by a high refractive index thin film, such as a perovskite single crystal, deposited on a glass substrate. It is an asymmetric cavity because it includes two different dielectric interfaces (SiO_2/AM and AM/air). Figure 1(a) and 1(b) illustrate this configuration and show the schemes utilized for modelling OT and PL measurements respectively. As a first approach, we have assumed that the light wave vector is perpendicular to the front surface of the sample. The fingerprint of such a cavity is a train of peaks produced by the optical resonant modes that appear in the OT (black curve in Figure 1(c)) as well as in the PL spectra (black curve in Figure 1(d)). This optical phenomenon is derived from the light confinement in the AM film through recursive internal reflections at the interfaces (Figure S1). However, in spite of their similar physical origin, the resonant modes in OT and PL spectra show notable differences in their envelope shapes, because they include distinct ingredients that should be taken into account, particularly in the PL spectra as we will see below. In the case of OT, the relation between the incident (Ein) and the transmitted (Eout) electromagnetic fields follows the well-known relation23 (see Section S2):

$$\frac{E_{out}}{E_{in}} = \frac{t_{12}t_{23}\left(\sqrt{a}e\right)^{i\beta L}}{1 - r_{23}(ar_{21})e^{i\beta 2L}} \qquad (1)$$

where the t_{ij}, r_{ij}, are the transmittance and the internal reflection coefficients of the dielectric interfaces, with [i, j] accounting for the incident and propagating material respectively, i.e. 1 the substrate, 2 the hybrid perovskite and 3 the air, (see Figure 1(a) and (b)), a is an

exponential term related to propagation losses ($a = e^{-2k_0 L n_i}$), k_0 is the free space wavenumber ($k_0 = \frac{2\pi}{\lambda 0}$), β is the propagation parameter ($\beta = k_0 n_r$), λ_0 is the free-space wavelength, L is the sample thickness, and n_r and n_i are the real and imaginary part of the refractive index respectively (see Section S1). From the Equation 1, we can derive the optical transmision parameter T.

$$T = \left|\frac{E_{\text{out}}}{E_{\text{in}}}\right|^2 = \frac{a t_{12}^2 t_{23}^2}{a^2 r_{21}^2 r_{23}^2 - 2a r_{23} r_{21} \cos(2\beta L) + 1} \quad (2)$$

This relation shows local maxima when the cosine term is maximized, that is when 2βL = 2πm (m = 1, 2, 3,….,). Each of them corresponds to a resonance condition with a m-number mode order. Therefore, they define a sequence of peaks in the spectrum. Figure 1(c) highlights two of those peaks (dotted curves) for modes m = 38 and m = 42, which have been decomposed from the total spectrum. They have a Lorentzian shape with a Full Width at Half Maximum ($\Delta\lambda_h$) that is modulated by the losses, related to the propagation (a) and the transmission through the interfaces (see SI). The Figure indicates three spectral regions with (a = 0.44), without (a = 1) and with intermediate propagation losses, which have been highlighted with red, blue and white background colours respectively. As expected (see Section S4), the $\Delta\lambda_h$ of the resonance occurring at the low losses region (m = 38) is substantially smaller than that of the resonance at the high losses region (m = 42). The upper (T_+) [blue curve] and lower (T_-) [green curve] bounds, and also the visibility factor (V) of the peaks can be written as:

$$T_{\pm} = \frac{a t_{12}^2 t_{23}^2}{(1 \mp a r_{23} r_{21})} \quad (3)$$

and

$$V = \frac{(T_+ - T_-)}{T_+} = \frac{4 a r_{23} r_{21}}{(1 + a r_{23} r_{21})^2} \quad (4)$$

Both numerator and denominator of T_+ (see Equation 3) lead to a decrease in transmittance for increasing losses. Also from Equation 3, it is important emphasizing the possibility to reach full transmittance

($T_+ = 1$) values for a propagation lossless (a = 1) symmetrical ($r_{21} = r_{23}$; $t_{12} = t_{23}$) cavity (see Section S2.1). These penalties from achieving full transmittance have been indicated in the Figure 1(c) by vertical arrows in the losses and in the lossless regions. Finally, an average curve T_{av} (dashed red line) could be defined as,

$$T_{av} = \frac{a t_{12}^2 t_{23}^2}{1 - a^2 r_{21}^2 r_{23}^2} \quad (5)$$

which describes the integral average of Equation 2 corresponding to the case of rough interfaces, this destroying the Fabry-Pérot resonances.

In the case of the PL spectrum, we show an example of the emission profile taking into account the attenuation through the AM layer of both, the laser pump source and the emitted signal (see Section S4). For understanding this process, Figure 1(b1) shows a simple scheme of the forward emission that corresponds to the most important PL contribution. We can consider the sample is divided into thin slices or sections along the pumping/collection direction. As an example, the Figure shows two slices (Emitter 1 and Emitter 2), which are characterized by being placed at different distances from the AM/air interface, where the collection of light takes place. The emission spectrum of a section consists of a wide bandwidth signal around the absorption edge. However, the blue-side of the emitted light is strongly absorbed when it propagates through the sample because of differences in the absorption with respect to the more transparent red-side of the spectrum. This results in an asymmetrical and red-shifted shaped signal. The position of each emitter determines the light l, path length inside the sample, and thus the final red-shift, of its PL contribution. This way, the light from Emitter 1/Emitter 2 will be highly/faintly blue-absorbed, provoking a large/small red-shift respectively of the normalized PL spectra.

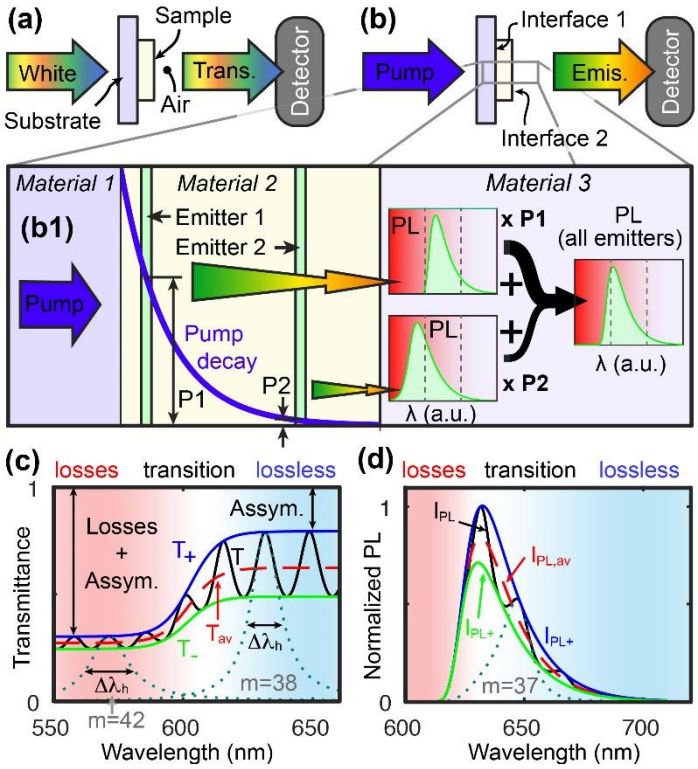

Figure 1. Schematic representation of the OT (a) and PL (b) experiments. (b1) Effect of the pump and PL propagation losses over the forward PL response. Here, the contributions to the emission of two slices of the active material, excited by P1 and P2 pump intensities, are highlighted. (c) Calculated transmittance (black curve) of an asymmetrical thin film cavity (r_{12} = 0.2, r_{23} = 0.6, n_r = 2.4). Three spectral regions corresponding to three different scenarios, one with moderate propagation losses (a = 0.44, red colour background), another one without losses (a = 1, blue colour background) and a transition region between them with intermediate losses (white colour background) have been considered. The transmittance T is limited by T_+ (blue line) and T_- (green line). These two limits comprise an average transmission T_{av} (dashed red line). The transmittance offset or penalty from a full transmittance has been indicated by vertical arrows and it is limited by both, the propagation losses and the cavity asymmetry. Two representative Lorentzian peak decompositions are plotted (dotted lines) for the propagation loss (m = 42) as well as the lossless (m = 38) scenarios (see SI). (d) Similar plot as (c) but for the PL emission. The parameters are the same with the exception of those of the losses region that are more realistic (n_i = 0.18, therefore a≈0). Only a Lorenzian peak in the transition region has been decomposed (m = 37). This peak is highly perturbed by the $I_{(PL)}$ envelopes.

This absorption process occurs as well for the pumping light, which is monochromatic with 405nm of wavelength in our case. Its intensity decreases as the distance from the entering interface (substrate/perovskite) increases (blue curve). Therefore, Emitter 1 and Emitter 2 are excited by intensities P1 and P2 respectively. In any case,

$$I_{PL} = \frac{I_E I_P t_{23}^2 t_{12(p)}^2}{a^2 r_{21}^2 r_{23}^2 - 2a r_{23} r_{21} \cos(2\beta L) + 1} \quad (6)$$

I_E is a term originated from the light emission according to the generalized Planck law:

$$I_E = \frac{2k_0 \xi n_i E_{ph}^2 N_{ph}}{e^{\frac{(E_{ph}-\mu)}{TK_B}} - 1} \quad (7)$$

and I_P is related to the pump and the emitted signal propagation losses through the perovskite material.

$$I_P = \frac{a}{2}\left(r_{21}^2 \frac{1 - e^{-2L\left(K_{0\,(p)} n_{i\,(p)} + K_0 n_i\right)}}{K_{0\,(p)}\, n_{i\,(p)} + K_0 n_i} + \frac{1 - e^{-2L\left(K_{0\,(p)} n_{i\,(p)} + K_0 n_i\right)}}{K_{0\,(p)}\, n_{i\,(p)} - K_0 n_i} \right) \quad (8)$$

In these Equations, $k_{0(p)}$, $t_{12(p)}$ and $n_{i(p)}$ account for the free space wavenumber, the transmission coefficient and the complex part of the refractive index for the pump signal respectively, x is related to the photogeneration efficiency, N_{ph} corresponds to the number of pumping photons, E_{ph} is the emitted photons energy, m is the chemical potential, k_B is the Boltzman constant and T is the sample temperature[25,26](see Section S4). In a similar manner as the OT in Equation 2, the PL formula has the same oscillatory term ($a^2r^2_{21}r^2_{23}$ - $2r_{23}(ar_{21})\cos(2\beta L)+1$). Therefore both, the PL and the OT spectra keep the same interference ingredients but with different envelopes. We can also define for the PL spectra three different spectral regions [see Figure 1(d)], one with losses ($a \approx 0$, red colour background) where in principle the resonant modes widen and finally disappear, followed by a transition zone (white colour background) where resonances are visible (see for instance the Lorentzian peak (dotted line) associated to

a mode with order m=37) and finally a lossless region (a ≈ 1, blue colour background) where the PL and their peaks disappear. We can also derive similar expressions for the upper I_{PL+} (blue curve) and lower I_{PL-} (green curve) bounds of the emission as well as for the average PL signal $I_{PL,av}$ (dashed red curve), this time restricted to the wavelength region of the light emission.

$$I_{PL} = \frac{I_E I_P t_{23}^2 t_{12\,(p)}^2}{(1 \mp a r_{23} r_{21})^2} \tag{9}$$

$$I_{PL,av} = \frac{I_E I_P t_{23}^2 t_{12\,(p)}^2}{(1 - a^2 r_{21}^2 r_{23}^2)^2} \tag{10}$$

2.2. Effect of the collection cone

Collection lenses allow magnifying optical signal by collecting light coming from different k-vector angles. The higher the numerical aperture (N.A.) of a lens, the larger the range of collected k-vector angles. In this way, the enlargement of the collecting angle leads to an increment in the number of wave components of the Fabry-Pérot resonances (see Sections S2-S4), and it can blur the visibility of the peaks, as shown in Figure 2. In general, the resonances appear much more pronounced in the OT spectrum than in the corresponding PL spectrum because of their different envelope curves, flat and with a pronounced slope respectively, around the wavelength region where absorption losses vanish. Therefore, the increase of the N.A. of the collection lens produces a more drastic effect in the PL spectra, where the train of peaks may even disappear for some cases. Figures 2(a)-(d) represent different scenarios for different collection cones, for a 3.96 µm thick perovskite layer that corresponds to the characterized sample in the Section 3. Since changing a particular collection angle from the normal direction is equivalent to increase the sample thickness, here the effect of the N.A. was calculated by averaging Equation 2 and 6 for OT and PL spectra respectively for several values of an effective thickness ($L/\cos(\Theta_r)$), where Θ_r varies from 0 to the limit refractive angle inside the perovskite layer. This limit angle can be easily calculated from the N.A. and the Snell law at each wavelength

value. In the case of the r and t parameters, their values are marginally affected by Θ_r because the refracted angle is much lower than the collection angle. A N.A. ≤ 0.26 influences marginally the peak contrast for thin cavities as we will see in the next section. Thus a regime of normal incidence/collection could be assumed in those cases. However, in general the effect of the collecting objectives should be considered in the model for N.A. ≥ 0.4. As it will be explained in the following paragraphs, the conjunction of the numerical aperture with the sample thickness plays a pivoting role in the observation of cavity peaks.

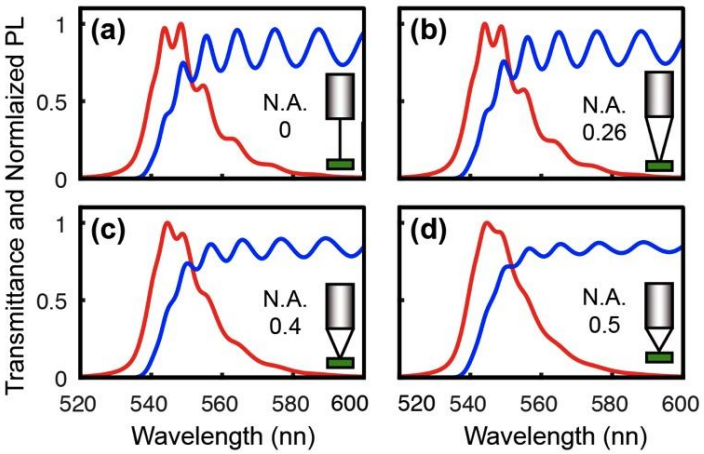

Figure 2. Transmittance (blue line) and Normalized PL (red line) spectra for different objectives: N.A. 0 (a), N.A. 0.26 (b), N.A. 0.4 (c), N.A. 0.5 (d) for a perovskite layer of 3.96 mm thick. The refractive index and extinction dispersion have been extracted from the fit of experimental data (see Figure 4).

2.3. Influence of the film thickness

The thickness of a Fabry-Pérot cavity influences strongly the peak visibility. Figure 3 shows contour-plot stacks of the OT (a) and the PL (b) response of a $MAPbBr_3$ perovskite thin film type cavity as a function of wavelength and thickness. We used the refractive index for this material (both real and imaginary values) obtained by the fitting process detailed in the following section, and we assumed a N.A. = 0.26 for the collection objective. Each oblique line accounts for a resonant mode m. This could be easily understood by examining the resonant

condition, which is a simple line Equation: L = $\frac{m\lambda_0}{2nr}$, whose slope depends on the mode order and the refractive index. The lack of a constant term in this first order polynomial form indicates that the m-lines start from a hypothetical wavelength origin. In the case of the OT, these m-lines extend over the large transparent region (red area in Figure 3(a)). However, they appear only within the bandwidth of the PL signal [Figure 3(b)]. It is worth underlining several properties of these contour-plots: (i) a horizontal cross section for a given thickness corresponds to the spectrum of a cavity with such a thickness value [Figures (a1-a4) for OT, and Figures (b1-b4) for PL]. (ii) each spectrum intercepts several m-lines depending on the layer thickness, the thicker the layer or the shorter the wavelength, the higher the density of such interceptions. This explain the behaviour of the free spectral range (FSR), which corresponds to the distance between successive Fabry-Pérot peaks (see Section S5), (iii) a larger refractive index value nr means a smaller m-line slope that results in an increase of the density of m-lines in any spectrum. The fact of assuming a finite N.A. in the calculations can be appreciated by considering the visibility and contrast of the interference peaks in Figure 3 (a1)-(a4). While these parameters are independent of the sample thickness at normal incidence in the region where absorption vanishes (see Equation 4), they are now reduced when layer thickness L and λ increases. The latter dependence is subtle, but it appears clearer in Figure 3 (a4). In fact, the thicker the sample the closer the m-lines (the smaller the FSR), and consequently the more pronounced are the effects of the numerical aperture because each angular component of the collection cone is described by an effective increase of the sample thickness ($L/\cos(\Theta_r)$). On the other hand, the increase of the slope of the m-lines at shorter wavelengths yields more similar angular components, thus reducing their influence in the N.A.

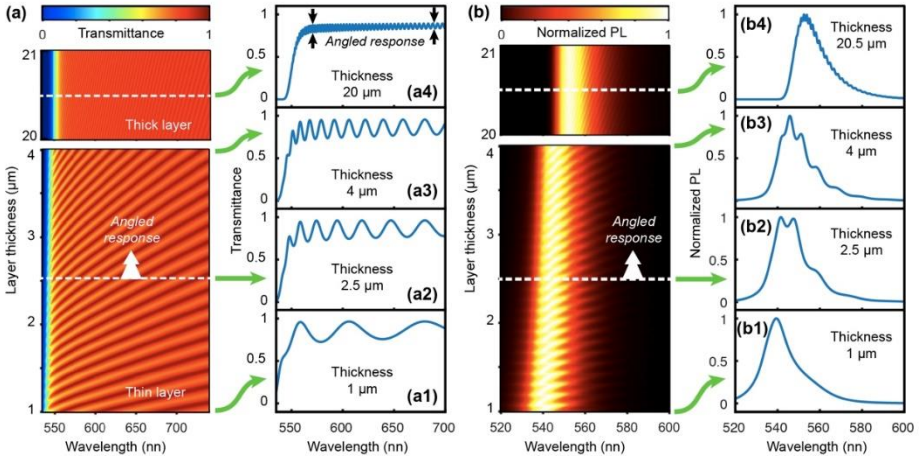

Figure 3. Calculated (a) Transmittance and (b) Normalized PL spectra of a $MAPbBr_3$ thin film as a function of the layer thickness for a collection objective of N.A.= 0.26 where (a1)-(a4) and (b1)-(b4) represent respectively 1, 2.5, 4 and 20.5 μm sample thickness. The refractive index and extinction dispersion have been extracted from the fit of experimental data (see Figure 4).

Finally is worth emphasising that sample thickness also changes both the peak position as well as the asymmetry of the PL background profile (see Figures 3(b1)-(b4)) because the optical path length determines the attenuation of the blue-side of the emitted signal.

3. RESULTS AND DISCUSSION

OT and PL spectra of perovskite optical-microcavities single crystals (Figure 4(a)) could be successfully fitted to those models that have been detailed in previous sections. Figure 4 (b) and (c) show experimental (black) and fitted (red) curves corresponding to OT and PL spectra respectively of a 3.96 μm thick $MAPbBr_3$ crystal deposited on a glass substrate. The thickness value was obtained from the fitting process itself. Besides Equation 2 and 6, other important ingredients of the fitting procedure are i) the use of polynomials, Sellmeier and Sigmoid curves for parametrizing the refractive index, ii) the N.A. of the collecting objective, 0.4 in our case, and iii) the fact that the fitting process is performed simultaneously for both OT and PL spectra. This helps disregarding spurious solutions and strengthens the reliability in the fitted parameters. Figures 4(d) and 4(e) show the fitted values

(dark brown curves) of the real and imaginary part respectively of the refractive index. They resemble other values reported in the literature, particularly those of J.-S. Park et al.[27] (blue curves) that were obtained by the ellipsometry technique. Here, the differences could be attributed not only to the distinct measurement method but also to different sample fabrication processes[28]. It is interesting to investigate the performance of the perovskite crystal as optical cavity through the Finesse (F) and the Quality Factor (Q) of its optical resonant modes, identified by their mode-order, m, (highlighted on top of each resonance peak in Figure 4(b) and (c)). These parameters are proportional to the amplification of light inside the crystal and to the peak isolation in the case of F, and cavity lifetime in the case of Q[23,24] (see Section S5). Therefore, high F and Q values are desired for large light-matter interactions. In the present case of the perovskite crystal, the maximum values for F (≈ 0.95) and Q (≈ 80.1) appear for modes m = 32 and m = 33 (see Figure 4(f) and 4(g) respectively), that are near the absorbance edge, where the refractive index is high and the losses are moderate (see Section S6). The development of future cutting edge applications in this area would require the improvement of these important parameters. This could be achieved for example by shaping the perovskite material in more effective geometries such as circular, spherical or photonic crystal (see Section S7). A high improvement of the cavity could help to boost, deepen into or discover new excellent or exotic properties of this material[29,30]. We think this constitutes a very interesting research branch for the future.

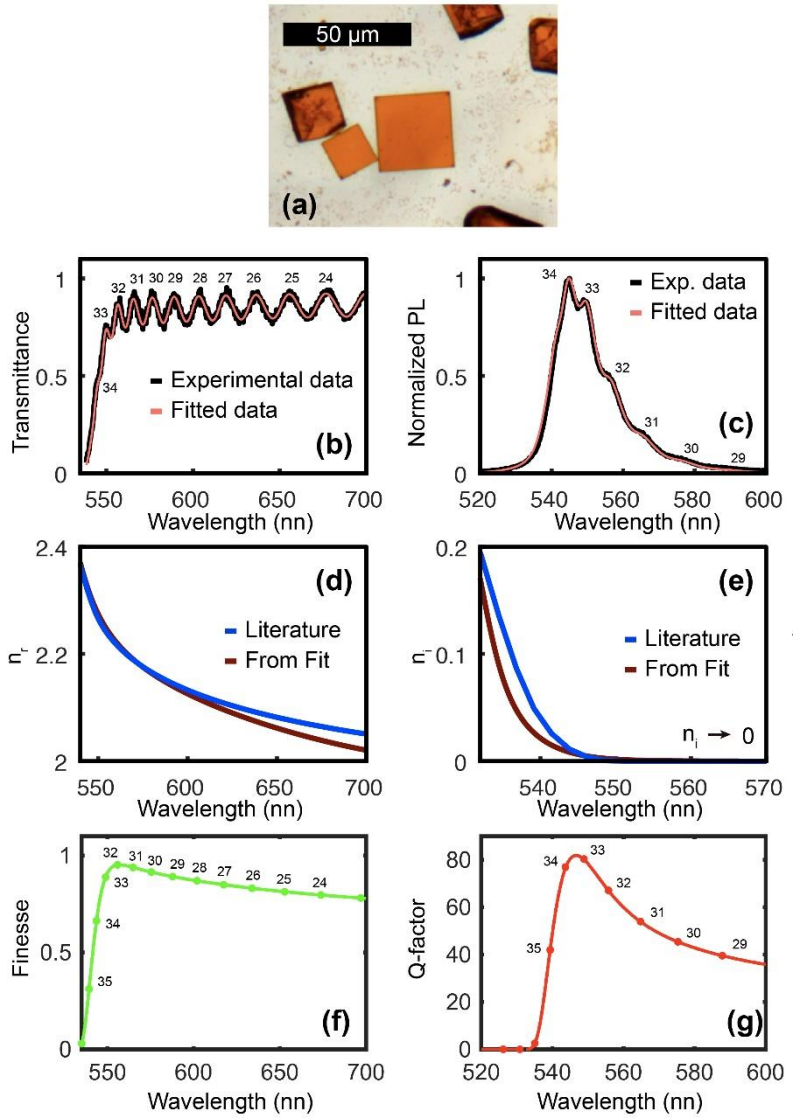

Figure 4. (a) Optical microscopy image of the measured $MAPbBr_3$ crystal microcavity (square structure at the center of the image). (b) and (c) Experimental data and fitted curves for the OT and the PL spectra respectively. Resonant modes are indicated on top of their resonance peak by their mode-order, m. (d) Real and (e) imaginary part of the fitted refractive index and that of ref 27 for comparison. (e) Finesse and (f) Quality Factor for all of the identified modes. The lines are to guide the eye.

4. EXPERIMENTAL SECTION

Micrometer size single crystals of $MAPbBr_3$ were synthesized from a precursor solution composed by methylammonium bromide (MABr) 1M and lead bromide ($PbBr_2$) 1M in N, N-dimethylformamide (DMF), and N-cyclohexyl-2-pyrrolidone (CHP) as additive. The $MAPbBr_3$ crystals were grown onto quartz substrates by spin-coating the precursor solution at 800 rpm at room temperature. The samples were annealed at 90°C during 2 minutes to remove the solvents and complete the crystallization process[31]. Then, the crystals were characterized by X-ray diffraction (XRD) and ultraviolet-visible spectrophotometry (UV-Vis)[32] (see Section S8). The optical setup for measuring the OT and PL spectra[31] consists of a microscope-based characterization system where the input signal is generated from either, a tungsten lamp (for transmission characterization) or a solid state 404 nm laser (for PL characterization) passing through a 20x 0.4 N.A. objective illuminating the sample with 0.1mW of optical power. The sample is placed in a 3-axis positioning stage for selecting the target planar microcrystal cavity. The output signal is collected with another objective with the same features, and then the light is focused in a pinhole for selecting a target area inside the sample. This permits to avoid any perturbation from the borders and to study faithfully the transmission spectrum by subtracting the AM transmitted intensity from a background signal, acquired from a void area. Finally, the light matches a spectrometer and the signal is detected by a nitrogen-cooled CCD array. The experimental data fitting has been performed by employing the mathematical commercial package Matlab.

CONCLUSIONS

We have shown a simple procedure to extract accurately both the real and the imaginary part of the refractive index in a wide wavelength region around the electronic band gap, and the thickness of a $MAPbBr_3$ single-crystal placed on a silica substrate. The method consists in a dual fit of the Transmittance and the Photoluminescence spectra to analytical models. Both spectra show Fabry-Pérot oscillations corresponding to resonant modes with different envelopes. We have analysed how the parameters of the models and

other external factors such as the numerical aperture of the collecting lenses influence the final shape of the resonances. At the same time, the models constitute a guide for finding the conditions for a thin film type microstructure to have an optical cavity response. The extracted information from an isolated single crystal could be useful for understanding or improving the macroscopic behaviour of polycrystalline materials, where crucial information, such as the described resonant phenomena, could be hidden behind the collective contribution to the material response.

Conflicts of interest

There are no conflicts to declare.

Acknowledgements

This work was supported by Spanish ministry of Economy, Industry and Competitiveness (MINECO) through the projects TEC2015-74405-JIN, MAT2015-69669-P as well as the regional projects of both Provincia Autonoma di Trento (PAT) of Italy, through the call Grandi Progetti 2012: SIQURO and the Comunidad Valenciana of Spain project PrometeoII/2014/026.

Notes and references

1. J.-H. Im, C.-R. Lee, J.-W. Lee, S.-W. Park and N.-G. Park,Nanoscale, 2011, 3, 4088–4093.

2. M. M. Lee, J. Teuscher, T. Miyasaka, T. N. Murakami and H. J.Snaith, Science, 2012, 338, 643–647.

3. M. Liu, M. B. Johnston and H. J. Snaith, Nature, 2013, 501,395.

4. L. M. Pazos-Outón, M. Szumilo, R. Lamboll, J. M. Richter, M. Crespo-Quesada, M. Abdi-Jalebi, H. J. Beeson, M. Vru´cini´c, M. Alsari, H. J. Snaith, B. Ehrler, R. H. Friend and F. Deschler, Science, 2016, 351, 1430–1433.

5. N. J. Jeon, J. H. Noh, W. S. Yang, Y. C. Kim, S. Ryu, J. Seo and S. I. Seok, Nature, 2015, 517, 476.

6. J. Burschka, N. Pellet, S.-J. Moon, R. Humphry-Baker, P. Gao, M. K. Nazeeruddin and M. Grätzel, Nature, 2013, 499, 316.

7. A. Kojima, K. Teshima, Y. Shirai and T. Miyasaka, Journal of the American Chemical Society, 2009, 131, 6050–6051.

8. H.-S. Kim, C.-R. Lee, J.-H. Im, K.-B. Lee, T. Moehl, A. Marchioro, S.-J. Moon, R. Humphry-Baker, J.-H. Yum, J. E. Moser, M. Grätzel and N.-G. Park, Scientific Reports, 2012, 2, 591.

9. W. S. Yang, B.-W. Park, E. H. Jung, N. J. Jeon, Y. C. Kim, D. U. Lee, S. S. Shin, J. Seo, E. K. Kim, J. H. Noh and S. I. Seok, Science, 2017, 356, 1376–1379.

10. H. Cho, S.-H. Jeong, M.-H. Park, Y.-H. Kim, C. Wolf, C.-L. Lee, J. H. Heo, A. Sadhanala, N. Myoung, S. Yoo, S. H. Im, R. H. Friend and T.-W. Lee, Science, 2015, 350, 1222–1225.

11. Z.-K. Tan, R. S. Moghaddam, M. L. Lai, P. Docampo, R. Higler, F. Deschler, M. Price, A. Sadhanala, L. M. Pazos, D. Credgington, F. Hanusch, T. Bein, H. J. Snaith and R. H. Friend, Nature Nanotechnology, 2014, 9, 687.

12. Y.-H. Kim, H. Cho, J. H. Heo, T.-S. Kim, N. Myoung, C.-L. Lee, S. H. Im and T.-W. Lee, Advanced Materials, 27, 2015, 1248–1254.

13. R. L. Z. Hoye, M. R. Chua, K. P. Musselman, G. Li, M.-L. Lai, Z.-K. Tan, N. C. Greenham, J. L. MacManus-Driscoll, R. H. Friend and D. Credgington, Advanced Materials, 27, 2015, 1414–1419.

14. N. K. Kumawat, A. Dey, K. L. Narasimhan and D. Kabra, ACS Photonics, 2015, 2, 349–354.

15. G. Li, Z.-K. Tan, D. Di, M. L. Lai, L. Jiang, J. H.-W. Lim, R. H. Friend and N. C. Greenham, Nano Letters, 2015, 15, 2640– 2644.

16. J. Wang, N. Wang, Y. Jin, J. Si, Z.-K. Tan, H. Du, L. Cheng, X. Dai, S. Bai, H. He, Z. Ye, M. L. Lai, R. H. Friend and W. Huang, Advanced Materials, 27, 2015,

2311–2316.

17. A. Sadhanala, A. Kumar, S. Pathak, A. Rao, U. Steiner, N. C. Greenham, H. J. Snaith and R. H. Friend, Advanced Electronic Materials, 2015, 1, 1500008.

18. J. C. Yu, D. B. Kim, G. Baek, B. R. Lee, E. D. Jung, S. Lee, J. H. Chu, D.-K. Lee, K. J. Choi, S. Cho and M. H. Song, Advanced Materials, 2015, 27, 3492–3500.

19. N. K. Kumawat, A. Dey, A. Kumar, S. P. Gopinathan, K. L. Narasimhan and D. Kabra, ACS Applied Materials & Interfaces, 2015, 7, 13119–13124.

20. O. A. Jaramillo-Quintero, R. S. Sanchez, M. Rincon and I. Mora-Sero, The Journal of Physical Chemistry Letters, 2015,6, 1883–1890.

21. H. Zhu, Y. Fu, F. Meng, X.Wu, Z. Gong, Q. Ding, M. V. Gustafsson, M. T. Trinh, S. Jin and X.-Y. Zhu, Nature Materials, 2015, 14, 636.

22. M. Lira-Cantu, Nature Energy, 2017, 2, 17115.

23. A. Yariv and P. Yeh, Optical Electronics in Modern Communications, 2007.

24. B. Saleh and M. Teich, Fundamentals of Photonics 2007.

25. S. Knabe, M. Langemeyer, F. Heidemann, R. Brüggemann and G. H. Bauer, Progress in Photovoltaics: Research and Applications, 2011, 19, 927–936.

26. O. Neumann, R. Brüggemann, N. Könne and G. H. Bauer, physica status solidi (a), 2014, 211, 1128–1133.

27. J.-S. Park, S. Choi, Y. Yan, Y. Yang, J. M. Luther, S.-H. Wei, P. Parilla and K. Zhu, The Journal of Physical Chemistry Letters, 2015, 6, 4304–4308.

28. M. E. Calvo, J. Mater. Chem. A, 2017, 5, 20561–20578.

29. H. Tahara, T. Aharen, A. Wakamiya and Y. Kanemitsu, Advanced Optical Materials, 2018, 6.

30. T. Handa, H. Tahara, T. Aharen and Y. Kanemitsu, Science Advances, 2019, 5.

31. R. García-Aboal, R. Fenollosa, F. Ramiro-Manzano, I. Rodríguez, F. Meseguer and P. Atienzar, ACS Omega, 2018, 3, 5229–5236.

32. J. H. Heo, D. H. Song and S. H. Im, Advanced Materials, 2014, 26, 8179–8183.

SUPPORTING INFORMATION: Optical properties of organic/inorganic perovskite microcrystals through the characterization of Fabry-Pérot resonances

Fernando Ramiro-Manzano,[a] Rocío García-Aboal,[a] Roberto Fenollosa,[a] Stefano Biasi,[b] Isabelle Rodriguez,[a] Pedro Atienzar,[a] and Francisco Meseguer[a]

[a]Instituto de Tecnología Química (CSIC-UPV), Universitat Politécnica de Valéncia,Av. Tarongers s/n, 46022 Valencia, Spain. E-mail: ferraman@fis.upv.es

[b]Laboratorio di Nanoscienze, Dipartimento di Fisica, University of Trento,Via Sommarive 14, 38123 Povo, TN, Italy

S1. Phase and propagation losses. Complex Refractive Index

The phase and losses of a wave could be expressed in a compact way employing the complex refractive index (nc) as follows:

$$e^{iK_0 x n_c} = e^{-K_0 x n_i} e^{K_0 x n_i} \quad \text{(S1)}$$

where $e^{(ik0nrx)}$ and $e^{(-k0nix)}$ account for the phase and losses respectively, $n_c = n_r + in_i$ is the complex refractive index, n_r/n_i are the real/imaginary part of the refractive index, $k_0 = 2\pi/\lambda_0$ is the free space wavenumber and λ_0 the free space wavelength. In a typical light-propagation device formed by a high refractive index value dielectric thin film material in air or deposited on a low refractive index substrate, the field is mostly confined in the high-refractive index material, and guided by total internal reflection. Neither the phase nor the losses could be expressed directly by the refractive index of the core, because part of the light is propagated via the evanescent field in the surrounding media. The phase is related to an effective refractive index n_{eff}, defining the propagation constant $\beta = 2\pi n_{eff}/\lambda_0$ and the losses are usually expressed in cm^{-1} (or decibels dB cm^{-1}), designed usually by α. The solutions are discrete, and are characterized by different n_{eff}, β, α and intensity profiles, which depend on the material and the geometry of the optical device. Each of these solutions or modes defines both, the light propagation as well as the resonant conditions.

In our first approximation, for simplicity, we consider a normal incident light propagating isotropically as a plane wave (with an infinite cross-section), so the form of the complex refractive index (Equation S1) of the bulk material could be used.

S2. Transmittance

Consider a plane-parallel sample, deposited on a glass surface (Figure 1). Therefore, the optical system is defined by three materials (1:substrate, 2:sample and 3:air) and two interfaces or semitransparent dielectric mirrors (interfaces 1 and 2). In a transmittance experiment, the sample is illuminated from one side, ideally by a planar wave defined by an electric field amplitude E_{in} and a free space wavelength λ_0. The light enters into the sample by crossing the first dielectric interface (see Figure S1). As a result, the wave is affected by a transmission coefficient (t_{12}). Next, it propagates into the material of interest, experimenting a wavelength change ($\lambda_m = \lambda_0/n_r$), a phase change and an attenuation (e^{ik0Lnc}). Finally a portion of light escapes through the second dielectric interface (t_{23}) arriving to the detector, or is reflected (r_{23}). The reflected light recursively returns to the first interface, is reflected again (r_{21}) and propagates through the sample for the second time ($e^{2ik0Lnc}$), loosing intensity on each round trip. In fact, part of this lost light is transmitted (t_{23}) towards the detector. In summary, the light behaviour could be expressed as:

$$E_{out} = E_{in}t_{12}t_{23}e^{iK_0Ln_c} + E_{in}\theta t_{12}t_{23}e^{iK_0Ln_c} + E_{in}\theta^2 t_{12}t_{23}e^{iK_0Ln_c} + \ldots + E_{in}\theta^N t_{12}t_{23}e^{iK_0Ln_c} + \cdots \quad \text{(S2)}$$

where Θ represents a round trip ($\Theta = r_{21}r_{23}e^{2ik0Lnc}$). Regrouping Equation S2 in a convenient way, Θ forms a geometrical series ($1+ \Theta + \Theta^2 + \ldots + \Theta^N + \ldots = 1/(1- \Theta)$). As a result, Equation S2 could be expressed in a compact way:

$$E_{out} = \frac{E_{in}\left(t_{12}t_{23}e^{iK_0Ln_c}\right)}{1 - \theta} \quad \text{(S3)}$$

Assuming the transmission and reflection coefficients as real, expanding the propagation of the round trip into its real ($a = e^{-2k0Lni}$) and imaginary parts ($b = e^{2\beta iL}$, where $\beta = k_0 n_r$), and considering the addition of the exponential with its conjugate ($b^* + b = 2\cos(2\beta L)$), the Transmittance (T) takes the form of:

$$T = \left|\frac{E_{out}}{E_{in}}\right|^2 = \frac{a t_{12}^2 t_{23}^2}{a^2 r_{21}^2 r_{23}^2 - 2a r_{21} r_{23} \cos(2\beta L) + 1} \qquad \text{(S4)}$$

where t_{12}, t_{23}, r_{21} and r_{23} coefficients could be calculated by employing the Fresnel Equations[1].

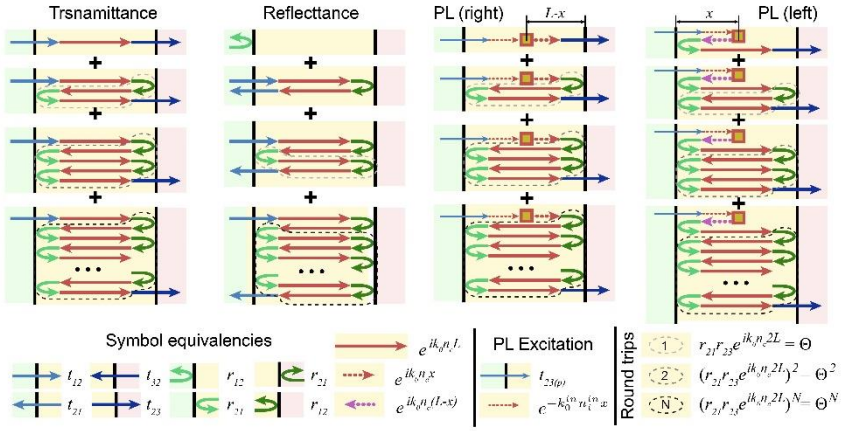

Figure S1. Scheme of light propagation in transmittance and PL

S2.1 Large transmittance and enhancement factor

The possibility of reaching full transmittance with a lossless (a = 1) and symmetrical cavity is mentioned in section 2.1. Here, we extend these concepts: Letâ˘A´Zs quantify the cavity asymmetry as the ratio between reflections $y = r_{23}/r_{21}$ (notice that y = 1 means a symmetrical cavity). Assuming lossless interfaces, $t^2_{ij} = 1 - r^2_{ij}$, for i,j = 1, 2, 3, Equation 3 and 4 turn into:

$$T_{\pm,lossless} = 1 - \frac{r_{21}^2 (1 \mp y)^2}{(1 \mp y r_{21}^2)^2} \qquad \text{(S5)}$$

and

$$V_{lossless} = \frac{4r_{21}^2 y}{(r_{21}^2 y + 1)^2} \quad \text{(S6)}$$

Equation S5 and S6 allow calculating the maximum transmittance T_+ and visibility V, as a function of the cavity asymmetry, y, for a lossless cavity. They confirm that full transmittance ($T_+ = 1$) is achieved for y = 1, i.e. when the cavity is symmetric. As a result, the asymmetry and the absorption act as transmission penalties. In order to diminish T_- and to maximize V, the lossless and symmetry conditions should be completed with a large reflectance. Those optical devices, that accomplish these conditions, are usually known as high- or ultrahigh-quality factor resonators (see Section S7)[1]. The possibility of obtaining a high output signal (T_+) is originated by an amplified intracavity propagating wave, that travels from the source to the output interface ($I_{1\to3} = I_{out}/t^2_{23}$). The interference of this forward signal with its backward reflection ($I_{3\to1} = I_{1\to2}r^2_{23}$) results in a standing wave featured by m-number of peaks with an enhanced intensity ($I_{inside} = I_{1\to3} + I_{3\to1} + 2\sqrt{I_{1\to3}I_{3\to1}}$)[2]. The relation between intracavity and excitation intensity defines the peak enhancement factor (PEF),

$$PEF = \frac{(r_{23} + 1)T_+}{t_{23}^2} \quad \text{(S7)}$$

As a consequence, light-mater interactions are expected to be magnified inside the cavity, thus boosting photochemical processes such as energy harvesting[3], and photocatalysis[4]. While T_+ is symmetric for an asymmetric cavity, in the sense that it does not depend on which face (substrate/active-material active-material/air) is chosen for inserting or extracting the light, PEF is asymmetric, therefore it changes depending on the orientation of the sample. Noteworthy, the magnified output intensity produced by the amplified intracavity light fulfills energy conservation rules since the reflection spectra presents dips on one face whenever transmission peaks appear in the other face (see Section S3).

S3. Reflectance

The reflectance could be calculated in a similar way as the transmittance. Here, a determinative element is present: the reflection from the 1st interface (r_{12} see Figure S1) that is collected by the detector. This wave will interfere with the backward transmitted light (t_{21}) from the series light round-trips inside the sample. The first round-trip is composed by a single reflection, and the following contributions are equal to those of transmission ($\Theta = r_{21}r_{23}e^{2ik0Lnc}$):

$$E_{out} = E_{in}\left(r_{12} + r_{23}t_{12}t_{21}e^{2iK_0Ln_c} + r_{23}t_{12}t_{21}\theta e^{2iK_0Ln_c} + \cdots + r_{23}t_{12}t_{21}\theta^N e^{2iK_0Ln_c} + \cdots\right) \quad \text{(S8)}$$

$$E_{out} = E_{in}\left(\frac{r_{23}t_{12}t_{21}e^{2iK_0Ln_c}}{1-\theta} + r_{12}\right) = E_{in}\frac{r_{23}(t_{12}t_{21} - r_{21}r_{23})e^{2iK_0Ln_c} + r_{12}}{1-\theta} \quad \text{(S9)}$$

Considering lossless interfaces, the time-reversal symmetry allow us, without loss of generality, to state $t_{12}t_{21}$-$r_{21}r_{23}$= -1[2]. So the Equation S9 assumes the compact form:

$$E_{out} = E_{in}\frac{r_{12} - r_{23}e^{2iK_0Ln_c}}{1-\theta} \quad \text{(S10)}$$

and the optical reflectance (R) takes the expression

$$R = \left|\frac{E_{out}}{E_{in}}\right| = \frac{(a^2r_{23})^2 - 2ar_{23}r_{12}\cos(2\beta L) + r_{12}^2}{a^2r_{21}^2r_{23}^2 - 2ar_{21}r_{23}\cos(2\beta L) + 1} \quad \text{(S11)}$$

under resonant condition (2bL = 2p),

$$R_{res} = \left|\frac{E_{out}}{E_{in}}\right|^2 = \left(\frac{r_{12} - ar_{23}}{1 - ar_{21}r_{23}}\right)^2 \quad \text{(S12)}$$

While the Transmittance shows a train of peaks, the reflexion spectrum shows dips. In this case, for obtaining an on-resonance null signal (the deepest dip), the numerator must be zero ($r_{12} = ar_{23}$). This is the so-called critical coupling. In this case, it can only happen when $r_{23} > r_{12}$, otherwise the optical system remains in an undercoupled regime, where the light injection underpass the lost light inside the resonator. For a symmetrical system, where $r_{12} = r_{23}$, the only

possibility to obtain critical coupling is the ideal case when the material losses are neglected (a = 1). In summary, for obtaining the deepest reflectance dip, the glass substrate should be the exposed area to the illumination, and the uncovered surface to the detector side because the reflectance coefficient of the perovskite/air interface is higher than that of the perovskite/glass interface. The reflectance characterization is more complex than the optical transmission because of the spurious reflection of optical components as well as the coupling conditions. This is the reason why we have employed the transmittance signal in this study.

S4. PL model

The Transmission and reflection spectra of the optical system help to understand the PL model. Although the PL emission occurs inside the cavity along all directions, since our approach is one dimensional, here we assume PL emission only in the forward and backward directions (see Figure S1). Each section of infinitesimal thickness of the sample (placed at x-distance from the first interface) is excited by the pump signal that has lost some intensity in its way from the interface to the section. This loss is related to the exponential term ($a_{(p)x} = e^{2x\text{-}k0(p)ni(p)}$). Here, the addition of (p) to the subindex implies the pump signal. Therefore, in this expression, $k_{0(p)}$ corresponds to the wave number in vacuum of the excitation light and $n_{i(p)}$ corresponds to the complex part of the refractive index for such wave number. dI_{PL} of Equation S13 expresses the PL intensity emitted by the section and it can be quantified according to the generalized Planck law[5,6].

$$Id_{PL} = \frac{2K_0 \xi n_i E_{hp}^2 N_{hp}}{e^{\frac{(E_{hp}-\mu)}{TK_B}}-1} dx \qquad \text{(S13)}$$

where E_{ph} is the energy of the emitted photons, μ is the Fermi level, k_B is the Boltzmann constant, T the temperature, dx is the thickness of the differential section, N_{ph} is the number of pumping photons, $\xi = \eta/(c^2h^3)$ includes the photogeneration efficiency η, h being the Plank constant, and c the light speed, so that $\xi \cdot N_{ph}$ allows us normalizing the PL intensity. The light emitted by a given section at the output

interface can be calculated by treating it as a transmittance problem (Figure S1), where the emitted light (dI_{PL}) weighted by the loss term of the pumping signal ($a_{x(p)}$) would represent the incident light intensity ($\approx|E_{in}^2|$) for that section. This yields Equation S14 and S15 for the forward and backward emissions respectively, which are similar to Equation S4, except for terms of losses: ($a_{L-x} = e^{2\text{-}k0ni(L-x)}$) and ($a_{L+x} = e^{2\text{-}k0ni(L+x)}$) where the distance from the entering interface, x, has been taken into account, and the term $t_{12(p)}$ that corresponds to the transmittance coefficient of the pumping signal, $t_{12(p)}$ could actually be included in the normalization term $\xi \cdot N_{ph}$.

$$PL - forward, dI_{otu-f} = \frac{a_{x(p)} dI_{LP} t_{23}^2 t_{12(p)}^2 a_{L-x}}{a^2 r_{21}^2 r_{23}^2 - 2 r_{23} a r_{21} \cos(2\beta L) + 1} \quad \text{(S14)}$$

$$PL - fbackward, dI_{otu-b} = \frac{a_{x(p)} dI_{LP} t_{21}^2 t_{12(p)}^2 a_{L+x}}{a^2 r_{21}^2 r_{23}^2 - 2 r_{21} a r_{23} \cos(2\beta L) + 1} \quad \text{(S15)}$$

The PL signal emitted by the sample (Equation 6), results from the integration of the incoherent addition of S14 and S15 over L.

S5. Spectral dependencies

From a Taylor expansion of the cosine term around the resonant condition of an m-order mode and neglecting the high order terms:

$$\cos(2\beta L) \approx 1 - 2L^2(\beta - \beta_m)^2 \quad \text{(S16)}$$

proceeding in a similar way with b

$$\beta = \beta_m + \frac{d\beta}{d\lambda}\Delta\lambda \quad \text{(S17)}$$

where

$$\frac{d\beta}{d\lambda} = K_0 \frac{dn_r}{d\lambda} - \frac{\beta}{\lambda} \quad \text{(S18)}$$

Defining the group index ng that takes into the account the dispersion,

$$n_g = n_r - \lambda \frac{dn_r}{d\lambda} \tag{S19}$$

then

$$\frac{d\beta}{d\lambda} = \frac{-K_0 n_g}{\lambda} \tag{S20}$$

and

$$\cos(2\beta L) \approx 1 - \frac{2L^2 \Delta\lambda^2 K_0^2 n_g^2}{\lambda^2} \tag{S21}$$

Substituting the last Equation S20 into the Transmission (Equation 2) and regrouping terms, we obtain the Lorenzian form,

$$T_{peak} \approx 1 - \frac{T_+ (\Delta\lambda^2/2)^2}{(\lambda - \lambda_r)^2 + (\Delta\lambda_h/2)^2} \tag{S22}$$

with a spectral broadness called Full Width at Half Maximum ($\Delta\lambda_h$)

$$\Delta\lambda_h \approx 1 - \frac{\lambda^2 (1 - a r_{21} r_{23})}{2\pi L n_g \sqrt{a r_{21} r_{23}}} \tag{S23}$$

As expected, resonant peak features in both, the Transmittance and the PL spectra get narrower by large values of the reflection coefficients r_{ij} and low attenuation losses (large a value). Other important parameter is the distance between peaks, the so-called Free Spectral Range (FSR). In this case we consider the relation of the propagation constant between two adjacent modes.

$$\beta_{m-1} \approx \beta_m - \frac{2\pi}{2L} \tag{S24}$$

Using Equation S17 and S20 for the Taylor series of β between β_{m-1} and β_m (assuming $\Delta\lambda << \lambda$), we can access $\Delta\lambda$, that permits to express the FSR as:

$$FSR = \Delta\lambda_{FRS} \approx \frac{\lambda^2}{2Ln_g} \tag{S25}$$

The parameter Finesse (F) of a resonance, is defined as the relation between the FSR and the peak broadening $\Delta\lambda_h$:

$$F = \frac{\Delta\lambda_{FSR}}{\Delta\lambda_h} \approx \frac{\pi\sqrt{ar_{21}r_{23}}}{1 - ar_{21}r_{23}} \quad \text{(S26)}$$

on another hand, it is also customary defining the quality factor Q as:

$$Q = \frac{\lambda}{\Delta\lambda_h} \approx \frac{2\pi Ln_g\sqrt{ar_{21}r_{23}}}{\lambda(1 - ar_{21}r_{23})} \quad \text{(S27)}$$

Noteworthy, resonators with high values of both F and Q factors feature low losses and high reflectance parameters, (r_{21}, r_{23} and a tends to one). Therefore, optical features of these resonators show isolated and well separated narrow peaks in their spectra.

S6. Additional results of the fitting process

Figure S2 (a) displays fundamental optical parameters showing an increase/decrease of the ratio r_{ij}/t_{ij} (i, j = 1, 2, 3) in the proximity of the absorbance edge (where a tends to zero) due to the increase of the refractive index contrast. This can explain why those resonances with maximum values of Q and F appear around this region with relative high light confinement and moderate absorption (Figure S2 (b)). This Figure shows that PEF is asymmetric and as expected is maximized when the light enters from the most transparent interface. Noteworthy F is proportional to PEF.

S7. Analogies between resonators

The same results of this study could be obtained by applying the more compact but probably less phenomenological coupled mode theory. Such a procedure is useful when the sample presents a multilayer structure[7] with more than two interfaces. It is worth to mention that the Fabry-Pérot cavity that we have analysed above is equivalent to a Whispery Gallery Mode (WGM) resonator coupled to two waveguides, where transmittance and reflectance correspond to drop and through ports response respectively. The amplitude coefficients (t and r) are related to the coupling/transmittance coefficients (with interchanged roles, represented usually by r or k,

and t respectively), the thickness of the Fabry-Pérot cavity is equal to the round-trip length (2L = 2πR for circular WGM resonators) and the refractive and group indexes are defined by effective values that depend on the cross section geometry and the excited propagation mode (see S1). Moreover, forcing r_{23} = 1 and t_{23} = 0 ($t_{add\rightarrow drop}$ = 1 and $k_{resonator\rightarrow drop}$ = 0 in a WGM cavity) the Equations become more compact and describe a simpler pass-trough WGM configuration with an only one buswaveguide. In this way, all the Equations and concepts could be directly extrapolated to a WGM resonator with one exception: the enhancement factor is lower in a WGM resonator because of the absence of a counter-propagating wave. However, the presence of surface roughness could excite the counter propagating mode and thus the formation of a stationary wave[8], with an increased enhancement factor, similar to that of the Fabry-Pérot resonator

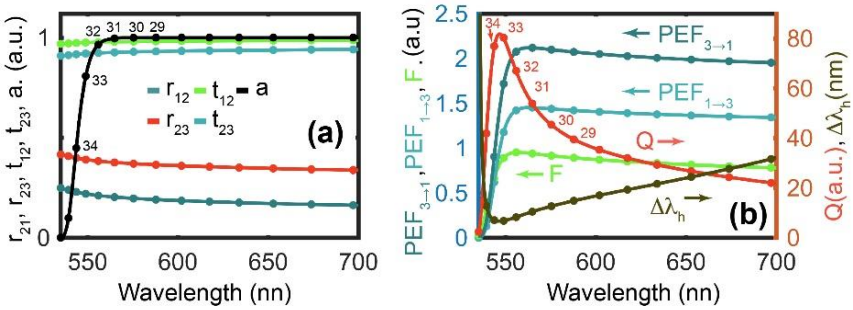

Figure S2. (a) Fundamental parameters that characterize the dielectric semi-transparent mirrors (r_{21}, r_{23}, t_{12}, t_{23}) and the term related to the absorption. (b) Resonator parameters under normal incidence/emission, derived from the fundamental optical parameters. The substrate is placed in the 2nd interface. The terms of the subindex (in) and (out) of $PEF_{in\rightarrow out}$ represent the incidence and output material respectively. The dots mark the resonant positions. The series of numbers represent the m-mode order.

S8. Material Characterization

Figure S3 shows the performed material characterization consisting in X-ray diffraction (XRD) and ultraviolet-visible spectrophotometry (UV-Vis) that corresponds to the formation of crystalline $MAPbBr_3$ Perovskite[9].

S9. Additional data

Figure S4 displays an additional spectra of OT(a) and PL(b) of a 8.65 µm-thick crystal. Comparing these curves to those of the sample of Fig4 (a,b), the spectral density of the ripples is clearly increased, or the FSR is diminished as expected(see 2.3). The real part (c) of the refractive index follows the same tendency of the imaginary part (c) for both samples. The small deviation could be due to slight differences in sample preparation, degradation as well as background and sample acquisition. In any case, the difference in the real part of the refractive index obtained from both measurements is at most around 1%, at the double fit spectral region, which is considerably smaller than the values dispersion obtained when comparing measurements from different laboratories[10].

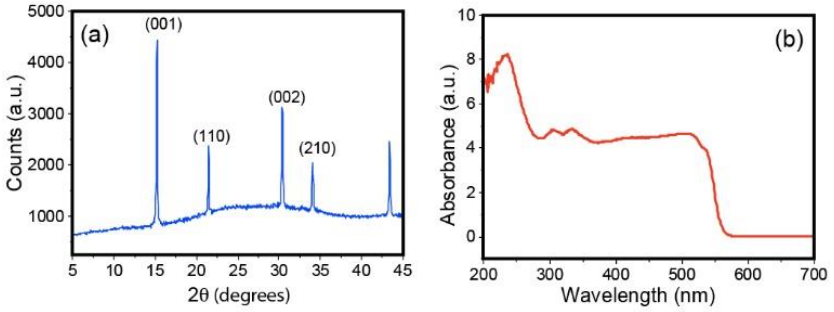

Figure S3. (a) X-ray diffraction (XRD) and (b) ultraviolet-visible spectrophotometry (UV-Vis) of the synthetized material.

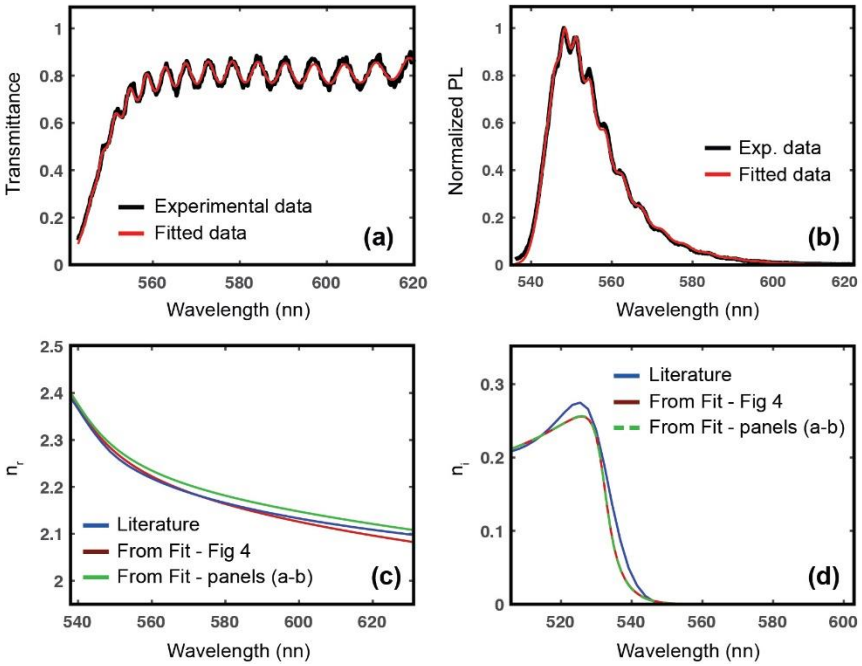

Figure S4. (a) Experimental data and (b) fitted curves for the OT and the PL spectra respectively of an additional sample. (c) Real and (d) imaginary part comparation of[11] and those extracted from the Fit of Fig 4 and pannels (a-b).

S10. Photocarrier and Thermo-optical effects

As it is mentioned in the methods, two different light sources are employed, a blue light for acquiring the PL signal and a white source for characterizing the transmittance. As a result, one is set inside the absorption spectral region and the other covers mostly the transparent one respectively. One can think that the excited photocarriers, radiative recombination and sample temperature are different for the PL and OT experiments. This could lead to a differences in the refractive index because of excited-carrier dispersion and thermo-optical effects. Although the employed power regimes could be considered so low for observing such effects the sample acts as a resonant cavity (with an enhancement lightmatter interaction) and the material could show a giant thermooptical coefficient (as another hybrid perovskite, $MAPbCl_3$[12,13]). Therefore it is not possible to fully discard refractive index deviations between PL and OT experiments. In

order to characterize this possible discrepancy, an additional parameter has been added to the fitting process. In particular, this new term registers the spectral deviation between curves. This results in around 0.03 nm that is below the monochromator resolution. As a result, possible refractive index discrepancies between OT and PL characterization could be considered as neglegible.

Notes and references

1. F. Ramiro-Manzano, N. Prtljaga, L. Pavesi, G. Pucker and M. Ghulinyan, Opt. Express, 2012, 20, 22934–22942.

2. A. Yariv and P. Yeh, Photonics, Optical Electronics in Modern Communications 2007.

3. D. A. Goldman, J. Murray and J. N. Munday, Opt. Express, 2016, 24, A925–A934.

4. X. Jin, J. Zhang, P. I. Morales-Guzman, J. Claverie and L. Razzari, Photonics North (PN), 2016, pp. 1–2.

5. S. Knabe, M. Langemeyer, F. Heidemann, R. Brüggemann and G. H. Bauer, Progress in Photovoltaics: Research and Applications, 2011, 19.

6. O. Neumann, R. Brüggemann, N. Könne and G. H. Bauer, physica status solidi (a), 2014, 211, 1128–1133.

7. J. M. Luque-Raigon, J. Halme and H. Miguez, Journal of Quantitative Spectroscopy and Radiative Transfer, 2014, 134, 9 – 20.

8. S. Biasi, F. Ramiro-Manzano, F. Turri, P. Larré, M. Ghulinyan, I. Carusotto and L. Pavesi, IEEE Photonics Journal, 2019, 11, 1–14.

9. J. H. Heo, D. H. Song and S. H. Im, Advanced Materials, 26, 2014, 8179–8183.

10. M. A. Martín, Doctoral thesis, Inorganic Chemistry Department Faculty of Chemistry, University of Seville, 2018, p. 46.

11. J.-S. Park, S. Choi, Y. Yan, Y. Yang, J. M. Luther, S.-H. Wei, P. Parilla and K. Zhu, The Journal of Physical Chemistry Letters, 2015, 6, 4304–4308.

12. H. Tahara, T. Aharen, A. Wakamiya and Y. Kanemitsu, Advanced Optical Materials, 2018, 6.

13. T. Handa, H. Tahara, T. Aharen and Y. Kanemitsu, Science Advances, 2019, 5.

SECCIÓN 3.3

GROOVES-ASSISTED SOLUTION GROWTH OF LEAD BROMIDE PEROVSITE ALIGNED NANOWIRES: A SIMPLE METHOD TOWARDS PHOTOLUMINESCENT MATERIAL WITH GUIDING LIGHT PROPERTIES

Isabelle Rodriguez, Roberto Fenollosa, Fernando Ramiro-Manzano, Rocío García-Aboal, Pedro Atienzar, and Francisco J. Meseguer.

Mater. Chem. Front. 2019, 3, 1754

DOI: 10.1039/c9qm00210

GROOVES-ASSISTED SOLUTION GROWTH OF LEAD BROMIDE PEROVSITE ALIGNED NANOWIRES: A SIMPLE METHOD TOWARDS PHOTOLUMINESCENT MATERIAL WITH GUIDING LIGHT PROPERTIES

Isabelle Rodriguez*[a], Roberto Fenollosa[a], Fernando Ramiro-Manzano[a], Rocío García-Aboal[a], Pedro Atienzar[a], and Francisco J. Meseguer[a].

[a]Instituto de Tecnologiía Química (CSIC-UPV), Universitat Politècnica de València, Av. Los Naranjos s/n, 46022 Valencia, Spain.

Abstract

High refractive index nanowires are very attractive because of their waveguiding properties and their multiple applications. In this sense, metal halide Perovskites, an emerging and appealing optoelectronic material, have also been tailored in nanowires structure. Here we present an easy, low-cost and versatile method that has allowed to achieve nanowires of controlled and uniform width. The method has been applied here to all-inorganic and hybrid lead bromide Perovskite ($CsPbBr_3$ and $CH_3NH_3PbBr_3$ respectively) materials. The procedure is based on the spin coating of precursors solutions, at room temperature, on PDMS replica of the periodic grooves and lands of commercially available Compact Disc (CD) or Digital Versatil Disc (DVD) polycarbonate plates. The method can be applied for the synthesis of others material nanowires before being transferred onto other substrates. The obtained $CsPbBr_3$ and $CH_3NH_3PbBr_3$ nanowires exhibit high photoluminescence and guiding light properties along the material.

1. INTRODUCTION

Nanowire-like nanostructured semiconductors have raised a great interest since they were discovered, two decades ago, as they exhibit unique electrical, and optical properties, making them suitable for applications in optoelectronics, photonic devices or energy generation[1,2]. Particularly, high refractive index nanowires can be used for confining and guiding light at the nano and micro-scale. That is the reason why they have become elements of paramount importance in

photonics, where a technological revolution is expected to happen, similarly to microelectronics in the past century. So far, different base materials have been used to develop nanowires, namely II-VI (ZnO), III-V (GaAs, InP, InSb, GaN, etc)[2], IV (Si, Ge)[3-5] semiconductors, and more recently metal Halide Perovskites could be shaped in nanowire structures.[6,7] That was a very important achievement because metal halide Perovskites (AMX_3) have emerged as an appealing optoelectronic material[8], with a high photoluminescence efficiency[9-13], high optical absorption[14], low charge carrier recombination coupled with high hole and electron mobility15 that make them very suitable for many optoelectronic applications16 such as solar cells devices[17-19], light emitting diodes[16,20-22] and optically pumped lasers[16,21,23-25]. Moreover, they can be easily synthetized by low-temperature solution processing and the band gap can be tuned through halide substitution or halide mixtures[26] and also by the divalent metal cation replacement.[27] However, in any case, and particularly for Perovskites materials, the shape of the nanowires somehow follows crystalline directions of growth, thus producing nanowires of a given dimension with triangular, or square like shaped cross sections, far from the cylindrical shape of conventional optical fibers. These geometrical parameters play a key role because they determine how light propagates through the nanowire: the losses, and the interaction of light with the nanowire itself and with the surrounding material. Therefore, in spite of the remarkable results obtained so far through chemical vapor deposition[28-37] or via solution phase synthesis[23, 38-51], it is very important to explore new routes that allow tuning the shape and dimensions of 1D Perovskite structures. In this way, recently $MAPbX_3$ nanowires arrays have been grown using PDMS rectangular groove templates obtained from replication of silicon masters previously prepared by photolithography[52]. Herein, we propose, a simple and low-cost method to obtain metal halide Perovskite nanowires based on the confinement of precursor solutions in submicrometer size grooves imprinted on the polycarbonate (PC) sheet of commercial recordable DVD or CD plates. Such method of preparation not only allows to obtain nanowires with homogeneous width and shape but also to choose between several width dimensions depending of the employed template. Indeed, as described below,

DVD and CD structures can provide plates of different grooves size and distribution.

2. RESULTS AND DISCUSSION

Recordable DVDs are made of two PC plates patterned with a spiral distribution of grooves and lands, the top one presenting the complementary geometry of the bottom one (See Fig. S1 ESI†). Due to the incompatibility of PC with most of the employed solvents for the synthesis of Perovskites, here, this kind of support cannot be used directly as template. Therefore, patterned Polydimethylsiloxane (PDMS) substrates were prepared via molding procedure of the lands and grooves array of DVD or CD polycarbonate masters. Fig. 1 shows an illustrative general scheme of the preparation and the features of the PDMS templates. The procedure to achieve the corrugated PC substrates is described in the experimental section. The PDMS replica were prepared by pouring the pre-polymer liquid (Sylgard 184 Silicone Elastomer Kit) over the PC plates, and then letting it cure at 60°C. After mechanically peeling it off from the master, the negative PDMS mold of CD or DVD was obtained (Fig. S2, ESI†). In order to enhance the wettability of the PDMS substrate surface, O_2 plasma treatment was used before the next step. Then, precursor solutions of metal halide Perovskite were drop-casted and spin-coated on the patterned PDMS substrates previously hydrophilized. With an adequate spin speed and time, upon solvent evaporation, nanowires are formed into the grooves of the template. Fig. 2 summarizes the different stages of the procedure. Hence, it can be seen that is a quite low cost and a versatile method that could be used for the preparation of nanowires of any other material from precursors solutions. We have applied this method for synthesizing both hybrid and all-inorganic lead halide perovskite nanowires. The first one, with the general structure $MAPbX_3$ (MA= Methylammonium, X= Cl, Br, I) has been largely studied and their efficiency proved.[18,53] Although some halide derivative seems to show higher stability, a drawback of organic-inorganic halide Perovskites is both, their sensitivity to moisture and O_2[54,55] as well as their thermal instability[56,57]. Theses disadvantages could be mitigated by the employ of all-inorganic lead halide Perovskites. In this sense, Cesium based lead halide Perovskites seem to combine performance

and stability[58-60] and moreover they tend to show a high defect tolerance.[61] Here, $CsPbBr_3$ Perovskite nanowires were synthesized starting from a stoichiometric mixture of dissolution of precursors, CsBr and $PbBr_2$, in Dimethyl Sulfoxide (DMSO).

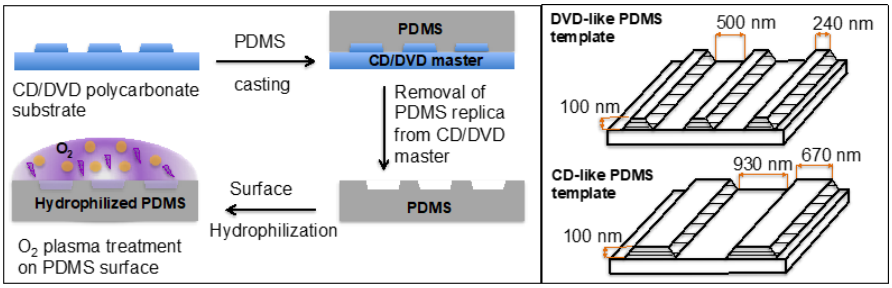

Figure 1. Schematic illustration of the preparation and features of the PDMS template.

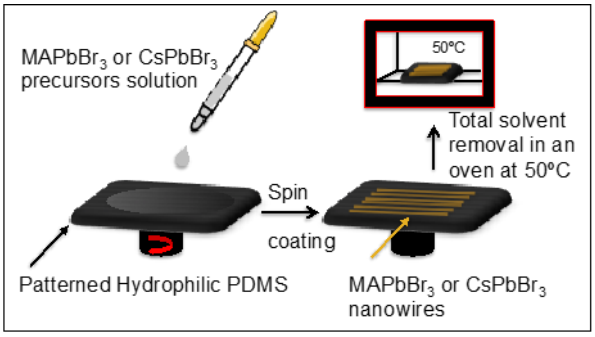

Figure 2. Preparation procedure of $MAPbBr_3$ and $CsPbBr_3$ nanowires into the grooves of hydrophilized PDMS templates obtained by replication of CD o DVD profiles.

Concerning Methylammonium Lead tribromide ($MAPbBr_3$) nanowires, dissolutions of CH_3NH_2Br and $PbBr_2$ in DMF were employed. A drop of the precursors solution was deposited onto a patterned PDMS stamp (1 cm^2), previously hydrophilized by O_2 plasma treatment. Then the stamp was spin-coated until solvent evaporation and formation of an orange/yellowish material occurred. Finally, the samples were kept at 50°C overnight for a complete removal of any rest of solvent. For the sake of clarity, only results concerning $CsPbBr_3$ material will be shown here (for $MAPbBr_3$ nanowires see supporting information). As it can be seen in the optical and electronic microscopy images in Fig. 3, the growth of $CsPbBr_3$ nanowires takes place into the

well-aligned periodic grooves of the PDMS substrates, which correspond to DVD and CD replica patterns.

Precursors solutions fill the grooves of the templates resulting in shape-controlled nanowires upon solvent evaporation. Therefore, the widths are uniform, with values, in the examples shown in fig. 3, of 500 nm and 930 nm for DVD-like and CD-like PDMS templates respectively. Nanowires of several dozen microns of length could be achieved. The cross section area of the obtained nanowires is uniform and it is determined by the size and shape of the patterned grooves in the PDMS template. Fig. 3d and Fig. 3e show Field-Emission Scanning Electronic Microscopy (FESEM) images of a transversal cut of a $CsPbBr_3$ nanowires sample realized by FIB (focused ion beam) milling after sputtered Au or/and Pt coatings to reduce samples charging and beam damage. It can be seen that the material has been conformed to the groove of the template by the spin process to form polycrystalline $CsPbBr_3$ nanowires. A similar behavior is observed for $MAPbBr_3$ material in Fig. S3 (ESI†). Therefore, nanowires features could be tuned by changing the template (and the master) characteristics as well as the precursor solution employed.

The X-ray diffraction (XRD) pattern of the $CsPbBr_3$ nanowires (Fig. 3c) shows 2 strong diffraction peaks with maximum at 2 theta angles of 15.46° and 31°, that match respectively to the (110) and (220) lattice planes of an orthorhombic Perovskite structure obtained at room temperature.[38]

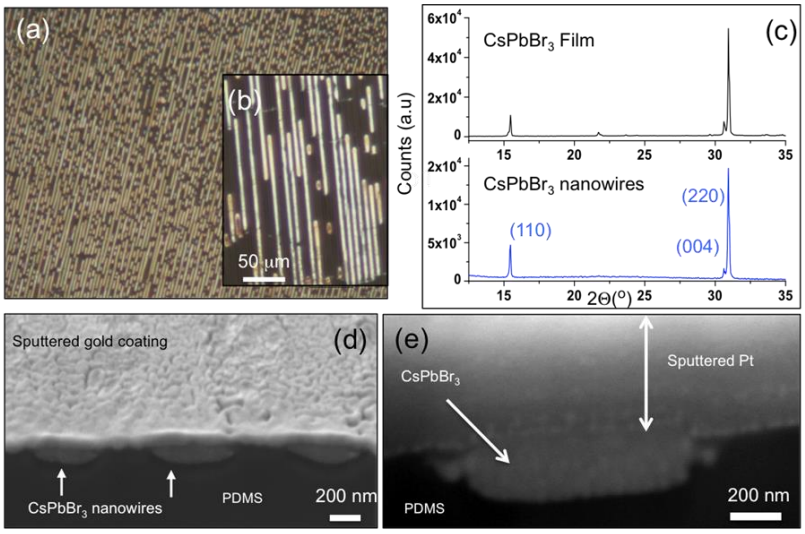

Figure 3. Polycrystalline $CsPbBr_3$ nanowires characteristics. Optical images of $CsPbBr_3$ Perovskite nanowires obtained on (a) DVD and (b) CD replica PDMS substrates. (c) XRD pattern of $CsPbBr_3$ nanowires and of a $CsPbBr_3$ film structure. (d) FESEM image of a lateral view of a sample of $CsPbBr_3$ nanowires (obtained on PDMS replica of DVD structure) cut by FIB milling perpendicularly to the surface and coated with sputtered gold. (e) FESEM image of the cross section of a $CsPbBr_3$ nanowire grown on PDMS replica of CD structure (Sputtered Pt coating was used to cover the sample before the FIB milling).

In order to confirm the feasibility of the synthesized material to yield photoluminescence (PL) and see if the emitted signal could be guided along the 1D structures, we performed confocal PL spectroscopy on single nanowires and varied the distance between the collection and the excitation points. Specifically, the collection point was fixed at one end of the nanowire so as to acquire the scattered light at that position, while the excitation point was shifted along it. Collection and excitation could be accomplished by using 20 x 0.4 NA objectives in both cases, mounted in forward configuration (Fig. S4 (ESI†)). They allow focusing and collecting light in areas of about 1 or 2 micrometers in diameter. As excitation source we used light of a 405 nm laser, with varying powers around 0.1 mW.

Fig. 4a, 4b, 4c, and 4d show optical microscopy images, recorded by the camera of the set up of Fig. S4 (ESI†), of two neighboring

isolated $CsPbBr_3$ nanowires supported on a PDMS replica of a DVD profile substrate (Fig. 3a). For the sake of simplifying the experimental procedure, we chose for the Photoluminescence (PL) measurements the shortest one, which is about 12 µm in length (see the color optical image at the top right of the fig. 4). The images correspond to different collection-excitation distances (d_{E-C}), which have been indicated under each picture. The white spots on the nanowire correspond to PL signals produced by the excitation laser. The intensities between the images are not comparable due to both camera autofocus and laser intensity adjustment. The bottom end of the nanowire corresponds to the collection point. Therefore, at d_{E-C} = 0 µm (Fig. 4 a), only one spot appears at that point. The other images, corresponding to d_{E-C} values different from zero (Fig. 4 b, c, d) show two spots, one coming from the direct excitation of laser upwards and another one, which is less intense, at the collection point. We associated the last signal to that light which is emitted at the excitation point where the laser is focused and travels towards the end of the nanowire, where it is scattered in all directions. Of course, light should travel to the other end of the nanowire as well, but it could not be always recorded by the camera, particularly for long distances from the excitation point. Fig. 4 shows as well the PL spectral evolution (blue, green, black and cyan curves) as a function of the collection-excitation distance (d_{E-C}).

In general, the intensity of light at the collection point decreases as d_{E-C} increases as previously reported in others studies[31,62-64]. Therefore, we adjusted the integration time of the detector and the power of the excitation laser so as to achieve a reliable detection and to obtain a qualitative optical behavior of the material. For this reason and for the sake of comparison, we have normalized all the spectra. At d_{E-C} = 0 (curve 'a', blue line), a Gaussian like peak with some asymmetry appears with its maximum centered at about 513 nm. As the excitation beam moves away from the collection point, this shape changes substantially. The spectra broaden and new features appear at longer wavelengths. We decomposed each spectrum into two peaks and associated them to two distinct effects by means of a fitting procedure (red dashed curves). Firstly, spectrum 'a' represents the direct-emission of a small portion of the material. The fit of this peak was

achieved by using the model described in ref. 65, and assuming a thickness of 106 nm that corresponds to the nanowire height. This permits to obtain the bulk extinction coefficient of the synthetized material. We call this peak as P0. Secondly, the other spectra (b, c, d) include the incoherent addition of P0 with some attenuation coefficient and another peak, P1 from now on, centered at longer wavelengths. We hypothesize that P1 arises from the guiding phenomenon of light from the excitation to the collection spot. This peak is red-shifted in comparison to P0 because the absorption coefficient is higher for shorter wavelengths within the PL emission of the material. P1 was fitted to the model mentioned above taking into account the $d_{E\text{-}C}$ value for each case. The obtained extinction coefficient from this fit takes, however, a lower effective value than that of the bulk one, regardless of $d_{E\text{-}C}$ and wavelength. We attributed this effect to the guiding mode field profile that probably forces the light to travel partially outside the nanowire core. It can be seen in figure 4 how the fitted spectrum "c" for example can be decomposed into two spectra, P0 and P1.

Finally, we would like to discuss about the presence of P0 at $d_{E\text{-}C}$'s different from zero. Pazos-Outón et al.[63] argued in a similar experiment that this kind of effect comes from a photon absorption-reemission phenomenon. However, we think that because the acquired signal is very weak, other effects such as a spurious acquisition of unguided PL from unwanted reflections or spurious excitation by the tail of the laser spot should not be disregarded. In any case, P0 almost disappears for $d_{E\text{-}C} > 12$ µm. Wider $CsPbBr_3$ nanowires (Fig. 3b and 3e), obtained by using the CD replica as template (Fig. 1, below right) yielded similar results to those of their narrower counterparts (Fig. S5, ESI†). However, the peak P0, that corresponds to the PL at $d_{E\text{-}C} = 0$ is centered in this case at about a slightly longer wavelength, λ=525 nm, in spite of being the same material.

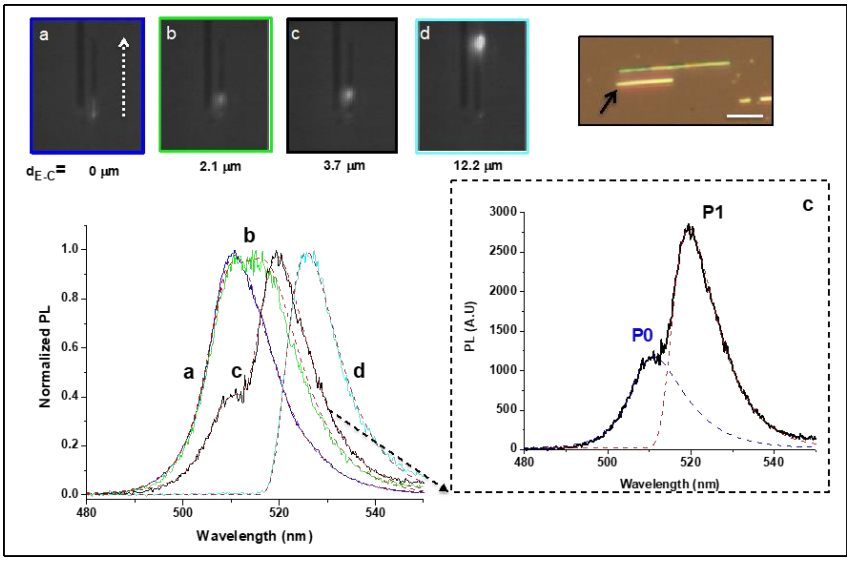

Figure 4. a, b, c, and d: optical images recorded by the camera of the set up described in Fig. S4 (ESI†) of two neighboring isolated $CsPbBr_3$ Perovskite nanowires obtained into a groove of a DVD based PDMS substrate. The chosen nanowire for PL experiments is indicated by a black arrow in the optical microscopy image at the top right of the figure (scale bar: 10 µm). The white spots on the images (a, b, c, d) correspond to PL signals produced by the excitation laser for several distances, d_{E-C}, specified under each image, between excitation and collection (bottom end of the nanowire) points. The intensities between the images are not comparable because they were recorded with different sensitivity conditions of the camera. Down Left of the figure: The solid color curves correspond to the PL spectra measured for each d_{E-C} case (same color and label as camera image frames), and the dashed red curves correspond to fits according a theoretical model described in ref. 65. As an example, the plot at the right side shows that the fitted spectrum "c" results from the overlap of two peaks, P0 and P1 (blue and red dashed curves), corresponding respectively to the direct emission of the nanowire and the guided light emission from excitation to collection area.

In fact, the origin of this red shift of the P0 peak comes from a higher thickness of the obtained nanowires and it is in accordance with previous published results.34 Indeed, from the fit of the spectrum, the thickness of the $CsPbBr_3$ nanowires obtained on PDMS replica of CD substrate is found to be 110 nm. In the same way, photoluminescence of $CsPbBr_3$ and $MAPbBr_3$ film samples is also red shifted in comparison with the nanowires of about 100 nm of thickness. (see Fig. S6, ESI†).

Similar optical studies have been realized on $MAPbBr_3$ Perovskite nanowires and can be seen in supporting information file. (Fig. S7 (ESI†)).

Preliminarily test to transfer nanowires onto other substrates have been performed. Fig. S8 (ESI†) shows an optical image of $MAPbBr_3$ nanowires on ITO glass substrate.

3. EXPERIMENTAL SECTION

DVD and CD polycarbonate substrates. Recordable DVDs are composed of two plates of polycarbonate that were mechanically separated. The bottom one PC sheet is patterned with a spiral periodic distribution of grooves (see Fig S1 of the ESI†) coated with a photosensible dye (where the data can be recorded by a laser beam) and a metallic film. The later one was peeled off by means of an adhesive tape. Then a mixture of water:ethanol (1:1, v/v) was employed to remove the dye coating as described in a previously work66 The top plate of the DVD presents the complementary profile of the bottom one, providing therefore a Polycarbonate template with wider grooves with less separation between them.

The CD structure is only composed of one plate of polycarbonate patterned with grooves periodically separated (Fig. S2, ESI†) also coated with a dye and a reflective layer that were removed through similar method than the one used for DVD and described above.

PDMS replica molding. Sylgard 184 elastomer kit prepolymer was mixed with the curing agent (10:1 ratio) and degassed under vacuum until removing all air bubbles. The PDMS mixture was then poured on top of the CD or DVD polycarbonate substrates placed in a glass Petri dish. After a curing process of 2h at 60°C, PDMS layer was mechanically peeled off from the PC plate.

$CsPbBr_3$ and $MAPbBr_3$ precursors solutions preparation. CsBr, MABr, $PbBr_2$, the solvents Dimethylformamide (DMF) and Dimethylsulfoxide (DMSO) were obtained from Sigma-Aldrich. $CsPbBr_3$ precursors solution was prepared by dissolving a stoichiometric mixture of 0.45M CsBr and 0.45M $PbBr_2$ in DMSO prepared at 50°C.

For $MAPbBr_3$ precursors solution, 1M MABr and 1M $PbBr_2$ in DMF was employed and mixed in a 1:1 ratio.[67]

$CsPbBr_3$ and $MAPbBr_3$ precursors solutions preparation. CsBr, MABr, $PbBr_2$, the solvents Dimethylformamide (DMF) and Dimethylsulfoxide (DMSO) were obtained from Sigma-Aldrich. CsPbBr3 precursors solution was prepared by dissolving a stoichiometric mixture of 0.45M CsBr and 0.45M $PbBr_2$ in DMSO prepared at 50°C. For $MAPbBr_3$ precursors solution, 1M MABr and 1M $PbBr_2$ in DMF was employed and mixed in a 1:1 ratio.[67]

Spin-coating experiments. They were realized on an Ossila spin coater system. Speeds of 2000 rpm (rotation per minute) and of 3000 rpm were used for $MAPbBr_3$ and $CsPbBr_3$ respectively.

Optical and Electronic microscopy. Optical images were taken by a Nikon Eclipse LV100 microscope. Field emission scanning electron microscopy (FESEM) images were obtained on a Carl Zeiss Ultra 55 instrument and the Focused Ion Beam (FIB) milling experiments were performed on a Carl Zeiss AURIGA compact FIB-FESEM workstation.

X-ray Diffraction. X-ray diffraction patterns were recorded on a Bruker D8 Advance A25 X-ray diffractometer operating at 45kV and 80 mA Cu Kα radiation (λ= 1.5406Å) equipped with a LYNXEYE XE 1-D detector

Photoluminescence measurements. The optical set-up scheme is represented in the Fig. S4 of the supporting information file (ESI†). A more detailed description of the components of the home built set-up can be found in the reference 68.

CONCLUSIONS

In conclusion, here we have shown a simple solution-based and low cost method of fabrication of nanowires with controlled and uniform size at room temperature. The process includes PDMS replica of DVD and CD profiles as substrates and it produces an array of aligned nanowires with a define width. We have applied this method to obtain all-inorganic lead halide $CsPbBr_3$ and hybrid $MAPbBr_3$ Perovskite nanowires starting from precursors solutions. However,

such procedure can be employed to achieve other material nanowires that can also be transferred to other suitable substrates.

The optical studies of all inorganic and hybrid lead Perovskite nanowires show the typical PL signal for these materials. Moreover, it can be excited at any point of the nanowire and guided along it towards its ends. Transport of light has been observed along the material for more than 12 μm. Experimental results are supported by theoretical simulation.

Acknowledgements

The authors would like to gratefully acknowledge financial support from Spanish Ministry of Economy and Competitiveness (MIMECO) (Severo Ochoa (SEV-2016-0683), MAT2015-69669-P projects) and Generalitat Valenciana (Prometeo II/2017/026 Excellency project). P.A. acknoledges the Fundación Ramón Areces (XVII Concurso Nacional para la adjudicación de Ayudas a la Investigación en Ciencias de la Vida y de la Materia) for its funding. F. R-M thanks the financial contribution of the Spanish Ministry of Economy and Competitiveness (MIMECO) through the program for young researchers support (TEC 2015 2015-74405-JIN). Finally, IR also thanks the Electron Microscopy Service of the Universitat Politècnica de València for their support in FESEM images acquisition and FIB milling, as well as Ana Moreno for her help in templates preparation.

Notes and references

1. Semiconductor nanowires: From next-generation Electronics to Sustainable Energy; W. Lu, J. Xiang, Eds; RSC Smart Materials Series, 2015

2. Semiconductor Nanowires, Materials, Synthesis, Characterization and Applications, J. Arbiol, Q. Xiong, Eds; Woodhead Publishing, 2015

3. K. Q. Peng, X. Wang, L. Li, Y. Hu, S.T. Lee, Nano today, 2013, 8, 75

4. M. Mikolajick, W. M. Weber, Silicon Nanowires in Anisotropic Nanomaterials, Q. Li, Eds; Springer, 2015, pp.1-25

5. M. Hasan, M. F. Z. Huq, H. Mahmood, Springer Plus, 2013, 2, 151

6. Z. Liu, Y. Mi, X. Guan, Z. Su, X. Liu, T. Wu, Adv. Optical Mater. 2018, 6, 1800413

7. Y. Fu, H. Zhu, J. Chen, M. P. Hautzinger, X.-Y Zhu and S. Jin, Nature Reviews Materials, 2019, 4, 169

8. J. S. Manser, J. A. Christians, P. V. Kamat, Chem. Rev. 2016, 116 (21), 12956

9. N. Kitazawa, Y. Watanabe, Y. Nakamura, J. Mater. Sci. 2002, 37, 3585

10. J. Albero, H. Garcia, J. Mater Chem. C, 2017, 5, 4098

11. G. Longo, M.-G. La-Placa, M. Sessolo, H. J. Bolink, ChemSusChem, 2017, 10, 3788

12. J. M. Richter, M. Abdi-Jalebi, A. Sadhanala, M. Tabachnyk, J. P. H. Rivett, L. M. Pazos-Outón, K. C. Gödel, M. Price, F. Deschler, R. H. Friend, Nature Comm. 2016, 7, 13941

13. F. Deschler, M. Price, S. Pathak, L. E. Klintberg, D.-D. Jarausch, R. Higler, S. Hüttner, T. Leijtens, S. D. Stranks, H. J. Snaith, M. Atatüre, R. T. Phillips, R. H. Friend, J. Phys. Chem., 2014, 5, 1421

14. S. De Wolf, J. Holvsky, S.-J. Moon, P. Löper, B. Niesen, M. Ledinsky, F.-J. Haug, J.-H. Yum, C. Ballif, J. Phys. Chem. Lett. 2014, 5, 1035

15. C. Wehrenfennig, G. E. Eperon, M. B. Johnston, H. J. Snaith, L. M. Herz, Adv. Mater., 2014, 26, 1584

16. B. R. Sutherland, E. H. Sargent, Nature Photonics, 2016, 10, 295

17. D. Bi, W. Tress, M. I. Dar, P. Gao, J. Luo, C. Renivier, K. Schenk, A. Abate, F. Giordano, J-P. Correa Baena, J.-D. Decoppet, S. M. Zakeeruddin, M. K. Nazeeruddin, M. Grätzel, A., Sci. Adv. 2016, 2 (1), e1501170

18. H. S. Jung, N-G. Park, Small 2015, 11 (1), 10-25

19. W. Zhang, G. E. Eperon, H. J. Snaith, Nature Energy, 2016, 1, 16048

20. Y-H. Kim, C. Wolf, Y.-T. Kim, H. Cho, W. Kwon, S. Do, A. Sadhanala, C. G. Parl,

S.-W. Rhee, S. H. Im, R. H. Friend, T.-W. Lee, ACS Nano 2017, 11, 6586-6593

21. S. A. Veldhuis, P. P. Boix, N. Yantara, M. Li, T.C. Sum, N. Mathews, S. G. Mhaisalkar, Adv. Mater., 2016, 28, 6804-6834

22. N. Wang, L. Cheng, R. Ge, S. Zhang, Y. Miao, W. Zou, C. Yi, Y. Sun, Y. Cao, R. Yang, Y. Wei, Q. Guo, Y. Ke, M. Yu, Y. Jin, Y. Liu, Q. Ding, D. Di, L. Yang, G. Xing, H. Tian, C. Jin, F. Gao, R. H. Friend, J. Wang, W. Huang, Nature Photonics, 2016, 10, 699-704

23. H. Zhu, Y. Fu, F. Meng, X. Wu, Z. Gong, Q. Ding, M. V. Gustafsson, M. T. Trinh, S. Jin, X-Y. Zhu, Nature Materials, 2015, 14, 636-642

24. J. R. Harwell, G. L. Whitworth, G. A. Turnbull, I. D. W. Samuel, Scientific Reports, 2017, 7, 11727

25. Y. Jia, R. A. Kerner, A. J. Grede, B. P. Rand, N. C. Giebink, Nature Photonics, 2017, 11, 784-788

26. G. Xing, N. Mathews, S. S. Lim, N. Yantara, X. Liu, D. Sabba, M. Gratzel, S. Mhaisalkar, T. C Sum, Nature Materials, 2014, 13, 476-480

27. S. Zhang, P. Audebert, Y. Wei, A. Al Choueiry, G. Lanty, A. Bréhier, L. Galmiche, G. Clavier, C. Boissière, J.-S. Lauret, E. Deleporte, Materials, 2010, 3, 3385-3406

28. M. Shoaib, X. Zhang, X. Wang, H. Zhou, T. Xu, X. Wang, X. Hu, H. Liu, X. Fan, W. Zheng, T. Yang, S. Yang, Q. Zhang, X. Zhu, L. Sun, A. Pan, J. Am. Chem. Soc., 2017, 139, 15592-15595-15595

29. J. Xing, X. F. Liu, Q. Zhang, S. T. Ha, Y. W. Yuan, C. Shen, T. C. Sum, Q. Xiong, Nano Lett., 2015, 15 (7), 4571−4577.

30. L. Gu, M. M. Tavakoli, D. Zhang, Q. Zhang, A. Waleed, Y. Xiao, K.-H. Tsui, Y. Lin, L. Liao, J. Wang, Z. Fan, Adv. Mater., 2016, 28 (44), 9713−9721.

31. Y. Wang, X Sun, R. Shivanna, Y. Yan, Z. Chen, Y. Guo, G-C. Wang, E. Wertz, F. Deschler, Z. Cai, H. Zhou, T-M. Lu, J. Shi, Nano lett., 2016, 16, 7974-7981.

32. K. Park, J. W. Lee, J. D. Kim, N. S. Han, D. M. Jang, S. Jeong, J. Park, J. K. J. Song, Phys. Chem. Lett., 2016, 7 (18), 3703−3710

33. J. Chen, Y. Fu, L. Samad, L. Dang, Y. Zhao, S. Shen, L. Guo, S. Jin, Nano Lett., 2017, 17, 460-466

34. H. Zhou, S. Yuan, X. Wang, T. Xu, X. Wang, H. Li, W. Zheng, P. Fan, Y. Li, L. sun, A. Pan, ACS Nano, 2017, 11 (2) 1189-1195

35. X. Wang, H. Zhou, S. Yuan, W. Zheng, Y. Jiang, X. Zhuang, H. Liu, Q. Zhang, X. Zhu, X. Wang, A. Pan, Nano Research, 2017, 10 (10), 3385-3395

36. E. Oksenberg, E. Sanders, R. Popovitz-Biro, L. Houben, E. Joselevich, Nanolett., 2018, 18 (1), 424-433

37. J. Chen, Z. Luo, Y. Fu, X. Wang, K. J. Czech, S. Shen, L. Guo, J. C. Wright, A. Pan and S. Jin, ACS Energy Lett., 2019, 4 (5), 1045

38. S. W. Eaton, M. Lai, N.A. Gibson, A. B. Wong, L. Dou, J. Ma, L-W Wang, S. R. Leone, P. Yang, PNAS, 2016, 113, 8, 1993-1998

39. M. M. Tavakoli, A. Waleed, L. Gu, D. Zhang, R.Tavakoli, B. Lei, W. Su, F. Fang, Z. Fan, Nanoscale, 2017, 9 (18), 5828−5834

40. J.-H. Im, J. Luo, M. Franckevičius, N. Pellet, P. Gao, T. Moehl, S. M. Zakeeruddin, M. K. Nazeeruddin, M. Grätzel, N.-G. Park, Nano Lett., 2015, 15 (3), 2120−2126

41. A. B. Wong, M. Lai, S. W. Eaton, Y. Yu, E. Lin, L. Dou, A. Fu, P. Yang, Nano Lett., 2015, 15 (8), 5519−5524

42. H. Deng, D. Dong, K. Qiao, L. Bu, B. Li, D.Yang, H.-E.Wang, Y. Cheng, Z. Zhao, J. Tang, H. Song, Nanoscale, 2015, 7 (9), 4163−4170.

43. M. Spina, E. Bonvin, A. Sienkiewicz, B. Náfradi, L. Forró, E. Horváth, Sci. Rep., 2016, 6 (1), 19834

44. M. J. Ashley, M. N. O'Brien, K. R. Hedderick, J. A. Mason, M. B. Ross, C. A. Mirkin, J. Am. Chem. Soc., 2016, 138 (32), 10096−10099

45. W. Deng, L. Huang, X. Xu, X. Zhang, X. Jin, S.-T. Lee, J. Jie, Nano Lett., 2017, 17 (4), 2482−2489

46. S. Wang, K. Wang, Z. Gu, Y. Wang, C. Huang, N. Yi, S. Xiao, Q. Song, Adv. Optical Mater., 2017, 5, 1700023.

47. A. A. Petrov, N. Pellet, J.-Y. Seo, N. A. Belich, D. Y. Kovalev, A. V. Shevelkov, E. A. Goodilin, S. M. Zakeeruddin, A. B.Tarasov, M. Graetzel, Chem. Mater., 2017, 29 (2), 587−594

48. Y. Fu, H. Zhu, C. C. Stoumpos, Q. Ding, J. Wang, M. G. Kanatzidis, X. Zhu, S. Jin, ACS Nano, 2016, 10 (8), 7963-7972.

49. D. Zhang, S. W. Eaton, Y. Yu, L. Dou, P. Yang, J. Am. Chem. Soc., 2015, 137, 9230-9233

50. D. Zhang, Y. Yang, Y. Bekenstein, Y. Yu, N. A. Gibson, A. B. Wong, S. W. Eaton, N. Kornienko, Q. Kong, M. Lai, A. P. Alivisatos, S. R. Leone, P. Yang, J. Am. Chem. Soc., 2016, 138, 13155-13158

51. Y. Fu, H. Zhu, A. W. Schrader, D. Liang, Q. Ding, P. Joshi, L. Hwang, X-Y. Zhu, S. Jin, Nano Lett., 2016, 16, 1000-1008

52. P. Liu, X. He, J. Ren, Q. Liao, J. Yao, H. Fu, ACS Nano, 2017, 11, 5766-5773

53. M. M. Lee, J. Teuscher, T. Miyasaka, T. N. Murakami, H. J. Snaith, Science, 2012, 338, 643-647

54. G. Niu, X. Guo, L. Wang, J. Mater. Chem. A, 2015, 3, 8970

55. T. A Berhe, W.-N. Su, C.-H. Chen, C.-J. Pan, J.-H. Cheng, H. –M. Chen, M.-C. Tsai, L.-Y. Chen, A. A. Dubale, B.-J. Hwang, Energy Environ. Sci., 2016, 9, 323

56. B. Brunetti, C. Cavallo, A. Ciccioli, G. Gigli, A. Latini, Scientific Reports, 2016, 6, 31896

57. B. Conings, J. Drijkoningen, N. Gauquelin, A. Babayigit, J. D'Haen, L. D'Oliestlaeger, A. Ethirajan, J. Verbeeck, J. Manca, E. Mosconi, F. De Angelis, H. -G. Boyen, Adv. Energy Mater., 2015, 5, 1500477

58. M. Kulbak, S. Gupta, N. Kedem, I. Levine, T. Bendikov, G. Hodes, D. Cahen, J. Phys. Chem. Lett., 2016, 7, 167-172

59. M. Saliba, T. Matsui, J-Y. Seo, K. Domanski, J-P Correa Baena, M. K. Nazeeruddin, S. M. Zakeeruddin, W. Tresss, A. Abate, A. Hagfeldt, M. Gratzel, Energy Environ. Sci., 2016, 9, 1989-1997

60. R. F. Service, Science, 2016, 351, 113-114

61. J. Kang, L.W. Wang, J. Phys. Chem. Lett., 2017, 8, (2) 489-493

62. Y. Wang, X. Sun, R. Shivanna, Y. Yang, Z. Chen, Y. Guo, G-C Wang, E. Wertz, F. Deschler, Z. Cai, H. Zhou, T-M. Lu, J. Shi, NanoLett., 2016, 16, 7974-7981

63. L. M. Pazos-Outón, M. Szumilo, R. Lamboll, J. M. Richter, M. Crespo-Quesada, M. Abdi-Jalebi, H. J. Beeson, M. Vruéinié, M. Alsari, H. J. Snaith, B. Ehrler, R. H. Friend, F. Deschler, Science, 2016, 351 (6280), 1430-1433

64. I. Dursun, Y. Zheng, T. Guo, M. De Bastiani, B. Turedi, L. Sinatra, Md A. Haque, B. Sun, A. A. Zhumekenov, M. I. Saidaminov, F. P. Garcia de Arquer, E. H. Sargent, T. Wu, Y. N. Garstein, O. M. Bakr, O. F. Mohammed, A. V. Malko, ACS Energy Lett., 2018, 3, 1492-1498

65. F. Ramiro-Manzano, R. García-Aboal, R. Fenollosa, S. Basi, I. Rodriguez, P. Atienzar, F. Meseguer, Optical properties of organic/inorganic perovskite microcrystals through the characterization of Fabry-Pérot resonances. 2019, submitted

66. F. Ramiro-Manzano, E. Bonnet, I. Rodriguez, F. Meseguer, Langmuir, 2010, 26 (7), 4559-4562.

67. R. García-Aboal, R. Fenollosa, F. Ramiro-Manzano, I. Rodriguez, F. Meseguer, P. Atienzar, ACS Omega 2018, 3, 5229-5236

68. R. Fenollosa M. Garín, F. Meseguer, Phys. Rev. B, 2016, 93, 235307

SUPPLEMENTARY INFORMATION: Grooves-assisted solution growth of lead bromide Perovskite aligned nanowires: a simple method towards photoluminescent material with guiding light properties

Isabelle Rodriguez[a]*, Roberto Fenollosa[a], Fernando Ramiro-Manzano[a], Rocío García-Aboal[a], Pedro Atienzar[a], and Francisco J. Meseguer[a].

[a]Instituto de Tecnología Química (CSIC-UPV), Universitat Politècnica de València, Av. Los Naranjos s/n, 46022 Valencia, Spain

Corresponding author: mirodrig@upvnet.upv.es

Contents of Supporting Information

S1. Field emission scanning electron microscope (FESEM) images of DVD polycarbonate substrates and PDMS replica.

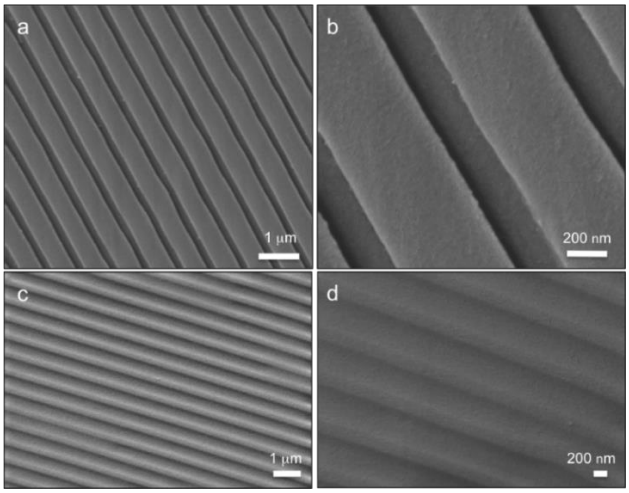

Figue S1. Images taken with a Field emission scanning electron microscope of (a) and (b): a polycarbonate bottom plate of a DVD; (C) and (d) PDMS replica of a polycarbonate bottom plate of a DVD.

S2. Field emission scanning electron microscope (FESEM) images of CD polycarbonate substrates and PDMS replica.

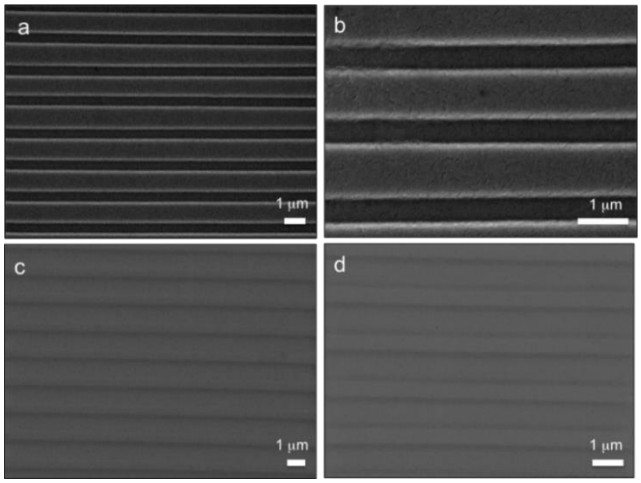

Figure S2. SEM images of (a) and (b): a polycarbonate bottom plate of a CD; (C) and (d) PDMS replica of a polycarbonate plate of a CD.

S3. $MAPbBr_3$ nanowires characterization.

In the case of $MAPbBr_3$ nanowires, XRD measurements also reveal a crystalline structure with the characteristic peaks of a cubic structure 1S. However, $MAPbBr_3$ nanowires seems to crystalize preferentially in the (001) direction compared to a film structured material (Fig. S3 (c)).

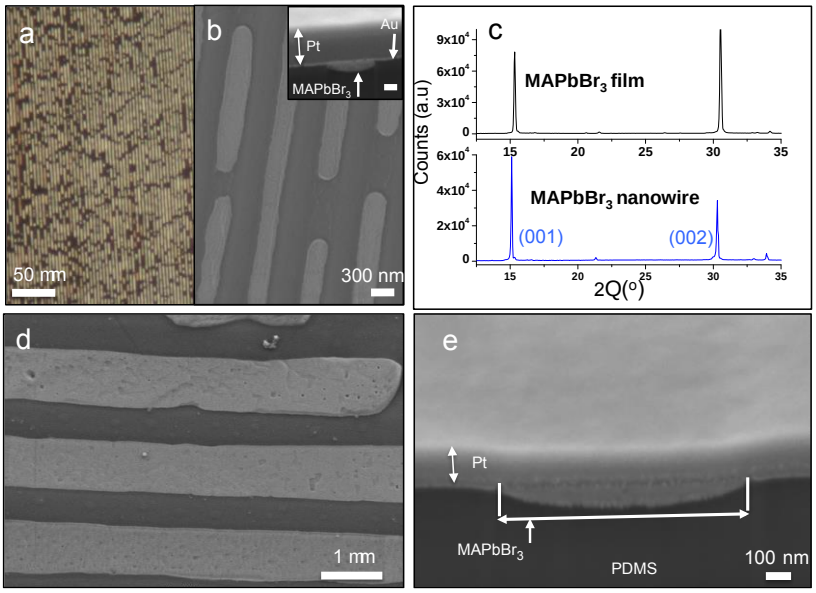

Figure S3. Polycrystalline $MAPbBr_3$ nanowires characteristics. (a) and (b) optical and FESEM images respectively of $MAPbBr_3$ nanowires obtained on PDMS replica of DVD structure. Inset: image of perpendicular cut by FIB milling (scale bar: 100 nm) (c) XRD patterns of $MAPbBr_3$ nanowires and of $MAPbBr_3$ film structure. (d) FESEM image of $MAPbBr_3$ synthesized on PDMS template replica of a CD substrate. (e) FESEM image of a transversal cut of a $MAPbBr_3$ nanowire (grown on CD-like PDMS template) by FIB milling (Sputtered Pt coating was used to cover the sample before the milling).

S4. Experimental optical set-up.

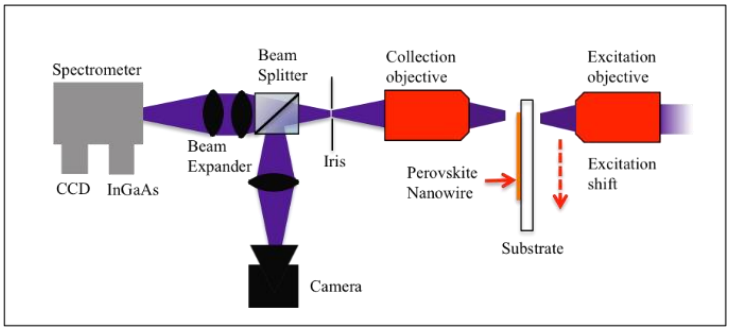

Figure S4. Home made experimental optical setup employed for the study of photoluminescence properties and the light transport phenomenon in single Perovskite nanowires. While the collection objective is focused at one end of the nanowire, the position of the excitation objective is shifted along it.

S5. $CsPbBr_3$ nanowires grown on PDMS CD-like substrate. Photoluminescence evolution along the nanowires as function of distance between excitation and collection point.

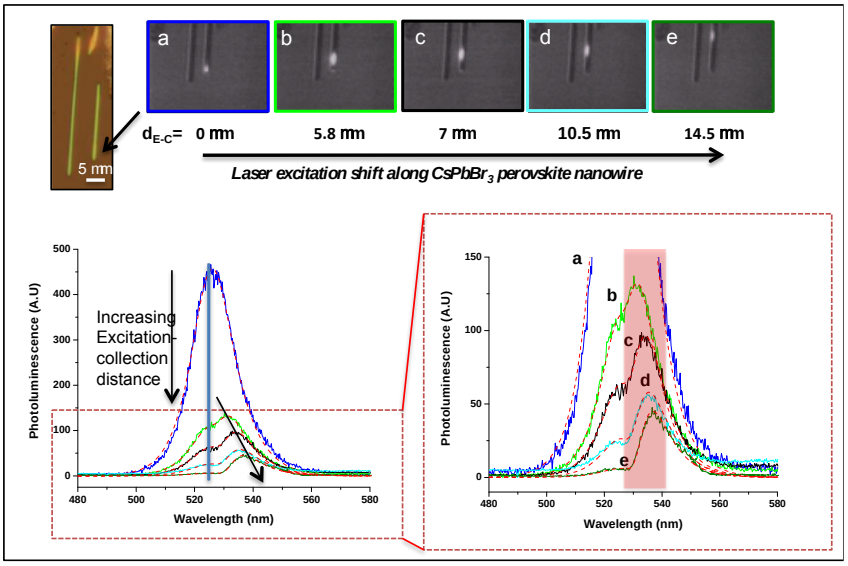

Figure S5. Same as Fig. 4 but for $CsPbBr_3$ Perovskite nanowires prepared over a PDMS substrate with CD replica features. Top left: color optical microscope image of 2 isolated $CsPbBr_3$ nanowires. The black arrow indicates the chosen nanowire for PL experiments. Images a, b, c, and d show the nanowire with the spot of the excitation light (white spot) for each d_{E-C} distance.

Below left: Photoluminescence spectrum for each d_{E-C} distance (blue: 0 µm; light green: 5.8 µm; black: 7 µm; cyan: 10.5 µm; green: 14.5 µm). The Blue line indicates the position of the peak of the primary emission of the PL. Black arrow on the PL spectra shows the shift of the maximum peak of PL that can be seen more easily on the zoom out of the figure (below right) The red fringe indicate the PL maximum.

S6. Photoluminescence spectra of $CsPbBr_3$ and $MAPbBr_3$ films

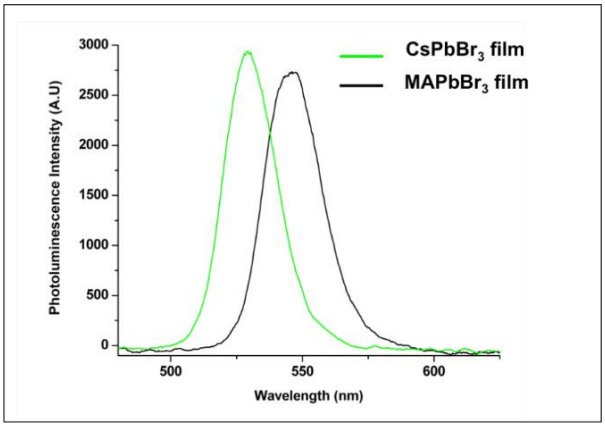

Figure S6. Photoluminescence spectra recorded on a $CsPbBr_3$ (green line) and $MAPbBr_3$ (black line) film. The maximum peaks are centered respectively at 530 nm and 546 nm for $CsPbBr_3$ and $MAPbBr_3$.

S7. Optical properties of $MAPbBr_3$ nanowires

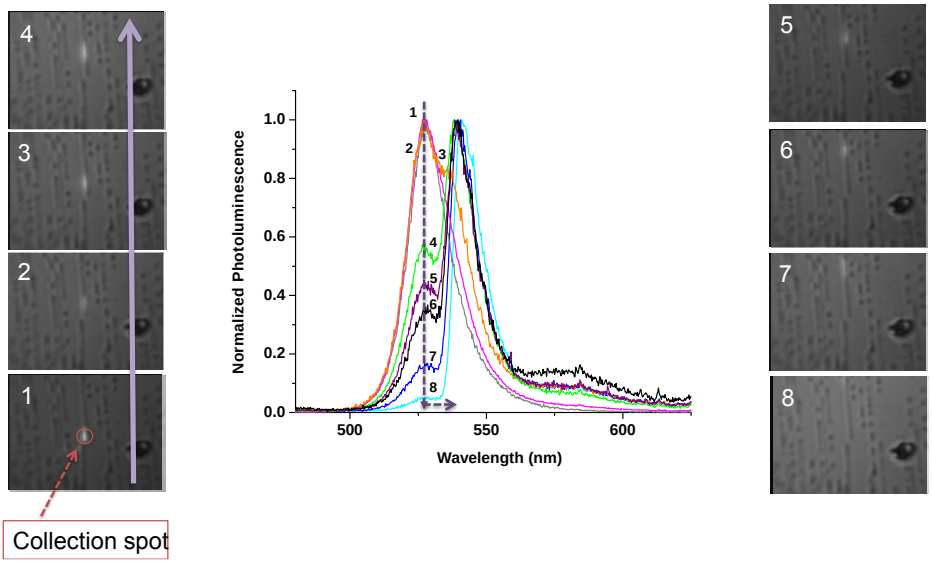

Figure S7. Photoluminescence evolution as increasing collection-excitation distance (labels 1 to 8) for $MAPbBr_3$ nanowire obtained into the groove of a PDMS replica of DVD substrate. The white spots represent the PL induced by a 405 nm laser excitation.

S8. Optical images of transferred $MAPbBr_3$ nanowires onto ITO substrate

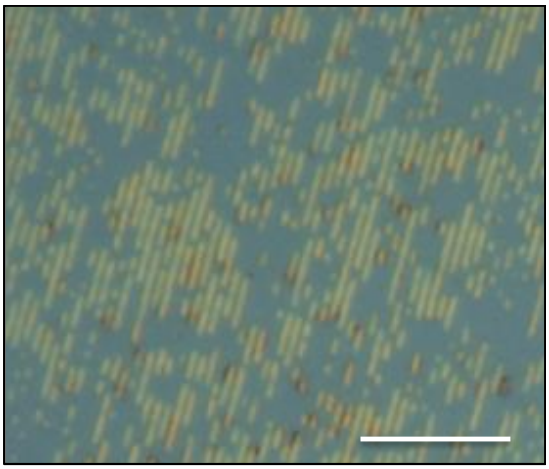

Figure S8. $MAPbBr_3$ nanowires grown on DVD-like PDMS template transferred onto ITO substrate via gel-pack film. Scale bar: 10µm

Reference:

1. 1S Q. Zhu, K. Zheng, M. Abdellah, A. Generalov, D. Haase, S. Carlson, Y. Niu, J. Heimdal, A. Engdahl, M. E. Messing, T. Pullerits, S. E. Canton, Phys. Chem. Chem. Phys. 2016, 18, 14933

CAPÍTULO 4

FOTOCATÁLISIS

SECCIÓN 4.1

VAPOR-PHASE PHOTOCATALYTIC OVERALL WATER SPLITTING USING HYBRID METHYLAMMONIUM COPPER AND LEAD PEROVSKITES

Teresa García, Rocío García-Aboal, Josep Albero, Pedro Atienzar and Hermenegildo García

Nanomaterials 2020, 10, 960

DOI: 10.3390/nano10050960

VAPOR-PHASE PHOTOCATALYTIC OVERALL WATER SPLITTING USING HYBRID METHYLAMMONIUM COPPER AND LEAD PEROVSKITES

Teresa García[a], Rocío García-Aboal[a], Josep Albero[a], Pedro Atienzar[a]* and Hermenegildo García[a]*

[a]Instituto Universitario de Tecnología Química CSIC-UPV, Universidad Politecnica de Valencia, Av. de los Naranjos s/n, 46022 Valencia, Spain

letuana_@hotmail.com (T.G.); rogarab@itq.upv.es (R.G.A.); joalsan6@upvnet.upv.es (J.A.)

* Correspondence: pedatcor@itq.upv.es (P.A.); hgarcia@qim.upv.es (H.G.)

Received: 09 April 2020; Accepted: 22 April 2020; Published: date

Keywords: hybrid perovskite; photocatalysis; water splitting; hydrogen production

Abstract

Films or powders of hybrid methylammonium copper halide perovskite exhibit photocatalytic activity for overall water splitting in the vapor phase in the absence of any sacrificial agent, resulting in the generation of H_2 and O_2, reaching a maximum production rate of 6 µmol H_2 x g $cat^{-1}h^{-1}$ efficiency. The photocatalytic activity depends on the composition, degreasing all inorganic $Cs_2CuCl_2Br_2$ perovskite and other Cl/Br proportions in the methylammonium hybrids. XRD indicates that $MA_2CuCl_2Br_2$ is stable under irradiation conditions in agreement with the linear H_2 production with the irradiation time. Similar to copper analogue, hybrid methylammonium lead halide perovskites also promote the overall photocatalytic water splitting, but with four times less efficiency than the Cu analogues. The present results show that, although moisture is strongly detrimental to the photovoltaic applications of hybrid perovskites, it is still possible to use these materials as photocatalysts for processes requiring moisture due to the lack of relevance in the photocatalytic processes of interparticle charge migration.

1. INTRODUCTION

Hybrid organic inorganic perovskites are attracting currently considerable attention due to their performance in photovoltaic devices, where efficiencies above 23%[1] have been achieved in a very short time compared to the slower progress that has characterized the efficiency increase evolution in dye sensitised solar cells[2–8]. Hybrid perovskites offer a large flexibility for tuning their optoelectronic and other properties including absorption spectrum, bandgap, and band level energy by controlling their composition, average particle size, and film preparation process[9–12]. The high coefficient of visible light absorption characteristic of hybrid perovskites, together with their efficient charge separation and charge carrier mobility, are among the main features responsible for the performance of this type of materials in photovoltaic cells[13,14].

These fundamental photochemical processes are also common in many other applications beyond solar cells[15–17]. Specifically in photocatalysis, the energy of the photons is frequently converted into a charge separation state that is able to promote the oxidation and reduction of substrates by holes and electrons, respectively[18].

In spite the fact that inorganic perovskites, such as those containing Ti and Ta, are among the most efficient photocatalysts for hydrogen generation from water by solar light and the large current interest in hybrid perovskites, there have been no reports of the use of hybrid perovskites as photocatalyst for overall water splitting[19–21]. The main reason for this lack of studies of the use of hybrid perovskites as photocatalysts for hydrogen generation is the well-known lack of stability of hybrid perovskites in the presence of water, light and even moisture[22–24]. Although the negative influence of the humidity in the performance of photovoltaic devices based on hybrid lead perovskites is a well-known fact, there is still an incomplete understanding of the reasons. One of the proposals is that moisture hydrates the external surface of hybrid perovskite grains in the film, decreasing its electrical conductivity by disfavouring interparticle electron migration[25]. In other studies, it has been proposed that water reacts reversibly with $MAPbI_3$ films through the initial formation of aqueous complexes that

finally degrade the generation of PbI_2[26]. Major studies have claim that the degradation promoted by hydration lead to the release of CH_3NH_2 and HI as gases[27]. In any case, according to the proposed degradation mechanism, one water molecule could be sufficient to completely degrade the $MAPbI_3$ film. Nevertheless, the degradation mechanism of hybrid lead halide is still under debate and further studies to understand the possible role of highly conductive PbI_2 hydrate are still attracting considerable attention[28].

In any case, even if the presence of moisture is strongly detrimental for photovoltaic devices, there could be still a possibility for efficient photocatalytic water splitting using hybrid metal halide if the photocatalytic reaction is sufficiently fast under the experimental conditions. In photocatalysis photogenerated electrons and holes do no need to migrate from particle to particle up to the external electrode because the reaction takes place just on the surface of each semiconductor particle where moisture should be reactive[26,29,30]. The main differences between the operation of a photovoltaic device and a photocatalytic reaction that will make feasible water splitting are summarized in Scheme 1. There are examples in the literature in which photocurrents are not observed, while the material exhibits photocatalytic activity[31]. Therefore, there is still a chance for observing highly efficient photocatalysis even though moisture plays a strong detrimental effect in photovoltaic devices[32].

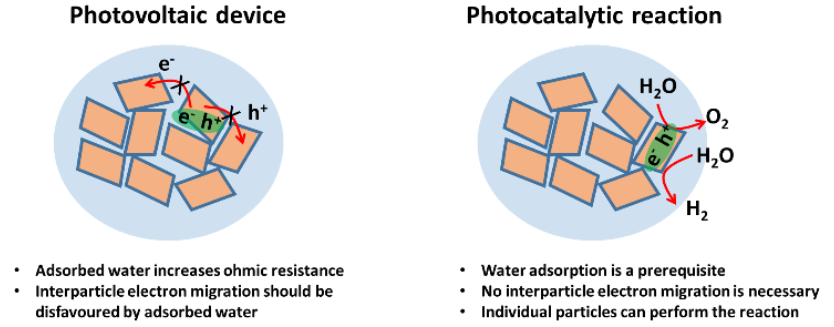

Scheme 1. Cartoon illustrating the main differences between the operation mechanisms of a photovoltaic device and a photocatalytic system. These differences can serve to rationalize why the detrimental effect of H_2O in solar cells could not preclude the occurrence of an efficient photocatalytic reaction.

Based on this consideration and aimed at providing information on the photocatalytic activity of hybrid perovskites, in the present study we report the photocatalytic activity for overall water splitting of lead-free copper-based hybrid methylammonium halide perovskite. The selection of this hybrid copper perovskite was made to avoid the use of toxic metals such as lead that in the present case is replaced by an Earth abundant first-row transition metal and also trying to study a material whose photochemical properties are less influenced by humidity, particularly when chloride is present in its composition[33–35]. The synthesis, structure, and energy levels of a series of $MA_2CuCl_xBr_{4-x}$ hybrid perovskites (MA: methylammonium) have been recently reported, including film preparation and photovoltaic activity of the material[36]. In the present study, we have selected $MA_2CuCl_2Br_2$ and $MA_2CuCl_{0.5}Br_{3.5}$ to determine their ability for photocatalytic overall water splitting upon simulated sunlight irradiation in the gas phase of films of these materials[36]. A comparison with the photoresponse of hybrid lead perovskite is also provided.

2. MATERIALS AND METHODS

2.1. Synthesis of $MA_2CuCl_xBr_{4-x}$ Perovskite Powders

Preparation of the hybrid perovskites was performed by crystallization of a mixture of MACl and MABr in slight excess with respect to a mixture of $CuCl_2$ and $CuBr_2$, as previously reported in the literature[36]. Powders of these copper perovskites were prepared by crystallization from ethanol solutions, employing 1.34 g of $CuBr_2$ (copper bromide, 99% Sigma-Aldrich, Darmstadt, HE, Germany), and 0.972 g of MACl (methylammonium chloride, 99% Sigma-Aldrich, Darmstadt, HE, Germany) for $MA_2CuCl_2Br_2$.

For the other mixed halide copper perovskites, the precursors were mixed in 100 mL of EtOH, using 1.2 equiv. of organic precursor with respect to a mixture of copper salts as previous reported in the literature[36]. Then, the solutions were stirred for 2 h at 60°C. Crystal growth was carried out by keeping overnight the ethanolic solutions in a freezer. The crystals were recovered by filtration, dried overnight at 60° C in a vacuum oven, and finally stored in glovebox.

2.2. Films Fabrication

DMF solutions of $MA_2CuCl_2Br_2$ (2 M) were prepared by dissolving powders of this perovskite at room temperature. After that, thin films of catalyst were made depositing 25 µL of the DMF solution in a 2 × 2 cm^2 quartz square by drop casting and annealing on a hot plate at 70 °C for 1 h. After film preparation, the specimens were kept in a glovebox.

2.3. Materials Characterization

XRD patterns of the powders and thin films were recorded on a Philips (Amsterdam, Netherlands) X'PERT diffractometer that was equipped with a proportional detector and a secondary graphite monochromator. The data were collected step wise over the range 2θ = 2–20°, at steps of 0.02°, an accumulation time of 20 s/step, using the Cu Kα radiation (λ = 1.54178 Å).

UV–Vis optical spectroscopy of the perovskite films was carried out using a Cary 5G spectrophotometer (Santa Clara, CA, USA) and CaSO4 as reference.

Field-emission scanning electron microscopy (FESEM) images were recorded with a Zeiss Ultra 55 field FESEM apparatus (Atlanta, GA, USA).

2.4. Transient Absorption Spectroscopy (TAS)

Transient absorption experiments were recorded using a home-built system as reported before[37]. The samples were excited with a Nd:YAD laser at 532 nm and 1 Hz repetition rate; <20 ns pulse duration. The resulting photoinduced changes in optical density were monitored by employing a 150 W Tungsten lamp, with 20 nm bandwidth monochromators before and after sampling, a home-built photodiode-based detection system, and a MDO-3034 Tecktronic oscilloscope.

2.5. Photocatalytic Measurements

The photoreactor to evaluate the photocatalytic activity of hybrid perovskites consists in a homemade stain steel body with a top quartz

window with a truncated conical shape. The total capacity of the photoreactor is 120 mL. The temperature and pressure inside the photoreactor were measured by an internal thermocouple and a manometer, respectively.

Supplementary Figure S1 shows a photograph of the photoreactor used, indicating location of the thermocouple and the distribution of the catalyst and the reagents inside the reactor. The photoreactor was located 20 cm below the solar simulator collimated beam and the maximum temperature of gas mixture was 40°C. Argon was introduced into the reactor to avoid the presence of oxygen and 1 mL of water was used as reagent. The water drops was placed in a separated container of 10 mL to keep constant the ambient humidity. The amount of photocatalyst was 10 mg. The evolution of hydrogen and oxygen was determined by direct connection of the photoreactor to an Agilent 490 Micro GC (Santa Clara, CA, USA) (Molsieve 5A column with Ar as carrier gas). The light source was a 150 W lamp. Simulated sunlight irradiations were carried out using a solar simulator (Sun 2000 ABET technologies 1000 W/m^2) (Milford, CT, USA) equipped with an AM 1.5G filter. Irradiation were performed in triplicate using samples prepared independently, the maximum error of the measurement was 15%. Analysis of the possible presence of H_2O_2 was carried out by washing the photocatalyst and photoreactor with Milli-Q water and proceeding with colorimetric test of H_2O_2. No evidence of the formation of any H_2O_2 was obtained (see Figure S2).

3. RESULTS AND DISCUSSION

3.1. Photocatalyst Characterization

The resulting powders were characterized by XRD (Figure 1) where the diffraction peaks expected for the hybrid MA_2CuX_4 perovskites were recorded, agreeing with the data of the original article in which the synthesis of these copper perovskites was reported[36].

Optical spectroscopy shows the Cl^- or Br^- to Cu electronic transitions at λmax 300 and 400 nm reaching up to 600 nm ($MA_2CuCl_2Br_2$) or 680 nm ($MA_2CuCl_{0.5}Br_{3.5}$) in accordance with the

literature[36]. Intraband d-d electronic transitions on Cu^{2+} ions were also observed in the 700–1000 nm region as reported (Figure 2).

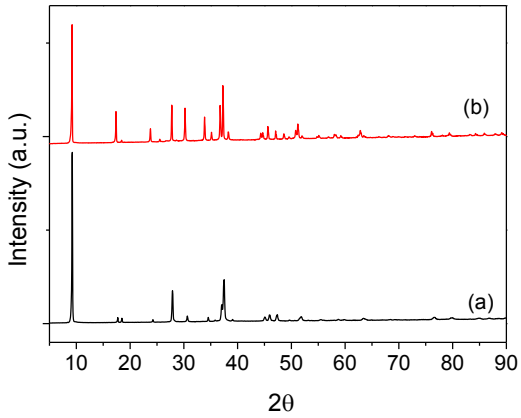

Figure 1. X-ray patterns of as-synthesized hybrid copper perovskites powders: a) $MA_2CuCl_2Br_2$ and b) $MA_2CuCl_{0.5}Br_{3.5}$.

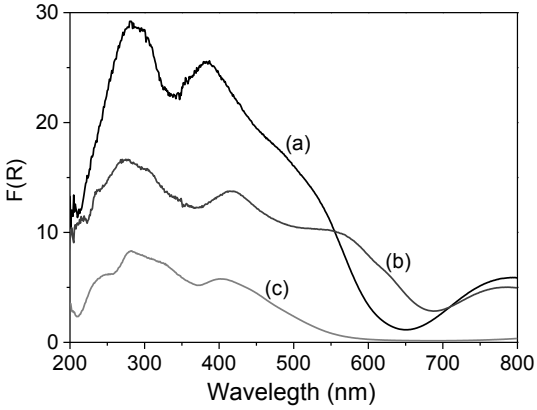

Figure 2. Diffuse reflectance UV–Vis absorption spectra (plotted on the Kubelka-Munk function of the reflectance, F(R) of hybrid copper perovskite powders: a) $MA_2CuCl_2Br_2$, b) $MA_2CuCl_{0.5}Br_{3.5}$ and c) $Cs_2CuCl_2Br_2$.

The morphology of the hybrid copper perovskites and the particle size can be determined by FESEM images. Figure 3 shows that the hybrid copper perovskites are constituted by very large particles between 40 and 100 µm formed by stacking of platelets of 50–100 nm thickness and much larger lateral area.

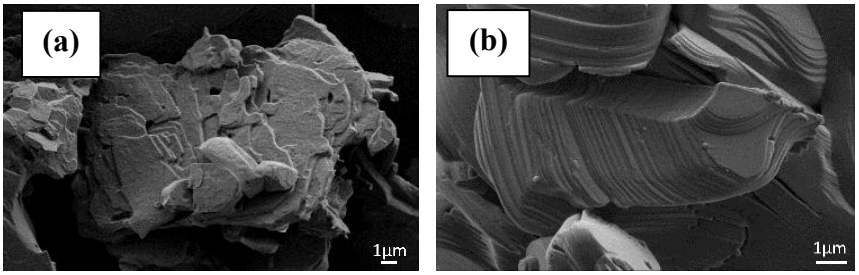

Figure 3. FESEM images of $MA_2CuCl_2Br_2$. Powder sample 4000x (a) and film sample 8000x (b).

As previously commented in the introduction, formation of aqua-complex seems to be the first step in the water promoted degradation of hybrid lead perovskite resulting in the deterioration of its photovoltaics response[26–28]. To addresses the possible formation of an aqua complex in the case of $MA_2CuCl_2Br_2$ the XPS spectra of the solid in the absence of humidity and after exposure to H_2O in a pre-chamber of the instrument, immediately prior to record the spectra were compared. XPS is a surface technique that proves the external source of the film in contact with H_2O and changes in the XPS $Cu2p_{3/2}$ peak should report on the possible H_2O coordination to Cu^{2+} or hydrolysis at the methylammonium group by changes in the binding energy and width of the peak. As shown in Supplementary Figures S3 and S4 a perfect coincidence of the $Cu2p_{3/2}$ and N1s peaks were recorded for the fresh and H_2O exposed $MA_2CuCl_2Br_2$ samples, indicating that formation of an aqua complex in where H_2O coordinates to Cu^{2+} replacing any of the halides coordinating to Cu^{2+} or hydrolysis of methyl ammonium does not occur in the presence of H_2O, in spite of detection of O1s peak in the case of H_2O exposed sample (see Figure S5). These XPS measurements suggest that H_2O physisorbed on the surface of $MA_2CuCl_2Br_2$ without affecting the coordination sphere of the Cu^{2+} ions. These coincidence upon prolonged (three weeks irradiation) also rules out that oxygen involved in the photocatalytic water splitting is consumed in the decomposition of the photocatalyst. Further details on the stability of $MA_2CuCl_2Br_2$ upon prolonged exposure to moisture under photocatalytic conditions are provide bellow.

3.2. Photocatalytic Measurements

Photocatalytic experiments were carried out by illuminating with a solar simulator (1000 W/m^2) powders or films of the hybrid perovskites at temperatures below 40°C in a sealed photoreactor saturated with H_2O vapor at atmospheric pressure that corresponds to a relative humidity of 100% (dewpoint). Supplementary Figure S1 shows a photograph of the setup used in these experiments. Since $MA_2CuCl_2Br_2$ dissolve in water, it is not possible perform the photocatalytic water splitting by suspending $MA_2CuCl_2Br_2$ in water. In contrast, it was found that exposure of $MA_2CuCl_2Br_2$ to H_2O vapour was sufficient to observe the photocatalytic reaction. In addition having the solid catalyst deposited on a surface can allow it to continuous flow photocatalytic experiments recirculating the gas phase. Hydrogen and oxygen evolution was quantified by a microGC connected in line with the photoreactor using a thermoconductivity detector and argon as carrier gas. Under these conditions, evolution of hydrogen and oxygen as a function of irradiation time was observed. Figure 4 shows a time evolution plot for a representative experiment. The apparent induction period for hydrogen evolution observed in Figure 4 is likely be due to some absorption phenomena, detection limit, and filling of the reactor volume.

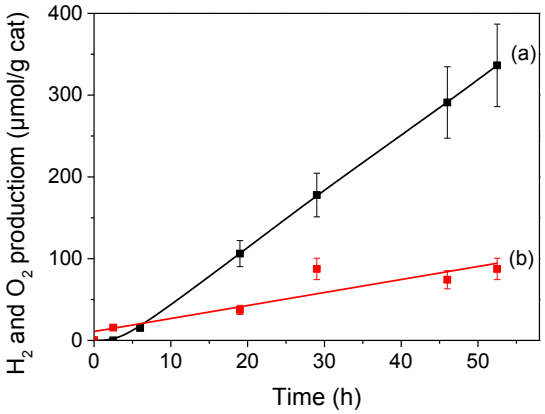

Figure 4. Temporal hydrogen (a) and oxygen (b) evolution upon simulated sunlight irradiation (1000 mWcm^{-2}) of $MA_2CuCl_2Br_2$ films exposed to a H_2O-satured atmosphere at 1 atm and 40 °C.

Control experiments in the absence of water vapor allowed detecting only negligible amounts of hydrogen (less 1% of the hydrogen measured when water vapors were present). Also oxygen was undetectable under this condition in the absence of water saturation. This control experiment indicates that water is needed to observe the generation of hydrogen and oxygen. The temporal evolution of hydrogen follows a linear relationship with time, supporting the stability of the material as photocatalyst under the irradiation conditions. A maximum amount of hydrogen of 340 μmol × g cat^{-1} was achieved at 50 h irradiation time. Although the temporal evolution of oxygen did not follow strictly the expected stoichiometry for overall water splitting because initial and final irradiation times were somewhat higher and lower, respectively, than expected, oxygen amounts were quantified, and the generation of oxygen was clearly measured. This lack of linearity of oxygen production and its apparent constant concentration beyond 24 h can probably reflect a consumption of some amount of photogenerated oxygen inside the photoreactor. To asses or rule out the possibility of O_2 consummation by formation of H_2O_2, analysis of the photocatalyst and photoreactor aim at detection of peroxides with Ti = O^{2+} was carried out. No evidence of the presence of peroxides was obtained. Analysis of the XPS $Cu2p_{3/2}$ peak of the $MA_2CuCl_2Br_2$ film after extensive irradiation in the presence of moisture (3 weeks) this not allow to detect significant variations in the binding energy and position of the peak respect to the fresh sample (Supplementary Figure S3). XPS data on the surface copper conclusively indicate that the photocatalyst is stable under the reaction conditions.

Overall water splitting typically requires co-catalyst in order to achieve measurable efficiencies. We speculated that in the present case overall water splitting activity could be favour by some CuO impurity acting as co-catalyst. Aim at clarify this issue we prepared an additional film in which CuO nanoparticles were deposited at 1% loading on $MA_2CuCl_2Br_2$ by impregnation by DMF. However, no enhancement of the photocatalytic activity for this Cu modified film was observed with respect to the $MA_2CuCl_2Br_2$ film lacking CuO nanoparticles.

The influence of the composition on the photocatalytic activity for overall water splitting under simulated sun light irradiation was addressed by performing analogous measurements using $MA_2CuCl_{0.5}Br_{3.5}$ as photocatalyst. As commented earlier, hybrid perovskite based exclusively in bromide is known to be more deliquescent than the mixed Cl/Br material. Therefore, the presence of Cl^- should increase the stability of the photoresponse of the material in the presence of moisture. The measurements indicate that $MA_2CuCl_{0.5}Br_{3.5}$ also exhibit photocatalytic activity for overall water splitting in the absence of the sacrificial agents, but with an efficiency about one half that of the $MA_2CuCl_2Br_2$ (Supplementary Figure S6). Furthermore, prolonged irradiation time indicates some photocatalyst deactivation for $MA_2CuCl_{0.5}Br_{3.5}$ as shown by the decrease hydrogen and oxygen production rate over the time.

For overall water splitting to occur, electrons in the conduction band (CB) and holes in the valence band (VB) must have adequate energy. Scheme S1 shows the reported potentials of VB maximum and CB minimum for $MA_2CuCl_2Br_2$. It is noted that according of these reported values not oxygen generation should be possible for $MA_2CuCl_2Br_2$, since it would require a potential about 5.4 eV[38,39]. However several possibilities can be considered to rationalize why oxygen evolves in the simulated sun light irradiation of $MA_2CuCl_2Br_2$ in contact with H_2O vapor. Thus, it has been reported that the Fermi level (EF) and work function (WF) of a given material can shift as much as 0.6 eV depending on the structure and surface morphology of the particles, exposure to the ambient and even the history of sample preparation[40]. For this reason, we proceeded to measure experimentally the VB energy maximum by XPS of our $MA_2CuCl_2Br_2$ sample freshly and immediately after exposure to moisture in the XPS prechamber. The results are presented in figure S7. The VB energy maximum was determined by extrapolation of the lineal slope of the peak intensity versus energy. As it can be seen in this figure, minor variations towards higher energy of 0.1 eV were determined upon moisture exposure from the initial 5.6 eV for the fresh sample. However, the necessary vacuum requirement of XPS could make that real value of VB maximum in the photocatalytic experiment could be

even higher due to the higher H_2O pressure. There are precedents in the literature showing a shift in the VB energy depending on the presence of water. Whatever the reason, generation of oxygen from H_2O in the absence of sacrificial electron donors opens new avenues for the development of visible light responsive photocatalyst based on hybrid perovskites.

It is known that in overall water splitting, oxygen generation is the rate determining step since it requires four holes for the formation of each O_2 molecule[41]. Accordingly, a general practice to determine the maximum hydrogen production rate is to perform photocatalytic experiments also in the presence of sacrificial electron donors, amines being among the preferred electron donors[42]. In these experiments, an excess of sacrificial agents is generally added in proportions as high as 30% with respect to water[43]. Unfortunately, triethylamine in excess produces the complete decomposition of $MA_2CuCl_2Br_2$ and this type of experiments of photocatalytic hydrogen generation could not be done under optimal conditions requiring an excess of amine as sacrificial agent. Nevertheless, measurements of hydrogen evolution using $MA_2CuCl_2Br_2$ as photocatalyst were done adding a minimal amount of methylamine. It was observed that the rate of hydrogen generation at 4 h irradiation time increases by a factor of about two, from 3.85 to 8.85 µmol H_2/g cat. when some amine is present. This influence of the presence of methylamine lends further support to the general assumption that also in the case of $MA_2CuCl_2Br_2$ the photocatalytic activity for hydrogen generation is limited by the slower O_2 evolution.

As commented before, photocatalytic experiments were performed using thin films of hybrid copper perovskite on quartz substrate prepared by casting the solid photocatalyst suspended in DMF 2M followed by slow evaporation of the solvent at 70 °C. An alternative procedure consists in performing the photocatalytic experiments with dry powders of the hybrid copper perovskite. Also, under these conditions, the exposure of the powders in thin bed (10 mg) to UV-Vis light in the presence of water vapour allows for the detection of the evolution of significant amounts of hydrogen and oxygen (see Figure 4). However, in this case, due to the use of an excess mass of the solid material with respect to the experiments in

where thin films were used, much lower specific evolution rates were measured. However, these experiments with dry powders complement the previous XPS data on $MA_2CuCl_2Br_2$ films, confirming the photochemical stability of the hybrid copper perovskite under photocatalytic conditions upon exposure for extended irradiation times. The use of powder $MA_2CuCl_2Br_2$ samples allows monitoring the XRD pattern as a function of the irradiation time. Minor changes in the XRD patterns of copper perovskite consisting in a broadening of the peak width (FWHP from 0.26 to 0.42 of the 006 peak) and a decrease of the 002 peak intensity (from 3 to 1 I002/I006) were observed. The results are presented in Figure 5. These changes were reversible in some degree and the same sample recover partially the intensity of the 002 peak and the peaks became narrower upon standing the material under the photocatalytic conditions without any treatment. This reversibility of XRD pattern changes in the presence of moisture have been reported for $MAPbI_3$ films and single crystals upon exposure to moisture and purpose to be due to hydration of the hybrid lead perovskite. Further experimental evidence support the stability of $MA_2CuCl_2Br_2$ under prolonged photocatalytic experiments was obtained by XPS (Supplementary Figure S3). Comparison of the high resolution XPS $Cu2p_{3/2}$ peak of the fresh and hydrated material with that after three weeks of continuous irradiation does not show any difference and the peaks were coincident. All these data support the stability of the material under the conditions where hydrogen and oxygen are formed. The conclusions based in XRD was mainly confirmed by XPS data of the sample after been used as photocatalyst by analysing the $Cu2p_{3/2}$ peak. However, deconvolution of the experimental XPS $Cu2p_{3/2}$ peak on the sample used of photocatalyst suggest, although the peak is almost unchanged, the presence of a minor component (about 20%) of a contribution of an additional component (binding energy 530 eV) that could correspond to the formation of a minor proportion of CuO on the outer moisture surface of the photocatalyst.

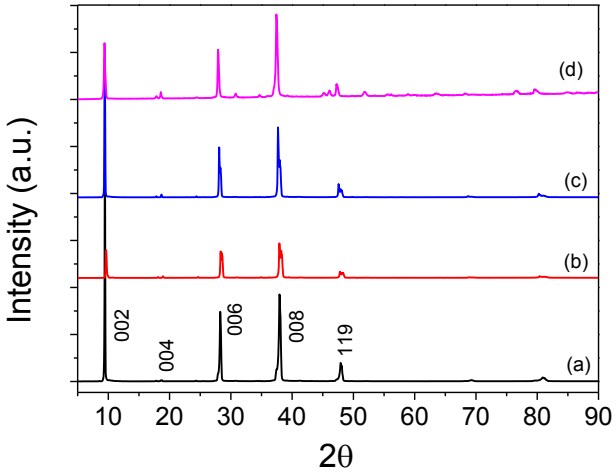

Figure 5. XRD patterns of $MA_2CuCl_2Br_2$ perovskite powders upon irradiation with a solar simulator (1000 W/m^2): a) fresh sample, b) after 24 h, c) 48 h and d) three weeks reaction. The relatively minor changes in the relative peak intensity and FWH peak are due to unavailable variation in the packing of the solid and surface levelling when filing the cell holder.

Besides hybrid copper perovskites and considering the large diversity of hybrid perovskites that have been prepared for evaluation in photovoltaic cells[44], we also screened the photocatalytic activity of some related hybrid perovskites. Specifically, to determine the role of the organic MA^+ ion a full inorganic copper perovskite in where the MA^+ was replaced by Cs^+ was also prepared and tested as photocatalyst for overall H_2O splitting. It is well known in the state of the art that the composition of perovskites exerts a large influence in the optoelectronic properties as well as in the efficiency of light-to-current conversion[45]. With these precedents in mind, it was expected that the replacement of MA^+ by Cs^+ should result in a change in the photocatalytic activity. The activity measured for $Cs_2CuCl_2Br_2$ in the overall water splitting is provided in Table 1.

Table 1. H_2 production data at 24 h of reaction for different types of perovskites*.

Photocatalyst	µmol H_2/gcat	AQY[a] (%)	TON[c]
$MA_2CuCl_2Br_2$	141.21	0.7153 (0.73)[b]	5.06 (12.05)[d]
$MA_2CuCl_{0.5}Br_{3.5}$	94.23	0.4773	4.00
$Cs_2CuCl_2Br_2$	9.03	0.0457	0.51
$MAPbBrI_2$	5.16	0.0261	0.30
$MAPbClI_2$	2.89	0.0146	0.15
$MAPbI_3$	2.69	0.0136	0.17
$MAPbCl_3$	2.54	0.0129	0.09
$MAPbBr_3$	2.11	0.0107	0.10

*Reaction conditions: photocatalyst 10 mg powder and irradiation with a solar simulator (1000 Wm^{-2}). aApparent Quantum Efficiency (AQY) calculated from the equation: AQY = 2·number of produced hydrogen molecules/number of incident photons. bApparent Quantum Efficiency for oxygen production. [c]TON: turnover number calculated at 24 h. [d]TON calculated at 52 h.

As shown in Table 1, although $Cs_2CuCl_2Br_2$ also exhibits photocatalytic activity for overall water splitting in the absence of any sacrificial agent, the activity determined for this material was significantly smaller than that achieved using $MA_2CuCl_2Br_2$ that was the best photocatalyst of the series (see Table 1). This lower activity of Cs^+ perovskite with respect to that of MA^+ hybrid perovskite has also been observed with regard to the photovoltaic efficiency in solar cell devices and has been attributed to the combination of several factors, the most important being the increase in the band gap of the Cs^+ material and possible structural changes. As it can be seen in the Figure 2 also in the present case $Cs_2CuCl_2Br_2$ exhibits larger bandgap than the analogous MA^+ hybrid perovskite, meaning that less photons in the visible range are absorbed in $Cs_2CuCl_2Br_2$ compared to $MA_2CuCl_2Br_2$ and this should result in lower photocatalytic activity. Concerning the spectral photoresponses, it can be assumed that they will follow a similar trend to the photocurrent performed for similar perovskites on photovoltaic devices, where the main photoresponse is observed for wavelengths shorter than 650 nm[36].

Besides copper perovskites, it was of interest to determine the possible photocatalytic efficiency of hybrid lead halide perovskites, since these materials are the ones that exhibit the highest light-to-current conversion efficiency in photovoltaic devices[36]. Although the

photocatalytic activity varied depending on the halide, being particularly active the one having Br and I, their efficiency was lower than those of copper perovskites.

To put the data shown in Table 1 in a broader context it should be noted that the STH data refer to overall water splitting in the absence of any noble metal co-catalyst. Values for other overall water splitting co-catalyst under comparable conditions (solar light, absence of sacrificial, absence of co-catalyst) give similar or lower STH values[46,47]. It should also be noted that, considering the flexibility in the synthesis of hybrid metal halide perovskites, other related perovskites could even exhibit higher efficiency.

As mentioned in the introduction, hybrid lead perovskites are influenced by the presence of moisture, but we have previously commented that this negative influence with respect to the photovoltaic efficiency due to the increase of the resistance of the interparticle migration of charge carriers should not be necessarily much detrimental for the photocatalytic activity. Interparticle charge migration is not an elementary process occurring in photocatalysis. Also the experimental conditions employed in the overall H_2O splitting only expose hybrid perovskites to water vapor and not to liquid water. Photocatalytic experiments using hybrid lead perovskite established also for this material as film on glass substrates their ability to generate hydrogen and oxygen upon irradiation with simulated solar light. The efficiency of the photocatalytic process also depends on the composition of the lead perovskite and among the materials tested, the most efficient one was $MAPbBrI_2$ that was somewhat more efficient than the other MA^+ lead perovskites tested, all of them exhibiting very similar performance. It is proposed that the higher activity of Br/I can derive from the band gap alignment in this material with respect to the potentials required for hydrogen generation and oxygen evolution and from its relatively narrow band gap (1.8 eV) that allows absorption of more photons in the visible range[13,40,48]. Other compositions of perovskites either have the absorption onset shifted towards the UV region or have too narrow bandgap to promote efficient overall water splitting. In any case, it seems that the efficiency

of lead halide perovskite is about four times lower than that presented in Figure 4 for hybrid copper perovskite.

3.3. Transient Absorption Spectra of $MA_2CuCl_2Br_2$

In order to gain some evidence in support of the photogeneration of electrons and holes upon light absorption in $MA_2CuCl_2Br_2$, a transient absorption study using 532 nm as excitation wavelength was carried out. The transient absorption spectra recorded for $MA_2CuCl_2Br_2$ at 100 and 1000 μs after laser excitation is presented in Figure 6. As it can be seen there, at short time delays after the laser pulse, the transient absorption consisted in two absorptions bands at λmax about 640 and 850 nm. At longer time delays the transient absorption at shorter wavelengths (λ < 600 nm) increases and the presence 640 nm band became less defined. This growth in the shorter wavelength region of the spectrum is clearly observed monitoring the transient signal at this region (inset of Figure 6). As it can be seen, the temporal profile of the signal at 580 nm grows in the first 500 μs and then becomes stationary during the longest time-window available in our nanosecond laser systems (2000 μs). It is proposed that this growth kinetics in the first 500 μs corresponds to kinetics of delocalization of electrons and holes within the $MA_2CuCl_2Br_2$.

To learn about the nature of these two absorption bands at 640 and 850 nm and the corresponding transient species, quenching experiments by methanol (electron donor quencher) and oxygen (electron acceptor quencher) were carried out. It was observed that methanol quenches the signal at 640 nm while it does not affect to the 850 nm band. This behaviour indicates that the two bands should correspond to two different species, the one at 640 nm corresponding to species with character of positive holes quenchable by methanol as electron donor, while this character of positive holes is not exhibited by the 850 nm band. Oxygen quenching leads to the complete disappearance of the transient signal in the submillisecond time scale at any wavelength. Since the 650 nm band was attributed based on methanol quenching to species with positive character, that in principle should not be quenchable by oxygen, it is more likely that besides oxygen as electron acceptor, it acts also as electron spin

quencher, deactivating in the present case precursors of the charge separated state with triplet character. Figure 7 shows representative transient signals to summarize the results of the methanol and oxygen quenching of the $MA_2CuCl_2Br_2$ photogenerated transients.

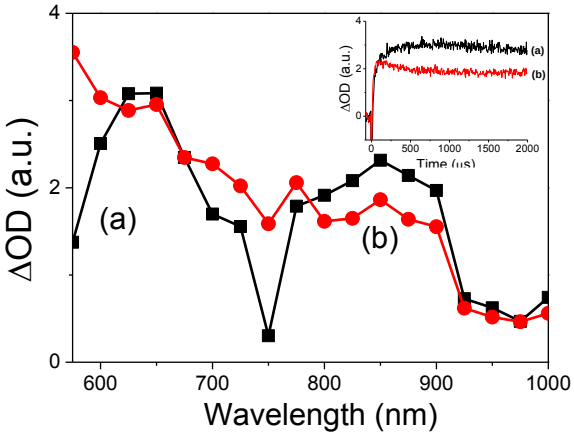

Figure 6. Transient spectra recorded at 100 (a) and 1000 μs (b) after 532 nm laser excitation of a N_2 purged film of $MA_2CuCl_2Br_2$. The inset shows the signal profiles monitored at 580 nm (a) and 850 nm (b).

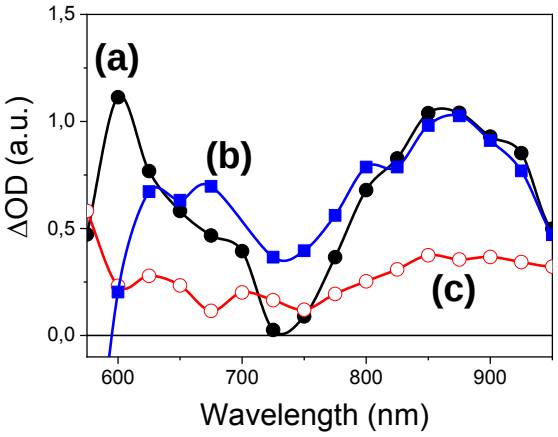

Figure 7. Transient spectra recorded at 100 μs after 532 nm laser excitation of a N_2 purged film of $MA_2CuCl_2Br_2$ (a) and after exposure to methanol (b) or oxygen (c).

After having addressed $MA_2CuCl_2Br_2$ stability to moisture and proved that the transients detected in the μs time regime react with

H_2O, quenching studies of $MA_2CuCl_2Br_2$ film transients upon excitation at 532 nm by H_2O-saturated N_2 were carried out. Figure 8 presents the main changes in the signal temporal profile monitored at 640 and 850 nm due to the presence of water vapour. It should be noted that both wavelengths undergo a clear quenching of the signal due to the presence of H_2O, in contrast with the previously commented results for methanol that is exclusively a hole quencher. These temporal profiles provide a sound evidence of the reactivity of the charge separation state generated on $MA_2CuCl_2Br_2$ with H_2O. However, it should be noted that the presence of H_2O at longer exposure times may cause a deterioration of the $MA_2CuCl_2Br_2$ film response, and for this reason, H_2O quenching experiments were performed exclusively with fresh samples.

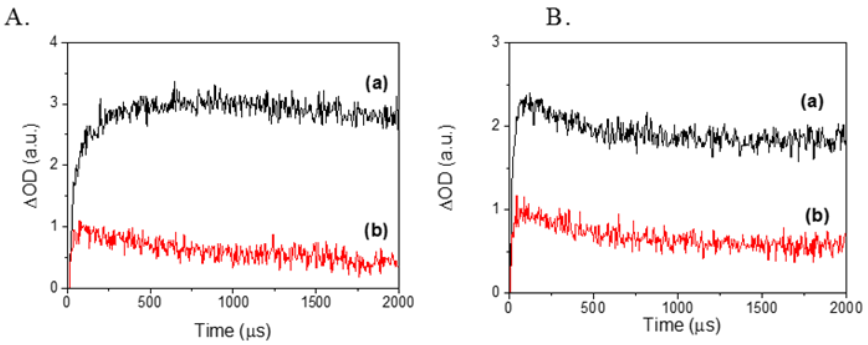

Figure 8. A) Signal decay monitored at 640 nm before (a) and after water vapor exposure (b). B) Signal decay monitored at 850 nm before (a) and after water vapor exposure (b).

The previous results, and particularly the quenching of the 640 and 850 nm bands by H_2O suggest that these transient signals correspond to a charge separation state and that water can quench both sites with hole and electron character, this being compatible with the observation of overall water splitting. Since Cortecchia et al. have assigned the 532 nm absorption to the electronic transition from Cl,Br_pπ electrons to Cu_dx^2_y^2, it is proposed that holes are localized at Cl,Br_pπ orbitals and they should be responsible for the 640 nm band. Electrons in the conduction band, on the other hand, will have a predominant location in Cu orbitals compatible with the long

wavelength of the 850 nm band in the region typically assigned to Cu electronic transitions. Scheme 2 illustrates our proposal.

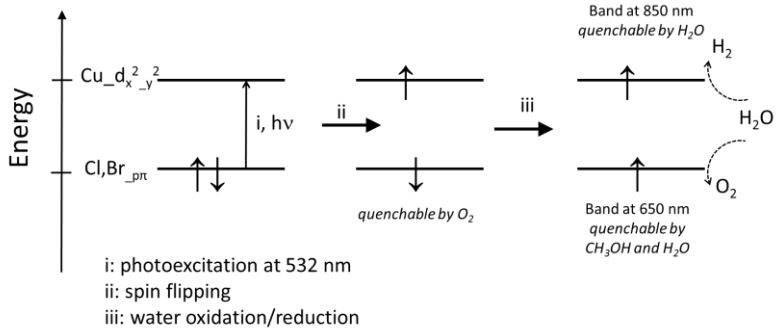

Scheme 2. Mechanistic proposal to rationalize the transient absorption spectroscopy study in the photoexcitation of $MA_2CuCl_2Br_2$.

CONCLUSIONS

In the present work, we have reported that hybrid perovskites have photocatalytic properties for overall water splitting in the absence of sacrificial agents under simulated solar light irradiation. Among the series, the studied copper methylammonium halide perovskites have been found to be the most efficient ones, reaching a specific hydrogen generation for $MA_2CuCl_2Br_2$ of 6 µmol of hydrogen per gram of catalyst/h under optimal conditions in where thin films of this hybrid copper perovskite are exposed to water vapour at temperature about 40 °C .The material appears to be stable under photocatalytic conditions according to XRD measurements that do not revealed changes in the crystallinity of powdered materials and also based on the linear temporal evolution of the hydrogen production. This photocatalytic activity seems to be general also for other hybrid perovskites, particularly those based on lead, although their efficiency is lower than that determined for $MA_2CuCl_2Br_2$. Considering the large variety of hybrid perovskites that are currently being prepared for their screening in photovoltaic devices, the present study opens the way for their evaluation also as photocatalysts, taking advantage of the narrow band gap and tunability of the optoelectronic properties that these hybrid perovskites can offer. The main limitation appears to

be stability under moisture, but this limitation can be overcome by performing photocatalytic experiments in the gas phase.

Supplementary Materials: The following are available online at www.mdpi.com/xxx/s1, Figure S1: Photocatalytic system, Figure S2: Colorimetric titration by titanyl on $MA_2CuCl_2Br_2$, Figures S3, S4 and S5: XPS analysis of $MA_2CuCl_2Br_2$, Figure S6: H_2 generation of hybrid lead halide perovskites, Scheme S1: Energy Level positions, Figure S7: VB determination of $MA_2CuCl_2Br_2$, Figure S8: Temporal evolution of H_2 generation for $MA_2CuCl_2Br_2$ perovskite, Figure S9: Temporal evolution of H_2 generation for $MA_2CuCl_2Br_2$ and $MA_2CuCl_{0.5}Br_{3.5}$ perovskites, Figure S10: Evolution of the optical absorption spectrum of the $MA_2CuCl_2Br_2$ upon laser irradiation.

Author Contributions: T.G. and R. G. performed the synthesis and photocatalytic studies; J. A. performed the TAS studies; P.A. and H.G. wrote the paper; all the authors revised the manuscript.

Acknowledgments: Financial support by Fundacion Ramon Areces (XVII Concurso Nacional para la adjudicación de Ayudas a la Investigación en Ciencias de la Vida y de la Materia), Intramural CSIC project 201680I006. Financial support by the Spanish Ministry of Spain (MAT2015-69669-P and Severo Ochoa SEV-2016-0683).

Funding: This research was funded by the Fundacion Ramon Areces (XVII Concurso Nacional para la adjudicación de Ayudas a la Investigación en Ciencias de la Vida y de la Materia), Intramural CSIC project 201680I006, and the Spanish Ministry of Spain Severo Ochoa Program, grant number SEV-2016-0683, grant number MAT2015-69669-P

Conflicts of Interest: The authors declare no conflict of interest.

References

1. National Renewable Energy Laboratory (NREL)–National Center for Photovoltaics: 'Research Cell Record Efficiency Chart'. Available online: https://www.nrel.gov/pv/assets/images/efficiency-chart.png (accessed January 19, 2020).

2. Noel, N.K.; Abate, A.; Stranks, S.D.; Parrott, E.S.; Burlakov, V.M.; Goriely, A.; Snaith, H.J. Enhanced Photoluminescence and Solar Cell Performance via Lewis Base Passivation of Organic–Inorganic Lead Halide Perovskites. ACS Nano 2014, 8, 9815–9821, doi:10.1021/nn5036476.

3. Beard, M.C.; Luther, J.M.; Nozik, A.J. The promise and challenge of nanostructured solar cells. Nat. Nanotechnol. 2014, 9, 951–954, doi:10.1038/nnano.2014.292.

4. Jean, J.; Brown, P.R.; Jaffe, R.L.; Buonassisi, T.; Bulovic, V. Pathways for solar photovoltaics. Energy Environ. Sci. 2015, 8, 1200–1219, doi:10.1039/c4ee04073b.

5. Wang, K.; Liu, C.; Du, P.; Zheng, J.; Gong, X. Bulk heterojunction perovskite hybrid solar cells with large fill factor. Energy Environ. Sci. 2015, 8, 1245–1255, doi:10.1039/C5EE00222B.

6. Kim, H.S.; Lee, C.R.; Im, J.H.; Lee, K.B.; Moehl, T.; Marchioro, A.; Moon, S.J.; Humphry-Baker, R.; Yum, J.H.; Moser, J.E.; et al. Lead Iodide Perovskite Sensitized All-Solid-State Submicron Thin Film Mesoscopic Solar Cell with Efficiency Exceeding 9%. Sci. Rep. 2012, 2, 591, doi:10.1038/srep00591.

7. Luo, D.Y.; Yang, W.Q.; Wang, Z.P.; Sadhanala, A.; Hu, Q.; Su, R.; Shivanna, R.; Trindade, G.F.; Watts, J.F.; Xu, Z.J.; et al. Enhanced photovoltage for inverted planar heterojunction perovskite solar cells. Science 2018, 360, 1442–1446, doi:10.1126/science.aap9282.

8. Pham, H.D.; Hayasake, K.; Kim, J.; Do, T.T.; Matsui, H.; Manzhos, S.; Feron, K.; Tokito, S.; Watson, T.; Tsoi, W.C.; et al. One step facile synthesis of a novel anthanthrone dye-based, dopant-free hole transporting material for efficient and stable perovskite solar cells. J. Mater. Chem. C 2018, 6, 3699–3708, doi:10.1039/c7tc05238c.

9. Gratzel, M. The light and shade of perovskite solar cells. Nat. Mater. 2014, 13, 838–842.

10. Zhang, W.; Anaya, M.; Lozano, G.; Calvo, M.E.; Johnston, M.B.; Miguez, H.; Snaith, H.J. Highly Efficient Perovskite Solar Cells with Tunable Structural Color. Nano Lett. 2015, 15, 1698–1702, doi:10.1021/nl504349z.

11. Stranks, S.D.; Snaith, H.J. Metal-halide perovskites for photovoltaic and light-emitting devices. Nat. Nanotechnol. 2015, 10, 391–402, doi:10.1038/nnano.2015.90.

12. Wang, F.; Bai, S.; Tress, W.; Hagfeldt, A.; Gao, F. Defects engineering for high-performance perovskite solar cells. npj Flex. Electron. 2018, 2, 22, doi:10.1038/s41528-018-0035-z.

13. Xing, G.C.; Mathews, N.; Sun, S.Y.; Lim, S.S.; Lam, Y.M.; Gratzel, M.; Mhaisalkar, S.; Sum, T.C. Long-Range Balanced Electron- and Hole-Transport Lengths in Organic-Inorganic CH3NH3PbI3. Science 2013, 342, 344–347, doi:10.1126/science.1243167.

14. Stranks, S.D.; Eperon, G.E.; Grancini, G.; Menelaou, C.; Alcocer, M.J.P.; Leijtens, T.; Herz, L.M.; Petrozza, A.; Snaith, H.J. Electron-Hole Diffusion Lengths Exceeding 1 Micrometer in an Organometal Trihalide Perovskite Absorber. Science 2013, 342, 341–344, doi:10.1126/science.1243982.

15. Kojima, A.; Teshima, K.; Shirai, Y.; Miyasaka, T. Organometal Halide Perovskites as Visible-Light Sensitizers for Photovoltaic Cells. J. Am. Chem. Soc. 2009, 131, 6050–6051, doi:10.1021/ja809598r.

16. Lee, M.M.; Teuscher, J.; Miyasaka, T.; Murakami, T.N.; Snaith, H.J. Efficient Hybrid Solar Cells Based on Meso-Superstructured Organometal Halide Perovskites. Science 2012, 338, 643–647, doi:10.1126/science.1228604.

17. Chen, B.; Yang, M.J.; Zheng, X.J.; Wu, C.C.; Li, W.L.; Yan, Y.K.; Bisquert, J.; Garcia-Belmonte, G.; Zhu, K.; Priya, S. Impact of Capacitive Effect and Ion Migration on the Hysteretic Behavior of Perovskite Solar Cells. J. Phys. Chem. Lett. 2015, 6, 4693–4700, doi:10.1021/acs.jpclett.5b02229.

18. Abe, R. Recent progress on photocatalytic and photoelectrochemical water splitting under visible light irradiation. J. Photochem. Photobiol. C Photochem. Rev. 2010, 11, 179–209.

19. Soldat, J.; Marschall, R.; Wark, M. Improved overall water splitting with barium tantalate mixed oxide composites. Chem. Sci. 2014, 5, 3746–3752, doi:10.1039/C4SC01127A.

20. Yang, Y.; Chen, Q.; Yin, Z.; Li, J. Study on the photocatalytic activity of K2La2Ti3O10 doped with vanadium (V). J. Alloys Comp. 2009, 488, 364–369.

21. Zhang, H.; Lü, M.; Liu, S.; Wang, L.; Xiu, Z.; Zhou, Y.; Qiu, Z.; Zhang, A.; Ma, Q. Preparation and photocatalytic property of perovskite Bi4Ti3O12 films. Mater. Chem. Phys. 2009, 114, 716–721.

22. Burschka, J.; Pellet, N.; Moon, S.J.; Humphry-Baker, R.; Gao, P.; Nazeeruddin, M.K.; Gratzel, M. Sequential deposition as a route to high-performance

perovskite-sensitized solar cells. Nature 2013, 499, 316–319, doi:10.1038/nature12340.

23. Niu, G.; Li, W.; Meng, F.; Wang, L.; Dong, H.; Qiu, Y. Study on the stability of CH3NH3PbI3 films and the effect of post-modification by aluminum oxide in all-solid-state hybrid solar cells. J. Mater. Chem. A 2014, 2, 705–710, doi:10.1039/C3TA13606J.

24. Wei, D.; Wang, T.; Ji, J.; Li, M.; Cui, P.; Li, Y.; Li, G.; Mbengue, J.M.; Song, D. Photo-induced degradation of lead halide perovskite solar cells caused by the hole transport layer/metal electrode interface. J. Mater. Chem. A 2016, 4, 1991–1998, doi:10.1039/c5ta08622a.

25. Zhang, L.; Ju, M.-G.; Liang, W. The effect of moisture on the structures and properties of lead halide perovskites: A first-principles theoretical investigation. Phys. Chem. Chem. Phys. 2016, 18, 23174–23183, doi:10.1039/C6CP01994C.

26. Leguy, A.M.A.; Hu, Y.; Campoy-Quiles, M.; Alonso, M.I.; Weber, O.J.; Azarhoosh, P.; van Schilfgaarde, M.; Weller, M.T.; Bein, T.; Nelson, J.; et al. Reversible Hydration of CH3NH3PbI3 in Films, Single Crystals, and Solar Cells. Chem. Mater. 2015, 27, 3397–3407, doi:10.1021/acs.chemmater.5b00660.

27. Frost, J.M.; Butler, K.T.; Brivio, F.; Hendon, C.H.; van Schilfgaarde, M.; Walsh, A. Atomistic Origins of High-Performance in Hybrid Halide Perovskite Solar Cells. Nano Lett. 2014, 14, 2584–2590, doi:10.1021/nl500390f.

28. Aranda, C.; Cristobal, C.; Shooshtari, L.; Li, C.; Huettner, S.; Guerrero, A. Formation criteria of high efficiency perovskite solar cells under ambient conditions. Sustain. Energy Fuels 2017, 1, 540–547, doi:10.1039/C6SE00077K.

29. You, J.; Yang, Y.; Hong, Z.; Song, T.-B.; Meng, L.; Liu, Y.; Jiang, C.; Zhou, H.; Chang, W.-H.; Li, G.; et al. Moisture assisted perovskite film growth for high performance solar cells. Appl. Phys. Lett. 2014, 105, 183902, doi:10.1063/1.4901510.

30. Zhao, Y.; Zhu, K. Organic-inorganic hybrid lead halide perovskites for optoelectronic and electronic applications. Chem. Soc. Rev. 2016, 45, 655–689, doi:10.1039/C4CS00458B.

31. Baldovi, H.G.; Albarracin, F.; Atienzar, P.; Ferrer, B.; Alvaro, M.; Garcia, H. Visible-light photoresponse of gold nanoparticles supported on TiO2: A combined photocatalytic, photoelectrochemical, and transient spectroscopy study. ChemPhysChem 2015, 16, 335–341, doi:10.1002/cphc.201402660.

32. Yang, J.; Siempelkamp, B.D.; Liu, D.; Kelly, T.L. Investigation of CH3NH3PbI3 Degradation Rates and Mechanisms in Controlled Humidity Environments

Using in Situ Techniques. ACS Nano 2015, 9, 1955–1963, doi:10.1021/nn506864k.

33. Panda, P.K. Review: Environmental friendly lead-free piezoelectric materials. J. Mater. Sci. 2009, 44, 5049–5062, doi:10.1007/s10853-009-3643-0.

34. Goyer, R.A. Lead toxicity: Current concerns. Environ. Health Perspect. 1993, 100, 177–187.

35. Slaveykova, V.I.; Wilkinson, K.J. Physicochemical aspects of lead bioaccumulation by Chlorella vulgaris. Environ. Sci. Technol. 2002, 36, 969–975, doi:10.1021/es0101577.

36. Cortecchia, D.; Dewi, H.A.; Yin, J.; Bruno, A.; Chen, S.; Baikie, T.; Boix, P.P.; Gratzel, M.; Mhaisalkar, S.; Soci, C.; et al. Lead-Free MA2CuCl(x)Br(4-x) Hybrid Perovskites. Inorg. Chem. 2016, 55, 1044–1052, doi:10.1021/acs.inorgchem.5b01896.

37. Haque, S.A.; Tachibana, Y.; Willis, R.L.; Moser, J.E.; Grätzel, M.; Klug, D.R.; Durrant, J.R. Parameters Influencing Charge Recombination Kinetics in Dye-Sensitized Nanocrystalline Titanium Dioxide Films. J. Phys. Chem. B 2000, 104, 538–547, doi:10.1021/jp991085x.

38. Xu, Y.; Schoonen, M.A.A. The absolute energy positions of conduction and valence bands of selected semiconducting minerals. Am. Mineral. 2000, 85, 543–556, doi:10.2138/am-2000-0416.

39. Walter, M.G.; Warren, E.L.; McKone, J.R.; Boettcher, S.W.; Mi, Q.; Santori, E.A.; Lewis, N.S. Solar Water Splitting Cells. Chem. Rev. 2010, 110, 6446–6473, doi:10.1021/cr1002326.

40. Kahn, A. Fermi level, work function and vacuum level. Mater. Horiz. 2016, 3, 7–10, doi:10.1039/C5MH00160A.

41. Gomes Silva, C.; Juárez, R.; Marino, T.; Molinari, R.; García, H. Influence of Excitation Wavelength (UV or Visible Light) on the Photocatalytic Activity of Titania Containing Gold Nanoparticles for the Generation of Hydrogen or Oxygen from Water. J. Am. Chem. Soc. 2011, 133, 595–602, doi:10.1021/ja1086358.

42. Ladomenou, K.; Natali, M.; Iengo, E.; Charalampidis, G.; Scandola, F.; Coutsolelos, A.G. Photochemical hydrogen generation with porphyrin-based systems. Coord. Chem. Rev. 2015, 304, 38–54.

43. Choi, H.-J.; Kang, M. Hydrogen production from methanol/water decomposition in a liquid photosystem using the anatase structure of Cu loaded TiO2. Int. J. Hydrog. Energy 2007, 32, 3841–3848.

44. Jeon, N.J.; Noh, J.H.; Yang, W.S.; Kim, Y.C.; Ryu, S.; Seo, J.; Seok, S.I. Compositional engineering of perovskite materials for high-performance solar cells. Nature 2015, 517, 476–480, doi:10.1038/nature14133.

45. Albero, J.; Asiri, A.M.; García, H. Influence of the composition of hybrid perovskites on their performance in solar cells. J. Mater. Chem. A 2016, 4, 4353–4364, doi:10.1039/c6ta00334f.

46. Mateo, D.; Esteve-Adell, I.; Albero, J.; Royo, J.F.S.; Primo, A.; Garcia, H. 111 oriented gold nanoplatelets on multilayer graphene as visible light photocatalyst for overall water splitting. Nat. Commun. 2016, 7, 11819, doi:10.1038/ncomms11819. Available online: https://www.nature.com/articles/ncomms11819#supplementary-information (accessed January 19, 2020).

47. Hisatomi, T.; Kubota, J.; Domen, K. Recent advances in semiconductors for photocatalytic and photoelectrochemical water splitting. Chem. Soc. Rev. 2014, 43, 7520–7535, doi:10.1039/c3cs60378d.

48. Kawai, H.; Giorgi, G.; Marini, A.; Yamashita, K. The Mechanism of Slow Hot-Hole Cooling in Lead-Iodide Perovskite: First-Principles Calculation on Carrier Lifetime from Electron–Phonon Interaction. Nano Lett. 2015, 15, 3103–3108, doi:10.1021/acs.nanolett.5b00109.

SUPPORTING INFORMATION: Vapor-Phase Photocatalytic Overall Water Splitting Using Hybrid Methylammonium Copper and Lead Perovskites

Teresa García[a], Rocío García-Aboal[a], Josep Albero[a], Pedro Atienzar[a]* and Hermenegildo García[a]*

[a]Instituto Universitario de Tecnología Química CSIC-UPV, Universidad Politecnica de Valencia, Av. de los Naranjos s/n, 46022 Valencia, Spain

A)

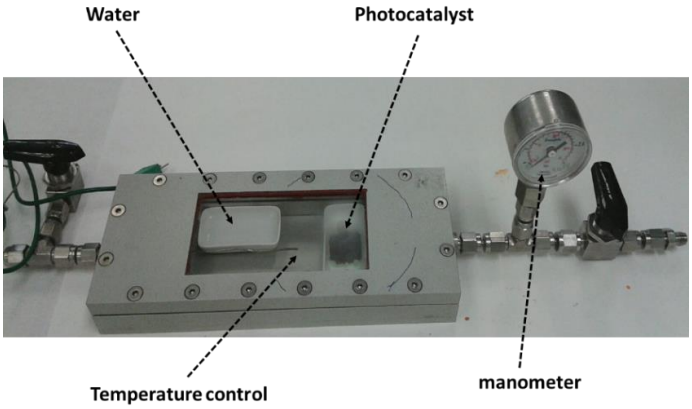

B)

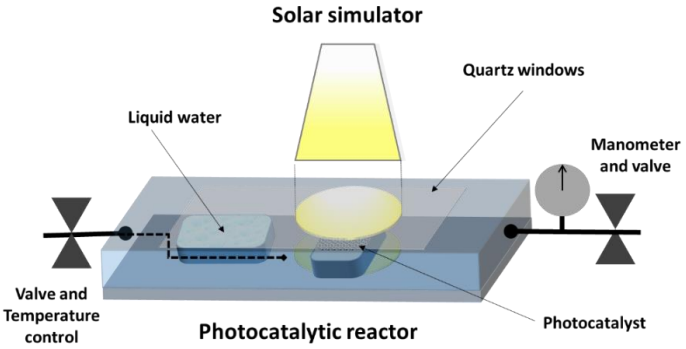

Figure S1. A) Home-made reactor employed for the photocatalytic activity measurements of the hybrid perovskites. Note that liquid water, providing the vapour for the photocatalytic reaction is in a separate container close to the hybrid metal halide photocatalyst. B) Representation of the photocatalytic system during the reaction process.

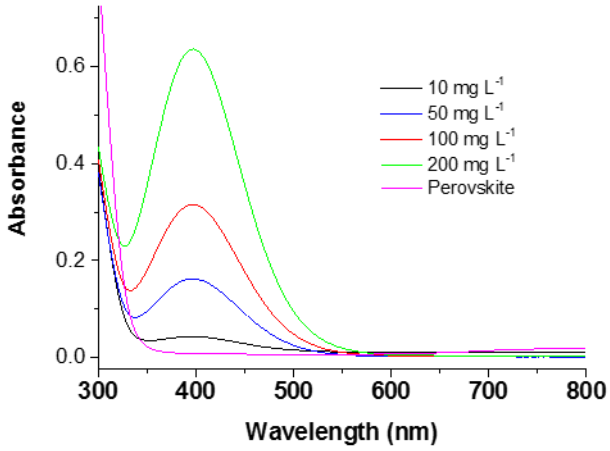

Figure S2. Colorimetric titration by titanyl on $MA_2CuCl_2Br_2$ to determine the H_2O_2 formation.[42]

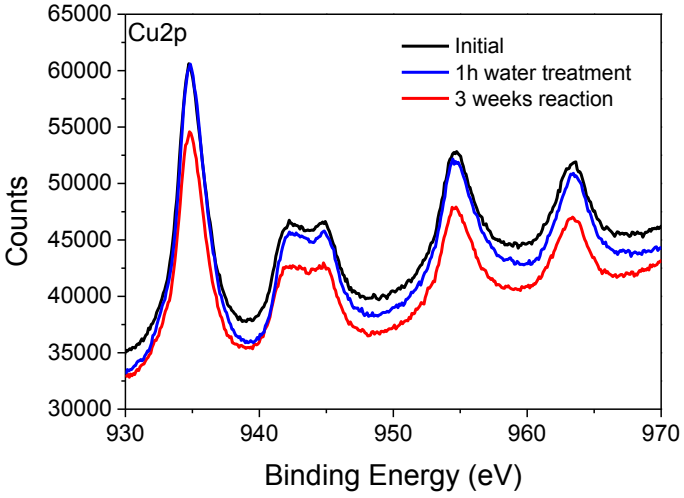

Figure S3. XPS analysis of $MA_2CuCl_2Br_2$ measured on a fresh sample, exposed to 1 hour water atmosphere (quickly measured) and after 3 weeks reaction.

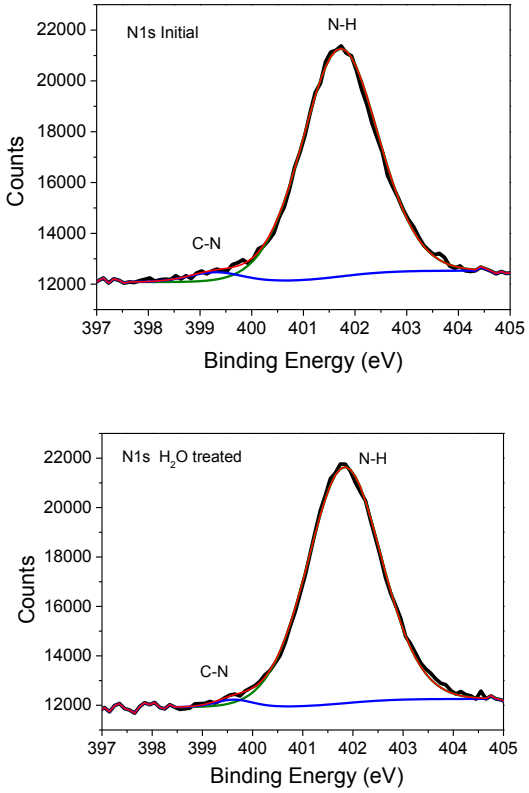

Figure S4. XPS analysis on $MA_2CuCl_2Br_2$ of N1s binding energy measured in a fresh sample (top), and after moisture exposure (bottomt).

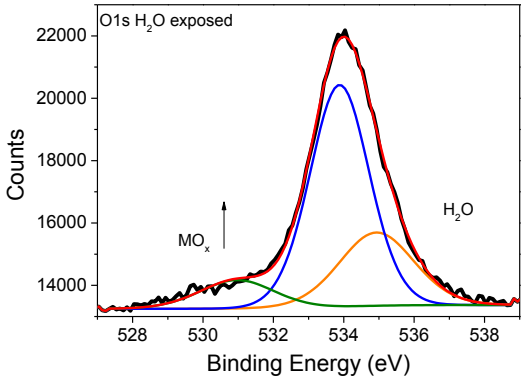

Figure S5. XPS analysis on $MA_2CuCl_2Br_2$ of O1s binding energy measured after moisture exposure.

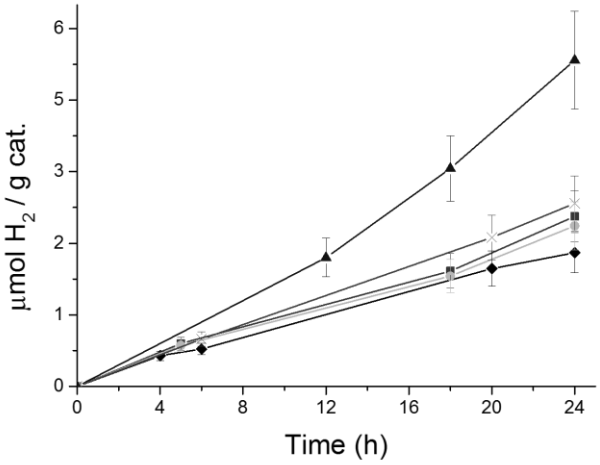

Figure S6. H_2 generation upon UV-Vis irradiation of hybrid lead halide perovskites: a) $MAPbBrI_2$, b) $MAPbClI_2$, c) $MAPbI_3$, d) $MAPbCl_3$ and e) $MAPbBr_3$ as function of time. Reaction conditions: 10 mg of photocatalyst as thick bed and irradiation with a solar simulator (1000 W/m^2).

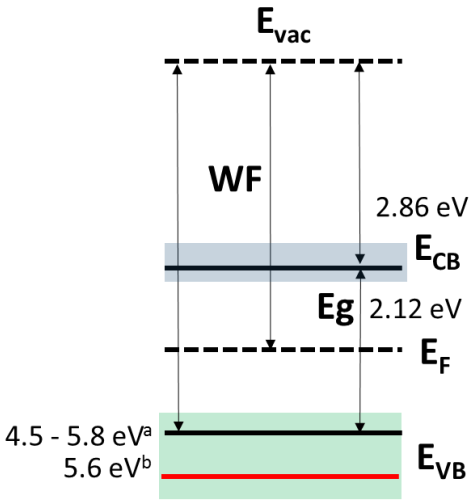

Scheme S1. Energy Level position based on the UPS measurements of the reference copper perovskite. [a]Based on data reported in reference 36, [b]based in our XPS measurements.

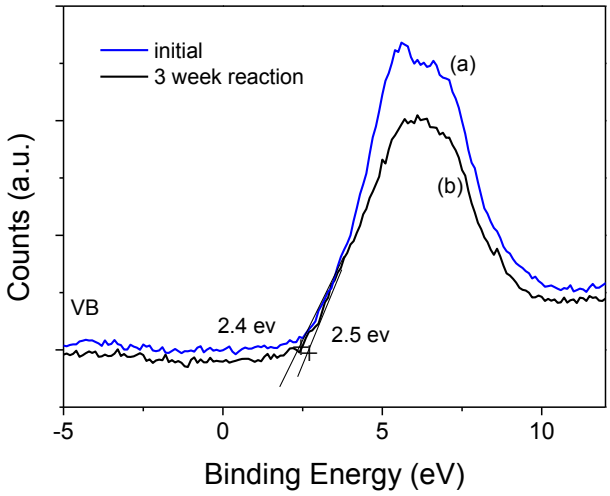

Figure S7. VB determination by XPS analysis of fresh $MA_2CuCl_2Br_2$ (a) and after moisture exposure (b).

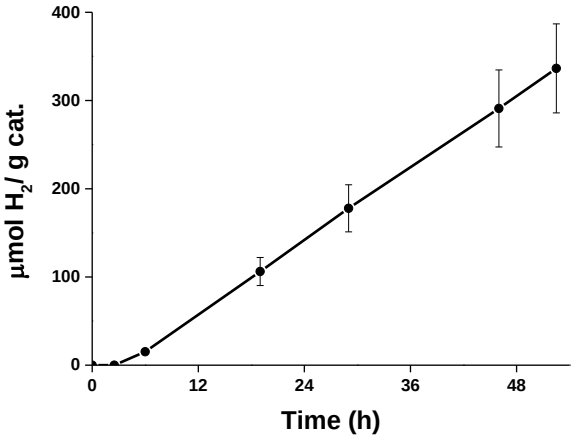

Figure S8. Temporal evolution of H_2 generation upon sunlight irradiation of H_2O vapors in the presence of hybrid copper halide perovskite $MA_2CuCl_2Br_2$.

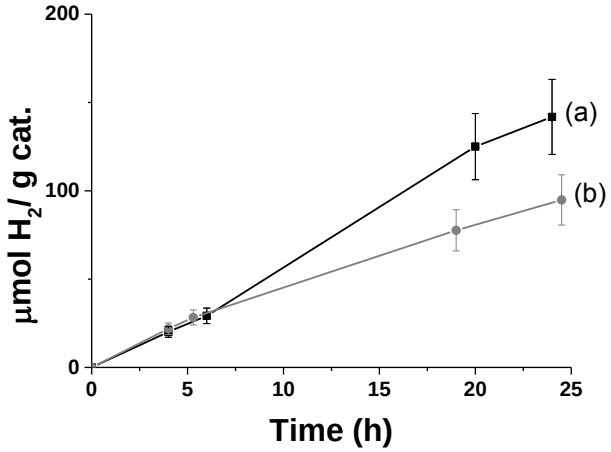

Figure S9. Temporal evolution of H_2 generation upon sunlight irradiation of H_2O vapors in the presence of hybrid copper halide perovskite $MA_2CuCl_2Br_2$ (a) and $MA_2CuCl_{0.5}Br_{3.5}$ (b).

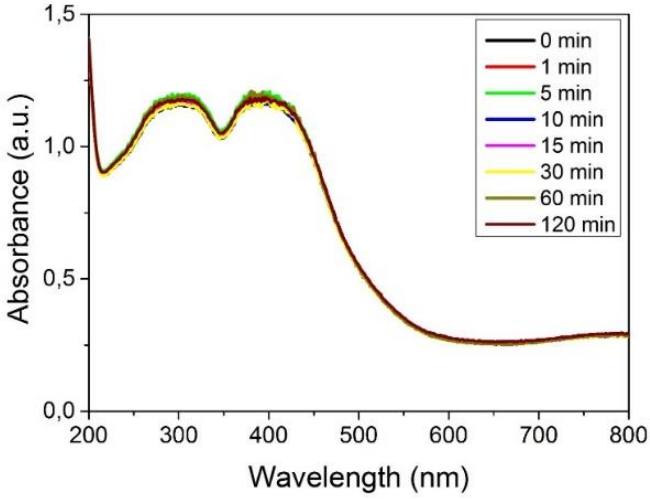

Figure S10. Optical absorption spectrum of the $MA_2CuCl_2Br_2$ film as a function of laser time irradiation.

CAPÍTULO 5

SENSOR DE GAS

SECCIÓN 5.1

THE ROLE OF ANION AND CATION IN THE GAS SENSING MECHANISMS OF GRAPHENE DECORATED WITH LEAD HALIDE PEROVSKITES NANOCRYSTALS

Juan Casanova-Chafer, Rocio Garcia-Aboal, Pedro Atienzar and Eduard Llobet

Chem. Comm. 2020, 56 (63), 8956-8959

DOI: 10.1039/d0cc02984j

THE ROLE OF ANION AND CATION IN THE GAS SENSING MECHANISMS OF GRAPHENE DECORATED WITH LEAD HALIDE PEROVSKITES NANOCRYSTALS

Juan Casanova-Chafer,[†a] Rocio Garcia-Aboal,[†b] Pedro Atienzar[*b] and Eduard Llobet[*a]

[a]MINOS, Universitat Rovira i Virgili, 43007 Tarragona, Spain.

[b]Instituto de Tecnología Química, CSIC-UPV, Universitat Politècnica de València, 46022 Valencia, Spain.

[c]E-mail: pedatcor@itq.upv.es and eduard.llobet@urv.cat

[d]† Authors that contributed equally to the work.

††Electronic Supplementary Information (ESI) available. See DOI: 10.1039/d0cc02984j

Abstract

We report the effects of both, anion and cation in lead halide perovskite-graphene hybrids applied to gas sensing. Ultra-fast sensors able to work at room temperature are developed and studied to elucidate the role in the gas sensing mechanisms of different ions in perovskite nanocrystals decorating graphene.

1. INTRODUCTION

During the last decades, air pollution has been increasing its noxious effects to our environment and human health. To tackle these problems and help protect the environment and the population well-being, ubiquitous and continuous monitoring of air pollutants is needed. However, the development of a widespread air quality sensor network would only be possible if reliable, low-cost and low-power consumption sensing devices became available. Such new sensing networks would complement the currently employed instrumental techniques, like gas chromatography and mass spectroscopy, which despite their accuracy and low detection limits, are bulky and expensive[1]. Among the different technological alternatives, chemiresistive sensors can be a suitable option thanks to their facile fabrication and use. Most resistive gas sensors developed and

commercialised to date employ metal-oxides (MOx) because they show interesting properties such as fair stability and high sensitivity[2]. However, MOx show important limitations that jeopardize their usefulness for being integrated in autonomous gas sensing networks. While the main drawback is their lack of selectivity, the fact they require high operating temperatures, and thus, high-power consumption is also an important barrier for their adoption[3].

In the last years, graphene has attracted great research interest for developing a new generation of low-power gas sensors. Ideally, graphene possesses the highest surface area to volume ratio (in atomically thin graphene all atoms are exposed to its chemical environment), high carrier density and mobility (associated to low noise)[4] and ability to show a chemiresistive behaviour at room temperature[5]. However, its pristine structure (sp^2 carbon configuration) exhibits chemical inertness, offering low gas sensitivity and selectivity. For that reason, the functionalisation of graphene has been envisaged. The most reported modification has been the decoration of carbon nanomaterials with catalytic metal or metal oxide nanoparticles[6]. This approach improves gas responsiveness and, to some extent, helps tuning selectivity. However, this approach involves raising the operating temperature of sensors above the ambient for nanoparticles to play their electronic and chemical sensitization roles. Conversely, other alternatives like plasma treating of graphene (promotes defects and grafting of functional groups) enable increasing responsiveness at room temperature but do not ameliorate selectivity to a very high extent[7]. Sensitivity is largely affected by how the graphene is prepared[8] (e.g. CVD growth, exfoliation or others, ESI†)).

In the last few years, increasing research efforts have been focused towards the development of gas sensors using perovskites. Perovskites can be easily implemented in room-temperature operating chemiresistive sensors via solution processing methods, which make them very attractive for their low-cost and facile synthesis. Additionally, perovskites show very interesting properties from the gas sensing point of view, such as tuneable bandgap, large adsorption coefficient and long carrier lifetimes[9]. Band gap tuning can

be accomplished by altering the perovskite structure ABX_3 via compositional substitution in the A, B, and/or X site. However, perovskites present as important drawback their instability under humid conditions[10], which has prevented their commercial application so far. Recently, the dispersion of perovskite nanocrystals on graphene has been shown very effective at protecting perovskites against the effect of ambient moisture and thus, at preventing their long-term degradation, thanks to the high hydrophobicity of graphene[11]. Therefore, the use of perovskite-loaded graphene holds promise for achieving sensitive, selective, low-cost and low-power consumption gas sensors.

Despite that a few reports are available on different perovskite configurations for gas sensing, a study about the effects of changing the perovskite composition on the resulting gas sensing properties is still missing. What is more, there is a lack of results clearly showing if changes in the cation (A) or the anion (X) in the ABX_3 perovskite structure have significant influence on gas sensing properties.

Therefore, in this paper we report the first comprehensive study on the role played by different cations (A) and halide anions (X) on the sensing properties towards volatile organic compounds (VOCs) exhibited by lead halide perovskite nanocrystals loaded onto graphene nanoflakes (Gf). Graphene flakes show a semi-metallic behaviour and their properties can be tailored by functionalization. The Gf used here are few-layer graphene flakes that show a small amount (less than 10%) of oxygen-containing groups, which confer enhanced hole transport properties to this carbon nanomaterial via shifting the Fermi level towards the valence band and increasing the work function (WF) value[12]. In addition, low-oxygen Gf retain the high hydrophobic characteristic of graphene, which has been shown to confer high stability to the gas sensing properties of perovskite-graphene hybrids, as mentioned above[11].

Thus, different perovskite nanocrystals (NCs) were synthesized (Text S1, ESI†). In particular, several syntheses[13–15] were followed to obtain NCs with three cations (methylammonium, MA ($CH_3NH_3^+$); formamidinium, FA ($(NH_2)_2CH^+$); caesium (Cs^+)), and the effect of three

halide anions (Cl^-, Br^- and I^-) was also studied. Nevertheless, the perovskite with triiodide anion ($MAPbI_3$) has been reported as a very unstable NC, even at room temperature. The main reason for their fast degradation is due to the change to PbI_2 in the presence of ambient moisture, resulting in a significant decrease in sensing performance[16]. For that reason, a mixture with bromide was prepared ($MAPbBr_{2.5}I_{0.5}$) for better understanding about the role of iodine and easier comparison with the $MAPbBr_3$ perovskite.

2. RESULTS AND DISCUSSION

For better comparing the performances of the different NCs and for achieving suitable graphene decoration, the synthesis processes were adapted to obtain perovskite NCs of 6 to 8 nanometres in size (Fig. 1), for any of the configurations studied (Fig. S1 and Table S1, ESI†). Additionally, XRD patterns (Fig. S2, ESI†) confirm the high crystallinity obtained for the NCs synthesised. Finally, the different NCs were used to obtain a quite homogeneous graphene decoration (Fig. S3, ESI†).

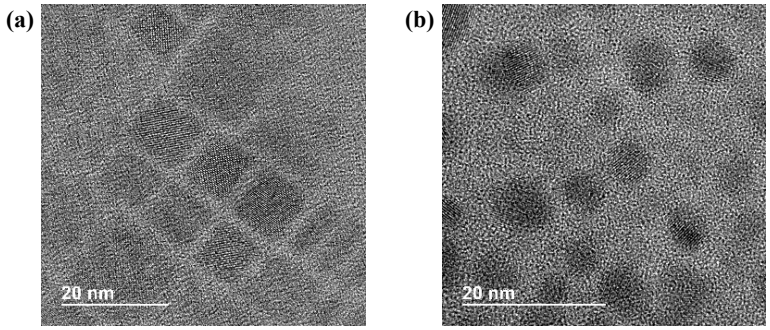

Figure 1. Example of HRTEM image $CsPbBr_3$ (a) and $MAPbCl_3$ (b) NCs (more details in Fig. S1, ESI†).

The resulting hybrid nanomaterials were deposited onto alumina substrates with interdigitated electrodes that were connected to a gas sensing mixture and delivery system (Text S2 and Fig. S4, ESI†).

The gas sensing devices were employed to detect aromatic VOCs such as benzene and toluene. Monitoring aromatic VOCs is of interest due to their dangerousness (e.g. benzene is carcinogenic), and their

detection at trace levels in the environment is very relevant for the petrochemical industry. Additionally, some VOCs constitute potential biomarkers for the detection of diseases at an early stage. For instance, the occurrence of some VOC concentration patterns in exhaled breath have been associated to sub-clinical lung cancer[17].

Despite that room temperature operation usually involves weak sensor baseline recovery due to the associated low desorption rate of adsorbed gas molecules during the cleaning phases of cycled gas exposures[18], here all measurements were run at room temperature. There are two reasons for this. First, assessing sensor performance under low-power consumption mode and second, to preserve perovskite NCs against their degradation, thus greatly improving sensor lifetime. Additionally, sensors were operated in a background of air, under low flow rates and subject to short exposure and recovery times in order to better match the operating conditions of a low cost air quality monitor.

Graphene with different perovskite NCs structures were exposed to continuous response and recovery cycles of 2, 4, 6 and 8 ppm of benzene and toluene (Fig. S5, ESI†). Some examples of the electrical responses registered upon the exposure to VOCs vapours are shown in Figure 2 (see a zoom in Fig. S6, ESI†). Gas exposure was limited to 1 min and baseline recovery was limited to 5 min in dry air. Highly reversible and reproducible responses were obtained (see also Table S2), despite the saturation of sensor response was not reached. This approach sacrifices response intensity but has the advantage of enabling faster measurements. The saturated response and full baseline recovery for a sensor are shown in Fig. S7 with a short discussion on our measurement approach, ESI†. In fact, an additional reproducibility analysis was performed (Fig. S8, ESI†) in order to confirm these results. Moreover, ultrafast responses (few tens of seconds) were achieved. It is well known that pristine graphene in a chemiresistor configuration shows very weak and very slow response to gas molecules[19]. However, since the direct adsorption of gas molecules onto graphene cannot be ruled out as responsible for the response recorded in perovskite-loaded graphene, measurements were also recorded with a bare graphene sensor. With the bare

graphene sensor exposed to VOC cycles, it was impossible to distinguish responses from the noise (Fig. S9, ESI†). Therefore, in perovskite NC loaded graphene chemiresistors, the responses obtained can be attributed to the effect of the different perovskite NCs, which play the role of chemical receptors, while graphene plays mainly the role of an efficient charge conductor, ensuring that the charges generated upon the interaction between VOC molecules and perovskite NCs reach the device electrodes.

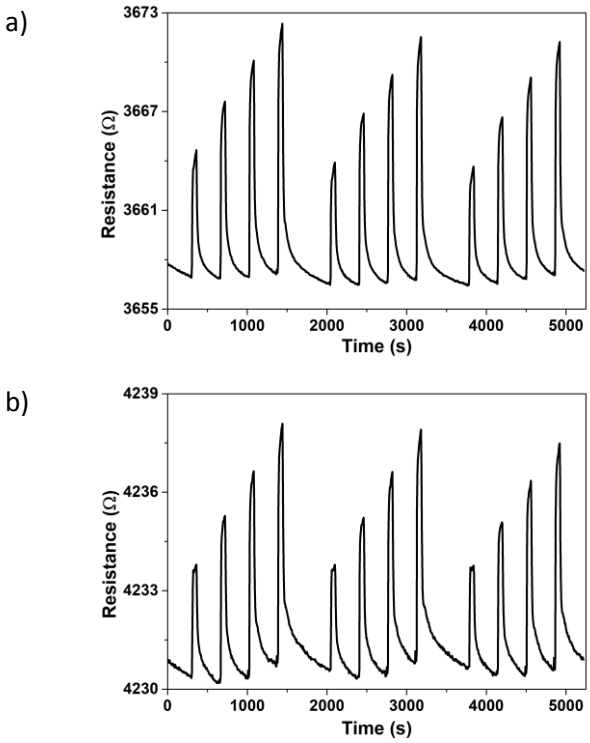

Figure 2. Examples of electrical responses to 2, 4, 6 and 8 ppm of benzene during 3 cycles by using $MAPbBr_3$ (a) and $MAPbCl_3$ (b) perovskites.

Figure 3 shows the benzene calibration curves obtained for the different cations (a) and halide anions (b) studied. Regarding the effect of the cation, MA shows a clear enhancement in the responses (up to 3-fold) against FA and Cs and in sensitivity (slope of the calibration curve). Meanwhile, the responses obtained by using different halide anions reveal that Br- anions offer higher response and sensitivity than

Cl^- and I^- anions. Equivalent behaviour was observed for toluene vapours (Fig. S10, ESI†).

Aromatic molecules such as benzene and toluene can act as electron donating groups because of their delocalised electrons. A significant effect of the cations Cs, MA or FA in the graphene decorated with perovskite NCs is clearly observed when they are exposed to benzene and toluene. In fact, higher electrical responses to both gases are registered when MA is present in the perovskite structure. These superior electrical properties are derived from the energy level positions (band structure) and concentration of trap defects. It is interesting to compare the band structure for the three cation-substituted perovskites with the expected WF of the Gf, according to its oxygen content[12] (Fig. 4a). In that sense, the $MAPbBr_3$ perovskite shows the better energy-level alignment with the Gf material for hole extraction, in comparison to the other two cation-substituted perovskites ($CsPbCl_3$ and $FAPbCl_3$). This probably explains the enhanced electrical response recorded for $MAPbBr_3$. Nevertheless, there are probably more reasons to explain this enhanced response. For instance, the superficial trap density from the under-coordinated Pb ions at the NC surface is one of the key processes in the interaction with external molecules. Recently, it has been reported that aromatic compounds can passivate the surface of NCs, thus modifying their electrical/electronic properties[20]. Therefore, it is postulated that $MAPbBr_3$ NCs have higher trap density than $CsPbBr_3$ and $FAPbBr_3$ NCs.

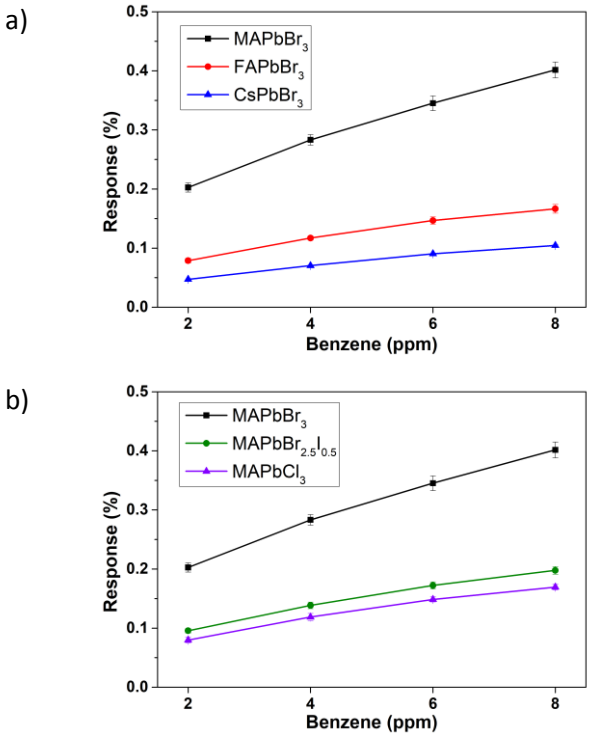

Figure 3. Calibration curves obtained for benzene detection using lead halide perovskites with different cation (a) and anion (b).

In fact, this is supported by the reported photophysical properties of perovskite nanocrystals with similar cation composition. Indeed, $CsPbBr_3$ and $FAPbBr_3$ NCs show slightly higher photoluminescence quantum yield than $MAPbBr_3$[25]. Because it is well known that defects, such as vacancies, act as carrier traps and, thereby, quench photoluminescence[26], it can be derived that $MAPbBr_3$ NCs contain more defects. An increased number of defects rises the availability of active sites for interacting with vapour molecules and increases the electrical response.

The influence of the halide anion in the response to VOCs was also studied. A series of lead halide perovskite NCs employing MA as cation and having the compositions $MAPbCl_3$, $MAPbBr_3$ and $MAPbBr_{2.5}I_{0.5}$ were synthesised, loaded to Gf and tested. Once more, $MAPbBr_3$ led to the best responses towards benzene and toluene vapours, in spite

of the fact that the $MAPbBr_{2.5}I_{0.5}$ perovskite shows a better energy-level alignment with the Gf material for hole extraction (Fig. 4b). Therefore, apart from having a suitable energy-level alignment for hole extraction, or a higher number of superficial defects, another reason could be intrinsically responsible for the better response recorded for the perovskite that contains bromide in its structure. In this regard, several studies have reported significant differences in carrier mobility for electrons and holes as a function of the halide anion used. For instance, while the iodine perovskite $MAPbI_3$ exhibits an ambipolar behaviour with similar mobilities for electron and holes, $MAPbBr_3$ exhibits a preferential unipolar behaviour with good p-type conductivity[27,28]. As a result, the excess of positive charges generated at the surface of the perovskite NCs upon their interaction with VOCs is transferred more efficiently to Gf, due to the high hole mobility in $MAPbBr_3$ NCs. This translates into an enhanced gas sensing response in comparison to the one of perovskites containing other halide anions.

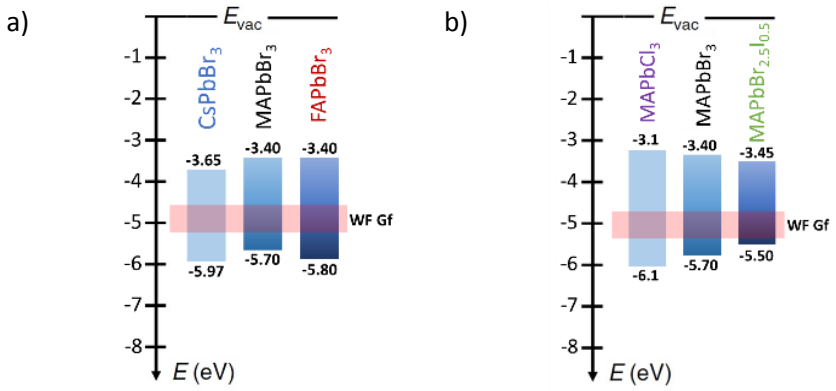

Figure 4. Band structure diagram of the perovskite NCs with different cations (a[21,22]) and anions (b[21,23]). $MAPbBr_{2.5}I_{0.5}$ values have been estimated according to the bibliography[23,24].

Therefore, based on the ionic–electronic properties of perovskite NCs decorating Gf, it can be assumed that undercoordinated lead atoms induce a net positive charge at the surface of the perovskite NCs due to the halide vacancies. When aromatic compounds such as benzene or toluene are in the environment acting as electron donating

molecules, they passivate the halide vacancies in the perovskite and reduce the total amount of positive charges in the nanomaterial, increasing its resistivity. When exposed to clean air, an exchange of charges at the interface occurs and this gives rise to an excess of free charges in the nanomaterial, increasing its conductivity.

Despite the detailed explanation offered for the detection of gases such as benzene and toluene, which have a dipole moment close to zero. Additional phenomena could be involved in the detection of other gases with different properties such as higher reactivity, binding energy or amount of charge transfer, to cite some. Interestingly, preliminary results for the detection of nitrogen dioxide (NO_2) and ammonia (NH_3) by using the different lead halide perovskites studied here reveal significant differences in sensitivity and selectivity. For instance, graphene decorated with $FAPbBr_3$ NCs shows high response towards NO_2, which is an electron withdrawing gas (Fig. S11a, ESI†). Meanwhile, no sensitivity was observed for NH_3 (Fig. S11b, ESI†), which corresponds to an electron donor. Moreover, graphene decorated with $MAPbCl_3$ NCs shows higher response (2-fold) to NH_3 than $MAPbBr_3$ (Fig. S11c, ESI†). These results obtained with FA and Cl^- indicate that additional sensing mechanisms cannot be ruled out and that more studies are needed to better understand these. However, considering the lack of previous studies about the changes in gas sensing properties derived from substituting cation and anion in lead halide perovskites, these preliminary results constitute a great step forward towards the development of selective gas sensors operating at room temperature.

CONCLUSIONS

This paper shows for first time that the anion and cation in the perovskite structure (ABX_3) have a significant effect on gas sensing performance. In particular, gas sensors employing graphene decorated with different perovskite configurations were successfully employed to detect VOC vapours at ppm levels. The devices developed achieve highly reproducible, reversible, sensitive and ultrafast detection of VOCs at room temperature. The low noise levels in sensor responses indicate that trace detection (at ppb levels) of VOCs would

be possible. These results pave the way towards the development of reliable, inexpensive, durable and low-power chemiresistive sensors for an ubiquitous air monitoring. Furthermore, the approach proposed has a high potential for greatly improving selectivity in a systematic way, which has been a major challenge with gas sensors. Indeed, the edition of a library of perovskite nanomaterials, via changing the cation and/or anion in the ABX_3 structure, realises the possibility of tailoring gas response to a wide spectrum of specific targets.

This work was supported in part by MICINN and FEDER via grants no. RTI2018-101580-B-I00, by AGAUR under grant. 2017SGR418. J.C.C gratefully acknowledges a postdoctoral fellowship from URV. R.G.A. acknowledges an FPI scholarship from MINECO TEC2015-74405-JIN and MAT2015-69669-P. P.A. acknowledges the financial support from the Spanish Government through 'Severo Ochoa" (SEV-2016-0683, MINECO) and PGC2018-099744-B-I00 (MCIU/AEI/FEDER). E.L. is supported by the Catalan institution for Research and Advanced Studies via the 2018 Edition of the ICREA Academia Award.

Conflicts of interest

There are no conflicts to declare.

Notes and references

1. Garg, M. Akbar, E. Vejerano, S. Narayanan, L. Nazhandali, L. C. Marr and M. Agah, Sensors Actuators, B Chem., 2015, 212, 145–154.

2. Y. B. Hahn, R. Ahmad and N. Tripathy, Chem. Commun., 2012, 48, 10369–10385

3. B. Zhang and P. X. Gao, Front. Mater., 2019, 6, 55.

4. C. Soldano, A. Mahmood and E. Dujardin, Carbon N. Y., 2010, 48, 2127–2150.

5. J. Casanova-Chafer and E. Llobet, in NATO Science for Peace and Security Series A: Chemistry and Biology, Springer Verlag, 2019, pp. 13–32.

6. A. V. Singhal, H. Charaya and I. Lahiri, Crit. Rev. Solid State Mater. Sci., 2017, 42, 499–526.

7. H. Wu, X. Bu, M. Deng, G. Chen, G. Zhang, X. Li, X. Wang and W. Liu, Sensors, 2019, 19, 625.

8. F. Ricciardella, S. Vollebregt, T. Polichetti, M. Miscuglio, B. Alfano, M. L. Miglietta, E. Massera, G. Di Francia and P. M. Sarro, Nanoscale, 2017, 9, 6085–6093.

9. Z. Zhu, Q. Sun, Z. Zhang, J. Dai, G. Xing, S. Li, X. Huang and W. Huang, J. Mater. Chem. C, 2018, 6, 10121–10137.

10. T. A. Berhe, W. N. Su, C. H. Chen, C. J. Pan, J. H. Cheng, H. M. Chen, M. C. Tsai, L. Y. Chen, A. A. Dubale and B. J. Hwang, Energy Environ. Sci., 2016, 9, 323–356.

11. J. Casanova-Cháfer, R. García-Aboal, P. Atienzar and E. Llobet, Sensors, 2019, 19, 4563.

12. R. Garg, N. Dutta and N. Choudhury, Nanomaterials, 2014, 4, 267–300.

13. L. C. Schmidt, A. Pertegás, S. González-Carrero, O. Malinkiewicz, S. Agouram, G. Mínguez Espallargas, H. J. Bolink, R. E. Galian and J. Pérez-Prieto, J. Am. Chem. Soc., 2014, 136, 850–853.

14. L. Protesescu, S. Yakunin, M. I. Bodnarchuk, F. Krieg, R. Caputo, C. H. Hendon, R. X. Yang, A. Walsh and M. V. Kovalenko, Nano Lett., 2015, 15, 3692–3696.

15. L. Protesescu, S. Yakunin, M. I. Bodnarchuk, F. Bertolotti, N. Masciocchi, A. Guagliardi and M. V. Kovalenko, J. Am. Chem. Soc., 2016, 138, 14202–14205.

16. Y. Zhao and K. Zhu, Chem. Commun., 2014, 50, 1605–1607.

17. A. G. Dent, T. G. Sutedja and P. V. Zimmerman, J. Thorac. Dis., 2013, 5, 540–550.

18. R. K. Paul, S. Badhulika, N. M. Saucedo and A. Mulchandani, Anal. Chem., 2012, 84, 8171–8178.

19. S. S. Varghese, S. Lonkar, K. K. Singh, S. Swaminathan and A. Abdala, Sensors Actuators, B Chem., 2015, 218, 160–183.

20. E. T. Vickers, T. A. Graham, A. H. Chowdhury, B. Bahrami, B. W. Dreskin, S. Lindley, S. B. Naghadeh, Q. Qiao and J. Z. Zhang, ACS Energy Lett., 2018, 3, 2931–2939.

21. S. Adjokatse, H. H. Fang and M. A. Loi, Mater. Today, 2017, 20, 413–424.

22. F. Li, L. Yang, Z. Cai, K. Wei, F. Lin, J. You, T. Jiang, Y. Wang and X. Chen, Nanoscale, 2018, 10, 20611–20617.

23. J. Huang, S. Xiang, J. Yu and C. Z. Li, Energy Environ. Sci., 2019, 12, 929–937.

24. A. Y. Lee, D. Y. Park and M. S. Jeong, J. Alloys Compd., 2018, 738, 239–245.

25. J. Chen, M. E. Messing, K. Zheng and T. Pullerits, J. Am. Chem. Soc., 2019, 141, 3532–3540.

26. X. Li, F. Cao, D. Yu, J. Chen, Z. Sun, Y. Shen, Y. Zhu, L. Wang, Y. Wei, Y. Wu and H. Zeng, Small, 2017, 13, 1603996.

27. L. M. Herz, ACS Energy Lett., 2017, 2, 1539–1548.

28. Y. Kang and S. Han, Phys. Rev. Appl., 2018, 10, 044013.

SUPPLEMENTARY INFORMATION: The role of anion and cation in the gas sensing mechanisms of graphene decorated with lead halide perovskite nanocrystals

Juan Casanova-Chafer,[†a] Rocio Garcia-Aboal,[†b] Pedro Atienzar[*b] and Eduard Llobet[*a]

[a]MINOS, Universitat Rovira i Virgili, 43007 Tarragona, Spain.

[b]Instituto de Tecnología Química, CSIC-UPV, Universitat Politècnica de València, 46022 Valencia, Spain.

E-mail: pedatcor@itq.upv.es and eduard.llobet@urv.cat

† Authors that contributed equally to the work.

Text S1. Perovskite nanocrystal syntheses.

It is well-known that lead halide perovskites present the following configuration: ABX_3. Where B is the Pb^{+2}, A corresponds to an organic or inorganic cation, in our case we employed MA ($CH_3NH_3^+$), FA ($(NH_2)_2CH^+$) and caesium (Cs^+). Meanwhile, X_3 represents the anion, in our work we used Cl^-, Br^- and I^-. To obtain the different perovskite nanocrystals, different synthesis routes were followed:

$MAPbX_3$ (where X = Br^-, Cl^-, I^-): the synthesis of perovskite NCs having MA cation was adapted from the method proposed by L. Schmidt et al[1]. First, a common solution for the next step was prepared, 85 mg of oleic acid (OA) were added to 2 mL of 1-octadene (ODE). The solution was stirred and heated to 80°C. Afterwards, 33.5 mg of octylammonium bromide (OABr) were added.

Then, another specific solution was prepared for each perovskite anion by using different precursors. In the case of $MAPbBr_3$ nanocrystals, 26.4 mg and 18.3 mg of methylammonium bromide (MABr) and lead (II) bromide ($PbBr_2$) respectively, were dissolved in 200 µL of Dimethylformamide (DMF). Meanwhile, 3.37 mg and 13.9 mg of methylammonium chloride (MACl) and lead (II) chloride ($PbCl_2$) respectively, were dissolved in 200 µL of Dimethylsulfoxide (DMSO) to form $MAPbCl_3$. Lastly, to prepare the $MAPbBr_{2.5}I_{0.5}$ nanocrystals, 2.7 mg, 3 mg and 18.5 mg of methylammonium iodine (MAI), methylammonium bromide (MABr) and lead (II) bromide ($PbBr_2$)

respectively, were added to 300 µL of DMF. The solutions were stirred until complete dissolution.

Finally, each solution with the specific precursors was added to the first reported solution. Then, the solutions were cooled to 60°C and 5 mL of acetone were added, inducing the immediate precipitation of the different nanocrystals. In fact, a yellow, white and yellow-orange precipitates were obtained for $MAPbBr_3$, $MAPbCl_3$ and $MAPbBr_{2.5}I_{0.5}$ respectively. Then, the solutions were centrifugated at 6000 rpm for 10 minutes in order to extract the precipitates. Afterwards, the precipitates were dispersed in Toluene.

$CsPbBr_3$: for the synthesis of this type of nanocrystals was followed the method proposed by L. Protesescu et al[2]. To prepare the Cs-oleate, a 3-neck flask was loaded with Cs_2CO_3 (814 mg), ODE (40 mL) and OA (2.5 mL). Then, the solution was mixed under stirring and was heated to 120°C for 1 hour. Afterwards, the temperature was increased up to 150°C under a nitrogen atmosphere to ensure the complete reaction of Cs_2CO_3 with the oleic acid. Then, the solution was cooled to room temperature, obtaining a precipitate of Cs-oleate.

Subsequently, another solution was prepared by mixing 69 mg of $PbBr_2$ and 5 mL of ODE in a 3-neck flask. Continuously, the solution was dried under vacuum at 120°C for 1 hour. Then, 0.5 mL of dried oleylamine (OLA) and OA were injected meanwhile a nitrogen atmosphere was created. After complete solubilization, the temperature was raised to 140°C and Cs-oleate solution (0.4 mL, preheated to 100°C before injection) was quickly injected. Five seconds later, the final solution was cooled down by using an ice-water bath. Finally, 5 mL of Tert-butyl alcohol (tBuOH) was added to help the complete NCs precipitation. After the centrifugation step reported in the previous synthesis, the $CsPbBr_3$ NCs were redispersed in hexane.

$FAPbBr_3$: NCs containing FA cation were prepared following the method proposed by L. Protesescu et al[3]. First, FA-oleate precursor was prepared, where a 3-neck flask was loaded with 521 mg of formamidinium acetate ($FA(CH_3COO)$) and 20 mL of OA in order to prepare the FA-oleate. Then, similarly to the above synthesis, the solution was heated to 120°C for 1 hour. Subsequently, the

temperature was increased up to 130°C until the complete reaction. Then, the FA-oleate was dried for 30 min at 50°C under vacuum and finally cool to room temperature.

Then, other solution was prepared by mixing ODE (5 mL) and $PbBr_2$ (69 mg) in a 3-neck flask. The solution was continuously dried under vacuum for 1 hour at 120°C. Afterwards, 0.5 mL of OLA and 1 mL of OA were injected at 120°C under nitrogen flow. After complete solubilization of the $PbBr_2$ salt, the temperature was lowered to 100°C. Then, 2.5 mL of FA-oleate solution was quickly injected and, 5 sec later, the reaction mixture was cooled by using an ice-water bath. Finally, 10 mL of toluene and 5 mL of acetonitrile were added to help the complete precipitation of NCs. Finally, the solution was centrifugated and the $FAPbBr_3$ NCs were redispersed in hexane.

In order to clarify the different synthesis, a summary is added:

Perovskite	Precursors	Synthesis Reagents	Solvent	Solvent Stabilizer
$MAPbBr_3$	26.4 mg MABr 18.3 mg $PbBr_2$	85 mg OA 2 mL ODE 33.5 mg OABr	5 mL Acetone 200 µL DMF	Toluene
$MAPBCl_3$	3.37 mg MACl 13.9 mg $PbCl_2$	85 mg OA 2 mL ODE 33.5 mg OABr	5 mL Acetone 200 µL DMSO	Toluene
$MAPbBr_{2.5}I_{0.5}$	2.7 mg MAI 3 mg MABr 18.5 mg $PbBr_2$	85 mg OA 2 mL ODE 33.5 mg OABr	5 mL Acetone 300 µL DMF	Toluene
$CsPbBr_3$	814 mg Cs_2CO_3 69 mg $PbBr_2$	45 ml ODE 2.5 mL OA 0.5 mL OLA	5 mL tBuOH	Hexane
$FAPbBr_3$	521 mg $FA(CH_3COO)$	21 mL OA 5 mL ODE 0.5 mL OLA	10 mL Toluene 5 mL Acetonitrile	Hexane

Text S2. Graphene decoration with perovskite NCs and gas sensing set-up.

Once the different perovskite NCs were synthesized, a graphene solution in toluene or hexane (0.5 mg/mL) was prepared by using graphene nanoflakes from Strem Chemicals, Inc. (US). Afterwards, the solution was placed in an ultrasonic tip to apply a pulsed sonication (1s on/2s off) at 280 W for 90 minutes. Then, once the graphene is properly exfoliated, perovskite NCs were added (5% wt.) to the

solution and the nanomaterials were mixed in an ultrasonic bath for 1 hour. Finally, the resulting graphene flakes decorated with perovskite NCs were deposited onto alumina substrates that comprised screen-printed platinum interdigitated electrodes by a spray pyrolysis technique.

It is important to note that the preparation of graphene has an essential role in gas sensing performance. In this paper, the lead halide perovskite nanocrystals are supported on liquid-phase exfoliated (LPE) graphene, an attractive preparation method given its low cost. It can be foreseen that higher responses could have been reached using more costly graphene, e.g. mechanically exfoliated graphene[4] or chemical vapor deposited (CVD). However, this general improvement in responsiveness would have not affected the relative performance of the anions/cations in lead halide perovskites.

The sensors developed were placed in an airtight Teflon chamber with a volume of 35 cm^3, which is connected to calibrated gas cylinders with pure dry air (Air Premier Purity: 99,995%) and the different gases tested. Then, different dilutions of target gases were performed in order to obtain different concentrations. The sensors were stabilized under synthetic dry air for 5 minutes before the application of the target gas concentration during 1 min of exposure. The total flow was adjusted to 100 mL/min using a set of Bronkhorst High-Tech B.V. (Ruurlo, The Netherlands) mass-flows controllers. And the resistance changes were registered using an Agilent HP 34972A multimeter connected to the test chamber. The responses were defined as ($\Delta R/R0$) expressed in percentage. Where ΔR is the resistance change over one minute of gas exposure, meanwhile R0 corresponds to the baseline resistance.

Figure S1. High-Resolution Transmission Electron Microscope (HRTEM) images of $MAPbBr_3$ (a), $CsPbBr_3$ (b), $FAPbBr_3$ (c), $MAPbCl_3$ (d) and $MAPbBr_{2.5}I_{0.5}$ (e) perovskite NCs.

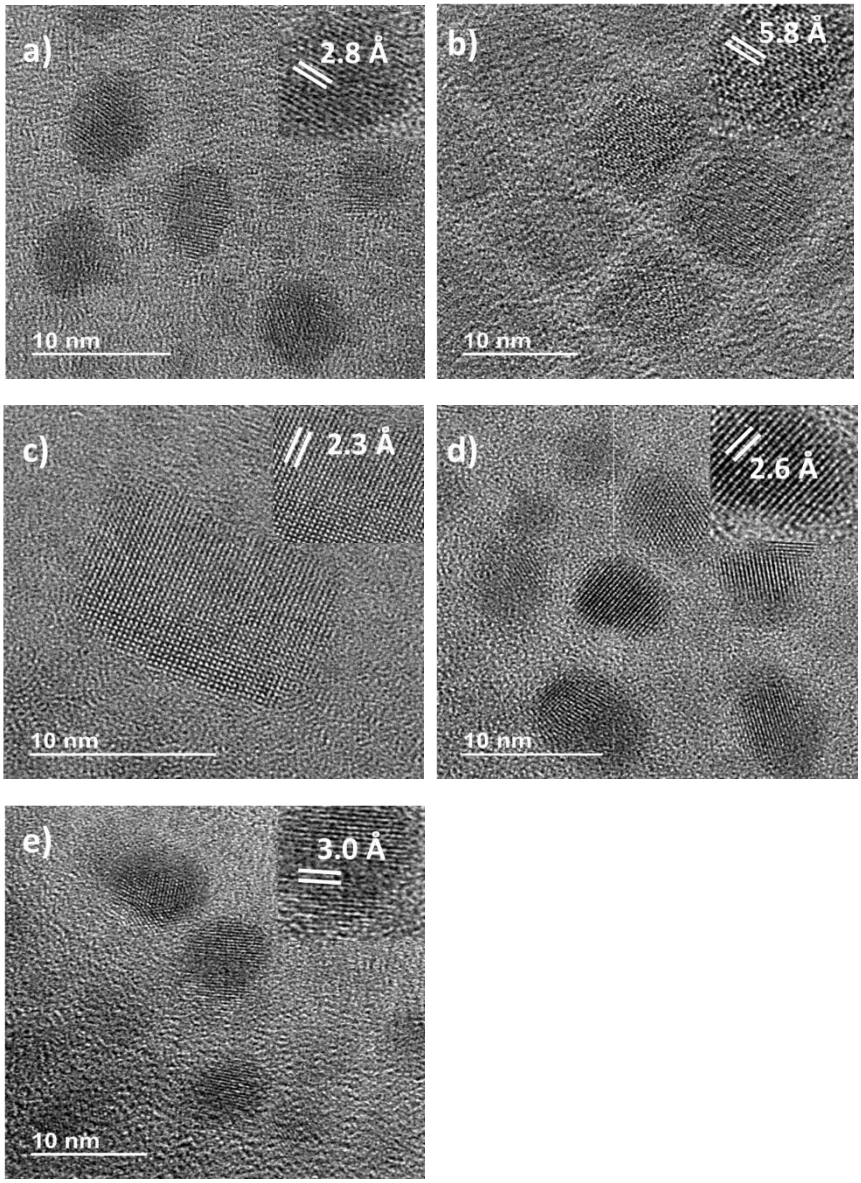

Table S1. Data extracted from the HRTEM images (Fig. S1).

Perovskite NCs	Average size (nm)	Interplanar distance (Å)
$MAPbBr_3$	7.2 ± 2.2	2.8
$CsPbBr_3$	8.7 ± 1.1	5.8
$FAPbBr_3$	6.9 ± 1.2	2.3
$MAPbCl_3$	5.6 ± 1.5	2.6
$MAPbBr_{2.5}I_{0.5}$	6.3 ± 0.6	3.0

Figure S2. X-Ray Diffraction (XRD) patterns for the different perovskite structures.

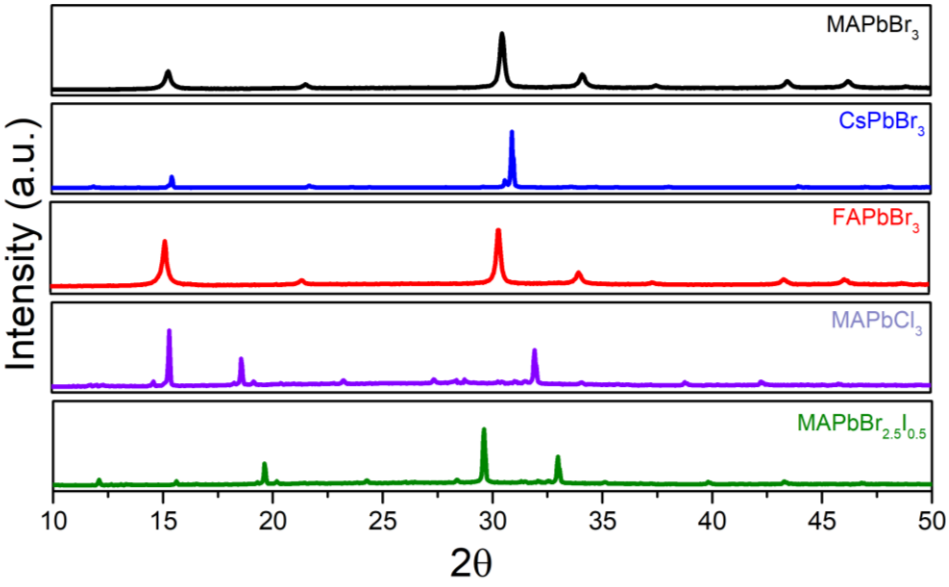

Figure S3. Field Emission Scanning Electron Microscope (FESEM) image showing the sensor surface (a), and image recorded with Back-Scattered Electron (BSE) detector (b). In this case, the bright spots correspond to the perovskite NCs, meanwhile, black background corresponds to graphene.

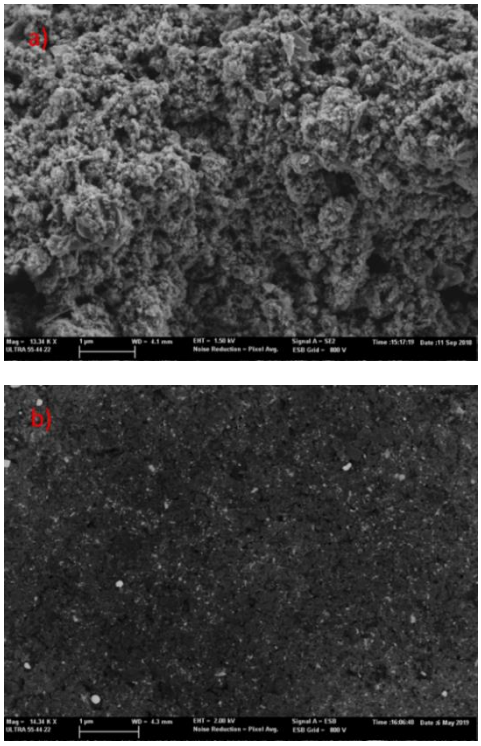

Figure S4. Graphene decorated with perovskite NCs layer deposited onto alumina substrate (a), and gas sensing chamber used (b).

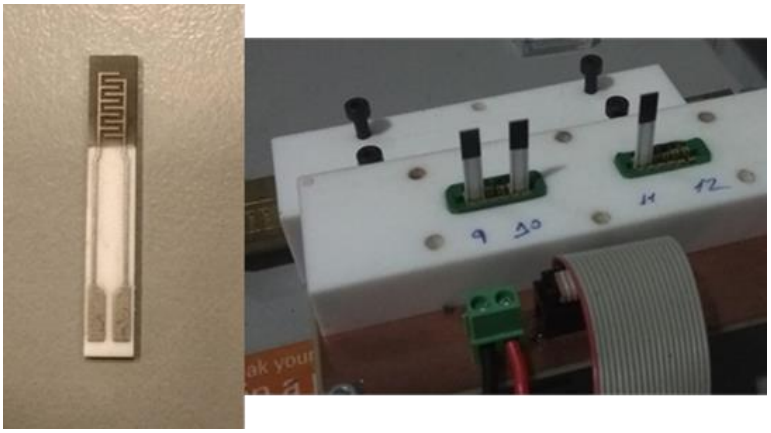

Figure S5. Responses obtained for benzene and toluene using graphene decorated with different perovskite NCs. For the two vapours, 2, 4, 6 and 8 ppm were applied in three consecutive cycles.

Perovskite NCs	Benzene	Toluene
$MAPbBr_3$	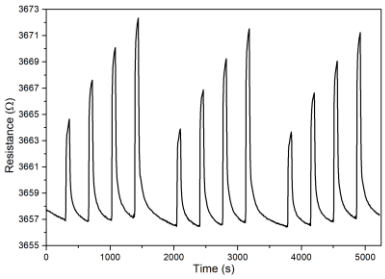	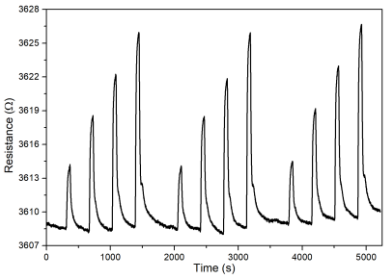
$CsPbBr_3$	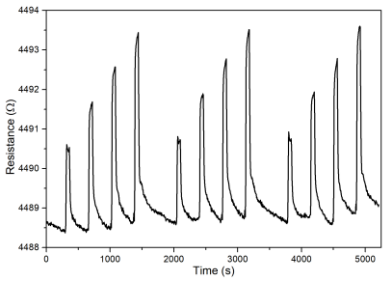	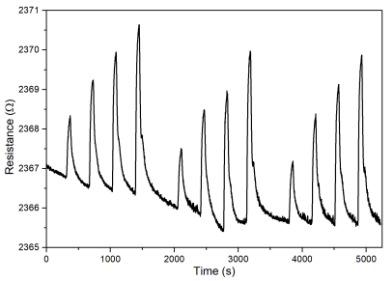
$FAPbBr_3$	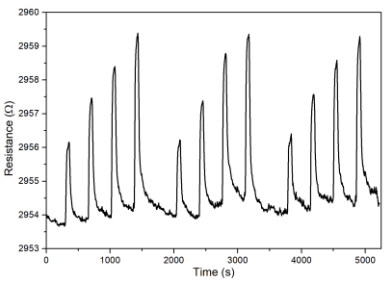	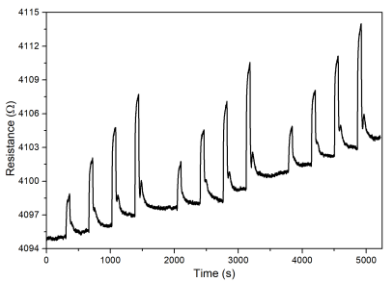

$MAPbCl_3$	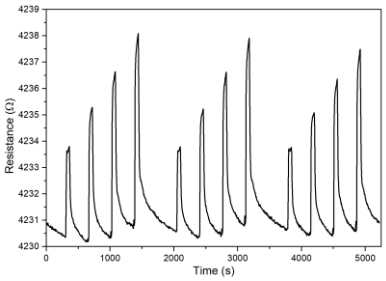	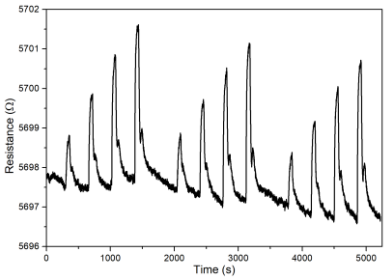
$MAPbBr_{2.5}I_{0.5}$	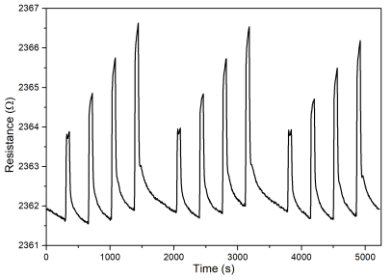	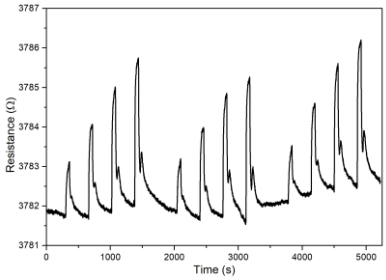

Figure S6. Zoom of the graph shown in Figure 2a. In particular, the present graph shows the resistance changes (black line) for graphene decorated with MAPbBr3 NCs under the exposure to increasing concentrations of benzene (red dashed line).

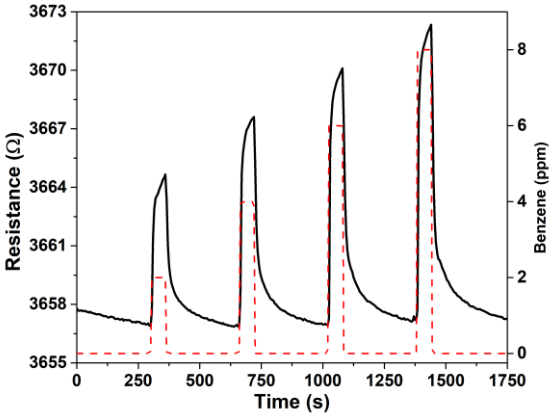

Table S2. Example of the average responses of graphene decorated with the different perovskite NCs towards benzene exposure.

C_6H_6 (ppm)	$MAPbBr_3$	$FAPbBr_3$	$MAPbBr_{2.5}I_{0.5}$	$MAPbCl_3$	$CsPbBr_3$
2	0.202 ± 0.007	0.079 ± 0.004	0.096 ± 0.004	0.080 ± 0.005	0.0472 ± 0.0001
4	0.283 ± 0.008	0.117 ± 0.004	0.139 ± 0.006	0.119 ± 0.006	0.070 ± 0.001
6	0.345 ± 0.012	0.147 ± 0.006	0.172 ± 0.006	0.149 ± 0.004	0.0904 ± 0.0005
8	0.402 ± 0.014	0.167 ± 0.007	0.197 ± 0.007	0.169 ± 0.005	0.104 ± 0.001

The measurement methodology used in this work results in highly reproducible (less than 5% of error), reversible (absence of significant baseline drift) and fast (1-minute exposure) responses at room temperature. A similar strategy has been reported by many authors[5–7], in which the measurements outside the steady-state regime enable achieving representative calibration curves with a low operating cost.

However, since the sensor behaviour during gas exposure until stabilization of the response is important, Figure S7 shows the sensor saturation and its baseline recovery. The response and recovery times (t90) are about 30 min for a flow rate of 400 mL/min.

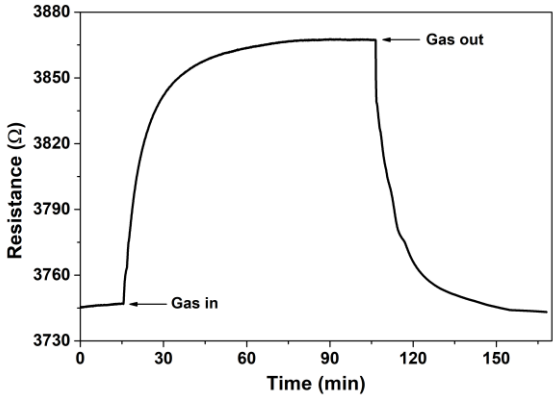

Figure S7. Typical response and recovery curve for a lead halide perovskite loaded graphene sensor operated at room temperature. Once the resistance baseline was stable in dry air, 10 ppm of toluene were applied until reaching the saturation of sensor response. Baseline recovery was achieved in pure air.

Figure S8. Reproducibility analysis using the $MAPbBr_3$ perovskite. Resistance changes (black line) under exposure to 10 ppm of benzene (red line) for long times (30 minutes) were registered.

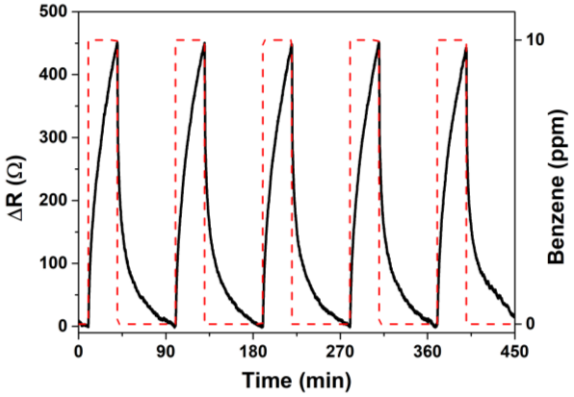

Figure S9. Comparison between the sensor signals registered for bare graphene (red line and right y-axis) and graphene decorated with $MAPbBr_3$ NCs (black line and left y-axis). The resistance changes correspond to one-minute exposures for 2, 4, 6 and 8 ppm of benzene during three consecutive, replicate cycles.

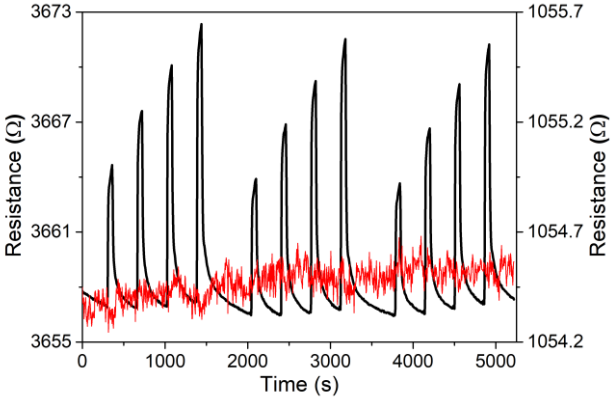

Figure S10. Calibration curves obtained for toluene detection using lead halide perovskites with different cation (a) and anion (b).

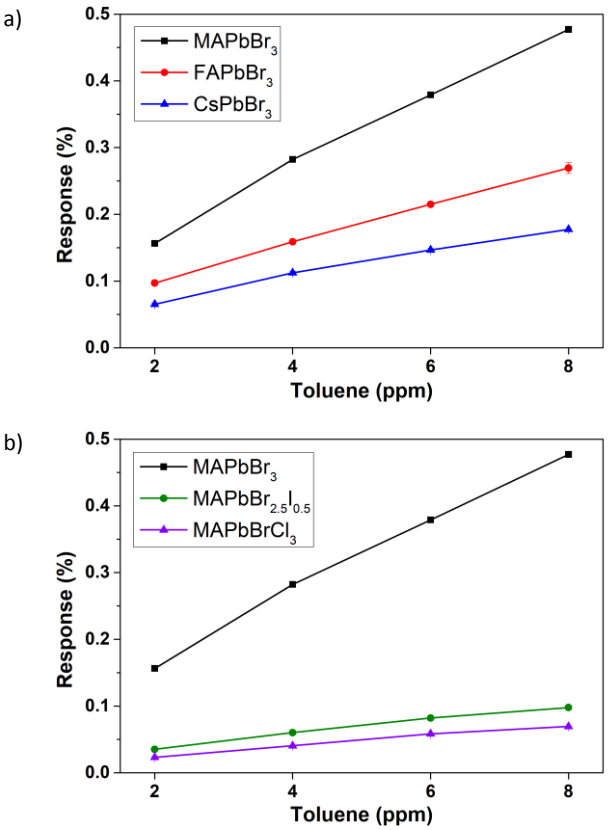

Figure S11. (a) Examples of electrical response to NO_2 using $FAPbBr_3$. Three consecutive, replicate cycles with four concentrations (250, 500, 750 and 1000 ppb) were applied for 1-minute exposure. Synthetic dry air was used for a five-minute cleaning between the different concentrations tested. (b) Gas exposure to different concentrations of NH_3 by using graphene decorated with $FAPbBr_3$ NCs. No sensitivity to ammonia was obtained because the resistance changes recorded remain almost identical for the different analyte concentrations. (c) Comparison of the electrical responses to NH_3 using $MAPbCl_3$ (black line) and $MAPbBr_3$ (red line). Three consecutive cycles with four concentrations (25, 50, 75 and 100 ppm) were applied for one minute. Again, five-minute cleaning in dry air periods were applied between ammonia exposures.

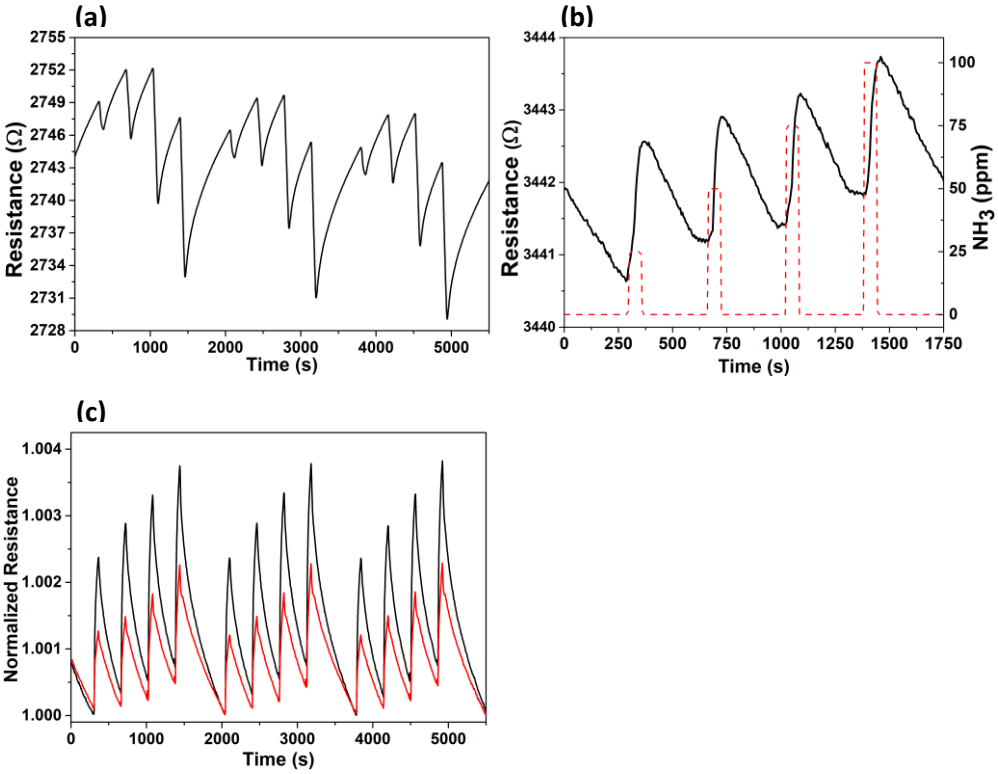

References

1. L. C. Schmidt, A. Pertegás, S. González-Carrero, O. Malinkiewicz, S. Agouram, G. Mínguez Espallargas, H. J. Bolink, R. E. Galian and J. Pérez-Prieto, J. Am. Chem. Soc., 2014, 136, 850–853.

2. L. Protesescu, S. Yakunin, M. I. Bodnarchuk, F. Krieg, R. Caputo, C. H. Hendon, R. X. Yang, A. Walsh and M. V. Kovalenko, Nano Lett., 2015, 15, 3692–3696.

3. L. Protesescu, S. Yakunin, M. I. Bodnarchuk, F. Bertolotti, N. Masciocchi, A. Guagliardi and M. V. Kovalenko, J. Am. Chem. Soc., 2016, 138, 14202–14205.

4. F. Ricciardella, S. Vollebregt, T. Polichetti, M. Miscuglio, B. Alfano, M. L. Miglietta, E. Massera, G. Di Francia and P. M. Sarro, Nanoscale, 2017, 9, 6085–6093.

5. F. Auerbach, in International Conference on Solid-State Sensors and Actuators, and Eurosensors IX, Proceedings, IEEE, 1995, 1, 791–794.

6. N. El Barbri, C. Duran, J. Brezmes, N. Cañellas, J. Ramírez, B. Bouchikhi and E. Llobet, Sensors, 2008, 8, 7369–7379.

7. V. Martini, S. Bernardini, M. Bendahan, K. Aguir, P. Perrier and I. Graur, in Sensors and Actuators, B: Chemical, Elsevier, 2012, 170, 45–50.

CAPÍTULO 6

DISPOSITIVOS FOTOVOLTAICOS

SECCIÓN 6.1

EXPANDING THE PHOTORESPONSE OF MULTIDIMENSIONAL HYBRID LEAD BROMIDE PEROVSKITES INTO THE VISIBLE REGION BY INCORPORATION OF SUBPHTALOCYANINE

Rocío García-Aboal, Hermenegildo García, Sonia Remiro-Buenamañana and Pedro Atienzar

Dalton Trans., 2021, 50, 6100

DOI: 10.1039/d0dt04132g

EXPANDING THE PHOTORESPONSE OF MULTIDIMENSIONAL HYBRID LEAD BROMIDE PEROVSKITES INTO THE VISIBLE REGION BY INCORPORATION OF SUBPHTALOCYANINE

Rocío García-Aboal[a], Hermenegildo García[a], Sonia Remiro-Buenamañana*[a] and Pedro Atienzar*[a]

[a]Instituto Universitario de Tecnología Química CSIC-UPV, Universidad Politecnica de Valencia, Av. de los Naranjos s/n, 46022 Valencia, Spain

Abstract

This work explores a new methodology to adsorb a subphthalocyanine molecule (SubPc) on a hybrid lead bromide perovskite crystal structure with the aim of extending its photoresponse into the visible region. This process consists in the preparation of multidimensional 2D-3D perovskites. The use of large organic cations allows the possibility to insert guest molecules in the crystal structure of the perovskite. In this work, layered and 3D materials are obtained modifying the ratio of the organic cations (A/R) in the perovskite structure $(RNH_3)_2A_{n-1}BnX_{3n+1}$. The present results show that incorporation of metal-free subphthalocyanine in the interlayer space provided by the 2D phase, is a valid procedure to enhance the photoresponse of the perovskite solar cells.

1. INTRODUCTION

Hybrid halide perovskite materials have attracted a great deal of attention in recent years, due to the fast photon to current efficiency reached in a very short period, having competitive values compared with silicon solar cells technology. In addition to photovoltaics, these materials show other promising applications as light emitting diodes[3], lasing materials[4] or gas sensors[5]. These hybrid perovskites adopt the chemical formula ABX_3 in three-dimensional (3D) structure, where A and B are cations of different sizes and X are halides. There are more than one hundred different possible perovskites[6], most of them still to be discovered. Although rapid progress has been made, these materials are still under intense study due to the various possibilities to modify their structure and composition.

Recently, 2D-3D multidimensional perovskites have emerged as promising materials because they combine the high performance of 3D perovskites, and the long-term stability of 2D perovskites. 2D perovskites contain hydrophobic bulky alkylammonium cations in their crystal structure to terminate the lattice, this could effectively block the interaction with the external moisture. Its generic formula is $(RNH_3)_2A_{n-1}B_nX_{3n+1}$, where RNH_3 is a primary aliphatic or aromatic alkylammonium cation, A is monovalent organic cation, B is a divalent metal, X is the halide ion, and "n" is the number of 3D perovskite layers separating the alkylammonium cation. The "n" value may vary from 1 to ∞, corresponding respectively, to a 2D or 3D structure.

Complete 2D structures present several drawbacks such as higher exciton binding energy and lower light absorption[7]. However, it has been demonstrated that multidimensional 2D–3D perovskites show enhanced carrier lifetime, mobility and diffusion length, and reduced trap density[8]. Depending on the bulky alkylammonium cation and the proportion with the organic cation, combined properties can be achieved[9]. Relative to the 3D materials, 2D-3D multidimensional perovskites are able to incorporate a wider range of large organic cations, and they possess the flexibility to introduce other guest molecules that confer new properties or functionalities. Although, this strategy has been used in other 2D materials such as layered double hydroxides or graphene-based materials,[10] herein, for the first time we report the incorporation of a subphthalocyanine into the interlayer space of multidimensional 2D-3D perovskites. At present, there are only scarce works dealing with the incorporation or doping of 2D-3D perovskites with small organic molecules[11,12] different from the typical cations and anions studied in the perovskite doping.[13] The inclusion of metal particles[14] has been demonstrated as valid approach to enhance the photoresponse of the active material. Therefore, the interlayer space of the 2D component in the 2D-3D multidimensional perovskite enables the capability of different types of guest molecules to be intercalated, while the pure 3D configuration shows a more limited possibility.

Boron subphthalocyanines (SubPcs) derivatives have received considerable attention for their use in photovoltaics[15-18]. SubPc are

aromatic chromophore molecules with cone-shaped structure, good solution processability, intense optical absorption in the visible spectral region, appropriate electron mobility, and tunable energy levels[19,20]. During the last decade, organic SubPcs have successfully been applied in the field of photovoltaics as light harvesters due to their excellent optical and semiconducting properties[21-24].

Recently, SubPcs have also been used as hole transport materials (HTM) for organometallic halide perovskite solar cells because of its stability and long excitation diffusion length,[16,25] showing its potential as alternative to the most commonly used spiro-OMeTAD[26,27]. A protective effect of the SubPc over the perovskite preventing from degradation has also been reported[16], or as passivating agent of the defects within the perovskite film.[28] The present manuscript deals with the incorporation of the phenoxy-iodo- boron subphthalocyanine (PhO,I-SubPc) derivatives onto 2D-3D lead bromide perovskites, increasing their visible light absorption, as well as improving their stability against degradation.

At the moment, organometallic halide perovskite solar cells having iodine in the structure, offer the maximum power conversion efficiency (PCE)[29,30], since these hybrid perovskites exhibit full coverage of the visible wavelength range. However, the introduction of iodine anion offers less stability against UV light and moisture compared with perovskites based on bromide[31]. Bromide perovskites offer good stability, but its optical bandgap of 2.31 eV limit light absorption in the yellow-red part of the visible spectrum. Herein, we combine the photoresponse of the hybrid bromide perovskite with the SubPc as light harvester, in order to maximize the absorption in the visible spectrum and as protective layer.

Hence, the incorporation of SubPc in the interlayer space of 2D-3D perovskites expands the photoresponse in the visible region. SubPc incorporation was achieved by selectively controlling the composition during the synthesis. This new strategy shows better photoresponse, demonstrated in polycrystalline samples and single crystal. The composition of SubPc and perovskite precursors was also evaluated in

order to properly incorporate the SubPc between the layered 2D-3D perovskite.

2. MATERIALS AND METHODS

2.1. Chemicals

All reagents were purchased from Sigma- Aldrich apart from ITO quartz substrates that were supplied by Ossila.

2.2. Synthesis of Subphthalocyanines

2.2.1. Synthesis of chloro, iodo-subphthalocyanine (Cl,I-SubPc)

Synthesis of Cl,I-SubPc was carried out following a modified version of the classical reported synthesis[32]. 4-iodophthalonitrile (0.9164 g, 3.61 mmol, 1.5 eq) was placed in a 2-necked round bottomed flask, anhydrous p-xylene (13 mL) was added, and the mixture was stirred under inert atmosphere until everything dissolved. BCl_3 (2.4 mL, 1eq) was then added dropwise and the reaction mixture was heated at reflux temperature (140 °C) for 4 h. The reaction mixture was cooled down to room temperature and the solvent evaporated under reduce pressure, the resultant crude was dried under vacuum. The resultant solid was washed first with cold methanol and then with cold hexane, followed by filtration. The title compound was isolated as dark purple solid (0.9168 g, 94%). 1H-NMR (300 MHz, $CDCl_3$, 298 K): δ (ppm) = 9.25 (br s, 3H), 8.60 – 8.57 (m, 3H), 8.27 – 8.23 (m, 3H). UV-Vis (CH_2Cl_2): λ max (nm) = 572.

2.2.2. Synthesis of phenoxy, iodo-subphthalocyanine (OPh,I-SubPc)

Synthesis of OPh,I-SubPc was carried out following the reported literature protocol[33]. Cl,I-SubPc (0.8111 g, 1.003 mmol, 1 eq) and an excess of phenol (0.4768 g, 5.015 mmol, 5 eq) were placed in a round bottomed flask and dissolved in toluene (3 mL). The mixture was refluxed under inert atmosphere until completion (24 h) and subsequently cooled down to room temperature. The resultant solid was then transferred to another flask and the solvent was evaporated under reduced pressure. This crude product was washed with cold hexane and cold methanol, and filtered to yield the pure title product

as purple solid (0.7904 g, 91%). 1H-NMR (300 MHz, $CDCl_3$, 298 K): δ (ppm) = 9.19 (br s, 3H), 8.54 (d, 3H, J = 8.4 Hz), 8.21 (d, 3H, J = 8.4 Hz), 6.76 (t, 2H, J = 7.5 Hz), 6.64 (t, 1H, J = 7.5 Hz), 5.35 (d, 2H, J = 7.5 Hz). UV-Vis (CH_2Cl_2): λ max (nm) = 569.

2.3. Synthesis of polycrystalline hybrid perovskite with 2D-3D structure (n=10 and 50)

Following this stoichiometry, $(R)_2(A)_{n-1}B_nX_{3n+1}$, perovskite structures from layered to 3D materials have been prepared modifying the ratio of organic cations A/R. This strategy is based on the use of large alkyl ammonium cations that form low-dimensional perovskites. Perovskite with n=10 is the focus of this paper, however, n=50 and 3D structure perovskites were also prepared for comparison. Solutions containing different concentrations of the precursors in DMF were prepared n= 10, 0.1M phenylethyl ammonium bromide (PEABr), 0.45 M methyl ammonium bromide (MABr), 0.5 M lead bromide ($PbBr_2$); n=50, 0.02 M PEABr, 0.49 M MABr, 0.5 M $PbBr_2$. In case of the 3D structure, the classic perovskite synthesis was followed[34]. Blank perovskite samples lacking OPh,I-SubPc were also prepared in order to verify the insertion of the OPh,I-SubPc into the structure.

The hybrid perovskite samples with and without OPh,I-SubPc were prepared following the drop casting method. The experimental protocol involves washing the quartz substrates with anionic detergent (Alconox) and milliQ water in an ultrasonic bath. The substrates were subsequently treated with a hydrochloric acid solution (1 M) for 24 h to increase the surface hydrophilicity. Finally, the quartz substrates were thoroughly rinsed with ethanol and dried. Then, the above mentioned precursor solutions in the appropriate concentrations were deposited onto the quartz surface (10 µL) in a ratio (1:1:1), and 1:1:1:1 when preparing the OPh,I-SubPc-containing materials. Hence, 10 µL of a previously prepared solution of SubPc (5 wt. %) in DMF was added. The mixture was left to slowly crystallize overnight at room temperature. Orange-pinkish crystals were obtained.

2.4. Synthesis of single crystal hybrid perovskite with 2D-3D structure (n=10) via antisolvent method

Single crystal hybrid perovskites were slowly crystallized following the antisolvent method, that consisted on dissolving the precursors (0.1 M PEABr, 0.45 M MABr, 0.5 M $PbBr_2$) in a small amount of DMF (1 mL), and adding an aliquot of the previously prepared solution of SubPc (20 µL). This mixture was placed in a quartz substrate on a Teflon stage in a close vial, and THF was used as antisolvent (5 mL). The vessel was fully closed and kept in the dark until small orange-pinkish crystals were observed. The crystals were manually selected with Gel-Pack and a micromanipulator to perform the corresponding characterization.

2.5 Preparation of hybrid perovskite solar cells

The following experimental protocol was followed for the preparation of the hybrid perovskite-SubPc solar cells: 1) ITO cleaning step: Quartz substrates containing ITO (thickness 1.1mm and specific size 20 mm × 15 mm) were washed with ethanol; 2) Preparation of TiO_2 dense layer: Firstly, the clean substrates were heated in a hotplate at 450 °C for 30 min. Then, titanium (IV) isopropoxide (0.762 mL), and acetylacetone (0.5125 mL) were dissolved in absolute ethanol (9 mL). The mixture was deposited by spray coating onto the quartz substrate (1.5 mL) that contain the ITO layer. An inert gas was used as carrier. Finally, the substrates were heated up to 450°C for 30 min and then cooled down to room temperature to obtain a completely dense TiO_2 film; 3) Preparation of mesoporous TiO_2 scaffold layer: A solution of a TiO_2 paste (18NR-T) (35 µL) diluted in absolute ethanol (0.020 g paste: 1mL ethanol) was deposited onto the substrates by spin-coating (2000 rpm/ 45 s). The films were firstly dried on a hotplate at 50°C for 30 min, then the substrates were annealed in an oven at 45 °C for 1 h, and finally they were cooled down to room temperature; 4) Preparation of SubPc@HP10 perovskite films: Following the stoichiometry to n=10 ($(RNH_3)_2(A)_9B_{10}X_{31}$) a mixture of perovskite precursor solutions 0.1 M PEABr, 0.45 M MABr, 0.5 M $PbBr_2$ and OPh,I-SubPc (10, 30, 50 wt.%) were deposited onto the substrate. This step was performed in a glove box under inert atmosphere; 5) Preparation of hole-transporting layer Spiro-OMeTAD: The preparation of hole-transporting layer was also

carried out in a glove box. First the lithium salt solution was prepared dissolving lithium bis(trifluoromethylsulfonyl)imide (0.170 g) in acetonitrile (1 mL). Then, 16.6 µL of this solution was mixed with chlorobenzene (1 mL), 4-tert-butylpyridine (TBP) (7.69 µL) and Spiro (0.200 g). The Spiro-OMeTAD solution (30 µl) was spin coated on the surface of the perovskite-SubPc films (3000 rpm for 45 s). The solvent was fully evaporated heating the sample in a hotplate at 110 °C for 1 hour; 6) Preparation of Au electrode: 40 nm layer of Au electrode was deposited onto the previously prepared substrate by vacuum evaporation coating.

2.6. Single crystal characterization

The optical and electrical properties, specifically photoluminescence (PL) and photocurrent, of single crystals were obtained by means of an in-house built setup[1,2]. Basically, it includes two branches, one for excitation and the other one for signal acquisition, both focused by 20× Mitutoyo objectives at the same spot, with a typical size of about 1 µm. In the experiments reported here, both branches were oriented so that the collected light was in forward direction with respect to the incident or exciting light. The signal acquisition branch includes an iris, where the spot is focused. It allows selecting the signal from a sample area of micrometer range and even submicrometer range. After the iris, a motorized mirror drives the signal either to a charge-coupled device (CCD) camera, by means of which, the exact part of crystal being examined can be visualized, or to a spectrometer (iHR320-HORIBA), which is equipped with a liquid nitrogen refrigerated Si-CCD, and it is used for measuring the spectrum of the collected light. For photoluminescence measurements, a 405 nm wavelength beam provided by a solid-state laser was used as excitation source. In all of the cases, to minimize crystal degradation, a moderate intensity of about 0.1 mW was used.

2.7. Characterization

XRD patterns of the powders and thin films were recorded on a Philips X'PERT diffractometer that was equipped with a proportional detector and a secondary graphite monochromator. The data were collected stepwise over the range 2θ = 2–20°, at steps of 0.02°, an

accumulation time of 20 s/step, using the Cu Kα radiation (λ = 1.54178 Å).

UV–Vis optical spectroscopy of the perovskite films was carried out using a Cary 5G spectrophotometer and $CaSO_4$ as reference.

Field-emission scanning electron microscopy (FESEM) images were recorded with a Zeiss Ultra 55 field FESEM apparatus.

2.8. PL measurements

PL spectra of the films were carried out using an optical microscope (Leica DM4000). It includes a module for fluorescence characterization, which consists of a mercury lamp and a Leica bandpass filter (340−380 nm) as illumination source, and an Avantes AvaSpec-2048 Fiber Optic Spectrometer, which provides a resolution better than 0.5 nm.

3. RESULTS AND DISCUSSION

3.1. Characterization

We first studied the incorporation of SubPc in pure 3D perovskite with $MAPbBr_3$ structure, however the incorporation of this macrocyclic compound was unsuccessful. This can be explained considering the rigid, close-packed structure of the cubic 3D configuration where substitution of the organic cation causes strong distortion of the octahedral framework due to the limited ionic radii of the methyl-ammonium cation. Figure S2 and S3 displays the scanning electron microscopy image (HRSEM) and the XRD spectrum. Large amounts of SubPc aggregates over the crystalline perovskite were observed (Figure S2), also the perovskite diffraction peaks did not suffer any change (Figure S3), and the ICP analysis confirmed the absence of SubPc in the 3D perovskite.

In comparison with close-packed 3D perovskite, 2D-3D perovskites depict a layered structure incorporating large organic cations that can facilitate insertion of SubPc molecules. As previously mentioned, n value relates to the number of perovskite layers in the 2D-3D configuration. In the preparation of the multidimensional perovskite,

we selected high n values (n =10 and 50) for the incorporation of the SubPc compound. These values correspond to a quasi-3D perovskite and provide the advantage of combining the outstanding properties of the 3D perovskites and the stability of the 2D structure.

As described in the preparation section, 2D-3D perovskites containing SubPc molecules were obtained following the typical one-step crystallization procedure employed for the preparation of crystalline perovskite layers[35]. Figure 1a indicates the different steps followed for the incorporation of SubPc in the perovskite structure. Basically, a solution of the different precursors in DMF is deposited by drop or spin coating on a clean substrate. Afterwards the sample is washed with toluene in order to remove any possible excess of SubPc. To obtain the reference sample, we also prepared 2D-3D perovskite without SubPc. In addition, Figure 1b shows a graphical representation of the SubPc molecules inserted in the interlayer space together with the PEA cation used for the formation of the 2D phase (SubPc@HP 2D-3D).

The samples were characterized by XRD, electronic microscopy and UV-Vis absorption. In the case of XRD characterization, all the prepared samples show the characteristic peaks at 2θ 14.77 and 29.95 assigned to the (100) and (200) crystal planes that correspond to the cubic phase and indicating high crystallinity. In addition, the influence of the SubPc loading with respect to the "n" value of the hybrid perovskites was studied. Table 1 shows the influence of the SubPc loading on the diffraction peak shift of hybrid perovskite samples at two different n values, 10 and 50 (SubPc@HP10 and SubPc@HP50). Typically, insertion of a guest in the layered space produces a change in the spacing between the layers, which results in a shift of the low-angle diffraction peak. Peak shifting was observed in both hybrid perovskite samples (n = 10 and 50). Nevertheless for the lower n value (n=10), the loading of SubPc was higher, and the shift of the diffraction peak (100) was, accordingly, more significant. Thus, the shift in the XRD (100) peak supports the incorporation of the SubPc in the interlayer structure (see Figure 2). In addition, this diffraction peak (100) is also dependent with the SubPc loading as it is show in Figure S4. This also supports the incorporation of the SubPc in the interlayer space.

The SubPc loading was measured by ICP, in all cases, a low dye loading, lesser than 3 wt.% was determined. This low amount of SubPc incorporated in the structure can be explained considering the limited interlayer space of the 2D phase and the crystal strain.

Table 1. 100 peak shift for SubPc@HP with n= 10 and n= 50.

Sample	SubPc loading (wt.%)[a]	Shift XRD peak position (100)
SubPc@HP10	0.65	0.08
SubPc@HP50	0.41	0.02

[a]Determined by ICP analysis measuring the boron content

a)

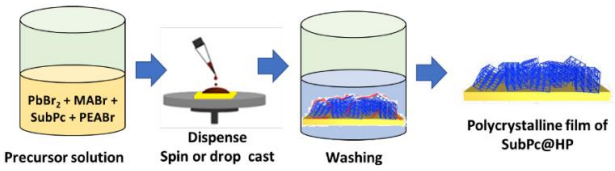

b)

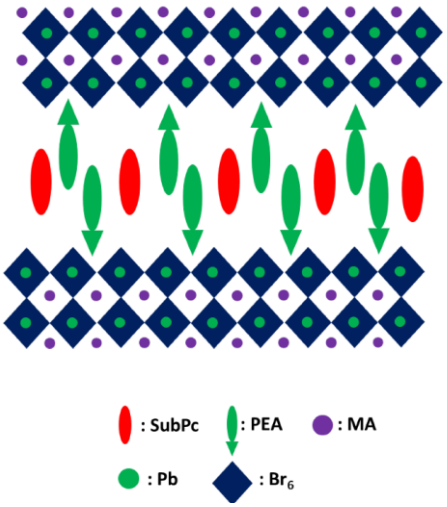

Figure 1. (a) Methodology used for the preparation of 2D-3D perovskite with SubPc. (b) Pictorial representation of the 2D-3D perovskite with SubPc in the interlayer space.

The samples were also characterized by electron microscopy (Figure 3); uniform crystal shapes were observed for both n= 10 or 50, however, for low "n" values, a more layered structure is apparent.

Moreover, in contrast with the full 3D structure where aggregates appeared on the external surface of the crystallites (Figure S2), the presence of SubPc was indistinguishable for the hybrid 2D-3D perovskite crystals. Both, XRD and FESEM data indicated that the incorporation of SubPc preserves the structure of perovskite and confirm the uniform formation of multidimensional 2D-3D perovskite. As long as similar results were observed for the n= 10 and 50, the subsequent presented results are focus on the n= 10 as the SubPc loading is somewhat higher (SubPc@HP10). Moreover, 3D molecular model shows that the interlayer space formed by the PEA cation is sufficient to incorporate the SubPc into the 2D perovskite phase (see Fig. S5†).

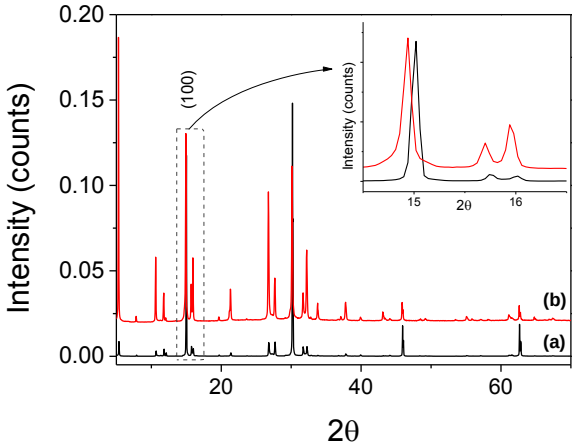

Figure 2. XRD pattern of a thin film of hybrid 2D-3D perovskite with n= 10 onto ITO substrate, a) without SubPc, and b) with 0.65 wt.% of SubPc. The inset shows an expansion of the (100) peak.

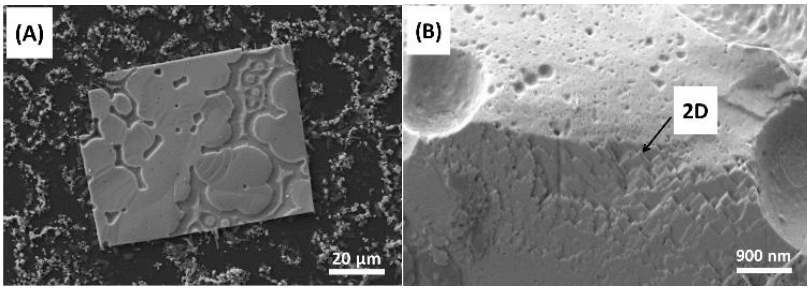

Figure 3. FESEM image of crystalline SubPc@HP10 sample (A), and local magnification indicating the layered structure (B) with the arrow.

3.2. Optical properties

The optical properties of the SubPc@HP10 material were determined by measuring the absorption and the photoluminescence spectra. Figure 4 shows the diffuse reflectance UV-Vis spectra of the polycrystalline thin films without and with incorporated SubPc. The appearance of a new absorption band in the region between 550 to 650 nm was attributed to the SubPc contribution (Figure 4, violet pattern), that interestingly remain visible even at low SubPc concentrations (loading less of 1%). This is due to the characteristic high absorption coefficients of subphthalocyanines, i.e. Q band ranging from $5–6\times10^4$ $dm^3mol^{-1}cm^{-1}$ [36, 37]. To study the influence of SubPc incorporation on the optical properties, the steady-state emission in the polycrystalline samples and single crystals was also measured (see Figure 5). In polycrystalline samples, a broad emission band between 450 to 750 nm is observed, with a less-defined peak maximum probably due to light scattering by the particles and the influence of defects on the surface and interphases. Single crystal characterization is a well know platform to study the intrinsic optical properties of materials due to the absence of grain boundaries, absence of non-crystalline domains and lesser influence of structural defects. In this regard, PL measurement using our in-house built confocal microscope (see experimental section) of a single crystal, shows a well-defined emission with two main bands at 550 and 600 nm that can be assigned based on the emission maxima of the perovskite and subphthalocyanine, respectively. The Q band of the SubPc suffers a hypsochromic shift when it is located inside the perovskite structure. This shift can be explained considering two main factors, the polarity of the surrounding ionic environment and steric stress of the SubPc molecules due to the crystal packing in the interlayer space.

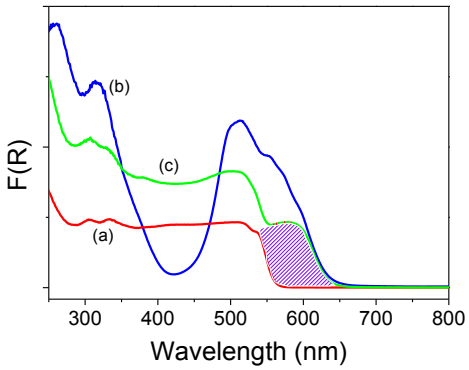

Figure 4. Diffuse reflectance UV–Vis absorption spectra (plotted on the Kubelka-Munk function of the reflectance), F(R) of: a) HP10 b) SubPc@HP10 and c) SubPc.

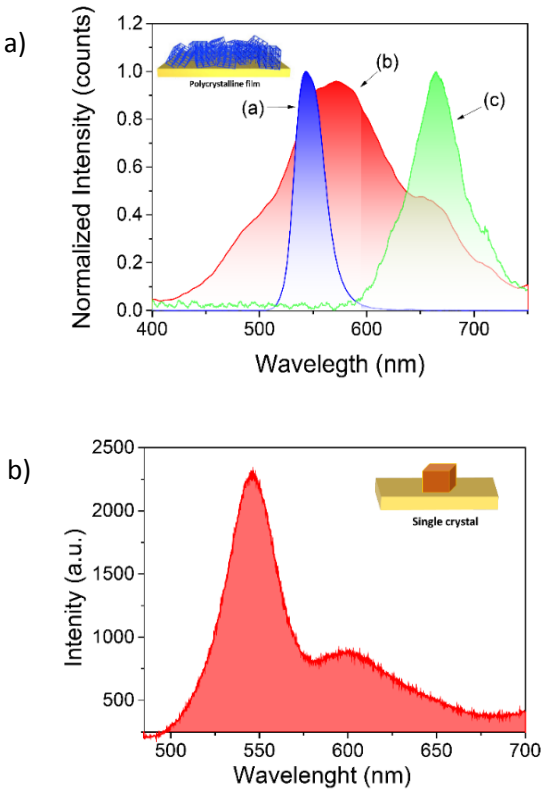

Figure 5. Photoluminescence of (A) polycrystalline samples: HP10 (a), SubPc@HP10 (b) and SubPc (c). B) PL of SubPc@HP10 single crystal.

3.3. Electrical characterization

To gain further insight into the optoelectronic properties of the new SubPc@HP material, we also measured the photocurrent spectra on isolated single crystals. For this purpose, a selected single crystal was firstly deposited onto a conductive ITO electrode, and a micrometric tip was used as top contact. A detailed description is given in the experimental section. The spectral response was measured at room temperature under a nitrogen flux. A tuneable monochromatic source was focused on a single crystal, recording the photogenerated short circuit current at the microcrystal. The set-up is schematically shown in Figure 6B and a detailed description is given in the Methodology section. The photocurrent measured at different wavelengths is depicted in Figure 6A, the response of the bromide perovskite increases in the visible region with a new band exhibiting current up to 650 nm. This enhancement in the photoresponse indicates that SubPc molecules are participating in the charge generation process upon illumination, and acts as light harvester for long wavelength radiations.

a)

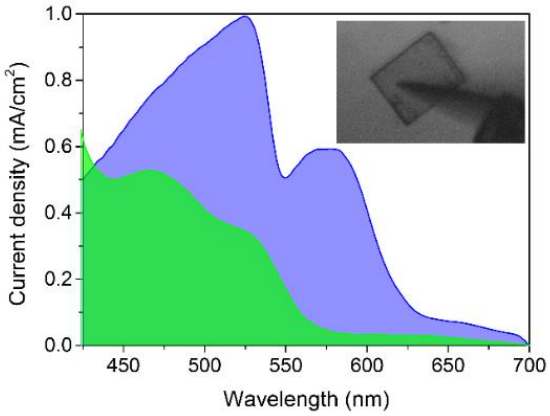

b)

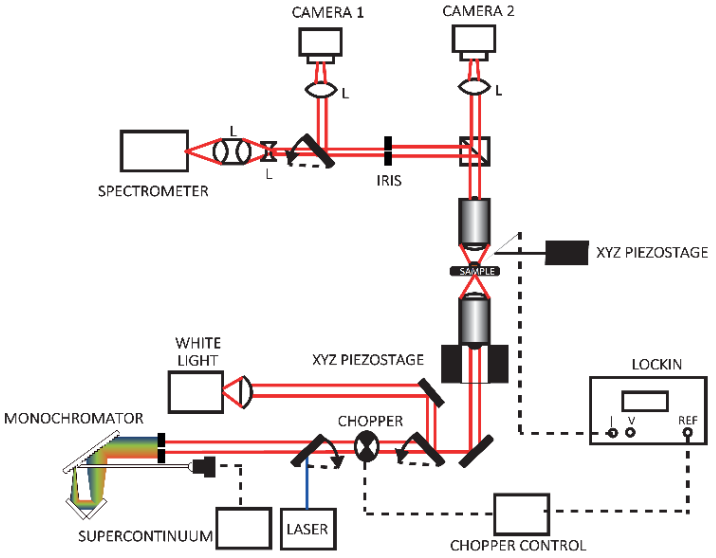

Figure 6. a) Measured photocurrent spectra for a single crystal of HP10 (green) and SubPc@HP10 (violet). The inset shows an optical microscopy image of the single crystal on conductive substrate, with the probing tip contacting the upper surface. b) Schematic representation of the setup used for measuring the PL and photocurrent spectra[1, 2].

3.4. Photovoltaic devices

After characterization of the optical and electrical properties of the SubPc@HP10 material, perovskite solar cells were prepared. A thin dense layer of TiO_2 was used as hole blocking layer (HBL) deposited over the transparent conducting electrode (ITO). Then, a thin porous layer of nanocrystalline TiO_2 (Dyesol) was deposited by spin coating onto the dense TiO_2 layer, and the layers were then sintered at 450 °C. The porous layer was infiltrated by spin coating with a solution of SubPc@HP10 and thermally annealed. Subsequently, hole transport layer of Spiro-MeOTAD was deposited on top of the active material (Scheme 1). Finally, a gold metallic layer was also deposited on top of the Spiro-MeOTAD as cathode electrode (see experimental section for more details).

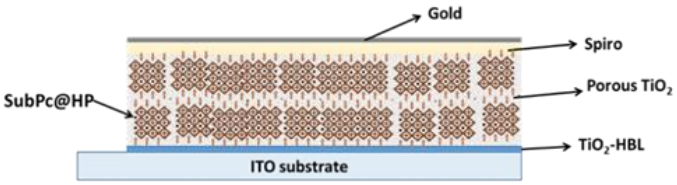

Scheme 1. Device configuration for SubPc@HP solar cell.

The SubPc loading into the hybrid perovskite sample employed in the preparation of the photovoltaic devices, was studied employing three different SubPc loadings of 0.65, 1.8 and 2.9 wt.%. It was determined that the maximum loading of SubPc inserted in the crystalline structure of HP was 2.9 wt.% (n =10). It was also observed that the use of higher concentrations of SubPc produces aggregation of the macrocyclic compound in the form of crystals on the perovskite surface, which has a negative effect on the performance of the perovskite solar cells. This is in agreement with the previous observation by Xu et al.[38], where large amounts of SubPc can hinder the electron transfer process.

The SubPc insertion in optimal amounts results in an improved device performance of the perovskite solar cells, and a 20% efficiency enhancement compared with the reference devices without SubPc molecules (Figure 7). This enhancement has been only observed when

concentrations of SubPc lower than 1 wt.% is used. This suggest, that although the current maxima at short circuit conditions increases due to the enhanced response in the visible region, the final Voc decreases, and this can be explained considering an increase of the internal resistance of the active HP layer after SubPc incorporation. In this regard, it has also been observed that the Voc in inverted perovskite solar cells using conducting polymers as hole selective contact, is influenced by the alignment of the energy levels of the active perovskite and the electron and hole transporting interfaces[39]. Therefore this reduction in the Voc could be due to internal resistance due to the shorter charge carriers migration paths in the hybrid SubPc∝HP material. A summary of the results obtained for the photovoltaic devices is summarized in Table 2. Furthermore, we have performed comparative stability measurements upon continuous irradiation in air conditions, without any encapsulation, and after 10 h the loss of efficiency is about 5% for the device that contains SubPc and 10% without SubPc (see Figure S6). This suggest that SubPc confers some protective effect and this agrees with the observation by other authors. [16, 28]

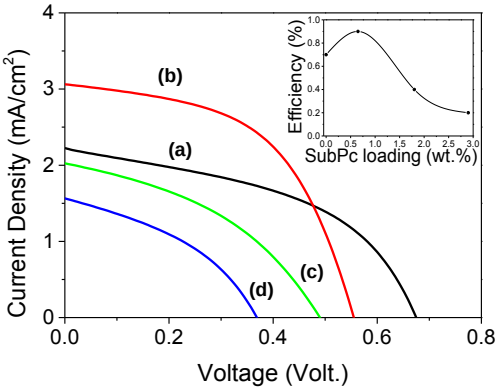

Figure 7. Comparative J-V curves measured for a reference sample of HP10, (a) and SubPc@HP10 prepared using three different concentrations (0.65 (b), 1.8 (c) and 2.9 % wt. (d)). The inset shows the influence of the SubPc loading on the efficiency of the photovoltaic devices.

Table 2. Performance of SubPc@HP solar cells

Device (% wt. of SubPc)	Voc (Volt.)	Jsc (mA/cm^2)	Fill factor (%)	Efficiency (%)
0	0.684	2.23	46.7	0.7
0.65	0.581	3.03	53.7	0.9
1.8	0.490	2.03	40.4	0.4
2.9	0.369	1.56	39.3	0.2

3.5. Proposed mechanism

The operation mechanism of 2D-3D mixed perovskites still remains unclear, this is due to the larger binding energy of photogenerated excitons in the layered structure and the boundaries for the diffusion of the free charge carrier along the structure. Some studies have proposed an energy transfer mechanism from layered to 3D-like perovskite network,[40] or that the local intrinsic electronic structure of the edges of the perovskite layers provides a dissociation process of the excitons into free carriers[41]. Herein, the energy level diagram shown in Scheme 2) is proposed, considering that for n=10 the energy of the CB/VB increases with respect to the 3D configuration[42]. A similar trend has been observed for quantum size effects in colloidal quantum dots.

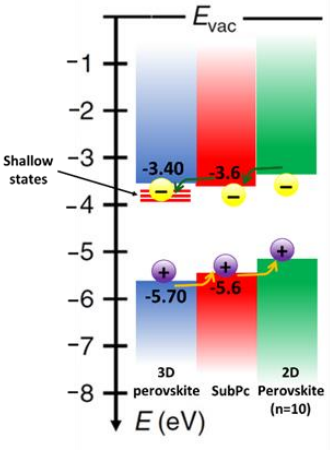

Scheme 2. Energy band alignment in 2D-3D mixed perovskites

Based on the band diagram it can be expected that the 2D component can favour the charge separation in the multidimensional 2D-3D crystal structure as previously described[43]. Besides, as proved by the photocurrent spectrum SubPc is a light harvester that due to the appropriate band alignment, can act as electron and hole relay between the 2D and 3D in the structures. This leads to a more favourable electron transfer from the SubPc and 2D structure, to the 3D phase and hole transfer from the 3D phase to the 2D layered structure (Scheme 2). The presence of different types of defects in 3D perovskites has been demonstrated experimentally and theoretically[44,45]. Common types of defects in perovskites act as shallow traps that introduce intermediate energy levels in the electronic structure due to vacancies and interstitial defects[46]. Normally, shallow traps only reduce mobility and delay the extraction process, resulting in diminution of the maximum current density extracted from the device. Nevertheless, in our case, it appears that the shallow levels facilitate the charge separation process from the perovskites phases and the SubPc, resulting in an increase of the current density of the SubPc@HP10. The smaller VOC can be attributed to the increase in internal resistance of the material due to the presence of SubPc.

CONCLUSIONS

A new approach to expand the photoresponse of hybrid lead bromide perovskites by incorporation of SubPc molecules in the interlayer space of the 2D structure is described. The new material has been characterized and studied in polycrystalline samples, and isolated single crystals, showing that a small SubPc loading enhance the photoresponse of the hybrid bromide perovskites, acting as light harvesting units. Measurements in perovskite solar cells confirm that this approach is a promising direction to enhance the efficiency of this family of materials. Although the overall efficiency still needs improvement, the results of SubPc@HP perovskites open new avenues for perovskite design, presenting many opportunities to design functional materials based on this outstanding class of chromophores.

Conflicts of interest

There are no conflicts to declare

Acknowledgements

We thank the microscopy service at Universitat Politècnica de València (UPV) for the support. S. R.-B. also thanks the Research Executive Agency (REA) and the European Commission for the funding received under the Marie Skłodowska Curie actions (H2020-MSCA-IF-2015/Grant agreement number 709023/ZESMO). R. G. A. acknowledges the FPI scholarship from MINECO MAT2015-69669-P. P. A. acknowledges the financial support from the Spanish Government through 'Severo Ochoa" (SEV-2016-0683, MINECO) and PGC2018-099744-B-I00 (MCIU/AEI/FEDER).

‡ Footnotes relating to the main text should appear here. These might include comments relevant to but not central to the matter under discussion, limited experimental and spectral data, and crystallographic data.

Notes and references

1. R. García-Aboal, R. Fenollosa, F. Ramiro-Manzano, I. Rodríguez, F. Meseguer and P. Atienzar, ACS Omega, 2018, 3, 5229-5236.

2. M. Garín, R. Fenollosa, R. Alcubilla, L. Shi, L. F. Marsal and F. Meseguer, Nature Communications, 2014, 5, 3440.

3. M. Sessolo, L. Gil-Escrig, G. Longo and H. J. Bolink, Topics in Current Chemistry, 2016, 374, 52.

4. M. Stylianakis, T. Maksudov, A. Panagiotopoulos, G. Kakavelakis and K. Petridis, Materials, 2019, 12, 859.

5. J. Casanova-Cháfer, R. García-Aboal, P. Atienzar and E. Llobet, Sensors, 2019, 19, 4563.

6. G. Kieslich, S. Sun and A. K. Cheetham, Chemical Science, 2015, 6, 3430-3433.

7. K. T. Cho, G. Grancini, Y. Lee, E. Oveisi, J. Ryu, O. Almora, M. Tschumi, P. A. Schouwink, G. Seo, S. Heo, J. Park, J. Jang, S. Paek, G. Garcia-Belmonte and M. K. Nazeeruddin, Energy & Environmental Science, 2018, 11, 952-959.

8. P. Li, Y. Zhang, C. Liang, G. Xing, X. Liu, F. Li, X. Liu, X. Hu, G. Shao and Y. Song, Advanced Materials, 2018, 30, 1805323.

9. F. Zhang, D. H. Kim and K. Zhu, Current Opinion in Electrochemistry, 2018, 11, 105-113.

10. W. Jones and C. N. R. Rao, Supramolecular Organization and Materials Design, Cambridge University Press, 2008.

11. T. Zhang, H. Li, H. Ban, Q. Sun, Y. Shen and M. Wang, Journal of Materials Chemistry A, 2020, 8, 4118-4124.

12. W.-Q. Wu, Q. Wang, Y. Fang, Y. Shao, S. Tang, Y. Deng, H. Lu, Y. Liu, T. Li, Z. Yang, A. Gruverman and J. Huang, Nature Communications, 2018, 9, 1625.

13. N. Phung, R. Félix, D. Meggiolaro, A. Al-Ashouri, G. Sousa e Silva, C. Hartmann, J. Hidalgo, H. Köbler, E. Mosconi, B. Lai, R. Gunder, M. Li, K.-L. Wang, Z.-K. Wang, K. Nie, E. Handick, R. G. Wilks, J. A. Marquez, B. Rech, T. Unold, J.-P. Correa-Baena, S. Albrecht, F. De Angelis, M. Bär and A. Abate, Journal of the American Chemical Society, 2020, 142, 2364-2374.

14. S. Carretero-Palacios, A. Jiménez-Solano and H. Míguez, ACS Energy Letters, 2016, 1, 323-331.

15. K. L. Mutolo, E. I. Mayo, B. P. Rand, S. R. Forrest and M. E. Thompson, Journal of the American Chemical Society, 2006, 128, 8108-8109.

16. G. Sfyri, C. V. Kumar, G. Sabapathi, L. Giribabu, K. S. Andrikopoulos, E. Stathatos and P. Lianos, RSC Advances, 2015, 5, 69813-69818.

17. P. Sullivan, S. Schumann, R. Da Campo, T. Howells, A. Duraud, M. Shipman, R. A. Hatton and T. S. Jones, Advanced Energy Materials, 2013, 3, 239-244.

18. B. Verreet, K. Cnops, D. Cheyns, P. Heremans, A. Stesmans, G. Zango, C. G. Claessens, T. Torres and B. P. Rand, Advanced Energy Materials, 2014, 4, 1301413.

19. C. Duan, G. Zango, M. García Iglesias, F. J. M. Colberts, M. M. Wienk, M. V. Martínez-Díaz, R. A. J. Janssen and T. Torres, Angew Chem Int Ed Engl, 2017, 56, 148-152.

20. M. Urbani, F. A. Sarı, M. Grätzel, M. K. Nazeeruddin, T. Torres and M. Ince, Chemistry – An Asian Journal, 2016, 11, 1223-1231.

21. G. Bottari, G. de la Torre, D. M. Guldi and T. Torres, Chemical Reviews, 2010, 110, 6768-6816.

22. G. Bressan, A. N. Cammidge, G. A. Jones, I. A. Heisler, D. Gonzalez-Lucas, S. Remiro-Buenamañana and S. R. Meech, The Journal of Physical Chemistry A, 2019, 123, 5724-5733.

23. A. Farhat, R. A. Khera, S. Iqbal and J. Iqbal, Optical Materials, 2020, 107, 110154.

24. G. E. Morse and T. P. Bender, ACS Applied Materials & Interfaces, 2012, 4, 5055-5068.

25. F. Wang, X. Liu, E. Rezaee, H. Shan, Y. Zhou and Z.-X. Xu, Royal Society Open Science, 2018, 5, 180617.

26. E. J. Juarez-Perez, M. Wuβler, F. Fabregat-Santiago, K. Lakus-Wollny, E. Mankel, T. Mayer, W. Jaegermann and I. Mora-Sero, The Journal of Physical Chemistry Letters, 2014, 5, 680-685.

27. H.-S. Kim, C.-R. Lee, J.-H. Im, K.-B. Lee, T. Moehl, A. Marchioro, S.-J. Moon, R. Humphry-Baker, J.-H. Yum, J. E. Moser, M. Grätzel and N.-G. Park, Scientific Reports, 2012, 2, 591.

28. C. Li, X. Lv, J. Cao and Y. Tang, Chinese Journal of Chemistry, 2019, 37, 30-34.

29. J. Li, H. Wang, X. Y. Chin, H. A. Dewi, K. Vergeer, T. W. Goh, J. W. M. Lim, J. H. Lew, K. P. Loh, C. Soci, T. C. Sum, H. J. Bolink, N. Mathews, S. Mhaisalkar and A. Bruno, Joule, 2020, 4, 1035-1053.

30. W. S. Yang, B.-W. Park, E. H. Jung, N. J. Jeon, Y. C. Kim, D. U. Lee, S. S. Shin, J. Seo, E. K. Kim, J. H. Noh and S. I. Seok, Science, 2017, 356, 1376-1379.

31. R. K. Misra, L. Ciammaruchi, S. Aharon, D. Mogilyansky, L. Etgar, I. Visoly-Fisher and E. A. Katz, ChemSusChem, 2016, 9, 2572-2577.

32. C. G. Claessens and T. Torres, Tetrahedron Letters, 2000, 41, 6361-6365.

33. D. González-Rodríguez, T. Torres, D. M. Guldi, J. Rivera and L. Echegoyen, Organic Letters, 2002, 4, 335-338.

34. J. H. Heo, D. H. Song and S. H. Im, Advanced Materials, 2014, 26, 8179-8183.

35. M. Istafaul, M. Ansari, A. Qurashi, M. Nazeeruddin and M. Nazeeruddin, Journal of Photochemistry and Photobiology C: Photochemistry Reviews, 2018, 35, 1-24.

36. C. G. Claessens, D. González-Rodríguez, M. S. Rodríguez-Morgade, A. Medina and T. Torres, Chemical Reviews, 2014, 114, 2192-2277.

37. C. G. Claessens, D. González-Rodríguez and T. Torres, Chemical Reviews, 2002, 102, 835-854.

38. M. Xu, J. Feng, X. Ou, Z. Zhang, Y. Zhang, H. Wang and H. Sun, IEEE Photonics Journal, 2016, 8, 1-7.

39. C. H. Ng, T. S. Ripolles, K. Hamada, S. H. Teo, H. N. Lim, J. Bisquert and S. Hayase, Scientific Reports, 2018, 8, 2482.

40. Y. Lin, Y. Fang, J. Zhao, Y. Shao, S. J. Stuard, M. M. Nahid, H. Ade, Q. Wang, J. E. Shield, N. Zhou, A. M. Moran and J. Huang, Nature Communications, 2019, 10, 1008.

41. J.-C. Blancon, H. Tsai, W. Nie, C. C. Stoumpos, L. Pedesseau, C. Katan, M. Kepenekian, C. M. M. Soe, K. Appavoo, M. Y. Sfeir, S. Tretiak, P. M. Ajayan, M. G. Kanatzidis, J. Even, J. J. Crochet and A. D. Mohite, Science, 2017, 355, 1288-1292.

42. M. Yuan, L. N. Quan, R. Comin, G. Walters, R. Sabatini, O. Voznyy, S. Hoogland, Y. Zhao, E. M. Beauregard, P. Kanjanaboos, Z. Lu, D. H. Kim and E. H. Sargent, Nature Nanotechnology, 2016, 11, 872-877.

43. T. Zhang, M. Long, M. Qin, X. Lu, S. Chen, F. Xie, L. Gong, J. Chen, M. Chu, Q. Miao, Z. Chen, W. Xu, P. Liu, W. Xie and J.-b. Xu, Joule, 2018, 2, 2706-2721.

44. J. W. Rosenberg, M. J. Legodi, Y. Rakita, D. Cahen and M. Diale, Journal of Applied Physics, 2017, 122, 145701.

45. H. Zhaosheng, Z. Lin, J. Su, J. Zhang, J. Chang and Y. Hao, Solar RRL, 2019, 3.

46. H. Jin, E. Debroye, M. Keshavarz, I. G. Scheblykin, M. B. J. Roeffaers, J. Hofkens and J. A. Steele, Materials Horizons, 2020, 7, 397-410.

SUPPLEMENTARY INFORMATION: Expanding the photoresponse of multidimensional hybrid lead bromide perovskites into the visible region by incorporation of subphthalocyanine

Rocío García-Aboal[a], Hermenegildo García[a], Sonia Remiro-Buenamañana*[a] and Pedro Atienzar*[a]

[a]Instituto Universitario de Tecnología Química CSIC-UPV, Universidad Politecnica de Valencia, Av. de los Naranjos s/n, 46022 Valencia, Spain

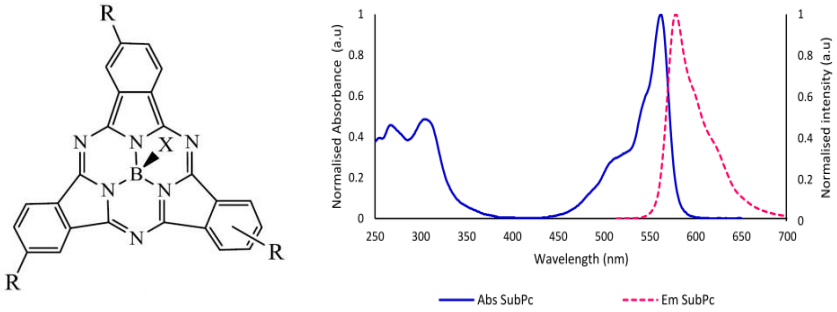

Figure S1. Left: Chemical structure of SubPc, X=Cl, OPh. Right: Absorption (blue) and emission (red, λ_{ex} 550 nm) of an acetonitrile solution of SubPc.

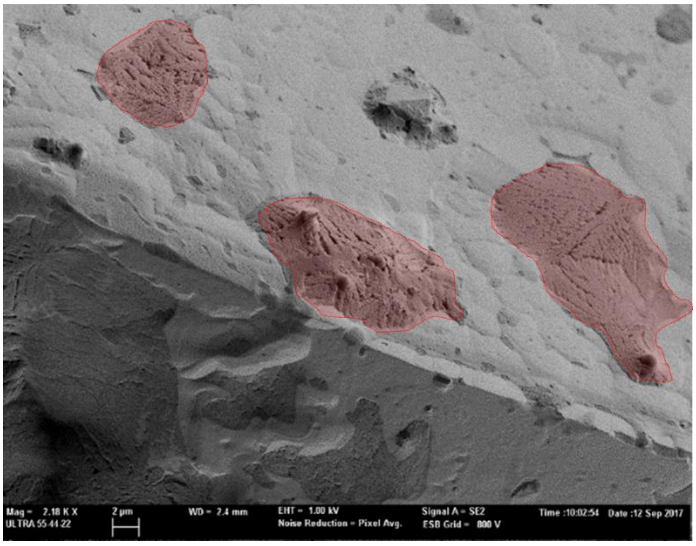

Figure S2. FESEM image of crystalline 3D perovskite ($MAPbBr_3$) with SubPc indicating with a red shadow the formation of SubPc aggregates on the crystal surface.

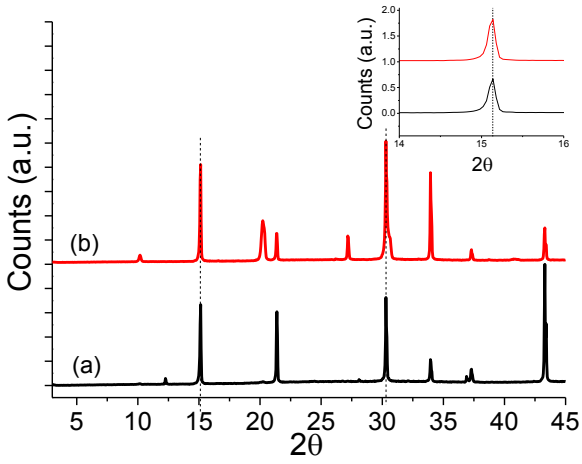

Figure S3. XRD spectra of 3D perovskite ($MAPbBr_3$) with (a) and without SubPc (b), the inset shows a magnification of the peak at 2θ = 15°, where no shift has been observed.

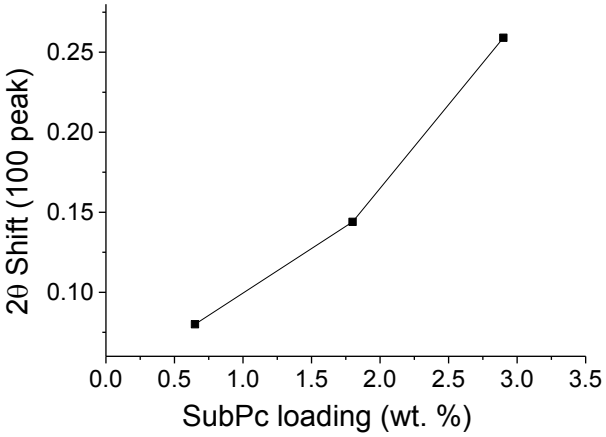

Figure S4. 2θ Shift of the (100) of thin films of SubPc@HP10 prepared using three different concentrations.

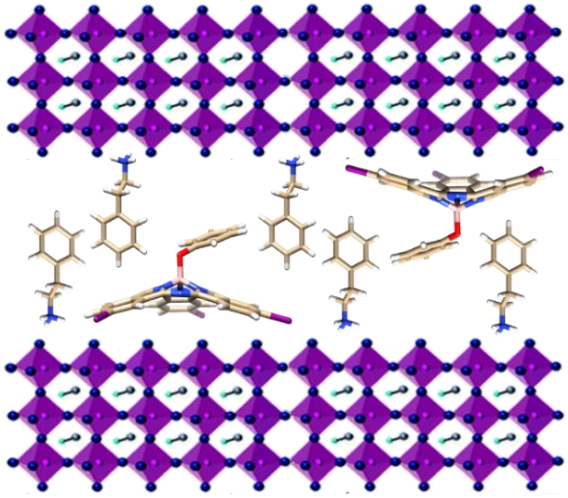

Figure S5. Pictorial representation of the HP10 interlayer space accommodating the large PEABr cation and the SubPc macrocycle.

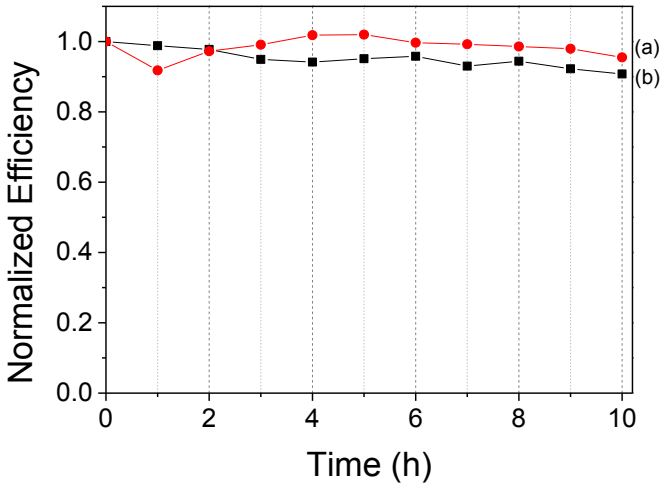

Figure S6. Normalized solar cell efficiency as function of illumination time of (a) SubPc@HP10 and HP10 (b) obtained by continuous illumination of 1000 Wm^2 AM1.5 light in air ambient conditions.

CAPÍTULO 7

DISCUSIÓN GENERAL

7. DISCUSION GENERAL

7.1. Propiedades ópticas en cristales micrométricos

El primer artículo de esta tesis describe un método para la obtención de cristales micrométricos de perovskita híbrida. Para llevar a cabo la síntesis, se ha usado el método de deposición de recubrimiento por giro, el cual permite estudiar la influencia de la velocidad de rotación en la geometría y tamaño del cristal. Los resultados experimentales revelan que el tamaño promedio de los cristales disminuye a medida que aumenta la velocidad de rotación. Se estudió que tanto el tamaño de los cristales como el grosor de la capa depositada vienen dados por la función $1/velocidad^{\gamma}$. Asimismo, los experimentos desarrollados indican que cuanto más rápida es la evaporación del disolvente, mayor es el número de centros de nucleación, resultando en un tamaño promedio menor.

Por otro lado, algunos trabajos demuestran que el uso de aditivos puede mejorar la cristalización del material. No obstante, los aditivos elegidos deben reunir ciertas características, como un alto punto de ebullición y una baja presión de vapor. Con ello se logra una evaporación del disolvente más lenta. Asimismo, el uso de aditivos generalmente permite obtener cristales con menor cantidad de defectos y geometrías más definidas. De forma que aunque en la gran mayoría de casos crecen en forma piramidal, también pueden apreciarse otras geometrías diferentes. Este efecto es más pronunciado con el CHP, ya que dependiendo de la concentración y velocidad pueden obtenerse también cristales con forma de varilla. En cuanto al tamaño, no se encuentra ninguna relación con las propiedades físicas del aditivo, ya que aumentando su concentración no se aprecia una variación significativa.

Estudiar las propiedades ópticas puede revelar la calidad de los cristales sintetizados. Si el cristal se comporta como cavidad óptica y presenta modos de resonancia se asocia una buena calidad del mismo. Para ello se estudia la fotoluminiscencia y transmitancia de cristales aislados utilizando un microscopio óptico confocal desarrollado en nuestro grupo de investigación (más detalles del equipo en el capítulo

3 y 6). Por ejemplo, un cristal con geometría adecuada y buena calidad se comportará como cavidad óptica presentado modos de resonancia.

Actualmente, existen pocos estudios teóricos sobre el fenómeno de cavidad óptica en cristales micrométricos. En esta tesis se propone un sencillo modelo teórico para determinar los parámetros ópticos de este tipo de estructuras. Con el modelo propuesto se puede determinar el índice de refracción del material, tanto la parte real como imaginaria, de una manera muy precisa. En el modelo también se consideran otros parámetros que afectan a la visibilidad de los modos de resonancia. Por ejemplo, el papel de la apertura numérica del objetivo produce un efecto muy drástico, especialmente en el espectro de fotoluminiscencia, provocando incluso la desaparición de las ondas características. Asimismo, el grosor de la muestra también es un parámetro relevante, puesto que a mayor espesor del cristal, más próximos están los modos de resonancia, y por consiguiente, más pronunciado es el efecto de la apertura numérica.

Además, se valida el modelo desarrollado utilizando una cavidad asimétrica, formada por un cristal plano aislado sobre un sustrato de cuarzo. La luz atraviesa dos interfaces, cuyos medios presentan una diferencia en el índice de refracción, favoreciendo así un comportamiento como cavidad óptica. De la misma manera, se evalúa el rendimiento de nuestro cristal como cavidad mediante los parámetros de Finura (F) y el factor de calidad (Q). Estos parámetros son equivalentes a la amplificación de la luz y a la duración del fenómeno, respectivamente.

El mismo modelo teórico ha sido empleado para evaluar y comprobar el comportamiento de un nanocable de perovskita como guía de onda. En este caso, se desea averiguar si la luz es capaz de desplazarse a lo largo de la estructura 1D. Para ello se desarrolla y se emplea un método sencillo y económico basado en el uso de plantillas, con el que se pueden obtener nanocables con una forma y dimensiones específicas, dependiendo de la plantilla empleada. Para confirmar las propiedades de guía de onda, se mide la fotoluminiscencia modulando la distancia de colección con respecto al punto de excitación. Como resultado, los espectros que se obtienen se

desplazan hacia longitudes de onda más largas debido al desplazamiento a lo largo de la estructura 1D.

7.2. Perovskita híbrida como fotocatalizador

La humedad presente en el ambiente es una de las principales causas de degradación y disminución de las eficiencias en dispositivos fotovoltaicos basados en perovskitas. A pesar de ello, se ha demostrado que en presencia de humedad es posible que la perovskita ofrezca cierta actividad fotocatalítica sin llegar a inducir su degradación. Por tanto, en uno de los trabajos derivados de esta tesis se lleva a cabo la fotólisis de agua empleando perovskita híbrida como catalizador en presencia de vapor. Estas condiciones se muestran aptas para llevar a cabo la reacción y mantener integra la estructura del material.

Concretamente, el trabajo se centra en la estabilidad y actividad fotocatalítica de la perovskita híbrida de cobre con fórmula $MA_2CuCl_2Br_2$, aunque también se evalúa la actividad de otras perovskitas similares y sus análogas de plomo. Como es esperable, las diversas composiciones presentan cambios estructurales y modificaciones de sus niveles energéticos, estudiándose cómo afectan en los resultados obtenidos. Esto es de suma importancia si se tiene en cuenta la gran variedad de perovskitas híbridas que se pueden obtener modificando su composición y podrían presentar mayores eficiencias.

La estabilidad del material tras llevar a cabo los diferentes procedimientos experimentales se ha demostrado mediante diversas técnicas de caracterización. Por ejemplo, se han hecho análisis de XPS, XRD y UV-Visible entre otros de la muestra, tanto antes como después de la reacción de fotocatálisis, resultando en una ausencia de diferencias significativas. Por tanto, se puede deducir que el vapor de agua interacciona con la superficie de la perovskita sin llegar a afectar a la esfera de coordinación del metal, y por lo tanto evitando su degradación.

La evolución de hidrógeno obtenida sigue una relación lineal con el tiempo. No obstante, aunque cabría esperar una relación lineal con

el oxígeno, esta condición estequiométrica no llega a cumplirse. Para demostrar que el origen del oxígeno producido no procede de otras fuentes que no sean la oxidación del agua, se realizan diferentes experimentos.

7.3. Perovskita híbrida como sensor de gas

A pesar de que en la bibliografía se reportan sensores de gases basados en diferentes perovskitas híbridas, hasta la fecha no existe ningún estudio comparativo donde se analice el efecto de la composición en sus propiedades de detección de gases. Por tanto, en esta tesis se presenta el primer estudio del papel que desempeñan diferentes cationes y aniones en la detección de COVs.

Concretamente, los sensores desarrollados están formados por materiales híbridos compuestos de perovskita híbrida y grafeno. Con la finalidad de dilucidar los efectos de la composición en el mecanismo de sensado, se sintetizaron nanocristales de perovskita con tres aniones y tres cationes diferentes. Además, cabe destacar que el grafeno utilizado contiene cierta cantidad de grupos oxigenados que le permite mejorar las propiedades de transporte a lo largo del material y mantener el carácter hidrofóbico que confiere estabilidad a los nanocristales de perovskita.

Los sensores se emplean para la detección a niveles traza de COV (benceno y tolueno) debido a su alta toxicidad. Los sensores desarrollados presentan un bajo consumo y capacidad para trabajar a temperatura ambiente. Asimismo, para potenciar su aplicabilidad en condiciones reales, se reproducen condiciones experimentales de monitorización ambiental. Las respuestas que se obtienen para ambos gases son altamente reproducibles y reversibles para todas las composiciones. No obstante, las mayores sensibilidades se registran para la perovskita con catión MA y anión Br. Esto puede ser debido a diversos factores, como una posición de los niveles energéticos favorables, la densidad de defectos superficiales o la movilidad de portadores.

7.4. Dispositivos fotovoltaicos

En un último artículo se plantea una nueva estrategia para incorporar huéspedes en la estructura de la perovskita, lo cual le confiere nuevas o mejores propiedades.

Las moléculas elegidas para ser introducidas como huésped son las SubPC, moléculas orgánicas cuya absorción complementa a la perfección con la perovskita multidimensional desarrollada en esta tesis. De forma que se logra expandir el espectro de fotorrespuesta del nanomaterial. De hecho, aunque la cantidad de SubPc incorporada es menor a un 3%, se consigue corroborar por diversas técnicas de caracterización su correcta incorporación en la estructura. Por ejemplo, mediante análisis de los picos de XRD, antes y después de incorporación de la SubPc. En estos espectros se aprecia un ligero desplazamiento en el pico de difracción.

Asimismo, se ha implementado este nuevo material híbrido en dispositivos fotovoltaicos. Aunque las eficiencias obtenidas son relativamente bajas, se demuestra que la estrategia diseñada para la inclusión de la SubPc es una estrategia válida.

CAPÍTULO 8

CONCLUSIONES

8. CONCLUSIONES

Las perovskitas híbridas han atraído un gran interés gracias a sus propiedades excepcionales, posicionándose como alternativa económica para diferentes campos de aplicación. En esta tesis se presentan diversos trabajos donde se demuestra que las perovskitas pueden ser exitosamente implementadas en aplicaciones de diversa índole. Cabe destacar, que el estudio de sus propiedades fundamentales también resulta de vital importancia. Por lo que asimismo se han estudiado con detalle los fenómenos ópticos que ocurren en su interior.

En los primeros trabajos de esta tesis se desarrollan dos métodos sencillos de síntesis para obtener cristales con una geometría definida. Se debe hacer hincapié en la importancia de obtener cristales de buena calidad para permitir el correcto estudio de sus propiedades ópticas, y así poder mejorar sus rendimientos en determinadas aplicaciones. Para ello, se estudian y optimizan diferentes parámetros de las síntesis. A modo de ejemplo, se demuestra que mediante el método de deposición por giro, ciertos parámetros como velocidad de rotación y el uso de aditivos permiten controlar los defectos, tamaño y geometría de los cristales.

Asimismo, en otro estudio relacionado se demuestra que es posible el uso de plantillas para conseguir cristales con formas específicas, permitiendo la creación de diversas composiciones de perovskita con estas formas determinadas. Cabe destacar que este método propuesto conlleva un bajo coste, ya que las plantillas utilizadas son obtenidas mediante réplicas en PDMS de un DVD o CD comercial.

Asimismo, el estudio de los fenómenos ópticos que ocurren en el interior del material ha revelado que los cristales con geometría plana presentan un comportamiento como cavidad tipo Fabry-Pérot. Mientras que las nanofibras pueden comportarse como guía de onda, permitiendo el transporte de la luz a lo largo de ella.

Para evaluar los resultados anteriores se propone un modelo teórico que permite obtener con precisión diferentes parámetros, y

con ello poder estudiar los procesos ópticos que ocurren en el material tras su iluminación. No obstante, existen ciertos parámetros externos que poseen una influencia significativa en la visibilidad de los fenómenos ópticos, limitando la información obtenida. Por tanto, el método desarrollado incluye como variables éstos parámetros externos. Además, con la obtención de esta información de manera individual (cristales aislados), se puede lograr una mejor comprensión del comportamiento macroscópico de material.

En cuanto a la aplicación de perovskitas en aplicaciones de fotocatálisis, es bien conocida la inestabilidad que presenta este tipo de materiales en condiciones ambientales y de humedad. Por ello, se ha llevado a cabo un estudio para demostrar que puede ser utilizada para la obtención de hidrógeno a partir de agua en determinadas condiciones y en ausencia de agentes sacrificantes. Por lo tanto, con este trabajo se abre la puerta a la utilización de las perovskitas híbridas halogenadas como fotocatalizador.

En relación al empleo de sensores de gases basados en perovskita, existe una información limitada acerca de las interacciones de este material con los gases. Asimismo, ningún estudio previo evalúa el sensado de gases mediante perovskitas con diferente composición. Por ello, esta tesis presenta por primera vez la comparación y estudio de la influencia de diferentes aniones y cationes en el mecanismo de sensado. Para ello, se han desarrollado sensores de gases basados en grafeno decorados con diferentes composiciones de perovskitas, con los que ha sido posible detectar COVs a niveles de ppm. Se obtienen respuestas variables según la composición de perovskita empleada, pero en todos los casos son reproducibles, reversibles, sensibles y ultrarápidas a temperatura ambiente. Estos resultados allanan el camino hacia el desarrollo de sensores económicos, duraderos y de bajo consumo energético para una potencial monitorización del aire. Además, se abre la puerta a crear una base de datos de composiciones de perovskita para adaptar la respuesta de los sensores a una gran franja de gases, punto importante para mejorar una de las limitaciones de los sensores químicos de tipo resistivo, que es la selectividad.

Por último, para aumentar las posibilidades y mejorar las limitaciones que presentan las perovskitas en su aplicación en el campo fotovoltaico, se busca una estrategia con una perovskita multidimensional 2D/3D mediante la inserción con moléculas orgánicas (SubPc). Para ello se desarrolla una metodología sencilla y prometedora con la que introducir moléculas fotoactivas en la estructura. De esta manera se consigue mantener las propiedades eléctricas idóneas de una estructura 3D, reduciendo la degradación del material gracias a las condiciones estructurales de una perovskita 2D y se expande la fotorrespuesta de nuestro material híbrido. Por lo que, se abre una nueva vía para diseñar materiales basados en perovskita.

En definitiva, de acuerdo con los resultados presentados, se puede concluir que se han alcanzado los principales objetivos de la tesis. Se ha mejorado el conocimiento sobre los fenómenos que ocurren internamente, logrando desarrollar nuevas aplicaciones para este tipo de material. Aunque todavía queda camino por recorrer antes de su aplicación comercial. Para ello, ciertos parámetros aún deben de ser mejorados y todavía es necesario un mayor conocimiento fundamental de las propiedades de las perovskitas.

Por ejemplo, para que una perovskita específica pueda actuar como guía de onda en aplicaciones ópticas resulta de vital importancia la ausencia de defectos. Pero, por el contrario, para el sensado de gases resulta interesante la presencia de defectos en el cristal, puesto que sirven como núcleos de interacción con los gases, mejorando su respuesta en la detección. Asimismo, según el compuesto que se quiera catalizar o el gas a detectar, una cierta composición puede ofrecer mejores resultados mientras pueden ofrecer resultados limitados para otros analitos.

Anexo A: Lista de publicaciones incluidas en la tesis

- **"Single Crystal Growth of Hybrid Lead Bromide Perovskites Using a Spin-Coating Method".**
  Rocío García-Aboal, Roberto Fenollosa, Fernando Ramiro-Manzano, Isabelle Rodríguez, Francisco Meseguer, and Pedro Atienzar.
  ACS Omega 2018, 3, 5229–5236. *DOI: 10.1021/acsomega.8b00447.*

- **"Optical properties of organic/inorganic perovskite microcrystals through the characterization of Fabry-Pérot resonances".**
  Fernando Ramiro-Manzano, Rocío García-Aboal, Roberto Fenollosa, Stefano Biasi, Pedro Atienzar, and Francisco Meseguer.
  Dalton Trans. 2020, 49, 12798. *DOI: 10.1039/d0dt02254c*.

- **"Groove-assisted solution growth of lead bromide perovskite aligned nanowires: a simple method towards photoluminescent materials with guiding light properties".**
  Isabelle Rodriguez, Roberto Fenollosa, Fernando Ramiro-Manzano, Rocío García-Aboal, Pedro Atienzar and Francisco J. Meseguer.
  Mater. Chem. Front. 2019, 3, 1754. *DOI: 10.1039/c9qm00210.*

- **"Vapor-Phase Photocatalytic OverallWater Splitting Using Hybrid Methylammonium Copper and Lead Perovskites".**
  Teresa García, Rocío García-Aboal, Josep Albero, Pedro Atienzar and Hermenegildo García.
  Nanomaterials 2020, 10, 960. *DOI: 10.3390/nano10050960.*

- **"The role of anions and cations in the gas sensing mechanisms of graphene decorated with lead halide perovskite nanocrystals".**
  Juan Casanova-Chafer, Rocío García-Aboal, Pedro Atienzar and Eduard Llobet.
  Chem. Comm. 2020, 56 (63), 8956-8959. *DOI: 10.1039/d0cc02984j.*

- **"Expanding the photoresponse of multidimensional hybrid lead bromide perovskites into the visible region by incorporation of subphthalocyanine".**
  Rocío García-Aboal, Hermenegildo García, Sonia Remiro-Buenamañana and Pedro Atienzar.
  Dalton Trans., 2021, 50, 6100. *DOI: 10.1039/d0dt04132g.*

Anexo B:

Lista de publicaciones no incluidas:

- **"Gas sensing properties of perovskite decorated graphene at room temperature"**
  Juan Casanova-Chafer, Rocio García-Aboal, Pedro Atienzar and Eduard Llobet.
  Sensors 2019, 19, 4563. *DOI: 10.3390/s19204563.*

- **"Enhanced photocatalytic activity and stability in hydrogen evolution of mo6 iodide clusters supported on graphene oxide"**
  Marta Puche, Rocio Garcia-Aboal, Maxim A. Mihaylov, Maxim N. Sokolov, Pedro Atienzar and Marta Feliz.
  Nanomaterials 2020, 10(7), 1259. *DOI: 10.3390/nano10071259.*

- **"Photoactive Zr and Ti Metal-Organic-Frameworks for Solid-State Solar Cells"**
  Arianna Melillo, Rocío García-Aboal, Sergio Navalón, Pedro Atienzar, Belén Ferrer, Mercedes Álvaro and Hermenegildo García.
  ChemPhysChem 2021, 22, 1 –8. *DOI: 10.1002/cphc.202100083.*

- **"Perovskite@Graphene Nanohybrids for Breath Analysis: A Proof-of-Concept"**
  Juan Casanova-Chafer, Rocio Garcia-Aboal, Pedro Atienzar, Carla Bittencourt and Eduard Llobet
  Chemosensors 2021, 9, 215. DOI: 10.3390/chemosensors9080215.

Patente:

- **"Sensores de gases". ES, P202030687**
  Fecha de prioridad: 03/06/2020

<u>Anexo C:</u> **1er Premio fotografía científica "La ciencia es FantástITQa" (2018)**

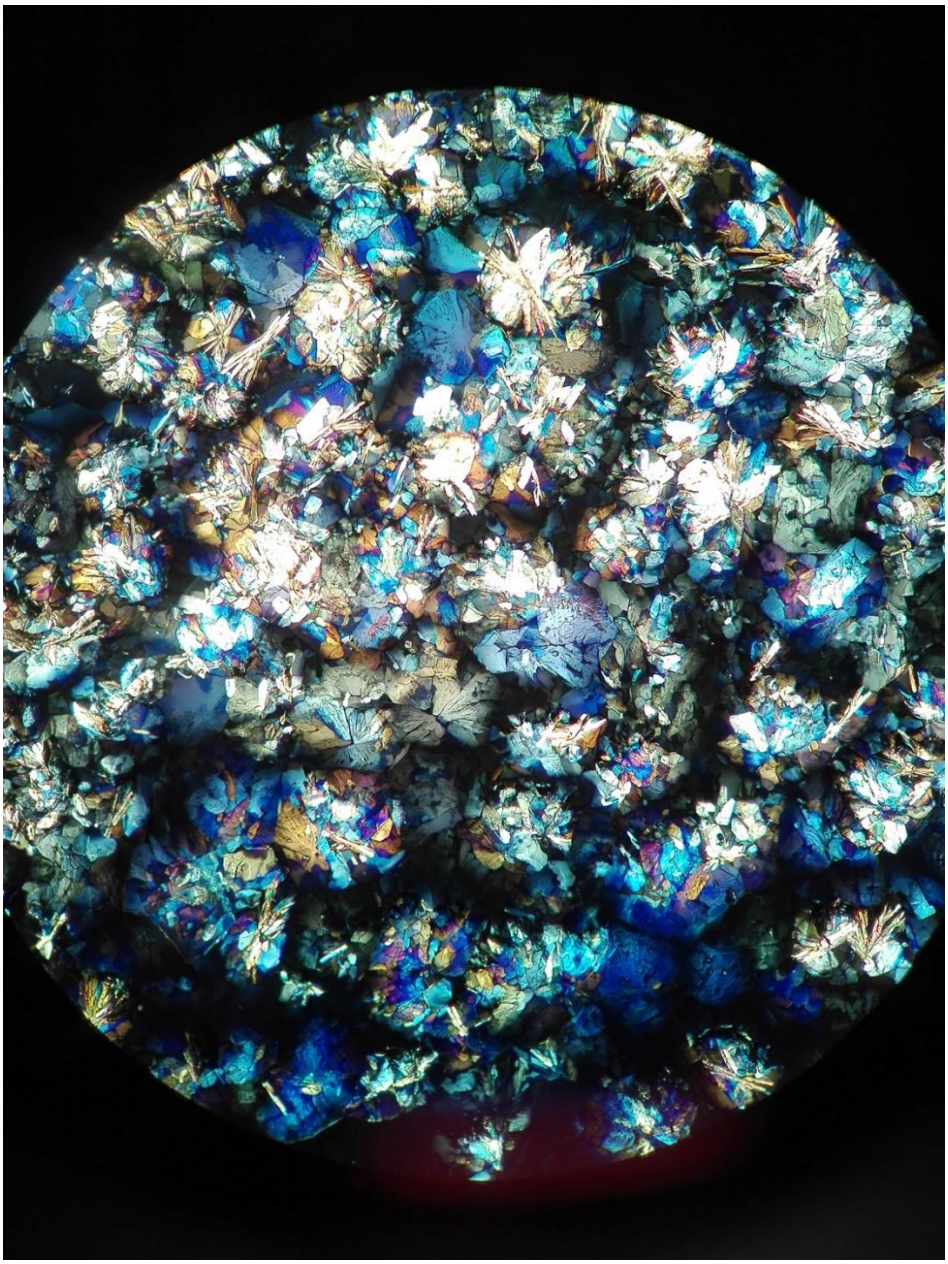

"CALEIDOVSKITA"

<u>Anexo D</u>: 1er Premio fotografía científica "La ciencia es FantástITQa" (2020)

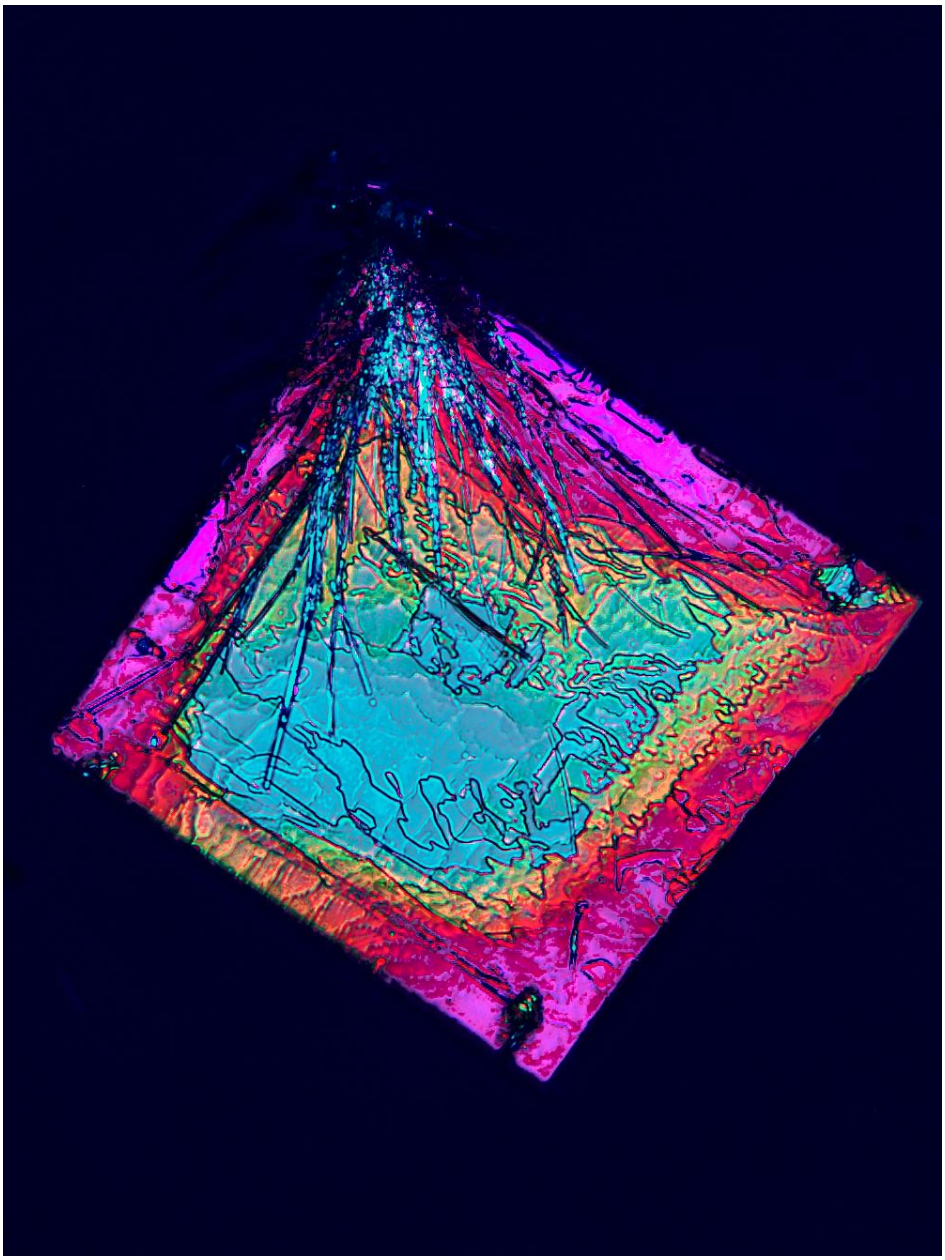

"VOLKANITA

ANEXO E:

Volume 3 | Number 9 | September 2019

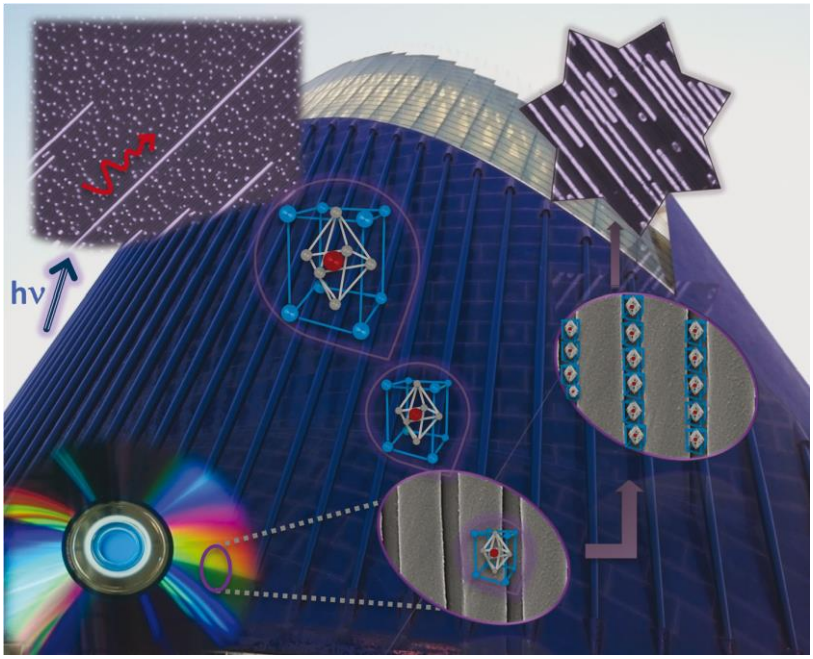

MATERIALS CHEMISTRY

FRONTIERS

CCS 中国化学会 CHINESE CHEMICAL SOCIETY
ICCAS
ROYAL SOCIETY OF CHEMISTRY | Celebrating IYPT 2019

ANEXO F:

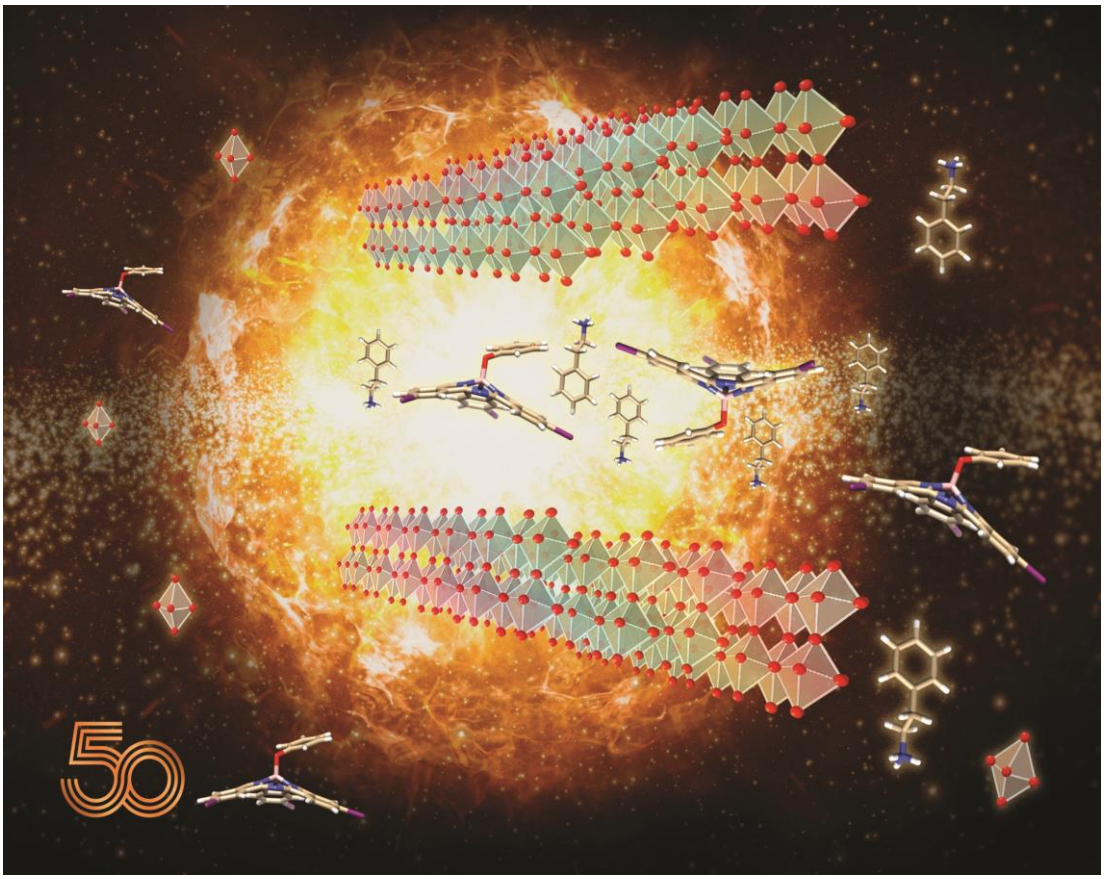

Showcasing research from Rocío García-Aboal, Hermenegildo García, Sonia Remiro-Buenamañana and Pedro Atienzar from Instituto de Tecnología Química, Universitat Politècnica de València-Consejo Superior de Investigaciones Científicas, Valencia, Spain.

Expanding the photoresponse of multidimensional hybrid lead bromide perovskites into the visible region by incorporation of subphthalocyanine

A new methodology to enhance the photoresponse of multidimensional 2D–3D perovskites is proposed. The use of large organic cations allows the possibility to insert guest molecules in the crystal structure of the perovskite. Incorporation of metal-free subphthalocyanine in the interlayer space is provided by the 2D phase.

As featured

See Sonia Remiro-Buenamañana, Pedro Atienzar et al., Dalton Trans., 2021, 50, 6100.